DYNAMIC MODELLING OF MINING-INDUCED FAULT-SLIP

By

Atsushi Sainoki

A thesis submitted to McGill University in partial fulfillment of the requirements of the degree of Doctor of Philosophy in Mining Engineering

Doctor of Philosophy

Department of Mining & Materials Engineering

McGill University, Montreal

February, 2014

Dedication

This work is dedicated to my father, mother, grandfather, and grandmother who raised me, respected the intention of mine, and supported my living.

Acknowledgements

I would like to express my gratitude to Prof. Hani Mitri. He has helped and supported me ever since I sent the first e-mail to him from Japan in order to join the Mine Design and Numerical Modelling Laboratory at McGill University. Without his support, I could not have come to McGill University to study for my PhD in mining engineering. I also would like to thank him with respect for his incisive opinions and outstanding ideas to my research, owing to which I could address the study problems in this thesis.

I wish to thank Dr. Denis Thibodeau and Ms. Lindsay Moreau-Verlaan at Garson Mine of Vale – Sudbury Operations. Dr. Denis gave me practical advice from the viewpoint of mining engineers working at mines. His advices have had a positive influence on my research. Ms. Lindsay processed the microseismic data and spent time with me explaining the database. I am grateful for her help.

I sincerely appreciate my Master's thesis supervisor Professor Katsuhiko Kaneko who taught me the fundamentals of numerical analysis, especially finite element method, as well as programing language. The knowledge that I gained under his supervision has greatly contributed to my PhD research at McGill University. I also wish to thank Dr. Daisuke Fukuda, who helped me improve my English writing and speaking skills before I came to Canada.

I would like to thank my colleagues in the Mine Design Laboratory, Dr. Shahe Shnorhokian, Dr. Tarek Hamade, Dr. G. D. Raju, Dr. Wael E. Abdellah, and Mr. Zaka Emad. I really enjoyed the discussions we exchanged about our research projects. I will never forget the time that I had with them in the Mine Design Laboratory.

Last but not least, I wish to express my sincere gratitude to my family and thank them from the bottom of my heart. Over the years, they gave me lots of support and encouragement, owing to which I was able to complete my study.

Contributions of Authors

This thesis is prepared in accordance with the guidelines of the Graduate and Postdoctoral Studies (GPS) office of McGill University for a manuscript-based thesis. The following six manuscripts are used to prepare this thesis:

1. **Sainoki, A.** and Mitri, H. S. (2014). Dynamic modelling of mining-induced fault-slip, Int. J. Rock Mechanics and Mining Sciences, Vol.66, pp.19-29

2. **Sainoki, A.** and Mitri, H. S. (2014). Dynamic modelling of Fault-slip with Barton's Shear Strength Model, Int. J. Rock Mechanics and Mining Sciences, Vol.67, pp.155-163

3. **Sainoki, A.** and Mitri, H. S. (2013). Dynamic Modelling of Fault-slip Induced by Stress Waves due to Stope Production Blasts, Rock Mechanics and Rock Engineering, Manuscript No.: RMRE-D-13-00344 (Under review)

4. **Sainoki, A.** and Mitri, H. S. (2014). Simulating Intense Shock Pulses due to Asperities on a Fault during Fault-slip, Journal of Applied Geophysics, Vol.103, pp.71-81

5. **Sainoki, A.,** Mitri, H. S., Shnorhokian, S., and Moreau-Verlaan, L. (2013). Back Analysis of Fault-slip in Burst Prone Environment (to be submitted)

6. **Sainoki, A.** and Mitri, H. S. (2013). Effect of Slip-weakening Distance on Seismic Source Parameters of Mining-induced Fault-slip, Int. J. of Rock Mechanics and Mining Sciences, Manuscript No. IJRMMS-D-14-00086

Papers Presented in Conferences

1. **Sainoki, A.** and Mitri, H. S. (2013). Dynamic Numerical Modelling of Seismic Response due to Fault-slip. Tunnels and Underground Spaces: Sustainability and Innovation, Montreal, Canada, Paper No.136.

2. **Sainoki, A.** and Mitri, H. S. (2013). Comparative Study of Shear Strength Models for Fault-slip Analysis. In the proceedings of Sinorock, Shanghai, China. Taylor & Francis Group, London, pp. 551-556.

3. **Sainoki, A.** and Mitri, H. S. (2013). Effect of Stope Production Blasts on a Nearby Fault, World Mining Congress, Montreal, Canada, Paper No. 175.

4. **Sainoki, A.** and Mitri, H. S. (2013). Dynamic Modelling of Mining-induced Fault-slip. In the proceedings of Eurock 2013, Poland, pp. 763-768

5. **Sainoki, A.** and Mitri, H. S. (2013). Effect of Fault Surface Asperities on Seismic Waves during Fault-slip. International Symposium on Mine Safety and Engineering 2013, Beijing, China.

The manuscripts 1, 2, 3, 4, 5 and 6 are presented as chapters 3, 4, 5, 6, 7, and 8 respectively in the thesis. The conference papers will not be presented in the thesis as they are already part of the journal manuscripts.

All of the manuscripts are co-authored by Prof. Hani S. Mitri, the supervisor of the thesis. Manuscript 5 is additionally co-authored by Dr. Shahe Shnorhokian, a research associate at McGill, and chief Engineer. Ms. Lindsay Moreau-Verlaan from Vale Ltd in Sudbury, Ontario. The co-authors provided support and reviewed the manuscripts. Also, this work is financially supported by a research grant from the Natural Sciences and Engineering Research Council of Canada (NSERC) in partnership with Vale Limited.

Table of Contents

List of Figures

List of Tables

Abstract

In deep hard rock mines where high stress conditions due to overburden pressure and plate tectonics take place, rockbursts are serious problems to cope with because rockbursts could result in devastating damage to mine openings. It is widely recognized that mining activities could reactivate faults in underground mines. The reactivation of faults could then cause fault-slip. More importantly, fault-slip gives rise to seismic waves, which inflict severe damage to mine openings when hitting their surfaces. Because the generation and propagation of seismic waves are dynamic phenomena, fault-slip needs to be also dealt with as a dynamic phenomenon entailing the release of seismic energy to surrounding areas. Both of the static and dynamic behaviour of faults should be examined, considering the effects of mining activities on the faults, in order to estimate the damage induced by the seismic waves arising from fault-slip.

First, a literature review is conducted with respect to constitutive models governing fault behaviour, fault characteristics, fault-slip simulation and seismic source parameters. The review has revealed that although a number of dynamic and static friction laws have been proposed, the friction laws have been rarely employed for the simulation of fault-slip taking place in underground mines. The review has also revealed that most of the simulations have been conducted in static conditions. In this thesis, dynamic modelling of mining-induced fault-slip is presented using a mine-wide model encompassing a fault running parallel to a steeply, dipping orebody. Furthermore, a case study of Garson Mine, Sudbury, Canada is carried out.

A parametrical study with a mine-wide 3D model has led to the following conclusions: (a) mining depth, friction angle of the fault, and fault locations exert a large influence on the maximum relative shear displacements on the fault, while the dilation angle and stiffness of the fault do not, (b) maximum slip rates appear to increase with the maximum slip, (c) extremely high rupture velocity could be induced when faults are parallel to the orebody. Results obtained from the numerical analysis in which Barton's shear strength model is implemented

have shown that fault surface roughness strongly affects the intensity of seismic waves arising from fault-slip and seismically radiated energy. The results imply that fault-slip taking place on faults with rough surfaces could become more violent. The effect of stope production blasts on a nearby fault is also examined while considering several types of blast sequences. The results obtained from the analysis have indicated that performing stope production blasts in timed sequence could induce a larger seismic event on the fault than triggering the blasts simultaneously. Dynamic analysis taking into account the collision and unloading of fault surface asperities is also conducted with Saeb and Amadei's constitutive model. It is found from the study that the release of normal stress due to fault unloading has a large influence on the intensity of seismic waves. When the stress release is significant, peak particle velocity could be three times as large as that obtained from a model assuming a completely planar fault. The effect of slip-weakening distance on seismic source parameters of fault-slip is also investigated with a linear slip-weakening friction law. The study has indicated that slip rates and seismically radiated energy are significantly affected by the slip-weakening distance, while seismic moment appears not to be susceptible to the slip-weakening distance in a case that fault-slip takes place only within limited areas.

Back analysis of fault-slip to estimate the physical and mechanical properties of shear/fracture zones is carried out for Garson Mine. The back analysis is conducted with respect to moment magnitude and peak particle velocities recorded by seismic monitoring systems installed in the mine. Fault surface roughness and a dynamic friction angle have been calibrated. Afterwards, the calibrated values are validated with peak ground acceleration recorded by the monitoring system. Through the study, a methodology to calibrate the physical and mechanical properties of faults by means of ground motion excited by seismic waves arising from fault-slip as well as seismic source parameters of the fault-slip has been developed.

Résumé

Dans les mines profondes ou des contraintes élevées se produisent due à la contrainte de surcharge ainsi que les plaques tectoniques, les coups de terrain sont un problème sérieux car les ils peuvent endommager les ouvertures minières. Il est largement reconnu que les activités minières peuvent réactiver des failles dans les mines sous-terraines. La réactivation de ces failles peut entrainer un glissement de faille. Surtout, le glissement de faille fait naitre des ondes sismiques qui infligent des dégâts sérieux quand elles frappent la surface des ouvertures minières. Le génération et la propagation des ondes sismiques sont des phénomènes dynamiques. Il s'ensuit donc que le glissement de faille doit être traité comme un phénomène dynamique, entrainant un dégagement d'énergie sismique dans son entourage. Le comportement dynamique ainsi que le comportement statique des failles doit être examiné en considérant les effets des activités minières pour estimer les dégâts causés par les ondes sismiques qui proviennent d'un glissement de faille.

Premièrement, un examen de la documentation est effectué sur les modèles constitutifs des failles qui gouvernent le comportement des failles, les caractéristiques de failles, la simulation de glissement de faille, et les paramètres de la source sismique. L'examen a révélé que même si un nombre de lois statiques et dynamiques de frottement ont été proposés, ces lois de frottement ont été peu employés pour simuler les glissements de faille que se déroulent dans les mines sous-terraines. La revue a aussi révélé que la majorité des simulations ont été conduites en conditions statiques. Dans cette thèse, la modélisation dynamique d'un glissement de faille induit par des activités minières est présenté. Le modèle englobe l'entièreté d'une mine, avec une faille qui est parallèle au gisement fortement incliné. En plus, une étude de cas pour la mine Garson à Sudbury, au Canada, est effectuée.

Une étude paramétrique avec un modèle de mine en trois dimensions mène aux conclusions suivantes: (a) la profondeur d'exploitation minière, l'angle de friction de la faille, et la position de la faille ont une grande influence sur les

déplacement relatifs en cisaillement d'une faille, tandis que l'angle de dilation de la faille et la dureté ont peu d'effet, (b) le taux de glissement maximal augmente en fonction du glissement absolu, (c) une très haute vélocité de rupture peut être induite lorsque la faille est parallèle au gisement. Les résultats obtenus du modèle numérique dans lequel le modèle de résistance au cisaillement de Barton est implémenté ont démontré que la rugosité de la surface de la faille affecte grandement l'intensité des ondes sismiques qui émanent du glissement de faille et l'énergie sismique propagée. Les résultats impliquent qu'un glissement de faille survenant à une faille rugueuse est plus violent. L'effet produit par un sautage de production sur une faille proche est aussi examiné en considérant plusieurs séquences de sautage. Les résultats de l'analyse indiquent qu'un sautage de production exécuté selon une séquence temporelle peut induire un plus grand événement sismique qu'un sautage simultané. Une analyse dynamique tenant compte la collision et le déchargement d'une faille selon le modèle constitutif de Saeb et Amadei est aussi conduite. Il est démontré que le relâchement de la contrainte normale à la faille a une grande influence sur l'intensité des ondes sismiques. Lorsque le relâchement de contraintes est importante, la vitesse de crête des particules peut être trois fois plus élevée que celle obtenue avec un modèle qui teins pour acquis une faille lisse. L'effet de la distance d'affaiblissement de faille due glissement sur les paramètres sismiques est aussi examiné avec une loi de friction linéaire d'affaiblissement due au glissage. L'étude indique que le taux de glissement et l'énergie sismique émanée sont significativement affectés par le distance d'affaiblissement de faille, tandis que le moment sismique n'est pas susceptible à la distance d'affaiblissement dans le cas ou le glissement de faille se déroule seulement dans une zone limitée.

Pour estimer l'effet des propriétés physiques et mécaniques de la zone de cisaillement, une analyse régressive est exécutée pour la mine Garson. L'analyse est conduite selon la magnitude du moment et la vitesse de crête des particules enregistrées par le système de contrôle sismique installé à la mine. La

rugosité de la surface de la faille et l'angle de friction dynamique sont étalonnés. Ensuite, les paramètres étalonnés sont validés par rapport à l'accélération maximale du terrain enregistré par le système de contrôle. À travers l'étude, une méthodologie pour étalonner les propriétés physiques et mécaniques de la faille selon l'étude du mouvement du terrain due aux ondes sismiques émanant d'un glissement de faille est développé.

CHAPTER 1

Introduction

1.1 General

There has been a great demand for mineral resources since the last century due to rapid economic growth in many countries, such as China and India; and it will continue to grow for many years to come so as to supply sufficient resources to all over the world. In order to meet the demand, underground mines have been developed at great depths (Ortlepp, 2000; Sneilling, Godin, & McKinnon, 2013). As mining depths increase, stress conditions become favorable for rockbursts to take place due to increasing overburden pressure and corresponding horizontal stresses affected by plate tectonics. Thus, it is indispensable to develop better understanding of rockbursts occurring in underground mines operated at great depths in order to prevent and control the occurrence of rockbursts. These knowledge leads to realizing stable production and safe operation at such great depths.

A Rockburst is defined as a sudden, violent failure of a large volume of overstressed rock, resulting in the instantaneous release of large amounts of accumulated energy (Blake & Hedley, 2003); and rockbursts taking place in underground mines are generally classified into three types, namely strain burst, pillar burst, and fault-slip burst. Although strain bursts and pillar bursts account for a large fraction of the incidence of rockbursts, the severity of damage inflicted by the rockbursts is not significantly high, compared to that caused by fault-slip bursts. This is because strain bursts and pillar bursts take place in relatively limited areas where stresses are locally concentrated due to stress re-distribution resulting from mining activities, such as the surfaces of mine openings and remnant pillars. As reported by Alber (2013), the magnitudes of strain bursts are generally less than 0; and the magnitudes of pillar bursts usually fall between 1.0

and 2.5. In contrast, seismic events induced by shear failure of rockmasses or fault reactivation have magnitudes greater than 2.5; occasionally the magnitude exceeds 4.0 (Alber, 2013; Hofmann & Scheepers, 2011), thus resulting in devastating damage to mine openings in a large area within underground mines.

Microseismic monitoring is widely recognized as a useful tool to estimate the locations and magnitudes of seismic events including rockbursts (Domanski & Gibowicz, 2008; Trifu & Urbancic, 1996); monitoring systems have been installed in a number of underground mines all over the world. Seismic source parameters, such as seismic moment, seismically radiated energy, and apparent stress, can be computed on the basis of waveforms recorded by the monitoring system. These parameters are helpful to characterize the seismic events, understand mechanisms involved, and estimate mining-induced stress changes that caused the seismic events. However, it is difficult to estimate the occurrence of possible rockbursts according to the progress of planned mining sequences. Hence, it is strongly required to develop a new methodology for estimating seismic source parameters of rockbursts prior to the occurrence, considering mine developments and mining activities.

1.2 Fault-slip in underground mines

Fault-slip bursts are caused by fault-slip along pre-existing faults (fault reactivation) and/or violent shear failure within intact rock. Such fault-slip is induced by stress waves arising from blasts performed in underground mines as well as mining-induced stress changes, which could result in an increase in shear stress and a decrease in normal stress acting on the fault. Damage inflicted by fault-slip is due to either slip movements along the faults (B. G. White & Whyatt, 1999) or seismic waves arising from fault-slip (Ortlepp, 1992). Importantly, the intensity of seismic waves arising from the fault-slip pertains to the dynamic response of the fault during fault-slip. In addition, the propagation of the seismic

waves through rockmasses is also a dynamic phenomenon, in which seismic wave attenuation must be taken into consideration. Thus, appreciation of the dynamic behaviour of faults during fault-slip is of pivotal importance in dealing with fault-slip.

The behaviour of faults is largely governed by frictional resistance of fault surfaces. A fault starts to slip when shear stress acting on the fault reaches the maximum shear strength determined by a static friction law. After the onset of fault-slip, the shear resistance of the fault varies, depending on induced shear displacements and slip rates. As for the static friction law determining the occurrence of fault-slip, many studies have been conducted in the field of rock mechanics. As a result, a number of shear strength models which can take into account the effect of fault surface asperities on the static shear strength of fault surfaces have been proposed. Regarding the dynamic friction law governing the dynamic response of faults, significant efforts have been made in the field of geophysics for the better understanding of the dynamic response as a source for large-scale earthquakes. Owing to the studies, many dynamic friction laws have been proposed, which allow for a change in kinetic friction dependent upon slip rates and relative shear displacement increments during fault-slip.

Applying the static and dynamic friction laws to fault-slip occurring in underground mines has been barely tried in mining contexts mainly because of the capability of commercial software available. The classical Mohr-Coulomb criterion has been widely used for fault stability analysis in underground mines because of its simplicity. However, the frictional resistance of fault surfaces is dependent upon many factors, such as the geometries of fault-surface asperities and slip movements. Furthermore, the characteristics of seismic waves arising from fault-slip relate to dynamic slip movements of the fault. Hence, it is necessary to consider such friction models capable of allowing for the

characteristics of faults for the better understanding of fault behaviour in both of static and dynamic conditions.

1.3 Numerical Analysis

Numerical analysis is one of the widely recognized methods that can be utilized to investigate the behaviour of faults in rock mechanics and geophysics. In the field of geophysics, the proposed dynamic friction laws have been applied to the simulation of fault-slip (Bizzarri, 2012; Oglesby & Mai, 2012; Tinti, Bizzarri, Piatanesi, & Cocco, 2004) with numerical methods, such as the finite element method and boundary integral method, for the purpose of elucidating the dynamic behaviour of faults as a source of earthquakes. In the field of rock mechanics, the simulation of fault-slip in underground mines has been carried out, aiming at estimating the mechanical properties of faults, evaluating fault-slip potential, and investigating the effect of faults on ambient stress states, albeit the classical Mohr-Coulomb criterion has been mainly used under static conditions (Alber, Fritschen, Bischoff, & Meier, 2009; Hofmann & Scheepers, 2011; Sneilling et al., 2013).

The mechanism of fault-slip taking place in underground mines, which is the same as that of earthquakes occurring at shallow depths (Gibowicz & Kijko, 1994), is accounted for by stick-slip (Brace & Byerlee, 1966). Thus, it is advisable to perform numerical analysis under dynamic conditions while applying the dynamic friction laws developed for simulating fault-slip during earthquakes. The study leads to the better understanding of fault-slip taking place in underground mines.

Nowadays, the capacity of personal computers has been drastically improving, especially in terms of memory size and CPU speed. Thus, it is possible to perform dynamic analysis with a mine-wide 3D model encompassing complex

geological structures extensively, and a large number of nodes and elements. In addition, it is also possible to examine the effects of the progress of mining sequences as well as the interaction of geological structures with faults by means of the model in which complex geometries of orebodies and geological structures are simulated. Performing the numerical analysis, which had been difficult to carry out in the past, is definitely of help for addressing problems related to mining-induced fault-slip.

1.4 Scope and Objectives

In the present study, fault-slip taking place in underground mines is investigated. Especially, hard rock mines located at great depths are focused on, which have a steeply dipping, tabular orebodies. As mentioned in the previous sections, fault-slip is intrinsically dynamic behaviour entailing seismic waves and ground motion, and involves a number of physical phenomena to consider; hence the dynamic behaviour of faults in underground mines has not yet been comprehended well. Although all of the physical phenomena should be taken into account when fault-slip is simulated, it is still impossible because an unrealistically large number of meshes are required; for instance, replicating geometries of the fault-surface asperities precisely is required to simulate the breakage process of fault-surface asperities during fault-slip. Evidently, it would take an immense amount of time to complete calculations. Hence, from amongst the mechanisms involved in fault-slip, the present study focuses on the following topics:

- The effect of physical and mechanical properties of a fault on seismic source parameters of fault-slip
- The effect of stope production blasts on a nearby fault

- The effect of fault-surface asperities on the intensity of seismic waves arising from fault-slip
- Estimating physical and mechanical properties of causative shear or fracture zones for fault-slip

Basically, a conceptual mine-wide model encompassing a fault running parallel to a steeply dipping, tabular orebody is used to investigate the dynamic behaviour of the fault, excluding the study to estimate the mechanical and physical properties of causative shear or fracture zones for fault-slip. As for the study, a case study is carried out on the basis of data collected from Garson Mine in Sudbury, ON, Canada; and a mine-wide model generated by Shnorhokian, Mitri, Thibodeau, and Moreau-Verlaan (2013) on the basis of the mine is used.

The objectives of this study is gaining a fundamental knowledge about fault-slip taking place in hard rock mines operated at great depths through examining the aforementioned topics under dynamic conditions. In addition, this study also aims at developing new methodologies to estimate the physical and mechanical properties of causative faults for fault-slip with back analysis in conjunction with waveform data recorded by microseismic monitoring systems.

1.5 Thesis outline

This thesis consists of the following chapters that cover the topics described in the previous section.

Chapter 1 presents general overview of mining-induced fault-slip, study problems to be addressed, and scope and objectives of this study.

Chapter 2 presents literature review of studies that have been done for the behaviour and characteristics of faults and rock discontinuities as well as numerical analysis used to simulate fault-slip.

Chapter 3 presents a model parametrical study carried out in order to investigate influencing factors on the behaviour of a fault, such as mining depths, the friction angle and stiffness of the fault, and fault locations. The effect of the factors on seismic source parameters of fault-slip is examined with the conceptual model.

Chapter 4 presents dynamic modelling of fault-slip with Barton's shear strength model. A fault-slip simulation technique to take into account fault surface asperities is developed; and the effect of fault-surface asperities on the dynamic behaviour of fault-slip is examined with the conceptual model.

Chapter 5 presents the effect of stope production blasts on a nearby fault. Stress waves induced by the production blasts are simulated after calibrating rockmass properties and borehole pressure by means of a charge weight scaling law. Fault-slip induced by the stress waves is simulated and discussed with respect to seismic source parameters of the induced fault-slip.

Chapter 6 presents the effect of fault surface asperities on the intensity of seismic waves arising from fault-slip. Stress changes due to the collision and unloading of fault surface asperities during fault-slip are simulated with Saeb and Amadei's model; and the influence of the stress change on seismic waves arising from the fault-slip is examined with respect to particle velocities of rockmasses.

Chapter 7 presents a methodology to estimate the physical and mechanical properties of causative shear and fracture zones for fault-slip with back analysis using the mine-wide Garson Model (Shnorhokian et al., 2013). The back analysis

is carried out using peak particle velocities and peak acceleration estimated from wave forms recorded by microseismic monitoring system installed in Garson Mine.

Chapter 8 presents the effect of characteristic slip-weakening distances on seismic source parameters of fault-slip. Fault-slip is simulated with a linear slip-weakening law, using Barton's shear strength model and the classical Mohr-Coulomb criterion as static and dynamic shear strength models, respectively. The importance of considering the characteristic slip-weakening distance in estimating the magnitudes and seismically radiated energy of fault-slip is discussed.

CHAPTER 2

Literature review

2.1 General

The behavior of faults is dependent upon a number of factors, such as static and dynamic friction laws, geometries of fault surface asperities, and its stiffness. Many studies have been conducted experimentally and numerically for the better understanding of the behaviour of faults in the fields of rock mechanics and geophysics. This chapter describes and summarizes the previous studies.

2.2 Static shear strength models

It is the classical Mohr-Coulomb criterion that is used the most widely for the stability analysis of faults in underground mines (Alber et al., 2009; Hofmann & Scheepers, 2011; Potvin, Jarufe, & Wesseloo, 2010; Sjoberg et al., 2012; Sneilling et al., 2013) because of its simplicity. The failure criterion is expressed as follows:

$$\tau_{\max} = \sigma_n \tan\phi_b \tag{2-1}$$

where τ_{max} is the maximum shear strength on a discontinuity; σ_n is normal stress acting on the discontinuity; ϕ_b is a basic friction angle, which is generally obtained from tilt tests. As shown in Equation 2-1, the failure criterion can be readily employed to analyze the behaviour of geological discontinuities given that the basic friction angle of causative geological discontinuities is already known. However, many studies have revealed that the shear strength of geological discontinuities is susceptible to many other factors, such as fault surface asperities and infilling materials.

A number of shear strength models have been developed, which can take into consideration the mechanical and physical properties of surfaces of geological discontinuities. As reviewed by Barton (1973), Newland and Allely (1957) proposed a shear strength model for rock joints with saw-tooth surfaces. The equation is given as:

$$\tau_{\max} = \sigma_n \tan(\phi_b + i) \tag{2-2}$$

where the angle, *i*, represents the angle of asperity. Although Equation 2-2 yields the shear strength of geological discontinuities with saw-tooth surfaces, the geometry of fault surface asperities is intrinsically susceptible to normal stress acting on the discontinuities. It means that the angle, *i*, should be a function of the normal stress. Shear strength models taking into account the effect of normal stress as well as fault-surface asperities on the shear strength of geological discontinuities have been thus developed. Barton (1973) proposed an empirical shear strength model for unfilled rock joints on the basis of experimental results from direct shear tests performed on artificial rough tension joints of a brittle model material. The proposed shear strength model is given as:

$$\tau_{\max} = \sigma_n \tan\left[JRC \log_{10}\left(\frac{JCS}{\sigma_n} \right) + \phi_b \right] \tag{2-3}$$

where *JRC* represents a joint roughness coefficient; *JCS* represents joint wall compressive strength. *JRC* ranges from 0 to 20. *JRC* of 0 can be considered a joint with a completely planar surface. It should be noted that when *JRC* is 0, Equation 2-3 becomes equal to the classical Mohr-Coulomb criterion defined by Equation 2-1. *JRC* of 20, on the other hand, corresponds with significantly rough joints generated from tensile failure. It is found from the term, $JRC\log10(JCS/\sigma_n)$, in Equation 2-3, that a joint roughness coefficient varies depending on normal stress acing on the joint, which means that Barton's model can takes into

account the deformation and breakage of joint surface asperities due to normal stress acting on the joint. Importantly, Barton's model is valid when the normal stress is less than joint wall compressive strength.

After Barton's shear strength model was initially proposed, many improvements have been made and incorporated into the shear strength model. For instance, Barton and Choubey (1977) used a residual friction angle, ϕ_r, for general expression instead of the use of a basic friction angle in Equation 2-3. In addition, Barton, Bandis, and Bakhtar (1985) considered the effect of increasing shear displacement increments during frictional sliding on the joint roughness coefficient since it is presumably expected that fault surface asperities are sheared off according to the increase in slip movements. The mobilized joint roughness coefficients are shown in Table 2-1. Table 2-1 shows the slip dependency of shear strength of rock joints; the increase in a mobilized joint roughness coefficient with shear displacement is attributed to an increase in a degree of interlocking of joint surface asperities; the decrease in the joint roughness after shear displacement reaches the peak value is due to abrasion of surface asperities. It is obvious that post-peak behaviour induced by the decrease in a joint roughness coefficient is of paramount importance for the better understanding of fault-slip. Recently, Asadollahi and Tonon (2010) proposed an empirical relationship between the decrease in joint surface roughness and increase in shear displacement on the basis of results obtained from direct shear tests. The proposed equation is expressed as follows:

$$\frac{JRC_{mobilized}}{JRC_{peak}} = \left(\frac{\delta_{peak}}{\delta} \right)^{0.381} \tag{2-4}$$

An important difference between $JRC_{\text{mobilized}}$ obtained from Table 2-1 and Equation 2-4 is that $JRC_{\text{mobilized}}$ derived from Equation 2-4 does not reach 0, which indicates that shear strength of rock joints continues to decrease with the increasing shear displacement.

Table 2-1: Relation between shear displacement increments and joint roughness coefficients

δ/δ_{peak}	$JRC_{mobilized}/JRC_{peak}$
0	$-\phi_r/i$
0.3	0
0.6	0.75
1	1
2	0.85
4	0.7
10	0.5
25	0.4
100	0

in which $i = JRC_p \log\left(\frac{JCS}{\sigma_n}\right)$; ϕ_r is a residual friction angle; δ_{peak} is peak shear displacement at which shear stress takes the maximum value.

The equations relating JRC with shear displacement increments suggest that a proper estimation of peak shear displacement is of pivotal importance in obtaining appropriate post-peak behaviour of rock joints. Barton and Choubey (1977) proposed the following relationship.

$$\delta_{peak} = \frac{L}{100} \tag{2-5}$$

where L represents joint length; the equation is based on an assumption that peak shear displacement is 1 % of joint length on which the shear displacement

is induced. Barton et al. (1985) developed the equation to take into consideration the effect of JRC on peak shear displacement on the basis of analysis of 650 shear test data, which is given as:

$$\delta_{peak} = \frac{L}{500}\left(\frac{JRC}{L}\right)^{0.33} \tag{2-6}$$

It is found from Equation 2-6 that joints with rough surfaces have large peak shear displacements. Asadollahi and Tonon (2010) has further considered the effect of normal stress acting on the joint as well as joint wall compressive strength on the peak shear displacement. A formula proposed by the authors is given as:

$$\delta_{peak} = 0.0077L^{0.45}\left(\frac{\sigma_n}{JRC}\right)\cos\left(JRC\log\frac{JCS}{\sigma_n}\right) \tag{2-7}$$

Scale effects are also an important aspect to consider for estimating joint shear strength and peak shear displacement appropriately since it has been found out that there are significant scale effects on the shear strength and peak shear displacement (Bandis, Lumsden, & Barton, 1981; Barton & Choubey, 1977), which in turn indicates that joint length exerts an influence on JRC and JCS. For instance, Figures 20 and 21 in the paper (Bandis et al., 1981) clearly show a decrease in JRC and JCS with increasing joint length, respectively. Barton and Bandis (1982) developed formulations to consider the scale effects on JRC and JCS, which are expressed as:

$$JRC_n = JRC_0\left(\frac{L_n}{L_0}\right)^{-0.02JRC_0} \tag{2-8}$$

$$JCS_n = JCS_0\left(\frac{L_n}{L_0}\right)^{-0.03JRC_0} \tag{2-9}$$

where subscripts, 0 and n, represent laboratory and in-situ scale values, respectively. JRC and JCS dependent on joint length can be estimated from Equations 2-8 and 2-9 on the basis of results obtained from laboratory tests.

Another shear strength model that takes into account the effect of joint surface asperities on its shear strength was proposed by Ladanyi and Archambault (1970), which is given as:

$$\tau_{\max} = \frac{\sigma_n(1-a_s)(\dot{v}+\tan\phi_u)+a_s s_r}{1-(1-a_s)\dot{v}\tan\phi_u} \tag{2-10}$$

where a_s represents a ratio of the sum of area of failure asperities to total sample area; $\dot{v}$ is a rate of dilation at failure; ϕ_u is a friction angle for sliding along the asperities; s_r is the shear strength of intact rock. The author recommended the use of an equation proposed by Fairhurst (1964) as s_r, which is given as:

$$s_r = C_0 \frac{\sqrt{1+N}-1}{N}\left(1+N\frac{\sigma_n}{C_0}\right)^{\frac{1}{2}} \tag{2-11}$$

where C_0 is the uniaxial compressive strength of the intact rock; N is a ratio of compressive over tensile strength defined as C_0 / T_0. The variables, a_s and $\dot{v}$, in Equation 2-10 are dependent on normal stress acting on the joint and given as:

$$\dot{v} = \left(1-\frac{\sigma_n}{\sigma_T}\right)^{k_2}\tan i_0 \tag{2-12}$$

$$a_s = 1-\left(1-\frac{\sigma_n}{\sigma_T}\right)^{k_1} \tag{2-13}$$

where i_0 represents an asperity angle; σ_T is transitional stress (uniaxial compressive strength is used); k_1 and k_2 are constants. Ladanyi and Archambault (1970) suggested using 1.5 and 4 for k_1 and k_2, respectively, when joint surfaces are rough. Equation 2-10 was re-examined by Saeb (1989) and Saeb (1990), then the following formula was proposed:

$$\tau_{\max} = \sigma_n (1 - a_s) \tan(i + \phi_u) + a_s s_r \tag{2-14}$$

where i represents a dilation angle dependent upon normal stress acting on the joints and is expressed as follows:

$$i = \tan^{-1} \dot{v} = \tan^{-1} \left[\left(1 - \frac{\sigma_n}{\sigma_T} \right)^{k_2} \tan i_0 \right] \tag{2-15}$$

It is clear that Equations 2-14 and 2-15 consider the effect of discontinuity surface asperities dependent upon normal stress acting on the discontinuity on shear strength. It is found that Equation 2-14 approaches to Equation 2-2 when the normal stress decreases to 0. In contrast, when the normal stress approaches to the uniaxial compressive strength, σ_T, the first term of the equation becomes negligible, and shear strength become a function of only s_r, which means that there is no longer effect of joint surface asperities on its shear strength since the asperities are presumably broken due to the normal stress exceeding the uniaxial compressive strength of the rock.

As can be seen from the shear strength models shown above, joint surface roughness (surface asperities) is of paramount importance in estimating its shear strength. In addition to the shown shear strength models, other shear strength models taking into account the surface roughness have been proposed (Homand, Belem, & Souley, 2001; Kulatilake, Shou, Huang, & Morgan, 1995; Lee, Hong, Bae, & Lee, 2006) as a result of detailed examinations of joint surface roughness

and its change dependent upon sliding movements. However, it is to be noted that considerable attention is required when the shear strength models are applied to fault stability analysis. This is because scale effects on joint roughness and joint wall compressive strength need to be considered. Although formulae to consider the scale effects have been proposed as shown in Equation 2-8 and 2-9, the applicability of the equations to faults extending over a large area in underground mines is still questionable, which implies that joint surface properties estimated from laboratory experiments cannot be simply utilized to analyze the behaviour of faults in underground mines.

The shear strength of geological discontinuities is largely dependent upon the properties of surface asperities as mentioned above. However, the shear strength is also affected by infilling materials of the surfaces. For instance, it is assumed that the shear strength and behaviour of faults are completely governed by the properties of fault gouge when the gouge is thick enough to cover fault surface asperities throughout. The degree to which such infilling materials are accumulated on geological discontinuity surfaces depends on a number of factors, such as the properties of rockmasses forming the discontinuities, in-situ stress fields, weathering, and shear displacements that had taken place on the discontinuities in the past. Importantly, the infilling materials reduce the shear strength of the discontinuities because of its low friction angles (Papaliangas, Lumsden, & Manolopoulou, 1993; Toledo & Freitas, 1993).

By means of Fourier analysis approach, Indraratna, Haque, and Aziz (1999) proposed a shear strength model that considers the effect of infilling materials based on a shear strength criteria proposed by Seidel and Haberfield (1995). Although the proposed shear strength model is applicable to estimating peak shear strength of infilled joints, the author found it inconvenience to use the shear strength model because of its complexity and constants to be estimated prior to

the application. The author improved the disadvantages and proposed a revise shear strength model (Indraratna, Welideniya, & Brown, 2005), which is given as:

$$\frac{\tau_{\max}}{\sigma_n} = \tan(\phi_b + i) \times (1-\kappa)^{\alpha} + \tan\phi_{fill} \times \left(\frac{2}{1+\frac{1}{\kappa}} \right)^{\beta} \quad (2\text{-}16)$$

$$\kappa = (t/a)/(t/a)_{cr} \quad (2\text{-}17)$$

Where t is the thickness of infilling material; a is asperity height; ϕ_{fill} is the friction angle of infilling material; α and β are empirical constants. The term, $(t/a)_{cr}$, in Equation 2-17 is a ratio at which the shear strength of infilled is determined only by the infilling material, i.e., the effect of joint surface asperities on its shear strength becomes negligible due to the accumulated infilling material. Equation 2-16 coincides with Equation 2-2 when the thickness of infilling material, t, is equal to 0. In contrast, when the infilling material is sufficiently thick, the shear strength is defined only by the friction angle of the infilling material. Equation 2-16 was further modified so as to take into consideration an influence of consolidation of infilling materials by Indraratna, Jayanathan, and Brown (2008). The revised equation is given as:

$$\left(\frac{\tau_{\max}}{\sigma'_n} \right)_{oc,n} = \tan(\phi_b + i) \times (1-\kappa_{oc,n})^{a_n} + \tan\phi'_{fill} \times OCR^{\alpha} \times \left(\frac{2}{1+\frac{1}{\kappa_{oc,n}}} \right)^{b_n} \quad (\kappa_{oc,n} < 1) \quad (2\text{-}18)$$

$$\left(\frac{\tau_{\max}}{\sigma'_n} \right)_{oc,n} = \left(\frac{\tau_{\max}}{\sigma'_n} \right)_{oc,1} \times OCR^{\alpha} \quad (\kappa_{oc,n} \geq 1) \quad (2\text{-}19)$$

$$k_{oc,n} = \left(\frac{t}{a} \right)_{oc,n} / \left(\frac{t}{a} \right)_{cr,n} \quad (2\text{-}20)$$

where $(t/a)_{oc,n}$ is a ratio of infill thickness to asperity height for *OCR* of n; $(t/a)_{cr,n}$ is critical t/a ratio for *OCR* of n; σ'_n is effective normal stress; ϕ'_{fill} is an effective friction angle of normally consolidate infill; a_n, b_n, and α are empirical constants. *OCR* is an over consolidated ratio, which is defined as the highest stress that the material experienced divided by the current stress. In some cases, taking into account the consolidation of infilling material may be crucial. This is because ongoing mining activities consistently affect stress states on nearby faults. In addition, palaeostress changes that the faults have experienced since its formation could have an influence on the degree of the consolidation of infilling materials. Hence, when a fault with thick infilling materials that appear to affect the shear strength of the fault is found in underground mines, it is advisable to consider their effects.

2.3 Dynamic friction laws

Fault-slip is a dynamic phenomenon that gives rise to seismic waves propagating through rockmasses. The shear strength models reviewed in section 2.2 is applicable only to static conditions; and the initiation of fault-slip can be predicted with the static shear strength models provided that the physical and mechanical properties of causative faults are already known. Although post-peak behaviour of rock joints have been examined in terms of the decrease in a joint roughness coefficient (Asadollahi & Tonon, 2010; Barton et al., 1985) with increasing shear displacements, the dynamic behaviour of fault-slip cannot be adequately described with the studies because other complicated processes, such as the flash heating of microasperity contacts and frictional melting of fault gouge, are involved when fault-slip occurs with high slip rates. To date, quite a few dynamic friction laws allowing for stress changes that take place during fault-slip have been proposed mainly in the field of geophysics. In this section, a review of the dynamic friction laws is provided.

Dynamic friction laws are generally classified into two types: slip-weakening friction laws and rate- and state-dependent friction laws. For the former, it is postulated that shear stress acting on a fault decreases from static to kinetic stress level with increasing shear displacement (Ida, 1972). Although this is similar to Barton's studies (Barton et al., 1985) in that the change in shear strength is related to shear displacement increments, slip weakening friction laws allows for the change in a friction angle from static to dynamic. For the latter, it is postulated that stress changes during fault-slip are associated with slip rates (fault slip velocity) and state variables, which are also a function of slip rates (Dieterich & Kilgore, 1996; Ruina, 1983).

2.3.1 Slip-weakening friction laws

As mentioned by Bizzarri (2011), slip-weakening friction laws are a widely employed friction law to simulate dynamic behaviour of fault-slip as a source for earthquakes (Bizzarri, 2012; Bizzarri, Cocco, Andrews, & Boschi, 2001; Oglesby & Mai, 2012; Tinti et al., 2004). A linear slip-weakening friction law is generally expressed as (Bizzarri, 2011):

$$\tau = \left[\mu_u - \left(\mu_u - \mu_f\right)\frac{u}{d_0} \right]\sigma_n^{eff} \quad \left(u < d_0\right) \tag{2-21}$$

$$\tau = \mu_f \sigma_n^{eff} \quad \left(u \geq d_0\right) \tag{2-22}$$

where μ_u and μ_f are coefficients of static and kinetic friction, respectively; u is shear displacement; d_0 is a characteristic slip-weakening distance. It is found from Equation 2-21 that static frictional resistance decreases to kinetic stress level as shear displacement increases to d_0. When the shear displacement exceeds d_0, shear stress is determined by normal stress acting on the fault and the coefficient of kinetic friction.

While Equation 2-21 assumes that shear stress on a fault linearly varies with the increasing shear displacement, non-linear slip-weakening friction laws have been also proposed. Ohnaka and Yamashita (1989) developed a non-linear friction law to understand constitutive behaviour near the rupture front during shear failure occurring along a pre-existing fault. The equation is given as:

$$\tau = (\tau_1 - \tau_d)[1 + \alpha \ln(1 + \beta u)]\exp(-\eta u) + \tau_d \quad (2\text{-}23)$$

where τ_1 is initial shear stress on the verge of slip; τ_d is dynamic friction stress; α and β are constants which defines the characteristic of slip-hardening behaviour; η is a constants determining slip-weakening behaviour. Equation 2-23 can allow for slip-hardening process that takes place at the onset of stick-slip behaviour (Ohnaka, Kuwahara, & Yamamoto, 1987; Ohnaka & Yamashita, 1989; Okubo & Dieterich, 1984) as well as slip-weakening behaviour.

Shear tests carried out for a thick gouge sample with a ring shear apparatus (Chambon, Schmittbuhl, & Corfdir, 2006a) revealed significant slip-weakening behaviour of the fault gouge over decimetric slip distances. Based on the results, Chambon, Schmittbuhl, and Corfdir (2006b) proposed a power law slip weakening model, which is given as:

$$\tau = \tau_r + \alpha(\delta_p - \delta_0)^{-\beta} \quad (2\text{-}24)$$

where τ_r is the asymptotic shear stress value; δ_0 is particular displacement for which the law is singular; δ_p is a shear displacement increment; α and β are two parameters. According to the author, β is approximately equal to 0.4.

Although a number of friction laws have been proposed as shown above, it is evident that a proper estimation of parameters related to slip-weakening behaviour in the slip-weakening friction laws plays a key role in simulating the

stress change during fault-slip. Oglesby and Mai (2012) assumed a slip-weakening distance of 0.4 m to simulate shear rupture propagation of an earthquake on a large scale. Bizzarri (2012), on the other hand, assumed 0.05 m as a slip-weakening distance to investigate spatial correlations between the maximum slip rate and rupture velocity. Okubo and Dieterich (1984) measured characteristic slip-weakening distances by performing laboratory tests, which showed that the characteristic slip-weakening distance falls between 20 and 40 μ m for a rough fault and between 2 to 20 μm for a smooth fault. Yuana and Prakash (2008) examined frictional slip resistance using a modified torsional Kolsky bar using rock-like materials; the experiment revealed that a few mm of slip is required for shear stress to decrease to the minimum values. The results obtained from these studies imply scale-dependency of a characteristic slip-weakening distance. According to Ohnaka (2003), characteristic slip-weakening distance can scale with characteristic length, λ_c, which represents a predominant wavelength component of geometric irregularity. In other words, faults with smooth surfaces have relatively small characteristic slip-weakening distance. In contrast, a large amount of slip is required for shear stress acting on a fault to drop to residual values in a case of faults with rough surfaces. The author indicates that a slip-dependent constitutive law is a unifying law that is capable of simulating a wide range of failure processes, such as failure within intact rock and frictional slip along a pre-existing fault, given that characteristic slip-weakening distance is properly estimated.

Although Ohnaka (2003) indicates that the frictional slip and shear failure occurring during earthquakes can be simulated with slip-dependent friction models, there is a clear disadvantage for the friction laws. As shown from Equation 2-21 to 2-24, the friction laws cannot simulate shear stress restrengthening that follows the slip-weakening behaviour. Many results obtained from laboratory-scale shear tests have demonstrated that shear stress increases after it decreases with increasing shear displacement (Yuana & Prakash, 2008).

The fault restrengthening is an important feature of stick-slip, which is considered mechanism of not only shallow earthquakes (Brace & Byerlee, 1966) but also fault-slip that occurs in underground mines (Gibowicz & Kijko, 1994).

2.3.2 Rate- and state-dependent friction laws

A rate- and state-dependent friction law (RS law) is another type of friction laws which are widely employed to simulate stress changes taking place on fault surfaces during earthquakes. The concept of RS laws has been generalized by Ruina (1983), which can be expressed as:

$$\tau = \sigma_n F\left(F, state\right) \tag{2-25}$$

$$\frac{d\left(state\right)}{dt} = G\left(V, state\right) \tag{2-26}$$

where V represents a slip rate. As can be seen from Equations 2-25 and 2-26, it is postulated that rock surfaces have a state at any instant time and that frictional resistance is dependent upon normal stress acting on the surfaces, the slip rate, and state. It is to be noted that RS laws are empirical friction laws, of which formulations are developed with invariables on the basis of results obtained from laboratory experiments.

Dieterich (1978) proposed a rate-dependent friction law accounting for time-dependency of static friction of rocks (Dieterich, 1972). The dependency is attributed to an increase in frictional resistance that results from an increase in the contact area by the creep behaviour of fault surface asperities. The formulation is given as:

$$\mu = \mu_0 + A\log\left(\frac{Bd_c}{V} + 1\right) \tag{2-27}$$

where μ is kinetic friction; μ_0 is static friction; d_c is interpreted to represents the displacement required to eliminate the population of contact characteristic of the previous velocity; A and B are constants. It is found from Equation 2-27 that frictional resistance increases with decreasing slip velocity, which results from the increase in contact area of rock surfaces.

To date, a number of rate- and state-dependent friction laws have been proposed by many researchers as shown in the study conducted by Bizzarri (2011). For instance, Dieterich and Kilgore (1996) has developed the following friction laws:

$$\tau = \sigma\left[\mu_0 + A\ln\left(\frac{V}{V^*}\right) + B\ln\left(\frac{\theta}{\theta^*}\right)\right] \tag{2-28}$$

$$d\theta = dt - \left(\frac{\theta}{D_c}\right)d\delta - \left(\frac{\alpha\theta}{B\sigma}\right)d\sigma \tag{2-29}$$

where μ_0 represents a coefficient of friction; A, B, and α are experimentally obtained constants; θ is a state variable; V^* and θ^* are normalizing constants; D_c is a characteristic sliding distance for evolution of the state. According to the author, A and B fall between 0.005 and 0.015 for silicates at room temperature; α falls in the range 0.25-0.50 for bare surfaces of Westerly granite. According to Bizzarri (2011), the constant, A, in Equation 2-28 is associated with a slip-hardening phase, while the constant, B, is related to long-range velocity strengthening. In addition, it is found from Equation 2-29 that the rate- and state-dependent friction law allows for the change in normal stress that could occur due to physical phenomenon during fault-slip, such as thermally pressurized pore fluid pressure. The state variable in Equation 2-28 has a unit of time and varies with time; hence this friction law is called RS law with true aging.

There is another type of rate- and state-dependent friction laws, which is referred to as RS law with slip evolution equation (Beeler, Tullis, & Weeks, 1994). For the RS law with slip evolution equation, the evolution of the state variables defined by Equation 2-29 is replaced with the following formulation:

$$d\theta = \left(\frac{\theta V}{D_c}\right)\ln\left(\frac{\theta V}{D_c}\right)dt \qquad (2\text{-}30)$$

While the state variable in Equation 2-29 varies with time regardless of slip velocity, the state variable in Equation 2-30 does not vary when slip velocity is equal to zero. In addition to the aforementioned rate- and state-dependent friction laws, other types of rate- and state-dependent friction laws, which are intended to take into account physical phenomena, such as sudden temperature changes on fault surface asperities during fault-slip, have been also proposed (Bizzarri, 2009; Chester, 1994; Nielsen & Carlson, 2000; Perrin, Rice, & Zheng, 1995). It should be bored in mind that these rate- and state-dependent friction laws are empirical laws in that constitutive parameters in the friction laws must be derived on the basis of laboratory experiments. Therefore, laboratory experiments or back analysis to obtain appropriate parameters are required when applying these friction laws to case studies.

Both of rate- and state- dependent friction laws and slip-weakening friction laws have been widely employed in conjunction with numerical analysis to investigate dynamic phenomena of fault-slip in geophysics (Bizzarri, 2012; Bizzarri & Belardinelli, 2008; Bizzarri & Cocco, 2003; Bizzarri et al., 2001; Boatwright, 1996; Cocco, Bizzarri, & Tinti, 2004; Helmstetter & Shaw, 2009; Rice & Ben-Zion, 1996; Tinti et al., 2004; J. Wang, 2009). However, such dynamic friction laws have been rarely applied to the simulation of fault-slip occurring in underground mines. As suggested by Gibowicz and Kijko (1994), the mechanism of shallow earthquakes is similar to that of mining-induced seismicity. Hence, in

order to achieve the better understanding of mining-induced fault-slip, it is suggested to apply the dynamic friction models to the simulation of the fault-slip.

2.4 Rock joint deformation and its stress evolution

The deformation and stress evolution of faults and rock joints, which are induced by combined effects of in-situ stresses with stress re-distribution resulting from mining activities, are strongly dependent upon their stiffness. The stiffness of rock joints and faults is a function of many factors, such as displacements along the joints, shear and normal stresses, and the geometries of surface asperities of the discontinuities. In this section, relationships between rock joint stiffness and the influencing factors are reviewed.

As reviewed by Kulhawy (1975), Clough and Duncan (1969) proposed a formulation to describe shear stiffness changes, considering a ratio of actual shear stress acting on a joint to the maximum shear strength. The same equation is also shown by Bandis, Lumsden, and Barton (1983), which is given as:

$$K_{st} = K_{si}\left(1 - \frac{\tau R_{fj}}{c_j + \sigma_n \tan\phi_j}\right)^2 \tag{2-31}$$

$$R_{fj} = \frac{\tau}{\tau_{ult}} \tag{2-32}$$

where K_{st} is the tangent shear stiffness of a discontinuity; K_{si} is its initial tangent shear stiffness; τ is mobilized shear stress acting on the discontinuity; R_{fj} is a failure ratio; τ_{ult} is a horizontal asymptote to a hyperbolic curve for a shear stress-shear displacement relationship; c_j is discontinuity cohesion; ϕ_j is the friction angle of the discontinuity. According to Kulhawy (1975), R_{fj} ranges from 0 to 1 and indicates the degree of nonlinearity. It is found from Equation 2-31 that the shear stiffness of the discontinuity becomes zero when shear stress reaches its

peak shear strength. According to Bandis et al. (1983), the initial shear stiffness is defined by the following equation:

$$K_{si} = K_j (\sigma_n)^{nj} \tag{2-33}$$

where K_j is a stiffness number; n_j is a stiffness exponent. According to the author, the stiffness number can be expressed as a function of JRC since it is postulated that the shear stiffness of rock joints are dependent upon the degree of interlocking of surface asperities. Experimental results obtained from shear tests shows a linear relationship between the stiffness number and joint roughness coefficient (Bandis et al., 1983), which is then given as:

$$K_j = -17.19 + 3.86JRC \quad (JRC > 4.5) \tag{2-34}$$

Equation 2-34 indicates that the shear stiffness of rock joints would significantly vary depending on their surface roughness, which in turn implies that rock joint deformation and its stress evolution could be strongly affected the physical properties of the joint.

Equations representing the normal stiffness of a discontinuity, which varies with normal stress and normal displacement, have been proposed by Bandis et al. (1983) based on a hyperbolic function. The authors found that the behaviour of interlocking joints is different from that of dislocated joints in terms of the variations of the normal stiffness. For interlocking joints, their normal stiffness is given as:

$$K_n = \frac{K_{ni}}{\left(1 - \frac{\Delta V_j}{V_m}\right)^2} \tag{2-34}$$

where K_n is the normal stiffness of a joint; K_{ni} is its initial normal stiffness; V_j is normal displacement; V_m is the maximum joint closure. As shown in Equation 2-34, the normal stiffness of rock joints can be expressed with a hyperbolic curve. The authors further developed equations to obtain the maximum joint closure and initial normal stiffness, which are presumably dependent upon the properties of joint surface asperities, joint wall compressive strength, and joint apertures. The experimentally-yielded equations are expressed as:

$$V_m = A + B(JRC) + C\left(\frac{JCS}{a_j}\right)^D \tag{2-35}$$

$$K_{ni} = -7.15 + 1.75(JRC) + 0.02\left(\frac{JCS}{a_j}\right) \qquad r^2 = 0.573 \tag{2-36}$$

where A, B, C, and D are constants calculated from regression analysis; a_j is an average aperture thickness. It should be noted from Equation 2-35 and 2-36 that the magnitude of normal stiffness of rock joints is also affected by the physical and mechanical properties of joint surfaces. Equations 2-34, 2-35, and 2-36 suggest that the normal and shear stiffness of rock joints could significantly vary within shear or fracture zones, depending on the physical and mechanical properties of discontinuity surfaces. Thus, it can be presumed that the variations in the shear and normal stiffness could generate stress concentrations within the zones, which in turn contribute to the occurrence of seismic events due to the sudden release of the stored energy.

In order to calculate the maximum closure and initial normal stiffness, the average aperture, a_j, in Equations 2-35 and 2-36 has to be known. Bandis et al. (1983) also proposed an empirical relationship to estimate the average aperture, which is given as:

$$a_j = \frac{JRC}{5}\left(0.2\frac{\sigma_c}{JCS} - 0.1\right) \quad (2\text{-}37)$$

Normal and shear stiffness of rock joints can be approximated with these equations given that a joint roughness coefficient and joint wall compressive strength are already known.

Equation 2-34 yields the normal stiffness for interlocking joints, while for dislocated joints, their normal stiffness can be expressed as:

$$K_n = \frac{q\sigma_n}{\log e} \quad (2\text{-}38)$$

where q is the slope of a line representing a relationship between $\log\sigma_n$ and a joint closure. The constant, q, is obtained from laboratory tests.

In a case of rockmasses that contain a single set of uniformly spaced joints, the normal and shear stiffness of the joints can be theoretically estimated from the following equations (Blake & Hedley, 2003):

$$K_n = \frac{EE_r}{s(E - E_r)} \quad (2\text{-}39)$$

$$K_s = \frac{GG_r}{s(G - G_r)} \quad (2\text{-}40)$$

where E and E_r are the moduli of elasticity for intact rock and rockmass, respectively; G and G_r are the shear moduli for intact rock and rockmass, respectively; s represents joint spacing. In a case that the parameters in Equations 2-39 and 2-40 can be estimated with in-situ measurements and back analysis, the stiffness of uniformly spaced joints can be approximated with the formulae.

Under in-situ conditions such as around mining openings where cable bolts and rock bolts are installed, normal stresses acting on rock joints vary depending on the movements of surrounding rockmasses since displacements on boundaries are fixed with the installed bolts. Saeb and Amadei (1992) has applied the boundary condition to the mechanical behaviour of a rock joint. In addition, the authors have related the shear displacement increments of the joint with an increase in normal stresses acting on the joint while considering joint dilation defined by Equation 2-12. The proposed formulae can be written as follows:

$$d\sigma_n = k_{nn} dv + k_{nt} du \tag{2-41}$$

$$k_{nn} = \frac{\partial \sigma_n}{\partial v} = \frac{1}{\dfrac{-uk_2}{\sigma_T}\left(1-\dfrac{\sigma_n}{\sigma_T}\right)^{(k_2-1)} \tan i_0 + \dfrac{V^2{}_m k_{ni}}{(k_{ni}V_m - \sigma_n)^2}} \tag{2-42}$$

$$k_{nt} = \frac{\partial \sigma_n}{\partial u} = \frac{-\left(1-\dfrac{\sigma_n}{\sigma_T}\right)^{k_2} \tan i_0}{\dfrac{-uk_2}{\sigma_T}\left(1-\dfrac{\sigma_n}{\sigma_T}\right)^{(k_2-1)} \tan i_0 + \dfrac{V^2{}_m k_{ni}}{(k_{ni}V_m - \sigma_n)^2}} \tag{2-43}$$

where v and u are normal and shear displacements of a joint. As can be seen from Equations 2-41 to 2-43 that normal stress acting on the joint increases with shear and normal displacements due to the effect of dilatancy. Shear stress acting on the joint is also a function of normal and shear displacements. For a constant displacement model, which postulates that peak shear displacement does not vary with normal stress acting on the joint, the evolution of shear stress is given as:

$$d\tau = k_{tn} dv + k_{tt} du \tag{2-44}$$

when $u < u_p$:

$$k_{tn} = \frac{\partial \tau}{\partial v} = \frac{u}{u_p} k_{nn} \frac{\partial \tau_p}{\partial \sigma_n} \tag{2-45}$$

$$k_{tt} = \frac{\partial \tau}{\partial u} = \frac{u}{u_p} k_{nt} \frac{\partial \tau_p}{\partial \sigma_n} + \frac{\tau}{u_p} \tag{2-46}$$

when $u_p < u < u_r$ and $\sigma_n < \sigma_T$:

$$k_{tn} = \frac{\partial \tau}{\partial v} = \frac{k_{nn}}{u_p - u_r} \times \left\{ \frac{\partial \tau_p}{\partial \sigma_n}(u - u_r) + (u_p - u) \times \left[\frac{\partial \tau_p}{\partial \sigma_n} \left(B_0 + \frac{1 - B_0}{\sigma_T} \sigma_n \right) + \frac{\tau_p}{\sigma_T}(1 - B_0) \right] \right\} \tag{2-47}$$

$$k_{tt} = \frac{\partial \tau}{\partial u} = \frac{\tau_p - \tau_r}{u_p - u_r} + \frac{k_{nt}}{u_p - u_r} \{ \frac{\partial \tau_p}{\partial \sigma_n}(u - u_r) + (u_p - u) \times \left[\frac{\partial \tau_p}{\partial \sigma_n} \left(B_0 + \frac{1 - B_0}{\sigma_T} \sigma_n \right) + \frac{\tau_p}{\sigma_T}(1 - B_0) \right] \} \tag{2-48}$$

when $u > u_r$ and $\sigma_n < \sigma_T$:

$$k_{tn} = \frac{\partial \tau}{\partial v} = k_{nn} \left\{ \frac{\partial \tau_p}{\partial \sigma_n} \left(B_0 + \frac{1 - B_0}{\sigma_T} \sigma_n \right) + \frac{\tau_p}{\sigma_T}(1 - B_0) \right\} \tag{2-49}$$

$$k_{tt} = \frac{\partial \tau}{\partial u} = k_{nt} \left\{ \frac{\partial \tau_p}{\partial \sigma_n} \left(B_0 + \frac{1 - B_0}{\sigma_T} \sigma_n \right) + \frac{\tau_p}{\sigma_T}(1 - B_0) \right\} = 0 \tag{2-50}$$

where τ_p is peak shear strength; τ_r is residual shear stress; u_r is residual shear displacement; B_0 is a ratio of residual-to-peak shear strength. For a constant

stiffness model, which postulates that the shear stiffness of rock joints remains the same regardless of the level of normal stress applied to the joint, the stiffness coefficients in Equation 2-44 are given as follows:

when $u < u_p$:

$$k_{tn} = \frac{\partial \tau}{\partial v} = 0 \tag{2-51}$$

$$k_{tt} = \frac{\partial \tau}{\partial u} = \frac{\tau_p}{u_p} \tag{2-52}$$

when $u_p < u < u_r$ and $\sigma_n < \sigma_T$:

$$k_{tn} = \frac{\partial \tau}{\partial v} = k_{nn} \frac{\partial \tau_p}{\partial \sigma_n} \frac{1}{\tau_p} \left(\frac{u_p \tau_r - \tau_p u_r}{u_p - u_r} \right) \tag{2-53}$$

$$k_{tt} = \frac{\partial \tau}{\partial u} = \frac{\tau_p - \tau_r}{u_p - u_r} + k_{nt} \frac{\partial \tau_p}{\partial \sigma_n} \frac{1}{\tau_p} \left(\frac{u_p \tau_r - \tau_p u_r}{u_p - u_r} \right) \tag{2-54}$$

when $u > u_r$ and $\sigma_n < \sigma_T$, k_{tn} and k_{tt} are defined as Equations 2-49 and 2-50. According to Saeb and Amadei (1992), by means of the aforementioned formulae, the shear behaviour of rock joints under applied constant or variable normal stiffness boundary conditions can be analyzed while assuming the following relationship:

$$d\sigma_n = K dv \tag{2-55}$$

where K is the applied stiffness which can be constant or vary with σ_n. It should be noted that K represents the stiffness of surrounding rockmasses. Substituting Equation 2-55 into 2-41 yields formulae relating shear displacement increments with an increase in normal stress and normal displacement as follows:

$$d\sigma_n = \frac{Kk_{nt}}{K - k_{nn}} du \tag{2-56}$$

$$dv = \frac{k_{nt}}{K - k_{nn}} du \tag{2-57}$$

Likewise, substituting Equation 2-55 into 2-44 gives the following relationship:

$$d\tau = \left(\frac{k_{tn} k_{tnt}}{K - k_{nn}} + k_{tt} \right) du \tag{2-58}$$

By means of equations shown above, the dilatant behaviour of rock joints, which is essentially involved during slip movements, can be simulated while considering the boundary conditions under which normal displacements on the boundary are constrained.

2.5 Characteristics of faults

Fault zones and its cores exhibit significant complexities with respect to geological structures and physical and mechanical properties, which are largely different from those of country rock where the faults have been formed. Therefore, the better understanding of characteristics of faults is of pivotal importance for modelling faults in a proper manner. Many investigations about the characteristics of faults have been conducted. Hobbs, Griggs, and Hobbs (1965) and Wallace and Morris (1986) have collected and scrutinized information about faults that were expose through mine developments in deep underground mines in North America. The authors reported the following characteristics.

- Faults are irregular, branched and curved.

- The widths of fault zones are susceptible to shear displacements along the faults, e.g., fault zones with kilometers of displacement tend to be 100 m or more wide, whereas those with only a few hundred meters of displacements commonly are only 1 m or less wide.

- Many fault zones are wet, even if they are located above the water table; and the fault zones serve either as paths through which underground water goes down or as dams that prevent water from moving horizontally.

- Fault zones consist of a discrete clay-like gouge zone, a zone of sheared rock, and a zone of fractured rock.

Mining-induced shear zones in the East Proprietary Mine, Boksburg, South Africa have been investigated by many researchers (Gay & Ortlepp, 1979; McGarr, Spottiswoode, Gay, & Ortlepp, 1979; Ortlepp, 1992, 2000). The studies have shown that the shear zones are made up of smaller, en echelon shear planes with a layer of finely comminuted gouge material, which was presumably generated with rapid movements of the shear planes. McGarr, Spottiswoode, et al. (1979) postulated that the geometry of the shear zones had been formed before a large scale of slip movements occurred, which thus indicates that the actual seismic event simply involved substantial increases in shear displacements along previously formed failure planes within the shear zones. Ortlepp (2000) investigates the fault gouge found on the mining-induced shear planes in the mine and suggests that fault surface asperities play an important role in the generation of intense seismic waves during fault-slip.

Also in the field of geology, significant efforts have been made in order to gain knowledge about fault structures and its characteristics. It is found out from the studies that fault zones generally consist of fault damage zones and fault cores,

to which shear displacements are localized (Bradbury, Barton, Solum, Draper, & Evans, 2007; Chester & Chester, 1998; Chester & Logan, 1986; Lutzenkirchen & Loew, 2011; Noda & Shimamoto, 2009). The fault cores are composed of fault gouge, clay-like materials or cataclasite layers, and significantly thin compared to the damage zones. For instance, Chester and Logan (1986) reports that the thickness of the gouge layer found in the Punchbowl fault zone ranges from 1 mm to 10 mm. Figure 2-1 depicts a ultracataclasite layer of the fault core of the Punchbowl fault, California (Chester & Chester, 1998). Prominent fracture surfaces where shear displacements are localized are located in the center of the layer.

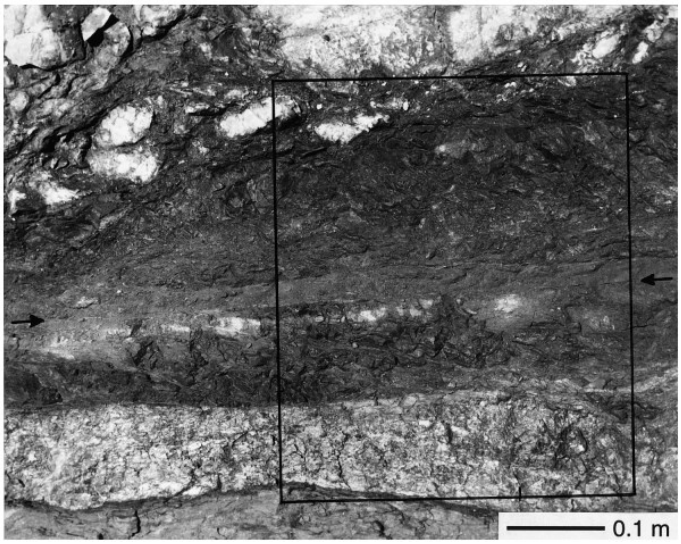

Figure 2-1: Fault core of the Punchbowl fault, San Andreas system, California, where shear displacement is localized (Chester & Chester, 1998)

The characteristics of fault zones have been further investigated as shown below. It is found out that the widths of fault cores and damage zones seem to scale with fault displacement and its length (Chester & Logan, 1986; Childs et al., 2009; Cowie & Scholz, 1992; Dawers & Anders, 1995; Schlische, Young, Ackermann, & Gupta, 1996; Shiption, Evans, Abercrombie, & Brodsky, 2006), which means that faults with large displacements tend to have wider damage zones and cores, compared to faults with small displacements. Characterization

of fault damage zones has been conducted by Kim, Peacock, and Sanderson (2004), by means of which fault damage zones can be classified into tip-, wall-, and linking-damage zones. Wilson, Chester, and Chester (2003) investigated microfractures within fault damage zones of Punchbowl Fault, and found out that the density of the microfractures increases toward fault surfaces, which in turn means a significant decrease in elastic moduli of rock surrounding the slip surfaces. With regard to slip surface properties, a relationship between shear displacement along the slip surfaces and evolution of fault surface roughness has been studied with laser-based methods by. Sagy, Brodsky, and Axen (2007). The study confirms that fault surface roughness evolves with increasing slip. Figure 2-2 depicts surface profiles of faults having different magnitudes of slip. It is found from the figure that faults with small shear displacements have rough surfaces. According to the author, for the small-slip faults, root mean square heights of fault surface asperities are 11.5±5 mm; on the other hand, the value decreases to 3 mm for a large-slip fault. Thus, there is a clear difference in the surface profiles between faults with large and small shear displacements. As can be seen from the static friction laws in section 2.2, fault surface roughness is of paramount importance for assessing whether faults are in stable conditions or not, because the roughness is directly related to the static shear strength of discontinuities.

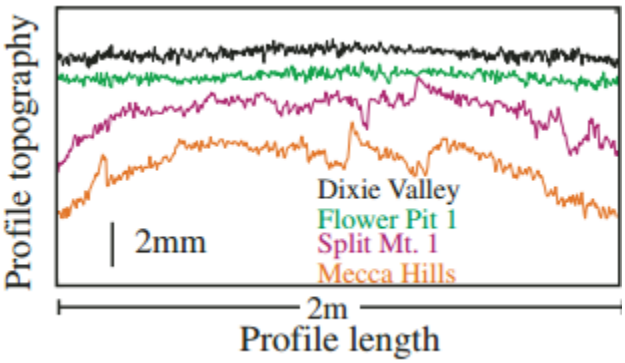

Figure 2-2: Surface topography of fault surfaces. Upper two profiles are faults with large slip and bottom two profiles are small-slip faults (Sagy et al., 2007)

Self-similarities of discontinuities within fault zones and the permeability of faults should be also considered important aspects of nature faults. The fractal properties of discontinuities of faults have been examined or reported by Ben-Zion and Sammis (2003); Cello et al. (2000); McGarr, Spottiswoode, et al. (1979). The studies have shown that faults are self-similar over a wide range of scales for both of mining-induced and natural faults. Regarding the permeability of faults, it is reported that central slip zone gouges have the lowest permeability among all of fault rocks found in Median Tectonic Line in Mie Prefecture (Wibberley & Shimamoto, 2003). Experimental data carried out by Chester and Logan (1986) have revealed that the permeability of fault zones increases toward the main gouge zones. This is because fracture density increases toward the fault core. Cello, Tondi, Micarelli, and Invernizzi (2001) indicates that whether active fault zones favour or impede fluid flow depends on lithology, structural properties and fault fabrics. Shan, Javandel, and Witherspoon (1995) provided analytical solutions to investigate water flow occurring in an aquifer-fault-aquifer system.

It is found from the aforementioned fault characteristics that there are significant complexities and important features for fault zones. Whether or not those features are taken into consideration when faults are numerically modelled may depends on the purposes of studies and the characteristics of causative faults. However, these studies conducted for the better understanding of characteristics of fault structures and fabrics suggest that faults should be appropriately modelled in order to obtain reasonable results.

2.6 Fault-slip types and its relation with mining activities

In underground mines, stress re-distribution induced mining activities could cause fault-slip along pre-existing faults or form faults to nucleate and propagate through intact rock while inducing seismic events, which have magnitudes greater than those of other types of seismic events, such as strain bursts and pillar bursts (Blake & Hedley, 2003). In this section, the types of fault-slip as well

as the mechanisms by which faults are reactivated are described for the better understanding of fault-slip in underground mines.

2.6.1 Fault-slip along a pre-existing fault

Pre-existing faults are reactivated due to stress re-distribution resulting from mining activities. Castro, Carter, and Lightfoot (2009) summarises possible factors that contribute to the occurrence of fault-slip along pre-existing faults as follows.

- Unclamping: Mining activities such as ore extractions could cause a decrease in normal stress acting on faults, which in turn reduce the maximum shear strength. When shear stress acting on the fault exceeds the maximum shear strength, fault-slip is induced. The authors mentioned two types of unclamping: local unclamping and regional unclamping. Local unclamping is defined as unclamping that occurs in the vicinity of active mining areas, where mining activities locally decrease normal stress acting on nearby faults. On the other hand, regional unclamping is defined as a regional decrease in normal stress, which is induced by a large size of extraction of orebodies. In a case of regional unclamping, fault-slip occurs at significant distances from active mining areas and could inflict severe damage due to seismic waves arising from the fault-slip. Recent studies done for Garson Mine, Sudbury, Canada (Bewick, Valley, runnals, Whitney, & Krynicki, 2009) shows that fault-slip related seismic events caused by regional unclamping tend to be violent because of large strain energy stored in the faults before the slip occurred (Castro et al., 2009).

- Day-lighting: Fault-slip could be caused when underground openings, such as stopes, drifts, and cross-cuts, intersect with the fault. A mechanism involved is local unclamping of the fault. This type of fault-slip could occur before the advancing face of mine openings reaches the fault. The author

suggests that additional rock support should be installed at least 15 m prior to approach of the fault.

- Stress rotation: Mining activities have an influence on in-situ stress fields, which result in stress rotation. An increase in shear stress acting on faults as well as a decrease in normal stress could result from the stress rotation. As a result, fault-slip is induced when the shear stress reaches the maximum shear strength.

Field observations and numerical analysis have been carried out for this type of fault-slip. For instance, Hofmann and Scheepers (2011) simulated fault-slip along a pre-existing fault that occurred in a South African deep-level gold mine. McGarr, Pollard, and Gay (1979) observed mining-induced shear zones generated within the East Rand Proprietary Mines, and assumes that a large seismic events was induced by slip along pre-existing faults that had been created quasi-statically prior to the occurrence of the seismic event. Trifu and Urbancic (1996) mentions aftershocks induced by the release of strain energy accumulated on fault surface asperities after a large seismic event took place. As can be seen from Barton's shear strength model defined by Equation 2-3, fault surface asperities increase the shear strength of faults to a large extent; thus a large amount of strain energy could be stored on the faults, depending on fault surface roughness. When the asperities are sheared off, resultant seismic events could become significantly violent while entailing intense seismic waves.

2.6.2 Seismic events induced by coalescence of microcracks

Seismic events are also induced by fault nucleation and/or coalescence of microcracks and fractures. The process in which faults are developed has been studied by many researchers. Experiments on quasi-static fault growth have been performed using a brittle rock sample with acoustic emission sensors by Lockner, Byerlee, Kuksenko, Ponomarev, and Sidrin (1991) and Reches and

Lockner (1994). The experiment results demonstrate that a fault propagates in its own plane by means of a leading process zone as shown in Figure 2-3.

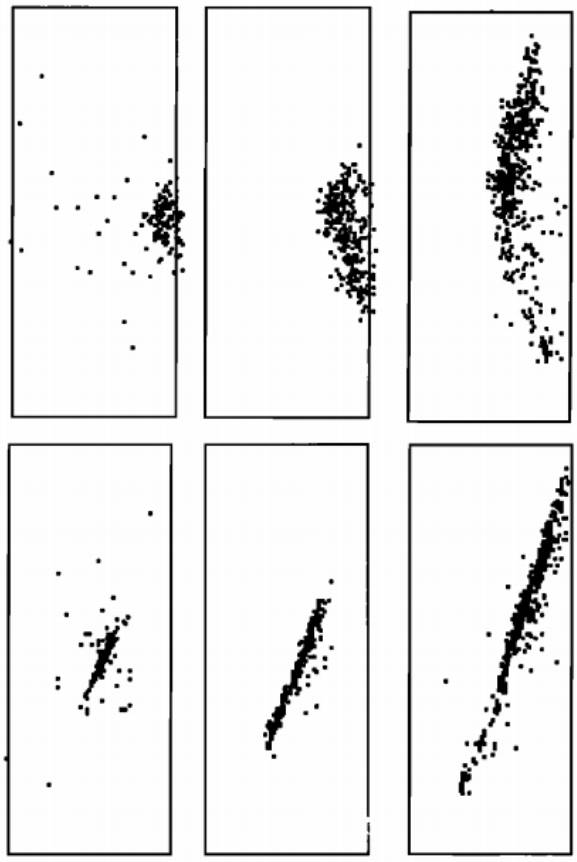

Figure 2-3: Computer-generated display of over 1200 acoustic emission showing Fault nucleation and fault growth. Bottom plots are viewed along the strike of the fault; top plots view developing fault surface face on (Reches & Lockner, 1994).

On the other hand, results obtained from experiments carried out by Shen, Stephansson, einstein, and Ghahreman (1995) show that faults grow with fracture coalescence that takes place with shear failure and/or tensile failure. Trifu and Urbancic (1996) investigated microseismic activities as a precursor of a large seismic event that took place in regions where the small seismic events had taken place by means of seismic monitoring systems installed in an underground mine, Sudbury, Canada. The data obtained from the monitoring

systems and numerically derived planes of maximum slip potential have indicated that a causative fault plane for the large seismic event appears to be related to the coalescence of fractures. It is further indicated that a reduction in stress release accompanying the increased tendency towards planarity prior to the large seismic events means the development of a large rupture surface along which fault-slip that caused the large seismic event occurred. The field data indicating the coalescence of fractures as a source of seismic events (Trifu & Urbancic, 1996) support the experimental result (Shen et al., 1995). From these studies, it is found that the coalescence of microcracks and/or fractures causes microseismic events, which could form a large fault plane that might induce severe seismic events. It is to be noted that the fault-slip taking place along the formed fault plane is regarded as fault-slip along a pre-existing fault.

Examination of fracturing process of a barrier located between two pre-existing faults has been carried out by Sobolev (1986) for the better understanding of the mechanism of earthquakes and rockbursts. The experiment shows processes during which the barrier is broken. The processes can be divided into three stages according to the study. At the first stage, the density of small tensile cracks increases; at the second stage, longer shear cracks are developed as a result of the coalescence of the tensile cracks; at the last stage, the main fracture is prepared and propagates. It is assumed that if the breakage of the barrier between pre-existing faults violently takes place, stored strain energy is radiated seismically, which could be the cause for rockbursts.

As shown in this section, fault-slip is induced by slip along a pre-existing fault or by the coalescence of microcracks and/or fractures, both of which could be sources for seismic events. More importantly, these studies indicate that completely different approach is required when simulating fault-slip, depending on the properties of causative fault zones. In the following section, numerical

approach that has been conducted to simulate fault-slip in underground mines is reviewed.

2.7 Numerical approach for fault-slip analysis

At the present day, a number of numerical simulation methods have been developed in a variety of fields to analyze physical phenomena, such as elastic wave propagation, ground motion induced by seismic waves, rockmass behaviour, and crack propagation within intact materials. In this section, numerical simulation techniques used to simulate fault-slip are first described. Afterwards, strong and weak points for the simulation methods are summarized.

2.7.1 Simulation methods used for fault-slip analysis

There are a couple of types of numerical methods that can be generally used for simulating the behaviour of faults in both of fields of rock mechanics and geophysics. Numerical analysis software, which employs finite difference methods (FDM), is used to simulate the behaviour of geological discontinuities (Cappa & Rutqvist, 2010; Hai-min, Yi-ming, & jun-gao, 2011; Zhi-hua, Lin-ming, Cai-ping, Zong-long, & An-ye, 2008). A boundary element method (BEM) is employed to simulate the areas of fault-slip that occurred in an underground mine, South Africa (Hofmann & Scheepers, 2011). Simon (1999) analyzed the behaviour of fault-slip in hard rock mines with BEM while applying a newly developed shear strength model. Alber et al. (2009) evaluates fault-slip tendency by carrying out static analysis with the finite element method (FEM). In the field of geophysics, Oglesby and Mai (2012) simulates dynamic shear rupture as a source of an earthquake that could occur on the North Anatolian Fault system in the Sea of Marmara, Turkey with a large-scale numerical model by means of numerical analysis software into which FEM is implemented. Potvin et al. (2010) and Sjoberg et al. (2012) use numerical analysis software, which employs a

distinct element method (DEM), in order to simulate fault-slip that occurs along geological structures in underground mines.

As shown above, in general, four types of numerical simulation techniques, namely FDM, BEM, FEM, and DEM, are used for the simulation of fault-slip, depending on the purposes of the studies. The general principles of the numerical simulation methods can be summarized as follows. For FEM, weak formulations of partial differential equations to be solved are derived with Galerkin method. A domain to be analyzed is discretized to small elements, and element stiffness matrices are calculated for each element. Afterwards, on the basis of the element stiffness matrices, a stiffness matrix is constructed and solved considering forces applied to the regions. FDM is a numerical simulation method to approximate the partial differential equations with finite difference equations while assuming Taylor Series expansion. The domain analyzed is discretized with grid points, based on which the difference equations are solved. On the other hand, BEM requires only the boundaries of the analyzed domain to be discretized. It is then performed to solve integral equations derived from linear partial differential equations that govern the behaviour of a medium. For DEM, the domain to be analyzed is divided into blocks, which may be considered rigid bodies. The divided blocks are connected with springs that consider normal and shear stiffness as well as damping behaviour, which make it possible to simulate the behaviour of significantly blocky rockmasses containing a number of discontinuities.

2.7.2 Advantages and disadvantages of numerical simulation technics

The numerical simulation techniques described in the previous section have their strengths and weaknesses inherent to their principles. Simon (1999) summarizes the strong and weak points of the numerical simulation methods as shown in Table 2-2.

Table 2-2: Advantages and limitations of numerical methods (Simon, 1999)

	Advantages	Disadvantages
Boundary element method	Far-field conditions inherently represented. Only boundaries require discretization	Coefficient matrix is fully populated. Solution time increases exponentially with number of elements used.
Finite-element and finite-difference methods	Material heterogeneity easily handled. Material and geometric non-linearity handled efficiently with explicit solution techniques. Matrices are banded with implicit solution techniques. When explicit solution techniques are used, less skill is required from user.	Entire volume must be discretized. Far-field boundary conditions must be approximated. For linear problems, explicit solution techniques are relatively slow. Solution time increases exponentially with number of elements used for implicit solution techniques.
Discrete (distinct) - element method	Data structures well suited to model systems with high degree of non-linearity from multiple intersecting joints. Very general constitutive relations may be used with little penalty in terms of computational efforts. Solution time increases only linearly with number of elements used.	Solution time seem much slower than for linear problems. Results can be sensitive to assumed values of modeling parameters.

As shown in Table 2-2, the coefficient matrix of BEM is fully populated; as a result, solution time significantly increases when handling large-scale numerical models, of which boundaries must be discretized into a considerable number of segments to obtain adequately accurate results. Although the stiffness matrix of FEM becomes large as well according to the number of nodes and degrees of

freedom, the stiffness matrix is considerably sparse, which allows us to use particular techniques to solve simultaneous equations efficiently, such as a preconditioned conjugate gradient method. In addition, FEM is capable of dealing with a wide variety of problems, e.g., material heterogeneity, elasto-plastic behaviour (Sainoki, Fukuda, Kaneko, & Kodama, 2009), and the effect of pore pressure (Sainoki, Fukuda, Kodama, & Kaneko, 2010) are readily taken into consideration. Moreover, FEM gives more accurate results than FDM when compared with analytically obtained solutions (Frehner, Schmalholz, Saenger, & Steeb, 2008). For these reasons, FEM appears to be the most popular simulation technic to handle various problems related to the field of rock mechanics and civil engineering (Dow, Jones, & Harwood, 1990).

2.7.3 Fault-slip simulation with a finite difference method

In the present study, FLAC3D code (Itasca, 2009), which employs an explicit finite difference method, is utilized. Although FEM is superior to FDM in terms of accuracy of its results, there are still advantages of employing FDM to simulate fault-slip. First, the explicit finite difference method is more suitable to dealing with a large-scale model with a number of grid points and zones since there is no need to store any matrices (Itasca, 2009) in its calculations. Considering the fact that simulating faults within a mine-wide model may require a densely discretized model within areas surrounding the faults, the feature is considered important. In addition, constitutive models are readily implemented into FDM codes, while it is not simple to incorporate new constitutive models into FEM codes because stiffness matrices need to be modified accordingly and/or different solution techniques need to be developed (e.g. calculations of residual stresses for plastic behaviour after simulating linear elastic behaviour). As described in section 2.2 and 2.3, many static and dynamic friction laws have been proposed in efforts to evaluate fault stability and simulate its behaviour. In the present study, the friction laws need to be implemented in order to examine the dynamic behaviour of faults during fault-slip, considering fault surface asperities and its dilation. For these

reasons, the use of FLAC3D code employing the explicit finite difference method is deemed appropriate for the present study.

2.8 Seismic source parameters

Seismic source parameters are extensively used to assess the magnitudes and intensity of seismic events. Seismic waves arising from seismic events that take place in underground mines can be detected by means of seismic monitoring systems installed in underground mines and/or near the ground surface. Seismic source parameters are computed on the basis of wave forms recorded by the seismic monitoring systems and used for understanding seismic activities (Bischoff, Cete, Fritschen, & Meier, 2010; Domanski & Gibowicz, 2008; Holub, 1996; Luo, Creighton, & Gough, 2010; Sileny & Milev, 2008; Urbancic & Trifu, 1998; Urbancic & Trifu, 2000). More importantly, seismic source parameters can be also computed based on results obtained from numerical analysis. Hence, seismic source parameters can be used for the calibration and validation of numerical models through comparison of numerically obtained results with those estimated from data recorded by the seismic monitoring systems. Furthermore, the seismic source parameters are also important in terms of predicting damage inflicted by seismic events (Hedley, 1992). In this section, the seismic source parameters that can be used to investigate seismic activities in underground mines are reviewed.

First, seismic moment and moment magnitude are generally used as indices for evaluating the intensity of microseismicity in underground mines. These parameters are given as the following equations (Hanks & Kanamori, 1979):

$$M_o = GDA \tag{2-59}$$

$$M_w = \frac{2}{3}\log M_o - 6.0 \tag{2-60}$$

where M_0 and M_w are seismic moment and moment magnitude, respectively; G, D, and A represent shear modulus, average shear displacement, and area where sliding takes place. By means of an empirical relation proposed by Hasegawa (1983), moment magnitude can be converted into Nuttli magnitude (Nuttli, 1973), based on which the significance of rockburst damage can be estimated, according to the distances from a hypocenter, as shown by Hedley (1992). Although there are several types of magnitude scales that are used to evaluate the intensity of seismic events including earthquakes, moment magnitude is basically adopted in the present study because it is the most representative in terms of the actual size of seismic events.

Seismically radiated energy, E_s, is also an important index to evaluate the intensity of seismic events. According to (Shearer, 1999), E_s can be approximated as follows:

$$E_s = 0.5\Delta\sigma DA \tag{2-61}$$

where $\Delta\sigma$ in Equation 2-61 represents a stress drop defined as the average difference between stresses on a fault before a seismic event takes place and after the seismic event. However, the energy defined by Equation 2-61 does not accurately coincide with actual energy radiated as seismic waves during earthquakes. According to Kanamori (2001), seismically radiated energy is defined as follows:

$$\Delta E_R = \Delta W - \Delta E_G - \Delta E_F \tag{2-62}$$

$$\Delta W = DA\left(\sigma_0 + \sigma_1\right)/2 \tag{2-63}$$

$$E_F = \sigma_f DA \tag{2-64}$$

where ΔE_G, and ΔE_F are fracture energy and frictional energy loss, respectively; and σ_0 is initial stress acting on the fault before an earthquake; σ_1 is the final stress after the earthquake; σ_f is dynamic frictional stress. As can be seen from Equations 2-61 to 2-64, Equation 2-61 is obtained while assuming that (a) the stress acting on the fault immediately drops to the dynamic frictional stress, (b) the dynamic frictional stress is consistent with the final stress, and (c) fracture energy can be negligible. In reality, the dynamic frictional stress varies depending on slip rates and shear displacements during earthquakes and is not necessarily consistent with the final stress level (McGarr, 1999). In order to calculate seismically radiated energy more accurately, McGarr and Fletcher (2001) proposed the following equation:

$$E_{nf} = \frac{A}{2}\rho\beta\int \dot{D}(t)^2 dt \tag{2-65}$$

where E_{nf} is near-field energy radiated from fault-slip; ρ and β are the density of rockmasses and S-wave velocity, respectively; $\dot{D}$(t) is a time-dependent slip rate. It is found from Equation 2-65 that seismically radiated energy is calculated on the basis of slip rates. It is to be noted that Equation 2-65 yields near-field energy, which denotes that the energy does not take into account fracture energy indicated in Equation 2-62 and energy dissipated as permanent deformation in the vicinity of the fault. As mentioned by McGarr and Fletcher (2001), it should be bored in mind that a small fraction of near-field energy estimated with Equation 2-65 is actually transferred into far-field as seismically radiated energy. Far-field energy that is radiated as seismic waves can be approximated as the following equation (Kanamori, 2001):

$$E_R = \int \left(\rho\beta\int \dot{u}^2 dt\right) dS \tag{2-66}$$

where $\dot{u}$ is particle velocity excited by seismic waves. Although energy that is transferred into far-field is estimated by means of Equation 2-66 on the basis of results obtained from numerical analysis, considering the fracture and dissipated energy is still required to estimate far-field energy accurately with numerical analysis. It is found from these equations that comparison of seismically radiated energy estimated from wave forms recorded by seismic monitoring systems with that computed from numerical analysis is expected to be quite difficult. Further consideration with respect to the dissipated energy is indispensable for the comparison. However, seismically radiated energy computed with Equations 2-61, 2-65, and 2-66 can be certainly useful indices to evaluate the intensity of fault-slip relatively.

CHAPTER 3

Dynamic modelling of mining-induced fault-slip

3.1 Abstract

Fault slip bursts induced by mining activities could inflict severe damage to nearby mine developments. Considering a variety of factors that might exert an influence on the fault slip, dynamic numerical analyses are conducted by means of FLAC3D for models having a fault parallel to a tabular ore deposit. The results obtained from the analyses show that the maximum dynamic shear displacement increment induced by stope extraction is significantly affected by the friction angle of the fault, as well as mining depth and position of fault with respect to the orebody, while the stiffness and the dilation angle of the fault do not have as much influence. Seismic source parameters are computed based on the numerical results and as is the case with the maximum relative shear displacements, the position and friction angle of the fault appear to have the strongest influence on seismic moment and energy released by fault slip. The limitations of Mohr-Coulomb criterion as applied to the dynamic analysis of fault slip bursts are discussed in light of the results obtained. Lastly, slip rates and rupture velocity are investigated. The results show that the maximum slip rates are associated with the maximum increments of relative dynamic shear displacement. It is shown that extremely high rupture velocity could be induced by stope extraction. This could be the cause for a severe seismic event.

3.2 Introduction

Since the last century, there has been a growing demand for mineral resources worldwide. As a result, the depth at which mineral deposits are mined has increased substantially reaching up to 3 km in Canada and 5 km in South Africa. Deep mining has been conducted under unfavorable in-situ stress conditions due to extremely large overburden pressure and tectonic movements. The extraction of ore deposits at such great depths could induce significant stress re-distribution and rotation to the area surrounding mine openings. The change in in-situ stress regimes, in turn, leads to the higher risk for the occurrence of dynamic phenomena, such as rockbursts.

Rockburst is one of the phenomena caused by stress re-distribution and rotation arising from mining activities. Many efforts have been made for better understanding of the mechanism of rockburst since the first rockburst had been reported in the gold mines of Witwatersrand in South America and Kolar Gold Field in India at the turn of the century (Blake & Hedley, 2003). Owing to the research on rockburst, the means by which the occurrence of rockburst can be controlled or predicted have been developed by many researchers (Feit, Malinnikova, & Zykov, 2002; Salamon, 1970; Tajdus, Flisiak, & Cala, 1997; J. A. Wang & Park, 2001), considering the work done by extracting ore, the mechanical properties of rockmass and stress field in mining area. However, the aforementioned methods cannot be applicable to all the types of rockburst, only to a certain type of rockburst called strain burst, which is caused by violent fracturing of intact rock and, in many cases, occurs in the vicinity of mining openings or pillars.

There is another type of rockburst, to which the methods cannot be applied, called fault-slip burst, which is caused by the movement of pre-existing fault or the formation of seismically active structural zones. In spite of the many attempts made for understanding of the mechanism of fault slip bursts, as of now, effective

means to predict the magnitude of the event and the damage caused by seismic waved resulting from the fault slip burst if it occurs have not yet been developed because of the following two reasons: the complexity of mechanism governing fault behaviour and the difficulty of precisely assessing the change in stress in complicated rockmass fabric. First, determining the physical and mechanical properties of the surface of faults is quite challenging though many studies have been conducted through laboratory experiments and numerical simulations with the data of fault-slip bursts measured in fields. At present, many types of friction models of fault-slip for simulating the dynamic behaviour of shear sliding have been proposed, such as static-dynamic friction model, velocity-dependent model, slip-weakening model, and rate-and state-dependent model. In spite of the efforts to develop the friction models, the dynamic behaviour of fault-slip has not yet been fully understood due to many physical phenomena to be taken into account and the uncertainty of scale effect on the physical properties of faults. Second, complicated geological structures in mining area also make it difficult to predict the occurrence of fault-slip burst, that is to say, stress re-distribution, which does not occur evenly around the area surrounding stopes and mining opening, depends on in-situ geological structures. In details, the change in stress induced by mining activities is transferred to surrounding area through not only elastic medium but also creep process, the fracturing of rockmass and geological discontinuities, such as rock joints. Additionally, in mining development, the information of geological structures far from ore deposits tend to be ignored compared to the area in the proximity of mining openings and ore deposits. Therefore, identifying the fault that has the possibility of being mobilized due to stress readjustment induced by mining activities is quite difficult in a real situation.

Many attempts have been made in understanding the relationship between extracting ore deposits and the properties of fault slip by means of numerical analysis while taking into account some of the factors described above. Alber et al. (2009) investigated the decrease of fault safety factor by using an elastic 3D

boundary element code for a coal mine where fault planes are present, assuming Mohr-Coulomb failure criterion as the friction model of the faults. Hofmann and Scheepers (2011) made an attempt in simulating fault slip area with Mohr-Coulomb failure criterion in which cohesive strength changes when sliding occurs. The relationship between the location of excavated area and the increment of shear displacement along faults has been studied with typical cases that would be encountered in underground mines by means of 2D finite element method by Castro et al. (2009). Bewick et al. (2009) showed that seismic events that occur far from mining area are dominated by the large scale interaction between geological structures, based on the seismic data, geological information and numerical analysis. The authors concluded that understanding the interaction necessitates the methodology that takes into account a fault system.

The aforementioned studies have been conducted for better understanding of fault-slip and seismic events in a mining context. In the studies, static analyses to investigate the relation between mining development and the occurrence of fault-slip have been mainly carried out assuming uncomplicated failure criterion to express the frictional strength of a fault. As it is clearly seen from fault-slip bursts and the damage inflicted by ground motion arising from seismic waves, shear sliding that could cause fault-slip bursts should be considered as a dynamic event possessing a similar mechanism to shallow earthquakes with seismic energy radiation. While few studies taking into account dynamic behaviour of faults have been made amongst mining engineers, the research on the dynamic behaviour of fault-slip has been addressed in geophysics for the purpose of simulating the rupture process that occurs on a fault during earthquakes. Owing to the studies, quite a number of friction models considering factors, such as slip rates, frictional heating, and restrengthening, have been developed by many researchers (Bizzarri & Cocco, 2006a, 2006b, 2006c; 1978, 1979a, 1979b; Ruina, 1983). The friction models have been applied to numerical analyses in order to simulate the dynamic sliding behaviour of a fault both at laboratory scale and at

global scale (Bizzarri, 2012; 2008; 2008; Oglesby & Mai, 2012). The analyses showed the characteristic of each dynamic friction model and provided clues as to the relationship between slip rates and rupture velocity as well as that between fault-slip and ground motion, though it has not yet been accomplished to model the process of occurrence of earthquakes completely.

As described above, static analysis using mine-wide models in which dominant geological structures are reconstructed have been attempted in a mining context. In geophysics, on the other hand, the dynamic features of fault-slip have been primarily investigated, paying attention to neither rockmass fabric nor geological structures. It is evident that combining knowledge gained from the two fields would be required in order to figure out the mechanism of fault-slip bursts and predict the magnitude of induced seismic events. If accomplished, the influence of fault slip bursts on mining openings could be evaluated prior to the occurrence of fault-slip, hence stable production and a safe environment for mining workers could be achieve. This study focuses on the numerical analyses of the dynamic behaviour of faults in a mining context, considering quite simple geological structures, mining sequences and a friction model. The simplification was intended to assess factors that could have an influence on the behaviour of faults in mining sequences. For the purpose, in the analyses conducted, various parameters, such as in-situ stress, the mechanical properties of fault, and geometry of the model were changed in order to yield insights into how such parameters affect the dynamic behaviour of faults. Thus, this study could lay a foundation for calibrating and assessing numerical models where complicated geological structures and dynamic friction models are applied.

3.3 Model description

To investigate fault slip induced by mining activities, numerical models are generated by means of FLAC3D, a three dimensional explicit finite-difference program, considering factors that might have an influence on the behaviour of

faults, such as physical properties of rock, in-situ stress regimes, fault properties and mining method. In the following sections, detailed descriptions of the 4 factors are given.

3.3.1 Ore deposit and proposed mining method

The geometries of ore deposits vary significantly with the origin of the deposits, metamorphism and subsequent alternation, in which the deposits have been involved since the deposits had formed in ancient times. In the present study, a steeply dipping and tabular ore deposit, which is frequently encountered at mine sites in Canadian Shield (Bewick et al., 2009), is modelled. Sublevel stoping method with delayed backfill is widely used in Canadian mines because of the advantages of safety, a high production rate, and the high percentage of ore recovery (Zhang & Mitri, 2008). This type of ore deposit and mining method are adopted as the model of this study.

3.3.2 Fault configuration geometry for numerical models

There exist quite a number of types of faults, depending on scale, structures involved, shape, fabrics and mechanical properties (Bewick et al., 2009; Kim et al., 2004; Ortlepp, 2000; Wallace & Morris, 1986). For each type of faults, the response to the change in in-situ stress fields induced by mining activities differs; some faults exhibit sliding behaviour along pre-existing geological discontinuities, and others respond to the stress re-distribution by creating a new fault surface or by interacting surrounding geological structures. Whether the response leads to seismic events that cause devastating damage to mine openings depends on the characteristics of the fault and in-situ stress regime. The behaviour of faults for seismic events related to fault-slip was classified by Carter and Bewick (2012) as: a) development of new faults through intact rock (Ortlepp, 1997); b) coalescence of en echelon fractures producing a linked fault (Trifu & Urbancic, 1996); or c) slip along pre-existing faults (Mikula, 2002). The formation of new

faults and coalescence of embryo fault systems tend to release comparatively small seismic energy during the process because the part of energy arising from stress re-distribution or stress drop is expended to generate new fault surfaces. Sliding along pre-existing faults, on the other hand, has the potential of releasing large energy during the slip and causing more severe damage far from the hypocenter of the event than other types of fault-slip, depending on the degree of interlocking and stored energy before the seismic event takes place. Thus, this study focuses on fault-slip that occurs along pre-existing, primary faults. Although there does not exist completely planar fault plane as reported by Wallace and Morris (1986), planar fault plane is modelled in the present study. Considering the fact that fault geometry exhibits characteristics that are extremely different from each other due to different in-situ stress states, palaeostress states and geological characteristics, it is reasonable to model a fault surface as planar, so that the sliding behaviour along pre-existing, planar surface fault can be understood before the numerical analysis for undulating, branching, anastamosing faults is attempted using geologic data collected from given mine sites.

3.3.3 Model geometry

3D numerical models adopting the geometry of ore deposit, the mining method and fault layout described above are generated. The parametric study, in which the model geometry was changed depending on factors to be considered, was conducted in the present study. The model geometry shown in Figure 3-1 represents a basic model to be compared to other models. As shown in Figure 3-1, the width, length and height of the model are 272m, 300m, and 300 m, respectively. A steeply dipping, narrow vein deposit is modelled, which is located at the center of the numerical model. The modelled ore deposit dips at 80˚, and the strike of the deposit is parallel to y-axis shown in Figure 3-1.

The purpose of this study is to gain comprehensive knowledge about the influence of mining activities on fault behaviour, using generally acceptable models. Therefore, in order to consider fault locations that could be causative for seismic events in developing underground mines, two different layouts of fault were taken into account. The first is of a fault dipping at 80˚ that is in the hanging wall (HW) and parallel to the ore deposit, and the second is for a fault in the footwall (FW). The fault locations analyzed are depicted as lines colored in brown in Figure 3-1.

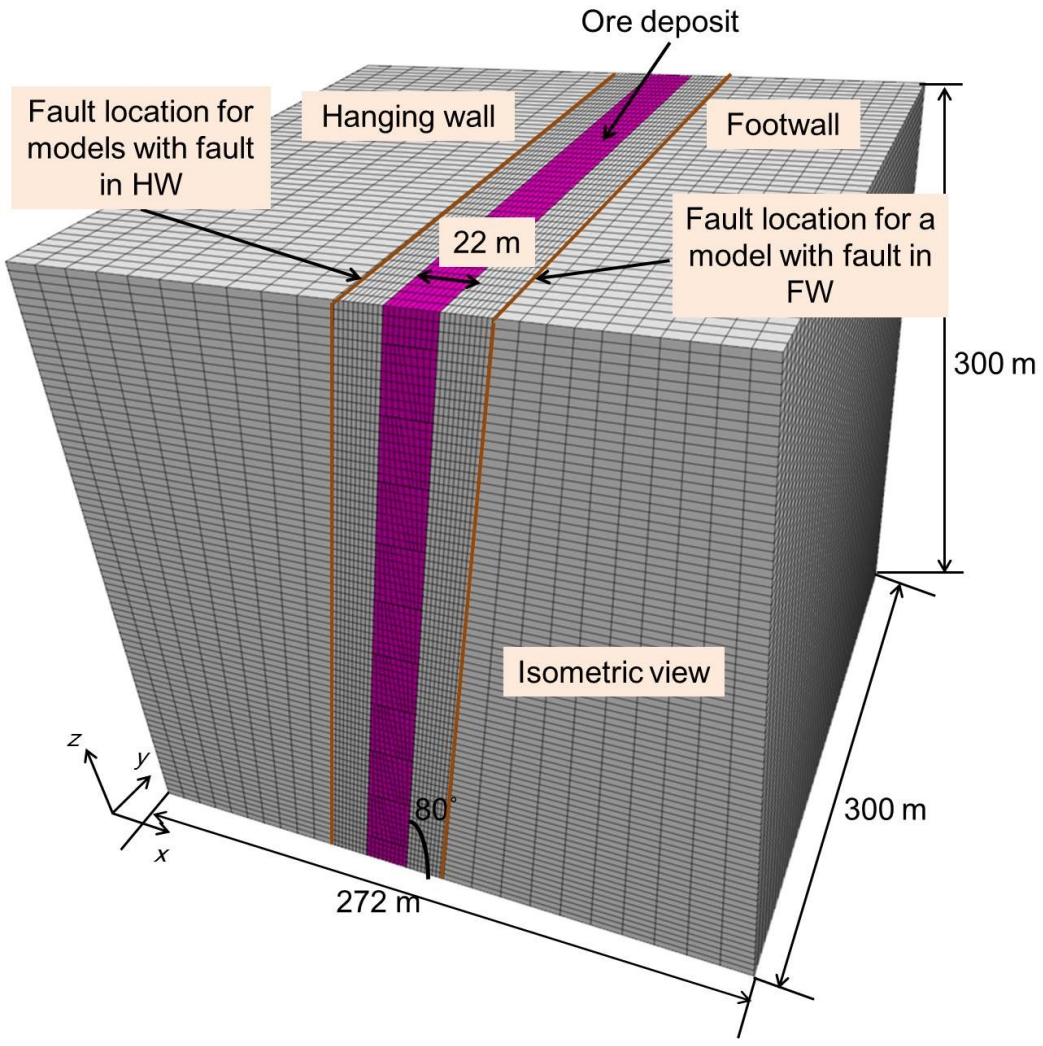

Figure 3-1: Basic model and fault locations analyzed

3.3.4 Proposed mining sequence

The ore deposit is extracted using sublevel stoping method, with which each

stope is drilled, blasted, and backfilled at each sublevel and bottom-up mining is carried out. Figure 3-2 shows the proposed mining sequences and stope geometry which were determined based on typical sublevel stope geometries in Canadian underground mines (Zhang & Mitri, 2008). As shown in Figure 3-2, the ore deposit is extracted from 9 sublevels, and the distance between sublevels is 30 m. On each sublevel, stopes are mined out from hanging wall to footwall. Mining rates vary from mine site to another, depending on production rate and the size of haulage drift. In this study, two stope strike lengths of 200 m and 25 m are considered to represent high and low mining rates. In the case of high mining rate, two stopes are extracted from HW to FW on each sublevel. In the case of low mining rate, each stope is extracted after stress re-distribution induced by previous excavation is completed. Mining progresses in retreat until 8 stopes along the level 200 m strike and extracted in 16 steps on each level.

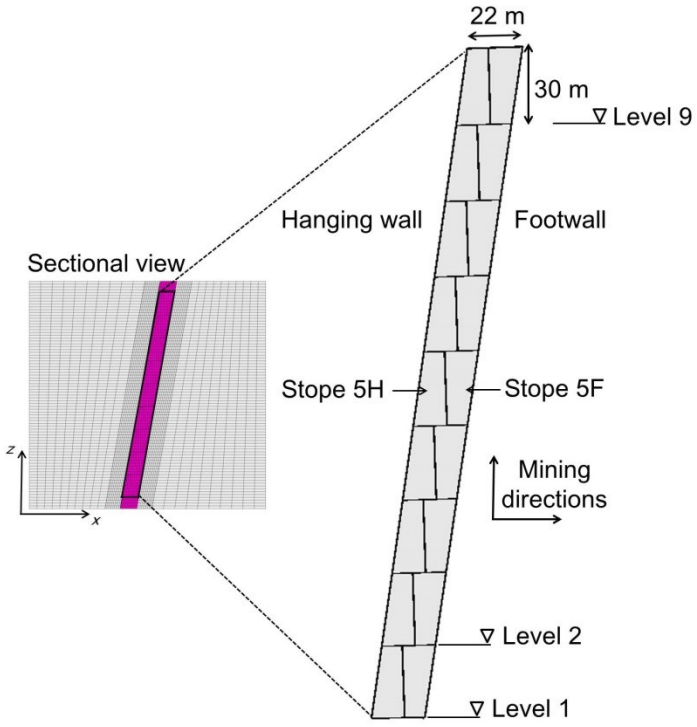

Figure 3-2: Simulated mining sequence

3.3.5 Distance between stope and fault

In addition to taking into account the location of fault and a mining rate, the

influence of distance between the ore deposit and the fault on the occurrence and magnitude of fault slip was investigated. Such distance was taken as 30, 60 and 90 m. The distances considered here are for better understanding of the influence of local stress re-distribution induced by mining activities on fault slip (Castro et al., 2009). As reported by Bewick et al. (2009) and B. G. White and Whyatt (1999), in some cases, fault slip bursts are caused far from mining area through the interaction of geological structures and development of embryo fault systems. The present research does not consider the phenomenon, but the results obtained from this research could give a clue as to whether fault slip is induced by local umclamping (Castro et al., 2009) or by mutual interaction between geological structures.

3.4 Numerical analysis

Static and dynamic analyses were conducted with finite difference method by means of FLAC3D software by Itasca (2009). In this section, a detailed description of the numerical analysis is given with respect to requisites to conduct the analyses, such as initial stress state and the physical properties of the rockmass and the fault, along with the procedure of analysis.

3.4.1 Interface

Interface elements are used for representing the faults with FLAC3D, which generate the interfaces as collections of triangular elements, each of which is defined by three nodes. Each interface node has an associated representative area shown in Figure 3-3 (Itasca, 2009), and the interface element, which is zero-thickness, is attached into target faces in a numerical model.

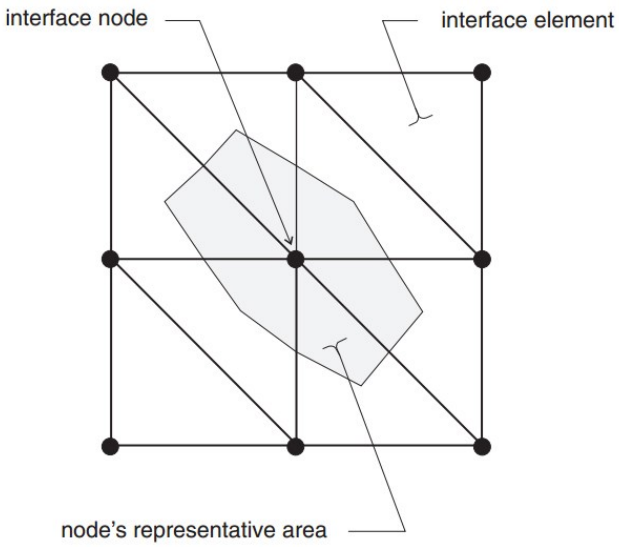

Figure 3-3: Distribution of representative areas to interface nodes (Itasca, 2009)

During each timestep, normal and shear force are computed at each node as follows.

$$F_n^{(t+\Delta t)} = k_n u_n A + \sigma_n A \tag{3-1}$$

$$F_{si}^{(t+\Delta t)} = F_{si}^{(t)} + k_s \Delta u_{si}^{(t+(1/2)\Delta t)} A + \sigma_{si} A \tag{3-2}$$

where $F_n^{(t+\Delta t)}$, u_n, k_n, and A are normal force at time (t + Δt), absolute normal penetration of the interface node into the target face, normal stiffness, and the representative area associated with interface node, respectively, and $F_{si}^{(t+\Delta t)}$, u_{si}, k_s, σ_{si} are shear force vector at time (t + Δt), incremental relative shear displacement vector, shear stiffness, and additional shear stress vector due to interface stress initialization, respectively. The shear force acting on interface element is limited to the value determined by Coulomb shear-strength criterion as shown below.

$$F_{s\max} = cA + F_n \tan\phi \tag{3-3}$$

where F_{smax}, c, and ϕ are shear strength of interface, cohesive strength and

friction angle, respectively. The normal force calculated from Equation 3-1 is substituted into Equation 3-3, and the comparison of shear strength F_{smax} along the interface with the shear force F_s from Equation 3-2 is made as follows. If $|F_s| \geq F_{smax}$, then sliding is assumed to occur, and $|F_s| = F_{smax}$, with the direction of shear force preserved. The interface element takes into account dilation that might be accompanied by sliding. The increase in normal stress due to dilation is computed as below.

$$\sigma_n = \sigma_n + \frac{|F_s|_o - F_{s\max}}{Ak_s} \tan\psi k_n \tag{3-4}$$

where $|F_s|_o$ is the magnitude of shear force before the above-mentioned correction is made and ψ is the dilation angle. Using the above-mentioned equations, the sliding behaviour can be determined during numerical analyses.

3.4.2 Initial stress state

The vertical in-situ stress, σ^o_v, which is in the z-direction in Figure 3-1, is given by the overburden pressure as follows.

$$\sigma^o{}_v = \gamma H \tag{3-5}$$

where γ and H are the unit weight of the rockmass and the depth below ground surface. According to Arjang (1991), steeply dipping orebodies in the Canadian Shield have the characteristics that the maximum horizontal stress is in the direction perpendicular to orebody and the direction of minimum horizontal stress is parallel to the orebody strike. This was adopted in the present study. The magnitude of maximum and minimum horizontal stresses were determined by Diederichs (1999).

$$k_{\max} = 1 + \frac{25}{\sqrt{H}} \tag{3-6}$$

$$k_{\min} = 1 + \frac{8}{\sqrt{H}} \tag{3-7}$$

$$\sigma^{o}{}_{H\max} = k_{\max}\sigma^{o}{}_{v} \tag{3-8}$$

$$\sigma^{o}{}_{H\min} = k_{\min}\sigma^{o}{}_{v} \tag{3-9}$$

where k is the ratio of horizontal stress to vertical in-situ stress. Thus, the maximum and minimum horizontal stresses expressed by Equations 3-8 and 3-9 can be derived from calculating the value of k by use of Equations 3-6 and 3-7. Mining depth was also considered as the factor that might affect the sliding behaviour of the faults, thus parametric study was conducted with respect to the depth. The depth at top boundary of the model was set at 1500 m, 2000 m and 2500 m, and unit weight of overlying rockmass was assumed 25.5 kN/m^3. This setting of initial stress state is based on the research by Zhang and Mitri (2008). Table 3-1 shows the calculated initial stress state at each depth.

Table 3-1: Initial stress state at different mining depth

Depth (m)	k_{max}	k_{min}	γ (kN/m^3)	σ_v (MPa)	σ_{Hmax} (MPa)	σ_{Hmin} (MPa)
1500	1.65	1.21	25.5	38.25	62.94	46.15
2000	1.56	1.18	25.5	51.0	79.5	60.12
2500	1.5	1.16	25.5	63.75	95.63	73.95

3.4.3 Mechanical properties of rockmass, backfill and fault

The mechanical properties of rockmass used for the analyses are based on the test results obtained from rock samples of Bousquet 2 Mine (Henning, 1998). Different properties for HW, ore body, and FW were assigned as shown in Table 3-2. Table 3-3 shows the mechanical properties of the cemented backfill material that was used in the numerical models.

Table 3-2: Rockmass mechanical properties

	Hanging wall	Ore body	Footwall
Modulus of elasticity (GPa)	31	115	49
Cohesion (MPa)	2.6	11.5	4.3
Friction angle (˚)	38	48	39
Poisson's ratio	0.21	0.10	0.15
Unit weight (kN/m^3)	25.51	25.51	25.51
Tensile strength (MPa)	1.1	5.9	1.8
Dilation angle (˚)	9.25	12.0	9.75

Table 3-3: Mechanical properties of cemented backfill material

	Backfill
Modulus of elasticity (GPa)	2.5
Cohesion (MPa)	0.1
Friction angle (˚)	35
Poisson's ratio	0.35
Unit weight (kN/m3)	23.00
Dilation angle (˚)	0

A model parametric study was conducted for the mechanical properties of the fault. This is because the mechanical properties of a fault are significantly affected by many factors that are quite difficult to determine. For instance, depending on the shear displacement that a fault has experienced since its formation and fault fabrics, a variety of materials could accumulate on the surface of the fault, and these materials dominate the characteristics or the mechanical behaviour of the fault (Bradbury et al., 2007; Chester & Chester, 1998). In addition, the mechanical properties determined from laboratory tests are scale dependent. Despite many attempts that have been made for understanding the

effect of scale on the mechanical properties of faults or rock joints (Barton, 1982), the scale effect on the mechanical properties of the fault is still unclear. For the aforementioned reasons, the mechanical properties of fault were set as follows. First, friction angles of fault of 15˚, 25˚ and 30˚ were adopted while considering three conditions, namely a fault infilled with clay, and a fault with thin layer of clay, and a fault without infilling the materials (Barton, 1973; Barton & Choubey, 1977). The shear and normal stiffness of fault were set at 10 %, 20 % and 30 % of the shear modulus of the surrounding rockmass. The dilation angle found in equation 4 was set at 0˚, 5˚, and 10˚.

Table 3-4 provides a list of the fault numerical models simulated. As can be seen, 17 models were generated to help examine the effect of fault location, stope length, mining depth, distance between the ore deposit and fault, friction and dilation angles of the fault and fault stiffness.

Table 3-4: Properties of fault numerical models simulated

Model	*FL*[1]	*SL*[2] *(m)*	*H*[3] *(m)*	*D*[4] *(m)*	ϕ[5] (˚)	k_n (GPa/m)	k_s (GPa/m)	ψ[6] (˚)
1	HW	200	1500	30	30	3.1	1.28	0
2								5
3								10
4						6.2	2.56	0
5						9.3	3.84	0
6				60	30	3.1	1.28	0
7				90	30	3.1	1.28	0
8			2000	30	30	3.1	1.28	0
9				60	30	3.1	1.28	0
10				90	30	3.1	1.28	0
11			2500	30	30	3.1	1.28	0
12				60	30	3.1	1.28	0
13				90	30	3.1	1.28	0
14			1500	30	25	3.1	1.28	0
15					15	3.1	1.28	0
16		20	1500	30	30	3.1	1.28	0
17	FW	200	1500	30	30	3.1	1.28	0

[1]Fault location

[2]Stope length

[3]Mining depth

[4]distance between fault and stopes

[5]friction angle of fault

[6]dilation angle of fault

3.4.4 Procedure of numerical analysis

Fault slip induced by mining is a dynamic behaviour from which seismic waves arise; hence it is desirable that dynamic analyses are conducted throughout the proposed mining sequence. However, the analyses would require considerable amount of time, depending on the capabilities of the computer used for the analysis and the number of grid points in the numerical model. In addition, the extraction of stopes at the beginning of the mining sequence does not cause significant unclamping along the fault to give rise to fault slip. For these reasons, static analyses are carried out until a certain amount of slip occurs along the fault in Model 1, which is the reference model. As a result, the state after extracting STOPE6F, the footwall side of stope on the 6th sublevel, was determined as the initial state for dynamic analyses. Thus, for Models 2 to 15 and 17, static analyses were carried out until the extraction of STOPE6F as well. As for Model 16, the state after extracting STOPE7F4, which is the 4th stope on footwall side on the 7th level, was considered as the initial state. Based on the initial state, the next stope was extracted with dynamic analysis for each model.

3.4.5 Analysis conditions of static and dynamic analysis

In static analyses, boundaries of the models were fixed in the direction perpendicular to the boundary, and initial stress fields were given following the Equations 3-5 to 3-9. The mechanical properties of rockmass, ore bodies, and faults were assigned as described in section 3.4.3. For the dynamic analyses, the boundary conditions were changed to viscous in order to prevent the model boundaries from reflecting elastic waves arising from fault slip and the extraction of stopes. The timestep used for the dynamic analysis is automatically calculated based on the volume of each zone of the model, P-wave velocity obtained from rockmass mechanical properties and the face area of each zone (Itasca, 2009). Regarding the attenuation of elastic waves, local damping embodied in FLAC3D was taken. According to the manual of FLAC3D, coefficient of local damping is given as:

$$\alpha_L = \pi D \tag{10}$$

where αL and D are the local damping coefficient and a fraction of critical damping. It operates by adding or subtracting mass from a grid point at certain times during a cycle of oscillation. Although local damping cannot capture the energy loss properly when wave forms are complicated, it enables frequency-independent damping. According to ABAQUS (2003), a fraction of critical damping for rock falls into 2 to 5 %. Thus, 5 % of critical damping is adopted for this study; and this damping system was deemed sufficient at this stage, considering the focus of the study.

Model sensitivity analysis was conducted prior to static and dynamic analysis in order to examine the effect of boundary conditions on the behaviour of faults. In the analysis, several types of numerical models that have different width, length and height shown in Figure 3-1 were generated, and the magnitude of shear displacement along the faults were compared after extracting the stopes with static analysis. The comparison indicated that the overall length and width of the numerical model are sufficiently large to prevent the boundary conditions from affecting the behaviour of the faults while it was shown that the height of the model affects the sliding behaviour; which is expected due to the modeled persisting of the fault.

3.5 Method to evaluate fault-slip

The results obtained from dynamic analyses for Models 1 to 17 are evaluated through various parameters that can express the magnitude and intensity of the fault slip induced by mining. A description of used parameters is given below.

3.5.1 Seismic source parameters

Seismic source parameters are widely used to evaluate the magnitude of

mining-induced seismicity, and the seismic source parameters calculated from the data obtained by seismic network installed on the ground surface or in underground are compared with those computed from numerical analysis (Hofmann & Scheepers, 2011; Potvin et al., 2010; Sjoberg et al., 2012). In the present study, the following seismic parameters were adopted to investigate dynamic sliding behaviour: seismic moment, Mo, moment magnitude, Mw, and energy released during fault slip, E_s. The seismic moment and moment magnitude are commonly used in the study of mining-induced seismicity (Domanski & Gibowicz, 2008; Hedley, 1992; Hofmann & Scheepers, 2011; Sneilling et al., 2013); they are given by

$$M_o = GDA \tag{3-11}$$

$$M_w = \frac{2}{3}\log M_o - 6.0 \tag{3-12}$$

where G, D, and A represent shear modulus, average shear displacement, and area where sliding takes place. The seismic energy E_s represents the sudden energy released along the faulting area “A” subjected to the slip “D” and is thus given by.

$$E_s = 0.5\Delta\sigma DA \tag{3-13}$$

$\Delta\sigma$ in Equation 3-13 represents stress drop defined as the average difference between the stress on a fault before a seismic event to the stress after the event and is expressed as follows.

$$\Delta\sigma = \frac{1}{A}\int_s [\sigma(t_2) - \sigma(t_1)]dS \tag{3-14}$$

Note that the calculated energy does not accurately represent seismically radiated energy, but considering the purpose of this research, the energy can be employed as an index to examine the influence of the factors on fault slip.

In this research, the calculations for the aforementioned seismic parameters are performed over the area where the increase of relative shear displacement during dynamic analysis exceeds 0.01 m and where the shear stress along a fault decreases. The threshold for the seismic parameters is determined based on the result obtained from the model, in which the mechanical properties of fault are set high enough to prevent fault slip from occurring whereby the elastic behaviour of fault without sliding can be estimated.

3.5.2 Slip rates and rupture velocity

Slip rates and rupture velocity, at which failure expands along the fault, are of great importance due to the fact that those parameters are associated with the generation of seismic waves that possibly pose a threat to mine openings far from the hypocenter of the induced fault slip. The attempt for better understanding of the influence of the slip rates and rupture velocity on the intensity of ground motion and the properties of seismic waves have been made by many researcher (Aki & Richards, 1980; Bizzarri, 2012; Dunham & Bhat, 2008; Francis, Thomson, & Kuenzler, 1972) in geophysics and seismology. Although the knowledge has been rarely applied to research on fault slip in a mining context, it must be applied because an appreciation of whether or not the sliding of fault can give rise to seismic waves is critical in order to design an appropriate support system for underground openings.

In the present research, the maximum slip rate and rupture velocity on a fault are investigated in order to gain basic knowledge of the behaviour of fault slip in underground mines. As a threshold for determining the onset of rupture, the

nodes at which a slip rate exceeds 0.1 m/s were considered to be ruptured during timestep of dynamic analysis.

3.6 Results and discussion

Numerical analyses for 17 models described in Table 3-4 were carried out following the procedure explained in section 3.4.4. This section provides the results obtained from the analyses and discussion about the influence of factors, such as the friction angle of a fault and initial stress state, on the fault slip caused during dynamic analyses. First, from the viewpoint of shear displacement, the result will be discussed. After that, seismic source parameters will be shown for each model. Lastly, the interpretation of slip rates and rupture velocity will be given.

3.6.1 Shear displacement along a fault

Figure 3-4 shows the maximum value of relative shear displacement increment along the fault. The values are calculated by subtracting the relative shear displacement on a fault before dynamic analysis from that after dynamic analysis for each model. As can be seen from the results of models 1 to 5, the dilation angle and the shear stiffness of the fault do not have a large influence on the maximum relative shear displacement increment, compared to the other parameters. Although the stiffness and the dilation angle of fault are difficult to estimate from rock samples because of scale effect and the complexity of fault plane, this result implies that some extent of error about these values would be tolerated when numerical modelling of fault slip is attempted. The influence of the distance between stopes and fault on the shear displacement can be determined from the results of models 6, 7, 9, 10, 12, and 13. As can be seen, when the distance is more than 60 m, there is much less shear displacement increment in spite of the mining depth. This indicates that the shear displacement increment of these models is excited by the elastic behaviour of the fault and that it is

important to comprehend the positional relationships between stopes and faults in mine sites because the sliding behaviour of the fault is sensitive to the distance. As for the friction angle of the fault and mining depth, it is evident from Models 8, 11, 14 and 15 that there are clear relationships between the change in the maximum shear displacement increment.

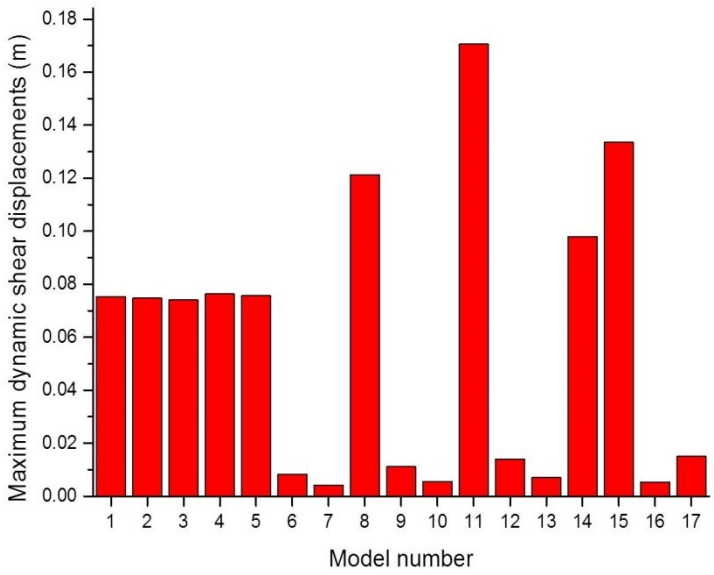

Figure 3-4: Predicted maximum dynamic shear displacements

For better understanding of the relationships, the detailed data is plotted in Figure 3-5. As can be seen, mining depth is proportional to the maximum shear displacement. The friction angle also has an almost linear relationship with the shear displacement. These results imply that the risk and magnitude of fault slip increase as mining progresses deeper and that the estimation of friction angle of faults is quite important in evaluating the magnitude of fault slip. Comparison of model 1 with model 16 gives an insight into the influence of mining rate on fault slip. Although the amount of extracted rock mass in model 16 eventually becomes the same as that in model 1, a low mining rate causes much less shear displacement on fault than a high one. This is because the energy released by the extraction of stope is much smaller in case of low mining rate and the unbalance force acting on the fault is released in small increment of fault slip at

the time of extraction of each stope. Thus, in terms of prevention of fault slip, it can be concluded that a mining rate as low as possible is desirable. Lastly, the result of model 17 shows that the shear displacement increment of approximately 0.015 m is induced on the fault in footwall. The value is much less than the 0.075 m of model 1. The difference in relative shear displacement increment for these two models can be explained by the change in shear and normal stress on the faults induced by extracting stopes. The stress paths for normal and shear stress are given in Figures 3-6 and 3-7. The horizontal and vertical axes in the figures represent normal and shear stress, respectively. The stress paths on the faults during dynamic analysis were recorded at the point close to the center of extracted stope, y = 150 m, z = 210 m, the point above the stope, y = 150 m, z = 255 m, and the point below the stope, y = 150 m, z = 165 m. Arrows in the figures denote the change in stress in the dynamic analysis. As can be seen, there is a clear difference in the stress path between the fault in HW and that in FW. First, for the fault in HW, normal stress at the point close to the center of stope, which is shown as black points in Figure 3-6, decreases from 70 MPa to almost 0 MPa. In contrast, for the fault in FW, the decrease in the stress at the point is approximately 45 MPa as shown in Figure 3-7. The graphs clearly show that the stress drop of shear stress, which gives rise to relative shear displacement increment along the fault, pertains to the decrease in normal stress. However, considering the fact that the distance between STOPE7H extracted in the dynamic analysis and the fault in HW is shorter than that between the stope and the fault in FW, there is a possibility that the difference in the change in normal stress is caused by the difference in distance between the stope and the faults, and not by the difference in positional relationships. Apart from the stress path at the point close to the center of the stope, attention must be paid to the stress path at the point above the stope, which is shown as red points in the figures. For the case that a fault exists in HW, shear stress at the point increases from 5 MPa to 15 MPa. For a fault in FW, on the other hand, the shear stress slightly decreases in the analysis. This indicates that, for the fault in HW, the

stress state on the fault at the upper part of mining area transitions to the state capable of causing more violent fault slip and that, for the fault in FW, sliding that occurs close to stope does not cause shear stress on the fault above the stope to increase. Thus, it can be concluded that as mining progresses upward, the fault slip induced by mining becomes more violent when the fault is located in the HW.

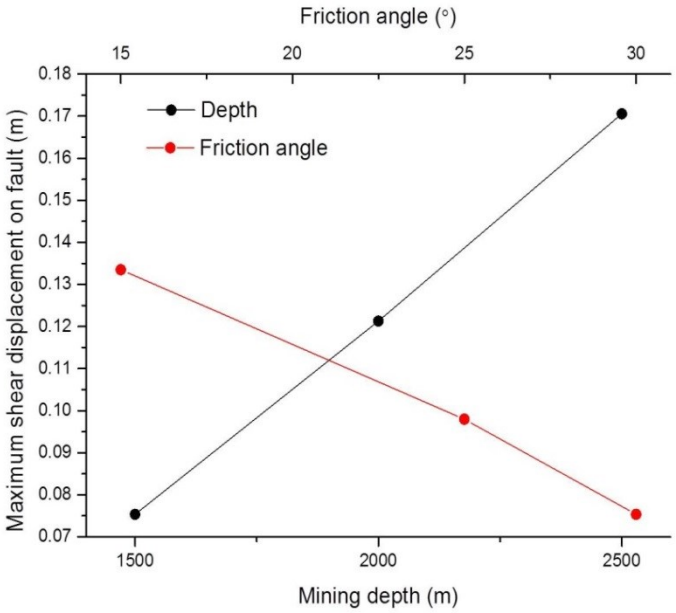

Figure 3-5: Effect of mining depth and fault friction angle on maximum shear displacement increment along the fault

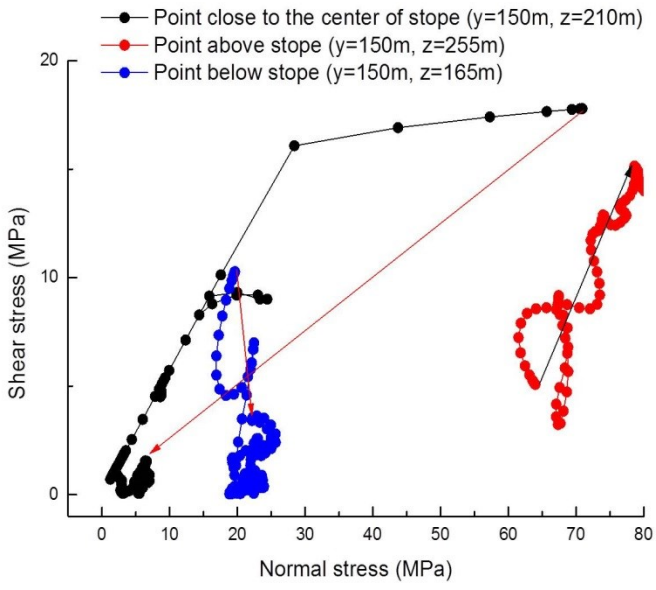

Figure 3-6: Stress path on a fault in HW at observation points

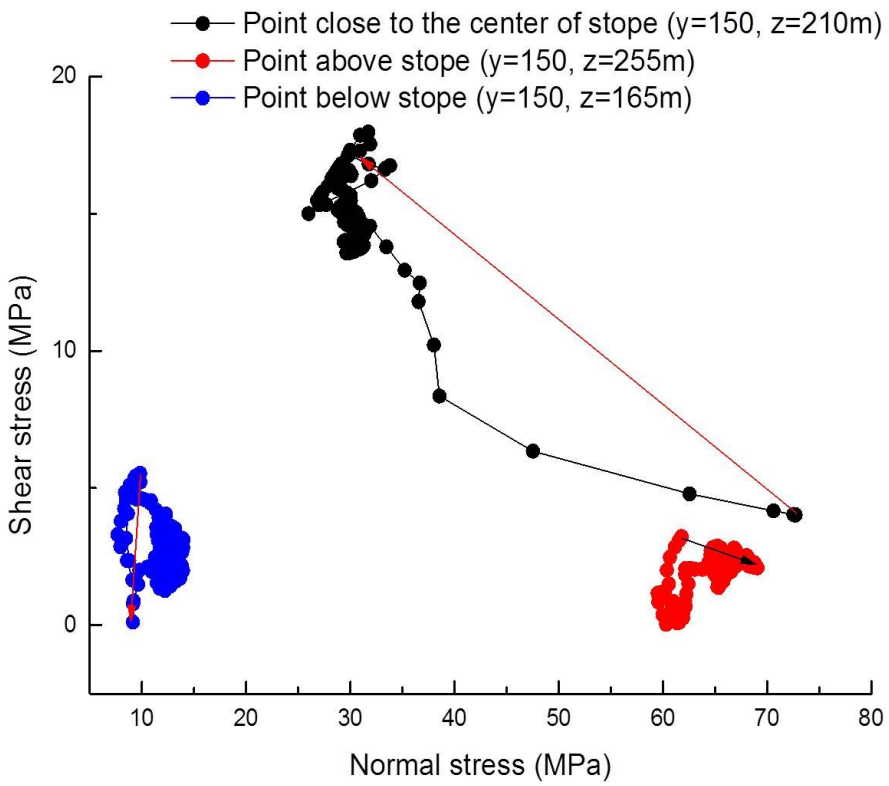

Figure 3-7: Stress path on a fault in FW at observation points

3.6.2 Seismic source parameters

Based on the results obtained from the dynamic analyses, seismic moment, moment magnitude and energy released by fault slip were computed following Equations 3-11 to 3-14 and thresholds for determining the occurrence of fault slip. Figure 3-8 depicts the seismic moment and the energy release results. As can be seen, the tendency of the influence of the variables on the seismic source parameters is similar to that shown for the maximum value of shear displacement increment in Figure 3-4, though there are slightly different points. First, the influence of the change in the dilation angle and the stiffness of faults is reflected more clearly in the results. As can be seen in the figures, both of the seismic moment and the energy decrease with increasing dilation angle and increase with increasing stiffness. This implies that the relative shear displacement and stress drop induced by stope extraction are affected by the dilation angle and the

stiffness across the whole ruptured area on fault. The feature was not readily interpreted for the maximum increment of relative shear displacement. It should be also noted that as is the case for the maximum shear displacement increment, the influence on seismic parameters is smaller compared to that of the mining depth and the friction angle of the fault.

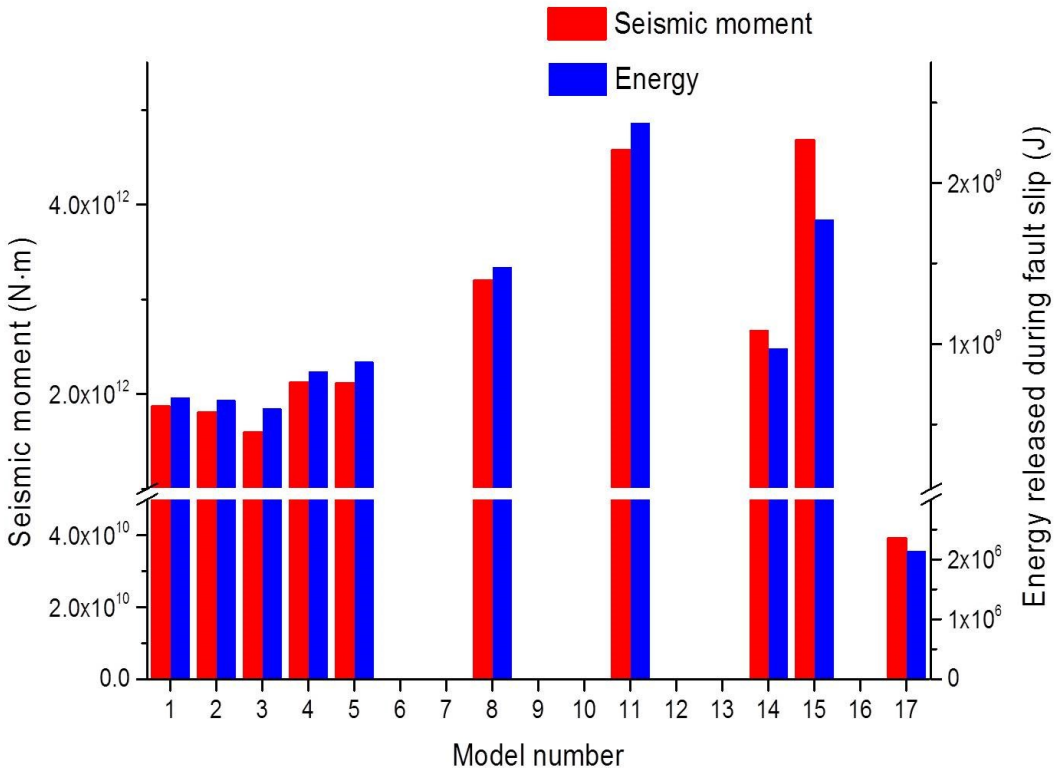

Figure 3-8: Computed seismic moments and energy released during fault-slip

The detailed data on depth and friction angle is shown in Figures 3-9 and 3-10. As shown in Figure 3-9, with the decrease in the friction angle, the seismic moment increases from 1.8×1012 N·m to 4.7×1012 N·m, and the energy released by fault slip increases from 6.5×108 J to 1.7×109 J. Likewise, as shown in Figure 3-10, with increasing mining depth, the seismic moment increases to 4.8×1012 N·m, and the energy increases to 2.4×109 J. These results suggest that the influence of the friction angle and mining depth are remarkable and that the influence of the factors, such as the depth, the stiffness of fault, on the behaviour of fault is reflected more clearly by seismic source parameters. The

results of models 6, 7, 9, 10, 12, 13, and 16 in Figure 3-8 indicate that there is no fault slip associated with seismic activities. The maximum shear displacements for models 9 and 12 shown in Figure 3-4 are greater than the threshold described in section 3.5.1 for determining the occurrence of fault slip, nevertheless, the seismic moment and the energy of the models are 0 as shown in Figure 3-8. This is because stress drop did not occur, i.e., the sliding behaviour can be considered elastic. As for the model with a fault in the FW, the seismic moment and the energy are extremely small compared to those of the model with a fault in the HW. The results of model 17 show approximately a fiftieth of seismic moment and a hundredth of seismic energy, compared to those of model 1. Thus, one can expect that the positional relationships between stopes and faults could be one of the most important factors that determine the magnitude and the occurrence of fault slip. Lastly, moment magnitude is shown in Figure 3-11. The difference in moment magnitude corresponds with that in seismic moment since moment magnitude is computed as a function seismic moment. The moment magnitude shown in Figure 3-11 except those for model 6, 7, 9, 10, 12, 13, and 16 can be regarded as the seismic events that have a possibility of causing damage to mine openings as can be seen in many reports (Blake & Hedley, 2003). However, these values are less than those reported in some mine sites. This highlights the limitation of the use of static friction laws, such as Mohr-Coulomb criterion, for analyzing fault-slip. With dynamic friction, larger seismic source parameters would have been captured in the model because the shear strength expressed by the dynamic friction laws varies with various factors that static laws do not take into account. Thus, the application of dynamic friction laws, such as rate-and state-dependent friction law (Dieterich & Kilgore, 1996; Ruina, 1983) and slip weakening friction law (Ida, 1972), is strongly required so as to estimate the magnitude of seismic events that might cause damage to mine openings.

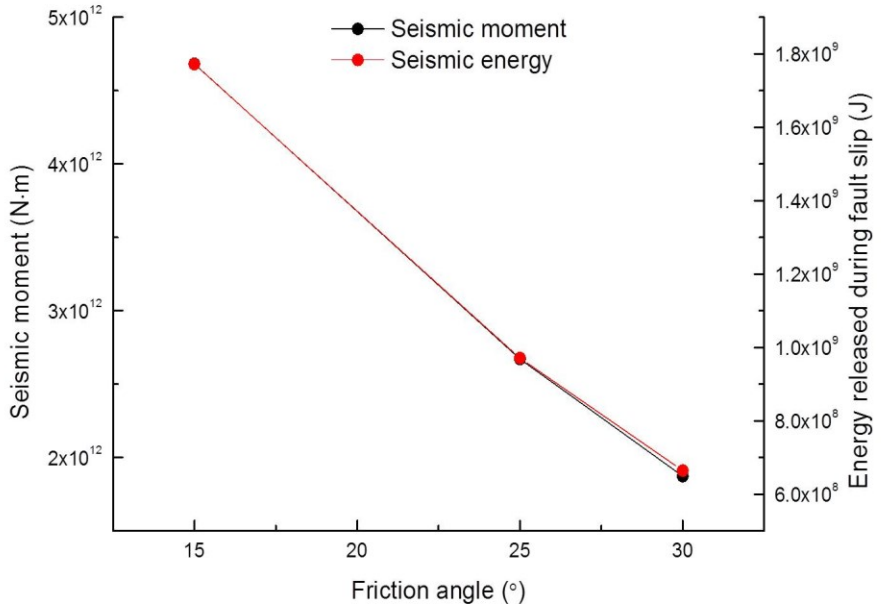

Figure 3-9: Effect of friction angle on seismic moment and energy released by fault-slip

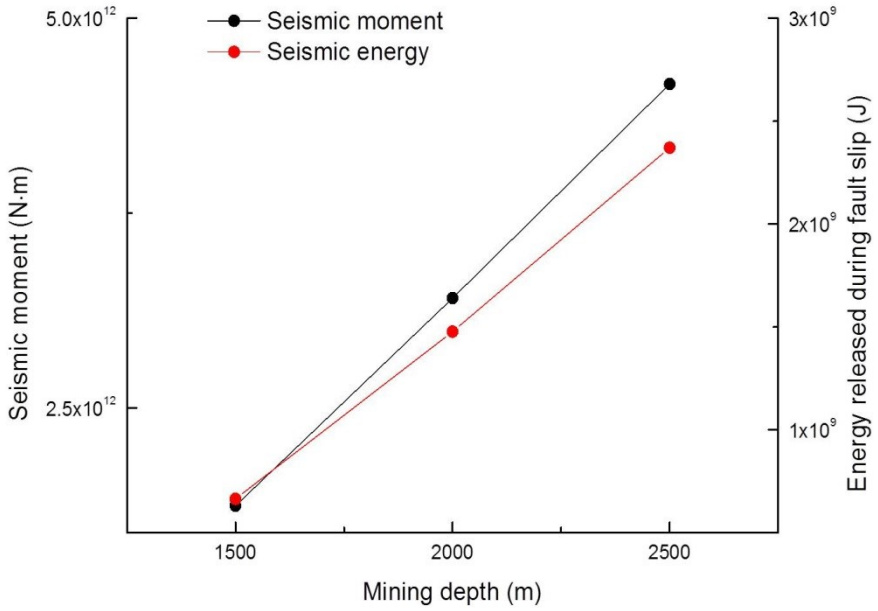

Figure 3-10: Effect of depth of the models on seismic moment and energy released by fault-slip

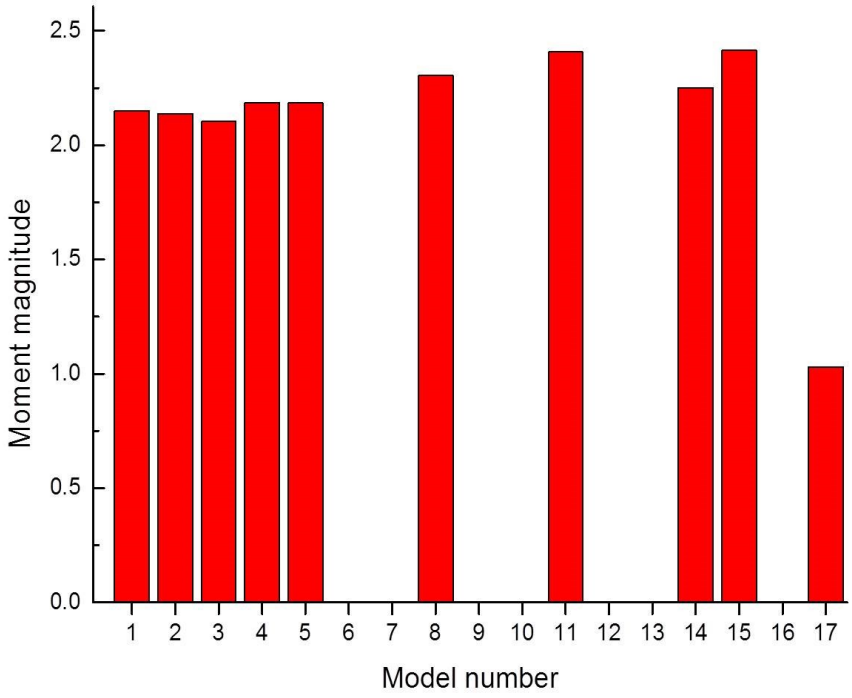

Figure 3-11: Computed moment magnitude

3.6.3 Slip rates and rupture velocity

As described in section 3.5.2, slip rates and rapture velocity are important indicators that pertain to the generation of seismic waves and ground motion induced by the waves. Figure 3-12 shows the maximum slip rates, which are calculated on the basis of the increment of relative shear displacement on the center line of the faults, i.e. the line of y = 150 m on the faults. As can be seen, for model 1, the maximum slip rate is approximately 4 m/s, which is high enough to generate seismic waves as shown in seismic data obtained from earthquakes (Ide & Takeo, 1972). Thus, if the fault-slip occurs in a mine, seismic waves are expected to be generated and inflict damage at the mine opening boundary. Regarding the influence of dilation angle on the slip rates, it seems to be negligible. Also, the effect of the stiffness of faults on the slip rates appears to be ambiguous. As shown in Figure 3-12, it is difficult to correlate the change in the

stiffness with the slip rates from the output data. It is, on the other hand, evident from the results of model 8 and 11that slip rates increase with increasing depth of mining. Likewise, there is a clear relationship between the friction angle of the fault and the maximum slip rate. These results indicate that the maximum slip rate has a correlation with the maximum relative shear displacement on a fault. The relationship is shown in Figure 3-13. Although there are some irregular points in the figure, in general, the slip rate can be correlated with the shear displacement.

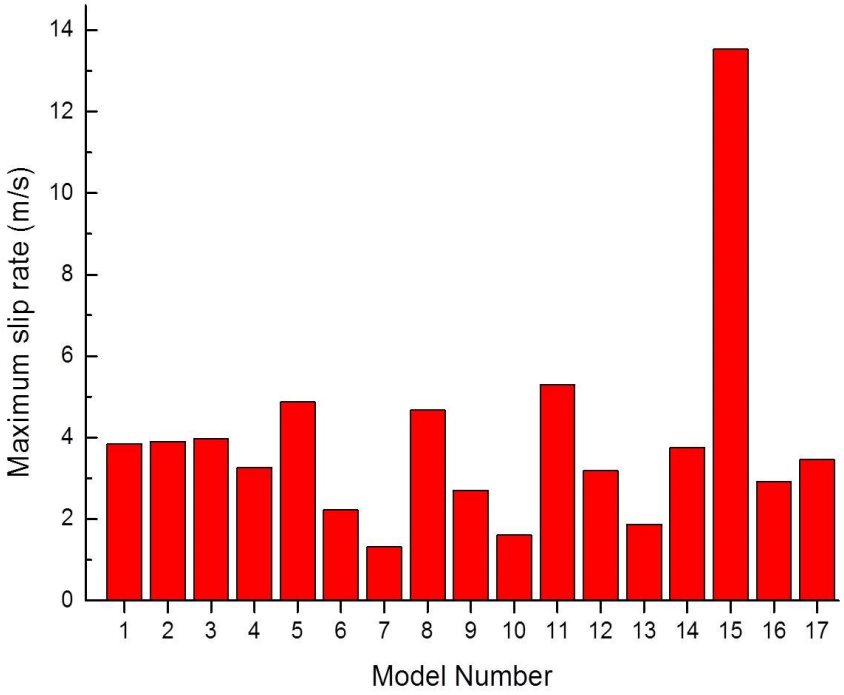

Figure 3-12: Maximum slip rates

Figure 3-14 represents the distributions of the increment of relative shear displacement and slip rates on the center line of the fault for model 1. The vertical axis, upper horizontal axis, and lower horizontal axis in the figure represent the distance from the bottom of the model, slip rates and the increment of relative shear displacement. The figure shows that the increment of relative shear displacement takes the maximum value at the point, z = 225 m, which is

the same level as that of the top of the extracted stope in the analysis, and that slip rate peaks at the point, z = 190 m, which is below the extracted stope. This characteristic that the point at which the increment of relative shear displacement peaks does not correspond to that for the slip rate was common to the other models except model 4 and indicates that seismic waves that might cause strong ground motion might be generated around the area away from the hypocenter of the fault slip, though the characteristics of seismic waves arising from fault slip are dependent upon not only the maximum slip rate but also the duration for which high slip rate continues. Further study would be required regarding the duration of high slip rate for better understanding of the relation between fault slip and the generation of seismic waves.

Lastly, rupture time and rupture velocity at the observation points along the center line of the fault in model 1 are plotted in Figure 3-15. As can be seen from the red dots in the figure, rupture starts in the area between z = 200 m and z = 225 m and extend across the fault. The point where rupture time is minimum value is considered as hypocenter of the induced fault slip. In this analysis, rupture time was calculated every 0.005 s, hence the same rupture time was derived around the hypocenter. The rupture velocity plotted as black dots in the figure is calculated by dividing the rupture time by the distance between adjacent red dots. The maximum calculated rupture velocity is approximately 8000 m/s; it decreases to 2500 m/s in the area far from the hypocenter. In seismology, the shear rupture, of which velocity exceeds S-wave speed of surrounding rockmass, is called super shear, and the distinct wave propagation and ground motion induced by the super shear have been reported by many researchers (Andrews, 2010; Bizzarri, 2012; Dunham & Bhat, 2008). In the case shown in Figure 3-15, super shear clearly occurs around the hypocenter of the fault slip because the S-wave velocity calculated from the material properties of hanging wall rock is 2220 m/s. It should be noted that the maximum rupture velocity is much higher than the S-wave velocity, and the reason for the high rupture velocity can be

explained by model geometries and elastic waves arising from the extraction of stopes. In case of earthquake, rupture along fault would be induced by the extension of failure of fault. On the contrary, for this case, rupture is induced by the elastic waves caused by the extraction of stopes, i.e., quite high rupture velocity is induced when the elastic waves reach the fault at the same time at different locations. It is quite possible that the situation could take place because the numerical models used for a series of analyses have faults parallel to the ore bodies. For other models, almost same results could be obtained, though rupture time will be different between the models, depending on the distance between stopes and the fault. Thus, it can be concluded that the fault slip induced by mining could result in extremely high rupture velocity which might cause severe damage due to strong ground motion, depending on the positional relationship between stopes and faults.

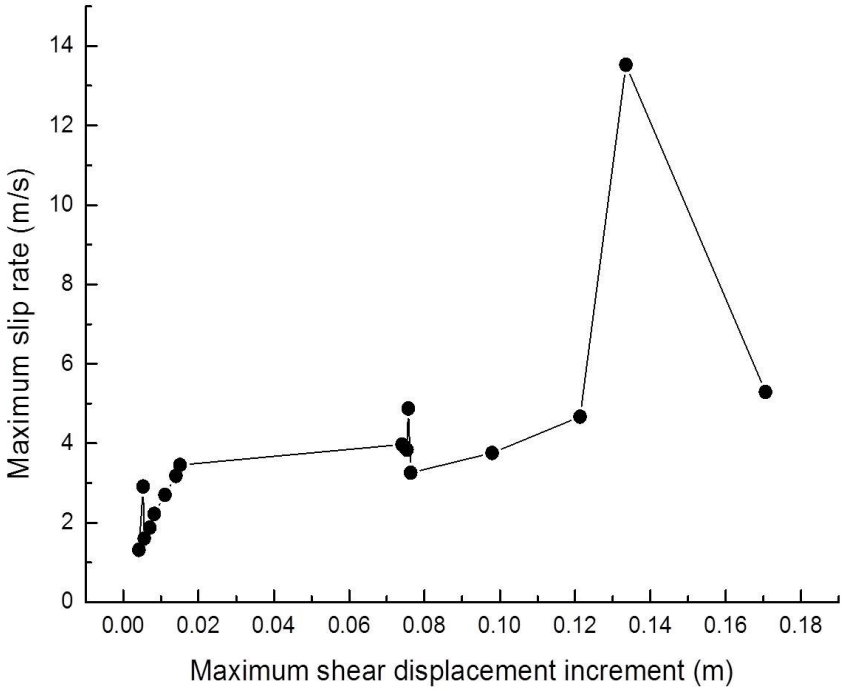

Figure 3-13: The relation between the maximum shear displacement and the maximum slip rate

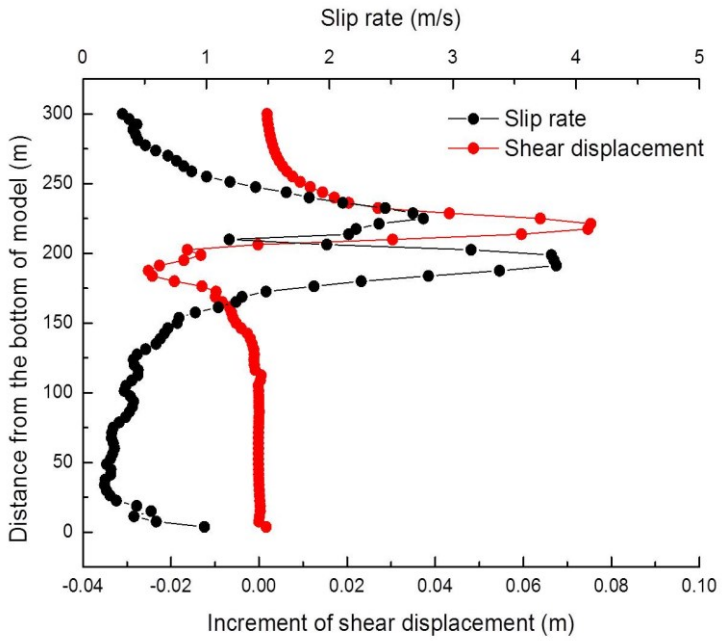

Figure 3-14: The relation between shear displacement increment and slip rate on the center line of the fault for Model 1

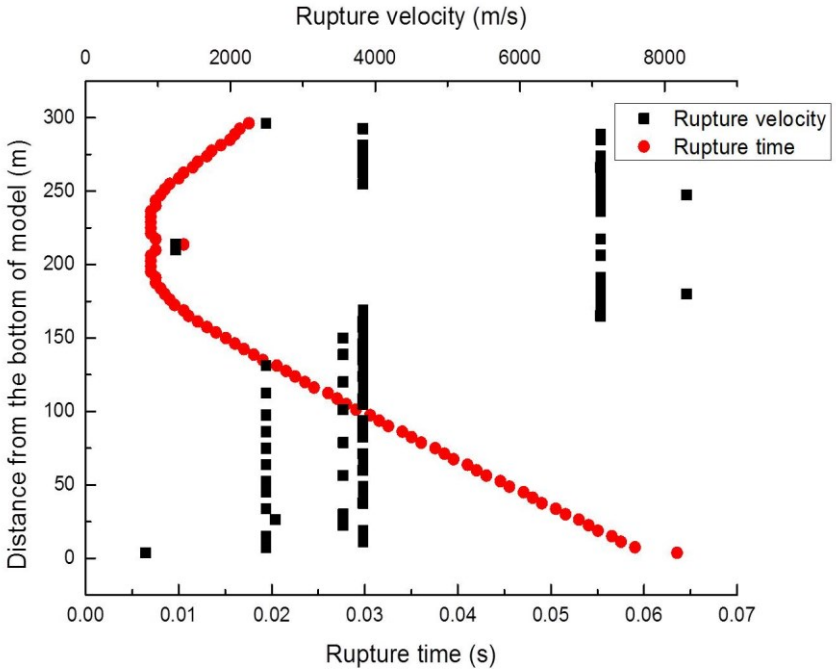

Figure 3-15: Rupture time and rupture velocity for model 1

3.7 Conclusion

In this paper, static and dynamic analyses are conducted in order to investigate the influence of the positional relationship between stope and fault, mining rate, and mechanical properties of the fault on fault slip induced by ore extraction. Numerical models of steeply dipping, tabular ore deposit, which are extracted by sublevel stoping method, and with a fault parallel to the ore deposit were generated by means of FLAC3D software. It can be concluded that mining depth, friction angle of the fault, and a fault located in the hanging wall strongly influence the maximum relative shear displacement increment along the fault, while the dilation angle and stiffness of the fault do not. Likewise, seismic source parameters (seismic moment and energy) due to stope extraction increase with the decrease of friction angle of a hanging wall fault. The maximum slip rates appear to increase with the maximum slip, although their locations do not coincide – this being the case due to stope extraction. It is also shown that extremely high rupture velocity could be induced by stope extraction. This could be the cause for a severe seismic event. It should be noted that the above-mentioned results are valid only for the case of a fault that is parallel to the orebody. In this study, the Mohr-Coulomb criterion has been adopted as it is commonly used in industrial practice of this type of problems. However, it is shown that simulating fault slip with the Mohr-Coulomb criterion could underestimate the magnitude of the fault slip since it considers neither the asperities on the fault surfaces nor its slip weakening behaviour. Research is currently underway to investigate the effect of fault-surface roughness on its seismic response. In addition, considering slip rate and rupture velocity, further research on seismic waves arising from fault slip is required for better understanding not only the prediction of the occurrence of fault slip but also the damage caused by seismic waves resulting from fault slip.

CHAPTER 4

Dynamic modelling of fault-slip with Barton's shear strength model

4.1 Abstract

Fault-slip bursts could inflict severe damage to mine openings. The occurrence and magnitude of fault-slip bursts are largely dependent on the shear strength of the fault, which represents the resistance to shear stresses acting on the fault as a result of nearby mining activities. At present, a number of shear strength models have been developed, taking into account many properties of faults and joints, such as roughness and infill materials. In this study, Barton's shear strength model is newly incorporated into FLAC3D code as a ubiquitous joint model using plastic flow rule. Comparison of the incorporated model with the classical Mohr-Coulomb model is conducted through a case study of a primary fault that is parallel to a steeply dipping tabular ore deposit, which is mined out by sublevel stoping method. Based on the results obtained from the numerical analyses, seismic source parameters are calculated and compared for each case. The results show that faults having rough surfaces tend to cause much larger seismic events than faults with smooth surfaces. In addition, parametrical study with respect to fault-surface roughness shows that seismic moment and radiated energy significantly vary with the fault-surface roughness and the seismic moment does not necessarily correlate with the radiated energy. Peak particle velocity excited by seismic waves arising from the simulated fault-slips is also examined. It is found out from the results that peak particle velocity is strongly dependent upon the fault surface roughness and has a correlation with the radiated energy, but not with seismic moment. This study develops the modelling technique for fault-slip taking into account fault-surface roughness and lays a foundation for better understanding of dynamic behaviour of the faults with rough surfaces.

4.2 Introduction

Fault-slip burst caused by mining activities is one of the most dangerous phenomena that occur in underground hard rock mines. According to case studies conducted by Blake and Hedley (2003), fault-slip burst that occurred at Wrigth-Hargreaves Mine recorded a magnitude of 4.2 and caused significant damage to mine openings ranging from 1143 m to 777 m below the ground surface. The authors indicated that the triggering mechanism of fault-slip bursts is a reduction in the clamping force acting on the fault, so that there are no warnings related to fault-slip bursts. Hence, predicting the fault-slip burst is quite challenging in mine sites, where complicated geological structures and stress regimes exist. To date, many attempts in examining the relation between mining activities and the occurrence of the fault-slip bursts have been made. Castro et al. (2009) investigated various types of case studies that possibly lead to fault-slip bursts due to the effect of mining activities, such as the unclamping of normal stress acting on faults and stress rotation induced by the extraction of stopes. Hofmann and Scheepers (2011) simulated fault-slip area with Mohr-Coulomb failure criterion by considering the reduction in the cohesive strength of a fault due to rupture so that the fault-slip area corresponds with that estimated from recorded data. Sainoki and Mitri (2012) modelled the dynamic behaviour of fault-slip induced by the extraction of stopes and estimated seismic source parameters of the fault-slip.

While modelling of the fault-slip in mining context has been attempted as shown above, the classical Mohr-Coulomb criterion has been mainly used for the shear strength model representing the resistance to shear stresses acting on the faults because of its simplicity to incorporate into the procedure for modelling the fault-slip. However, fault surfaces observed in mine sites are never planar (Wallace & Morris, 1986) due to a variety of factors which influence fault formation, such as rockmass fabrics, in-situ stresses, and geological structures. Dieterich and Kilgore (1996) indicated that asperity of the surfaces of faults

depends on the net slip that the faults experience and that asperity controls friction as well as slip type and velocity. Hence, it is evident that the use of Mohr-Coulomb criterion as the shear strength model of the faults could lead to inaccurate results when fault-surface roughness is large enough that the surface cannot be regarded as planar. To take into account the asperity of the fault or joint surfaces, many shear strength models have been proposed theoretically and experimentally. Barton (1973) proposed an empirical shear strength model taking the surface roughness into consideration, based on the experimental results from direct shear tests performed on artificial rough tension joints of brittle model material. Saeb (1989) and Saeb and Amadei (1992) modified Ladanyi and Archambault's shear strength model that considers the angle of asperity dependence upon the ratio of normal stress to uniaxial compressive stress. Indraratna et al. (2005) proposed a shear strength model that takes into account the thickness of infilling materials, based on the shear strength model proposed by Patton (1966). The use of these models makes it possible to allow for fault-surface roughness, such as undulation and asperity, which is dependent upon normal stress acting on the fault and the strength of fault surfaces.

Not only the mechanical properties of the fault surfaces but also the dynamic phenomena involved in fault-slip should be taken into account when modelling the fault slip burst. During the fault-slip, fault surfaces undergo drastic changes, depending upon the properties of fault surfaces, infilling materials, and slip rates, e.g. the macroscopic and microscopic asperity of the surfaces are sheared off (Ryder, 1988). In order to take into account such phenomena, a number of rate- and state-dependent friction laws have been proposed to simulate fault-slip that pertains to earthquakes (Dieterich, 1978; Dieterich & Kilgore, 1996; Perrin et al., 1995; Ruina, 1983). In these friction laws, shear strength is slip-rate dependent, and slip weakening and strengthening behaviour can be simulated, which is strongly related to the mechanism of earthquakes that occur at comparatively shallow depths (Byerlee, 1968). More importantly, the earthquake mechanism is

quite similar to that of fault-slip induced by mining activities in deep underground mines (Gibowicz & Kijko, 1994).

In recent decades, possibility of the occurrence of large fault-slip bursts has been increasing due to unfavorable stress regimes at great mining depths. Hence, better understanding of the mechanism of fault-slip bursts is imperative in order to estimate the location and magnitude of fault-slip bursts during the life of a mine plan. To date, little or no attempts have been made to model fault-slip in hard rock mines taking into account fault-surface conditions and dynamic response of the fault. In this study, Barton's shear strength model, which is widely accepted due to its simplicity and being consonant with experimental results, is newly incorporated into FLAC3D software – a three dimensional explicit finite-difference program. To do that, the ubiquitous joint model in FLAC3D is employed together. Through a sequence of static and dynamic analyses, the relation between stope extractions and the occurrence of fault-slip is examined with a model having a fault parallel to a steeply dipping ore deposit that is mined out with sublevel stoping method for both of Barton's model and Mohr-Coulomb model. In order to allow for the dynamic behaviour of fault-slip, in which the friction angle of the fault changes, the friction angle is altered to dynamic friction angle when slip occurs during the dynamic analysis. Based on the results obtained from the analyses, a comparison between the two models is made with respect to peak particle velocity (PPV) excited by seismic waves arising from fault slip as well as seismic source parameters, considering the fault-surface roughness.

4.3 Barton's shear strength model

Barton (1973) performed direct shear tests with samples for rock joints having rough surfaces and proposed the following formulation that represents the shear strength model taking into account the roughness and compressive strength of the surfaces. The equation is given as below.

$$\tau = \sigma_n \tan\left[JRC \log_{10}\left(\frac{JCS}{\sigma_n} \right) + \phi_b \right] \qquad (4\text{-}1)$$

where σ_n and ϕ_b are effective normal stress acting on the joint and the basic friction angle of the joint, respectively. *JRC* and *JCS* in Equation 4-1 are the joint roughness coefficient and the joint wall compressive strength. According to Barton (1973), *JRC* ranges from 0 to 20, where *JRC* of 20 represents the roughest, undulating tension surfaces that would normally be found in a rockmass. Typical roughness profiles are illustrated in Figure 4-1. *JCS* can be estimated based on the uniaxial compressive strength of the rockmass, considering the degree to which the joint surfaces are weathered (Barton & Choubey, 1977) (e.g. in common intermediate stage, the *JCS* of weathered, water conducting joints is approximately some fraction of uniaxial compressive strength of rockmass).

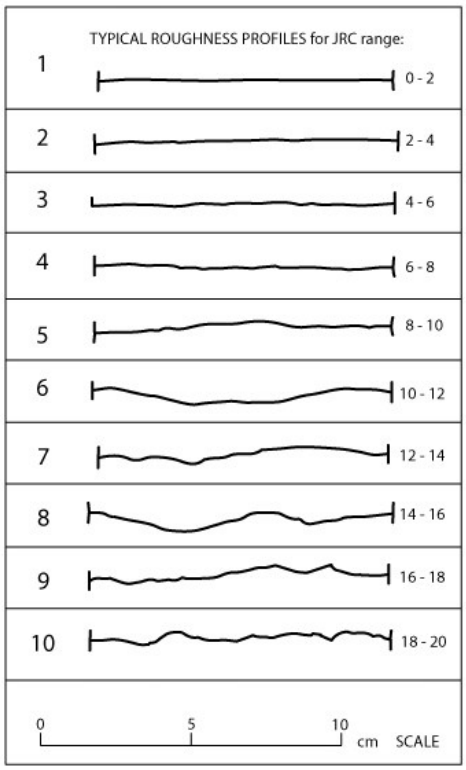

Figure 4-1: Roughness profiles showing the typical ranger of *JRC* values after Barton and Choubey (1977)

It is important to note that Barton's shear strength model is valid when *JCS* is greater than normal stress acting on the joint, and as shown in Figure 4-2, the peak shear strength calculated from Barton's model is always greater than that calculated from Mohr-Coulomb failure criterion. To date, many modifications have been made in order to take into account joint properties, such as scale-dependency of *JRC* and the effect of increase in shear displacement on *JRC* and *JCS* (Barton et al., 1985). In this study, Barton's model given by Equation 4-1, in which both of *JRC* and *JCS* are constant, is employed.

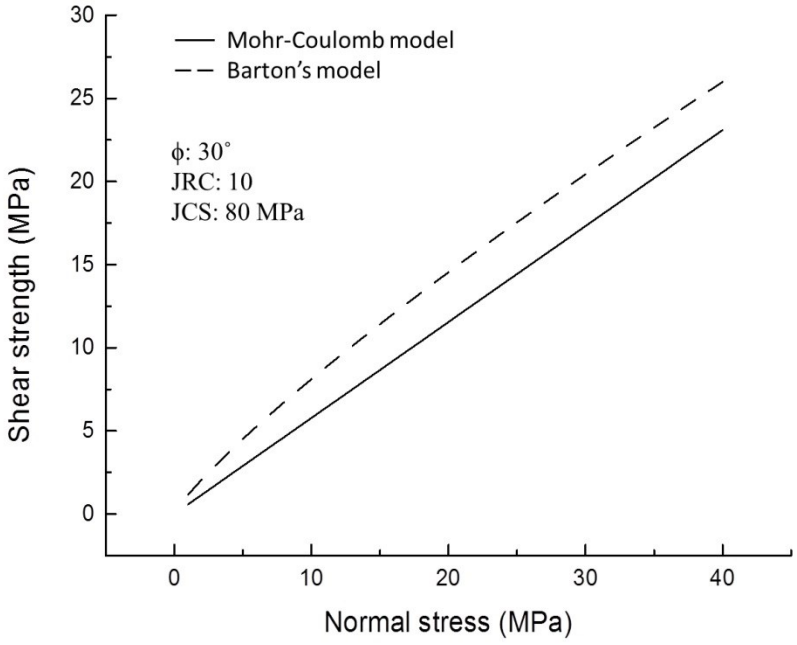

Figure 4-2: Comparison of Mohr-Coulomb model with Barton's model

4.4 Implementation of Barton's model into FLAC3D code

FLAC3D code is capable of implementing new constitutive models that are not initially available in the code (Itasca, 2009). For instance, Hai-min et al. (2011) developed a shear strength model that allows for slip-weakening behaviour of rock joints with FISH, which is a programming language embedded within FLAC3D; Cai, Kaiser, and Martin (2001) developed a damage-driven numerical model by incorporating a new constitutive model by use of C++

programming language. In this study, Barton's shear strength model is implemented into FLAC3D with C++ language by modifying the code for ubiquitous joint model as incorporating new shear strength models into the interface model embedded within FLAC3D is not allowed for users. In terms of the slip behaviour and stress states of joints, the ubiquitous joint model represents the same behaviour as the interface model (Cappa & Rutqvist, 2010). Schematic illustration of modelling pre-existing fault plane with the ubiquitous joint model is depicted in Figure 4-3.

Barton's shear strength model is implemented into the ubiquitous joint model with plastic flow rule, whereby the increment of plastic strain is expressed as (Itasca, 2009).

$$\left\{\Delta\varepsilon^{p}\right\} = \lambda\left\{\frac{\partial g}{\partial\{\sigma\}}\right\} \tag{4-2}$$

where $\Delta\varepsilon^{p}$, g and σ represent the increment of plastic strain, plastic potential, stresses acting on joints and constant, respectively; and λ is a scalar variable that controls the magnitude of the plastic strain increment. The plastic potential and yield function specified for Barton's shear strength model are expressed as follows.

$$f = \tau + \sigma_{z'z'} \tan\left[JRC \log_{10}\left(\frac{JCS}{|\sigma_{z'z'}|}\right) + \phi_b\right] \tag{4-3}$$

$$g = \tau + \sigma_{z'z'} \tan\left[JRC \log_{10}\left(\frac{JCS}{|\sigma_{z'z'}|}\right) + \psi\right] \tag{4-4}$$

$$\tau = \sqrt{\sigma^2{}_{x'z'} + \sigma^2{}_{y'z'}} \tag{4-5}$$

where ψ is the dilation angle of rock joint, and τ and $\sigma_{z'z'}$ are shear and normal

stresses acting on the joint, respectively. Note that compressive stress is treated as negative in Equations 4-3 and 4-4. The subscripts represent stress components of local coordinate system, assuming that the z´-direction is perpendicular to the joint surface. When failure takes place, the yield function satisfies the following equation.

$$f(\{\sigma\}) = 0 \tag{4-6}$$

As the stress state on the joint changes, the requirement of the new stress-vector components to satisfy Equation 4-6 is given by the total derivative of Equation 4-6 as follows.

$$\left(\frac{\partial f}{\partial \{\sigma\}}\right)^T \{\Delta\sigma\} = 0 \tag{4-7}$$

Equation 4-7 is referred to as the consistency condition, and the increment of stress [$\Delta\sigma$] in Equation 4-7 can be expressed as shown below using plastic flow rule.

$$\{\Delta\sigma\} = [D]\{\Delta\varepsilon\} - \lambda[D]\left\{\frac{\partial g}{\partial \{\sigma\}}\right\} \tag{4-8}$$

where [D] and [$\Delta\varepsilon$] are stiffness matrix and total strain increment vector, respectively. Substituting Equation 4-8 into Equation 4-7 yields the following equation.

$$\lambda = \frac{\left(\frac{\partial f}{\partial \{\sigma\}}\right)^T [D]\{\Delta\varepsilon\}}{\left(\frac{\partial f}{\partial \{\sigma\}}\right)^T [D]\left\{\frac{\partial g}{\partial \{\sigma\}}\right\}} \tag{4-9}$$

The derivatives of yield function and potential function with respect to normal stress and shear stress acting on the joint in Equation 4-9 are given as follows.

$$\frac{\partial f}{\partial \sigma_{z'z'}} = \tan\left[JRC \log_{10}\left(\frac{JCS}{|\sigma_{z'z'}|} \right) + \phi_b \right] - \frac{\pi}{180} \frac{JRC}{\cos^2\left[JRC \log_{10}\left(\frac{JCS}{|\sigma_{z'z'}|} \right) + \phi_b \right] * \ln 10} \tag{4-10}$$

$$\frac{\partial g}{\partial \sigma_{z'z'}} = \tan\left[JRC \log_{10}\left(\frac{JCS}{|\sigma_{z'z'}|} \right) + \psi \right] - \frac{\pi}{180} \frac{JRC}{\cos^2\left[JRC \log_{10}\left(\frac{JCS}{|\sigma_{z'z'}|} \right) + \psi \right] * \ln 10} \tag{4-11}$$

$$\frac{\partial f}{\partial \sigma_{x'z'}} = \frac{\partial g}{\partial \sigma_{x'z'}} = \frac{\sigma_{x'z'}}{\tau} \tag{4-12}$$

$$\frac{\partial f}{\partial \sigma_{y'z'}} = \frac{\partial g}{\partial \sigma_{y'z'}} = \frac{\sigma_{y'z'}}{\tau} \tag{4-13}$$

Substituting Equations 4-10 to 4-13 into Equation 4-9 yields the constant, λ, and the plastic strain increment can be obtained from Equation 4-2. The source codes to program the equations above are newly implemented into codes for the ubiquitous joint model within FLAC3D software.

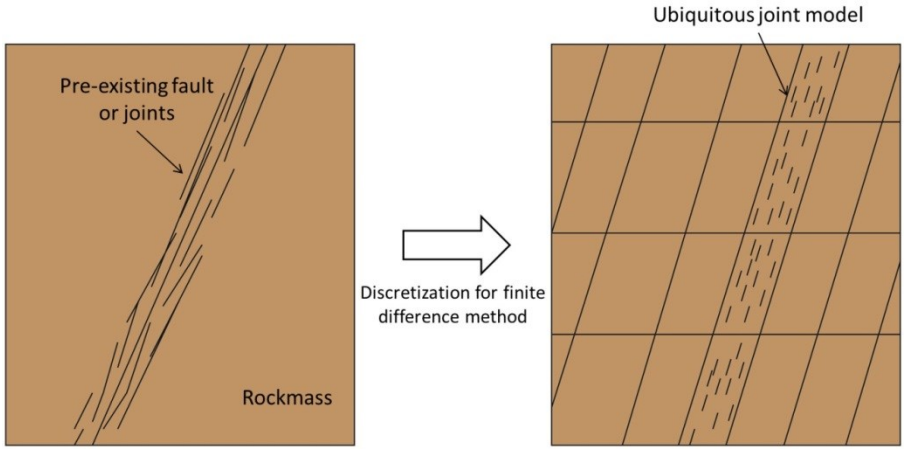

Figure 4-3: Schematic illustration showing discretization for finite difference method with ubiquitous joint models representing pre-existing faults

4.5 Numerical analysis

Static and dynamic analyses are conducted with finite difference method by means of FLAC3D software (Itasca, 2009). In this section, a detailed description of the numerical analysis is given with respect to requisites to conduct the analyses, such as initial stress states and the physical properties of the rockmass and the fault, along with the procedure of analysis.

4.5.1. Model description

To investigate the fault slip induced by mining activities, a numerical model as shown in Figure 4-4 is generated by means of FLAC3D. As can be seen in the figure, a steeply dipping, tabular ore deposit is modeled. This type of deposit is frequently encountered in hard rock mines in Canadian Shield (Bewick et al., 2009; Blake & Hedley, 2003). The ore deposit is mined out with sublevel stoping method with delayed backfill. The width, length and height of the model are 332 m, 300 m, and 300 m, respectively. The modelled ore deposit dips at 80˚, and the strike of the deposit is parallel to y-axis of the model as shown in Figure 4-4. In the model, a fault parallel to the ore deposit is modelled with the ubiquitous joint model, and the distance between the fault and the ore deposit is 30 m.

Figures 4-5 and 4-6 illustrate the proposed mining sequence and stope geometry, respectively, which were determined based on typical sublevel stope geometries in Canadian underground mines (Zhang & Mitri, 2008). As shown in Figure 4-5, the ore deposit is extracted in an upward direction from 9 sublevels, and on each sublevel, stopes are mined out from hanging wall to footwall, according to the stope numbers depicted in Figure 4-5. The height and strike length of the stopes are 30 m and 200 m, respectively. The stope strike length, which is longer than that usually planned in mine sites, represents high mining rate (Sainoki & Mitri, 2012).

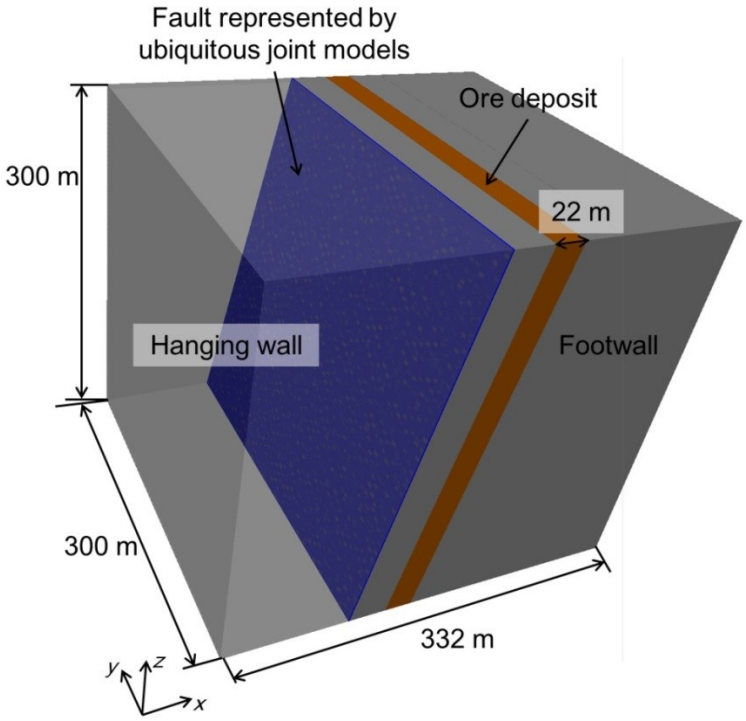

Figure 4-4: Isometric view of model to be analyzed

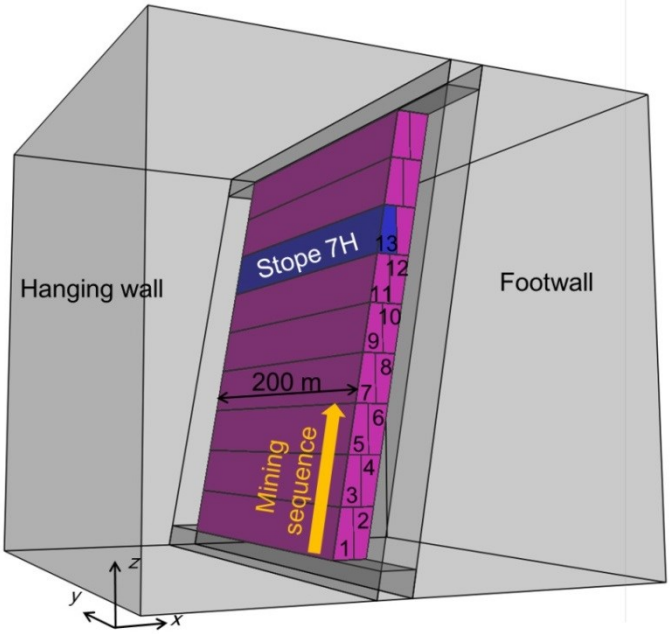

Figure 4-5: Stopes and mining sequence representing sub-level stoping method.

Dynamic analysis is conducted based on the stress states after extracting stope7H.

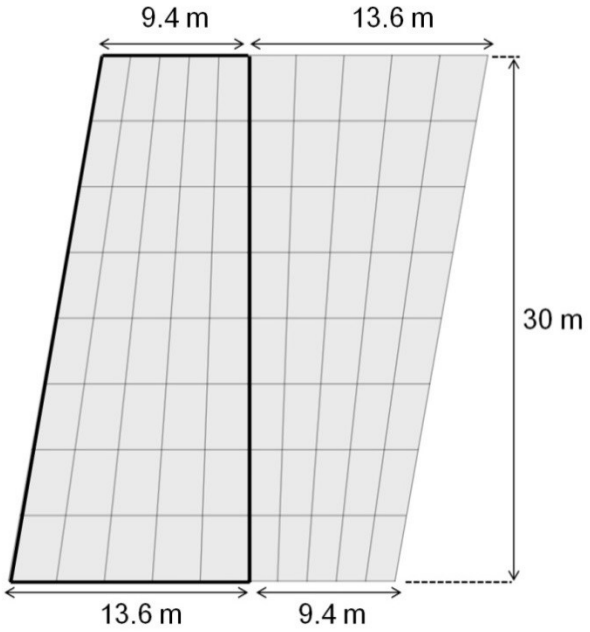

Figure 4-6: Stope geometry in sectional view

4.5.2 Procedure of numerical analysis

Fault-slip bursts induced by mining activities can be characterized as dynamic phenomena from which seismic waves are caused; hence it is ideal that dynamic analyses are conducted throughout the proposed mining sequence. However, the analyses would require considerable amount of time, depending on the capabilities of the computer used for the analyses and the number of grid points in the 3-dimensional numerical model. In addition, the extraction of the stopes at the beginning of the mining sequence does not cause unclamping effects along the fault that are significant enough to cause fault slip. For these reasons, static analysis is initially carried out until the extraction of stope7H shown in Figure 4-5. Based on the stress state after extracting stope7H, the dynamic analysis for simulating fault slip is carried out.

During the dynamic analysis, fault slip is simulated by altering the fault-surface roughness and friction angle in Equation 4-1 since it can be assumed that the fault-surface properties change during the fault-slip due to the dynamic slip behaviour of the fault (e.g. asperities of fault surfaces are sheared off (Ryder,

1988), and slip rate as well as shear displacement induced by the fault slip affects the frictional behaviour of the fault (Dieterich, 1979a)). Excess shear stress arising from the change in fault-surface properties drives the fault slip during the dynamic analysis. In this study, the change in fault-surface properties in the dynamic analysis is conducted as follows. At the beginning of the dynamic analysis, the stress states of the fault are investigated, and the fault-surface properties are changed in the area where the shear stress acting on the fault is greater than the shear strength calculated from Equation 4-1, or the difference between the shear stress and the shear strength is less than 0.1 MPa. The area can be considered the hypocenter of the fault-slip. In addition, during the dynamic analysis, for the area where shear stress exceeds the shear strength due to the induced fault-slip, fault-surface properties are changed as well. Figure 4-7 depicts the concept of the change in the friction law and the excess shear stress that causes shear instability along the fault.

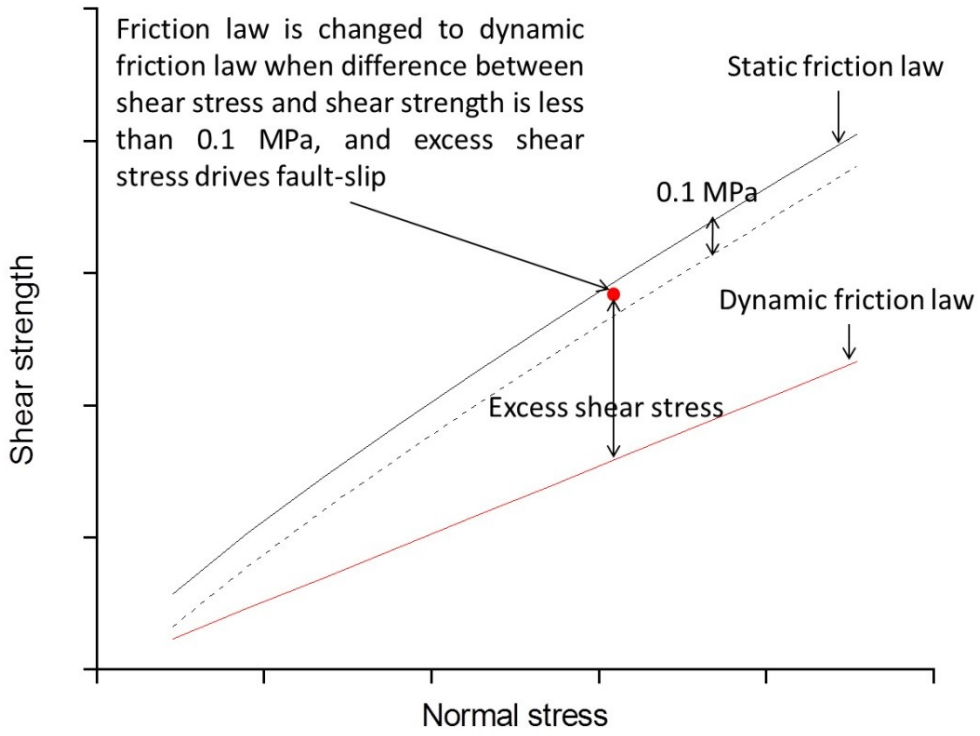

Figure 4-7: Schematic illustration representing the change from static friction law to dynamic friction law

The procedure adopted in the present study is summarized as follows. The ore extraction carried out in the static analysis has the effect of regional unclamping of the fault. It should be borne in mind that without the effect of the ore extraction, fault-slip would not occur. It is also to be noted that reducing the fault shear strength with the decrease in fault surface roughness during the dynamic analysis is intended to simulate fault-slip driven by asperity shear. Considering these facts, the proposed procedure has been adopted in the present study.

4.5.3 Initial stress states

The vertical in-situ stress, σ^o_v, which is in the z-direction in Figure 4-4, is given by the overburden pressure as follows.

$$\sigma^o{}_v = \gamma H \tag{4-14}$$

where γ and H are the unit weight of the rockmass and the depth below ground surface. According to Arjang (1991), steeply dipping orebodies in the Canadian Shield have the characteristics that the maximum horizontal stress is in the direction perpendicular to orebody and the direction of minimum horizontal stress is parallel to the orebody strike. This is adopted in the present study. The magnitude of maximum and minimum horizontal stresses is determined by the following equations proposed by Diederichs (1999).

$$k_{\max} = 1 + \frac{25}{\sqrt{H}} \tag{4-15}$$

$$k_{\min} = 1 + \frac{8}{\sqrt{H}} \tag{4-16}$$

$$\sigma^o{}_{H\max} = k_{\max}\sigma^o{}_v \tag{4-17}$$

$$\sigma^{o}{}_{H\min} = k_{\min}\sigma^{o}{}_{v} \quad (4\text{-}18)$$

where k is the ratio of horizontal stress to vertical in-situ stress. Thus, the maximum and minimum horizontal stresses expressed by Equations 4-17 and 4-18 can be derived from calculating the value of k by use of Equations 4-15 and 4-16. In this study, the depth at the top boundary of the model is set at 1500 m, and the unit weight of overlying rockmass is assumed to be 25.5 kN/m3. This setting of initial stress states is based on the research by Zhang and Mitri (2008).

4.5.4 Mechanical properties of rockmass, backfill material and fault

The mechanical properties of rockmass used for the analyses are based on the test results obtained from rock samples of Bousquet 2 Mine (Henning, 1998). Different properties for HW, ore body, and FW are assigned as shown in Table 4-1. The mechanical properties of the backfill material used in the numerical model are also shown in Table 4-1. As for the properties of the fault, a parametrical study is conducted with respect to fault-surface roughness. Table 4-2 shows the mechanical properties of the fault represented by ubiquitous joint models. As described above, joint roughness coefficient and friction angle of ubiquitous joint models in the area where slip occurs are changed in the dynamic analysis. Note that the mechanical properties remain the same in the area without slip behaviour in the dynamic analysis. It is also to be noted that although the dilation angle of the fault, which is represented as ψ in Equation 4-4, is set to zero as shown in Table 4-1, fault dilation is taken into account with the term, $JRC \cdot \log(JCS / \sigma)$, in the equation. As mentioned by Barton and Choubey (1977), that term represents dilation. The term increases as joint roughness increases; and decreases as joint roughness decreases. The term also includes the effect of normal stress on dilation. More importantly, the term becomes zero when JRC is equal to 0. When fault surfaces are completely planar, no dilation occurs. Thus it is possible to consider fault dilation while assuming that ψ is equal to zero.

Table 4-1: Rockmass mechanical properties

	E (GPa)	C (MPa)	ϕ (˚)	ν	γ (kN/m3)	σT (MPa)	ψ (˚)
HW[1]	31	2.6	38	0.21	25.5	1.1	9.3
Ore	115	11.5	48	0.1	25.5	5.9	12.0
FW[2]	49	4.3	39	0.15	25.5	1.8	9.5
BF[3]	2.5	0.1	35	0.35	23.0	N/A	0.0

[1] Hanging wall

[2] Footwall

[3] Backfill

Table 4-2: Properties of ubiquitous joint model representing the fault

	Static analysis	After slip occurs in dynamic analysis
Joint roughness coefficient[1]	0~20	0
Friction angle	30	25
Cohesion (MPa)	0	0
Tensile strength (MPa)	0	0
Dilation angle (˚)	0	0
Modulus of elasticity (GPa)	3.1	3.1
Poisson's ratio	0.21	0.21

[1]Joint roughness coefficient of 0, 2.5, 5, 7.5, 10, 12.5, 15, 17.5 and 20 is taken for the parametrical study.

4.5.5 Conditions of static and dynamic analyses

In the static analysis, model boundaries are fixed in the direction perpendicular to the boundary surface. For the dynamic analysis, the boundary conditions are changed to viscous in order to prevent the model boundaries from

reflecting elastic waves arising from fault slip. The timestep used for the dynamic analysis is calculated based on the volume of each zone of the model, P-wave velocity and the face area of each zone (Itasca, 2009). Regarding the attenuation of elastic waves, local damping embodied in FLAC3D is taken. This was deemed sufficient at this stage, considering the focus of the study.

Model sensitivity analysis was conducted prior to static and dynamic analyses in order to examine the effect of boundary conditions on the behaviour of the fault. In the analysis, several types of numerical models that have different width, length and height shown in Figure 4-4 were generated, and the magnitude of shear displacement along the faults were compared after extracting the stopes with static analysis. The comparison indicated that the overall length and width of the numerical model are sufficiently large to prevent the boundary conditions from affecting the behaviour of the faults while it was shown that the height of the model affects the sliding behaviour; which is expected due to the modeled persistence of the fault.

4.5.6 Seismic source parameters

Seismic source parameters are widely used to evaluate the magnitude of earthquake and mining-induced seismicity, and the seismic source parameters calculated from the data obtained by seismic network installed on the ground surface or underground are compared with those computed from the numerical analysis (Hofmann & Scheepers, 2011). In the present study, the following two seismic parameters are adopted to investigate dynamic sliding behaviour: seismic moment, M_o (Aki & Richards, 1980)and energy released during fault slip, E_s (Kostrov, 1974). The parameters can be derived from the following equations.

$$M_o = GDA \tag{4-21}$$

$$E_s = 0.5\Delta\sigma DA \tag{4-22}$$

where *G*, *D*, and A represent shear modulus, average shear displacement, and area where sliding takes place. $\Delta\sigma$ in Equation 4-22 represents stress drop defined as the average difference between the stress on a fault before an earthquake and the stress after the earthquake (Shearer, 1999) and is expressed as follows.

$$\Delta\sigma = \frac{1}{A}\int_{s}[\sigma(t_2)-\sigma(t_1)]dS \tag{4-23}$$

In this study, the calculations for the aforementioned seismic parameters are performed over the area where the increase of relative shear displacement during dynamic analysis exceeds 0.005 m and where the shear stress along a fault decreases.

4.6 Results and discussion

As described above, static analysis is conducted until the extraction of stope7H, according to the stoping sequence shown in Figure 4-5. Based on the stress states obtained from the static analysis, the dynamic analysis is conducted while changing the mechanical properties of the fault where fault slip is detected to those corresponding to the dynamic friction law. Seismic source parameters computed from the results of the dynamic analysis and peak particle velocity excited by seismic waves arising from the fault slip are examined and discussed in this section.

4.6.1 Relation between joint roughness coefficient and seismic source parameters

Figure 4-8 represents joint roughness coefficient (JRC) versus seismic moment and energy radiated during the fault slip. Note that Barton's shear strength model with joint roughness coefficient of 0 corresponds to Mohr-

Coulomb failure criterion. Thus, in the static analysis, Mohr-Coulomb criterion with a peak friction angle (static friction angle) is employed; and in the dynamic analysis, the Mohr-Coulomb criterion used in the static analysis is changed to Mohr-Coulomb criterion with a residual friction angle (dynamic friction angle) for fault regions where shear stress acting on the fault has reached the maximum shear strength. As shown in the figure, the seismic moment increases from 4.8×10^{18} dyne·cm to 9.5×10^{18} dyne·cm with increasing *JRC* until *JRC* of 7.5. After that, seismic moment keeps decreasing, and it finally becomes 0 when *JRC* is equal to 20. This behaviour of the seismic moment can be explained from the relation between excess shear stress, which is defined by the difference between static and dynamic friction laws, and shear strength determined by Equation 4-1. When *JRC* is small, the excess shear stress, which serves to drive fault slip, is also small because the term including *JRC* in Equation 4-1 becomes small. This means that for faults with smooth surfaces, forces that drive fault slip are smaller compared with the faults with rough surfaces. Thus, from the viewpoint of excess shear stress, it can be expected that the magnitude of induced fault slip increases with increasing *JRC*. However, in terms of shear strength, the magnitude of fault slip is expected to become smaller with increasing *JRC*. This is because the shear strength represents the resistance to shear stress acting on the fault. Hence, the balance between the excess shear stress and shear strength determines the magnitude of the fault slip induced during the dynamic analysis.

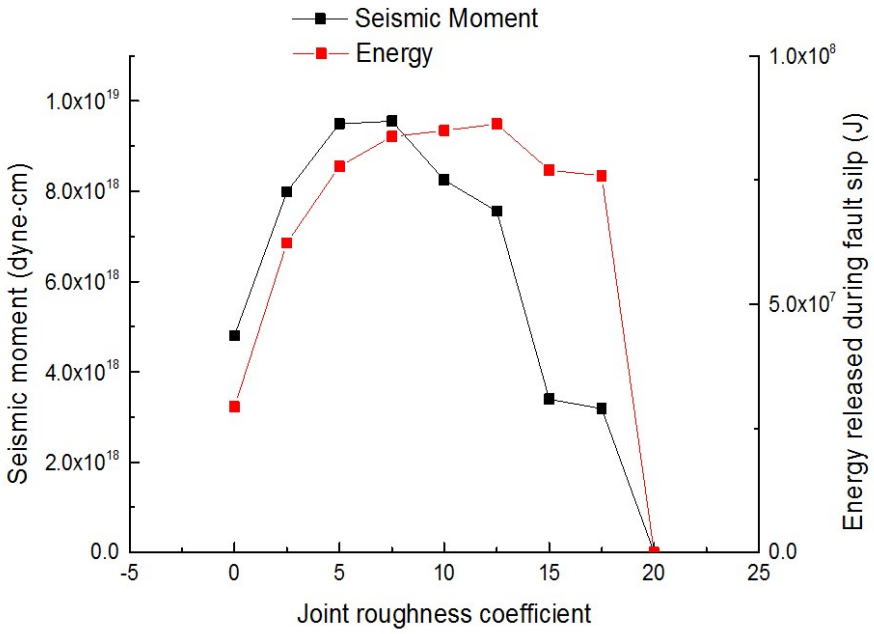

Figure 4-8: Relation between joint roughness coefficients and seismic source parameters

For better understanding of this mechanism, the distribution of shear displacement increment on the fault due to the fault slip induced during the dynamic analysis is depicted in Figure 4-9. In the figure, the area where shear displacement increment is less than 0.005 m is colored in blue. As can be seen, while the area where the shear displacement increment is greater than 0.005 m starts decreasing when *JRC* becomes greater than 7.5, the maximum shear displacement increment keeps increasing until *JRC* of 17.5. This is because the excess shear stress keeps increasing at the hypocenter of the fault slip, though the increase in shear strength serves to prevent fault slip from expanding. The area takes the maximum value with *JRC* of 7.5, which corresponds with the behaviour of the seismic moment in Figure 4-8. The behaviour of energy released during the fault slip in Figure 4-8 can be explained in the same way from the viewpoint of the balance between excess shear stress and shear strength. However, while the increase in seismic moment ceases at *JRC* of 7.5, the energy keeps increasing up to *JRC* of 12.5. In addition, the ratio at which the

energy decreases after taking the maximum value is smaller compared with that for seismic moment. This implies that the excess shear stress around the hypocenter of the fault slip plays an important role in the energy of the fault slip and that, in contrast, the magnitude of seismic moment is affected by overall behaviour of area where slip occurs. It can be concluded from these results that fault-slip tends to become the most severe in terms of seismic moment when the fault surfaces have intermediate roughness represented by *JRC* between 5 and 8. In contrast, in terms of the energy of fault slip, intensely undulating fault surfaces could release more severe energy, especially to the area around the hypocenter of the fault slip. In addition, it is revealed that simulating fault slip bursts with the classical Mohr-Coulomb failure criterion could lead to significantly underestimating the magnitude of the fault-slip.

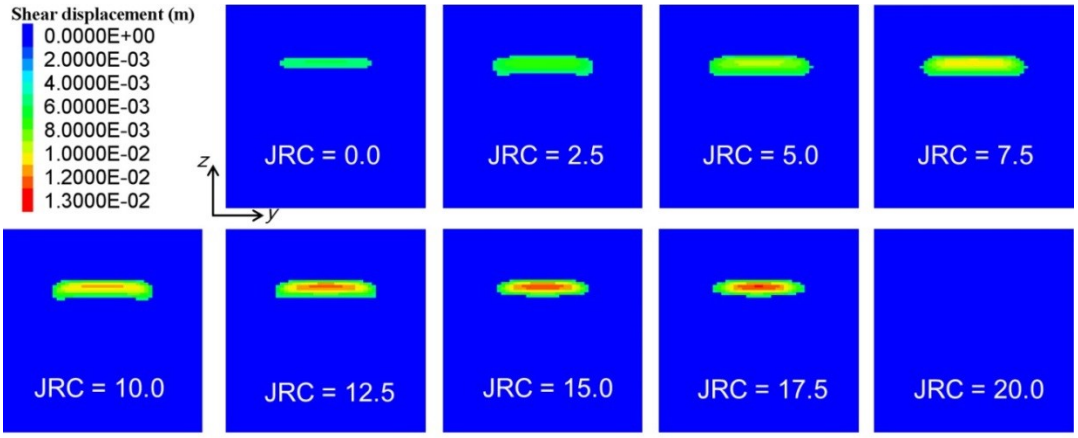

Figure 4-9: Shear displacement increments due to fault-slip during dynamic analysis. Area where the shear displacement increment is less than 0.005 m is colored in blue.

4.6.2 Investigation of PPV excited by seismic waves

Peak particle velocity (PPV) is of quite an importance in evaluating the damage induced by seismic waves arising from fault slip bursts that take place in mine sites (Hedley, 1992). In this study, the PPV induced by the fault slip in the

dynamic analysis is examined at the observation point shown in Figure 4-10, for better understanding of the relation between PPV and seismic source parameters. Figure 4-11 presents the relation between *JRC* and PPV at the observation point. As can be seen, peak particle velocity increases with increasing *JRC*, and it takes the maximum value of 1.06 m/s when *JRC* is 15. It is interesting to see that there is a significant difference between PPVs simulated with Mohr-Coulomb criterion and Barton's shear strength model when *JRC* is comparatively large. According to Hedley (1992), fracturing of intact rock starts at PPV of approximately 0.3 m/s, and severe damage is caused at 0.6 m/s. Based on the information, it is expected that the seismic event due to the fault-slip simulated with Mohr-Coulomb model in this study would not inflict severe damage to surrounding mine openings, whereas the fault slips simulated with Barton's model with high *JRC* should cause critical damage. These results highlights the importance of considering fault-surface roughness in modelling fault-slip bursts when estimating and predicting the damage expected from fault slip bursts.

Considering the results presented in Figures 4-8 and 4-11, one can delineate the relation between seismic source parameters and PPV. To illustrate this further, Figures 12 and 13 are generated. Figure 4-12 presents the influence of *JRC* on the energy released during fault-slip and peak particle velocity. Figure 4-13 denotes the relation of *JRC* and seismic moment with peak particle velocity. As can be seen in Figure 4-12, as the energy increases with *JRC*, PPV also increases, and PPV begins to decrease as the energy decreases. On the contrary, there is no clear relationship between seismic moment and PPV as shown in Figure 4-13; the plotted results do not show any clear tendency. Hence, it can be said from there results that PPV has a strong correlation with the energy released during fault slip, but not with seismic moment. In addition, as shown in Figures 4-8 and 4-9, the excess shear stress largely contributes to the energy released during fault slip. Thus, these results indicate that calculating the excess

shear stress while investigating the static and dynamic friction laws governing the slip behaviour of the fault greatly helps estimating PPV induced by fault-slip. Based on the estimated PPV, designing support system taking into account the dynamic behaviour of the rockmass can be achieved.

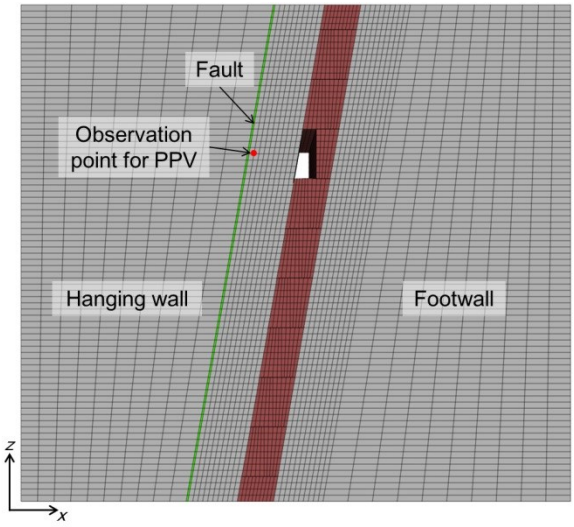

Figure 4-10: Observation point (x = 140 m, y = 150 m, z = 210 m) for examining PPV in the dynamic analysis model

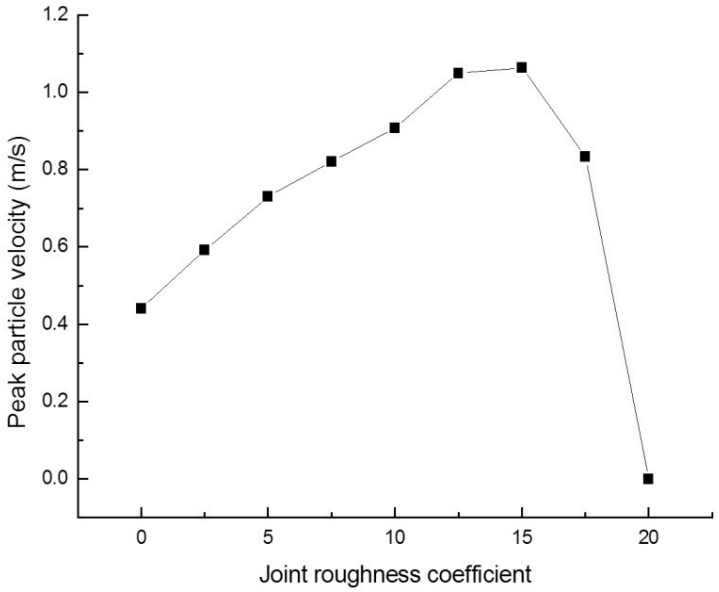

Figure 4-11: Influence of the Joint Roughness Coefficient on peak particle velocity at the observation point

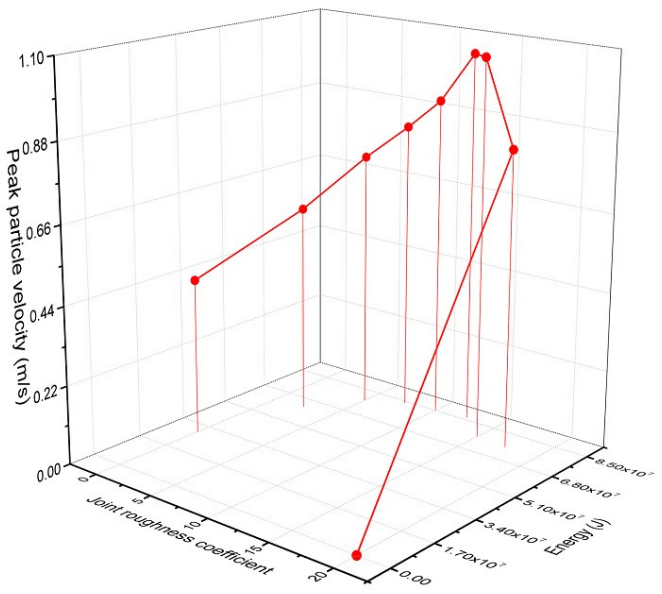

Figure 4-12: Relation between the Joint Roughness Coefficient, energy released, and peak particle velocity during fault-slip

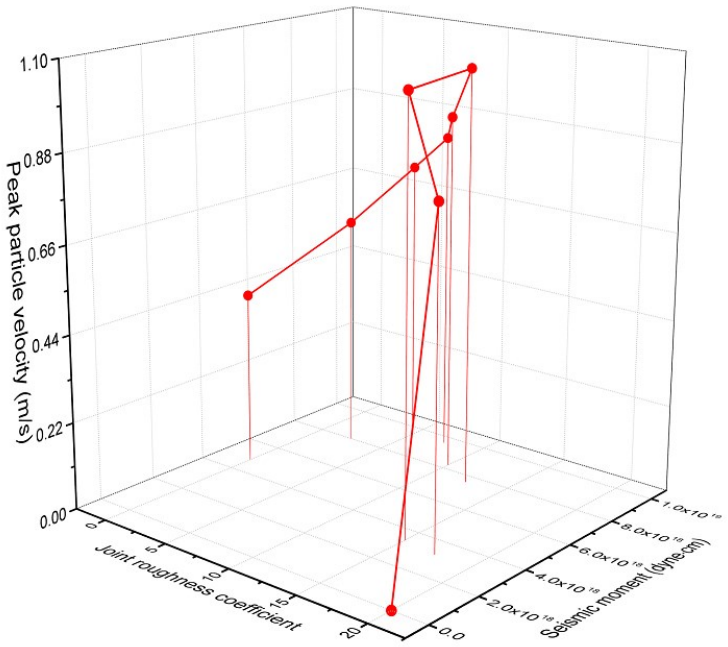

Figure 4-13: Relation between the Joint Roughness Coefficient, seismic moment and peak, particle velocity during fault-slip

4.7 Conclusions

In this paper, a numerical model of a fault parallel to a steeply dipping ore deposit that is mined out with sub-level stoping method is generated with FLAC3D code. With the model, fault-slip analysis is conducted using Barton's shear strength model, considering the change from static friction law to dynamic friction law. Based on the results obtained from dynamic analysis, the relation between the Joint Roughness Coefficient (JRC), seismic source parameters and PPV excited by seismic waves arising from the fault slip is examined.

The following conclusions can be drawn from the results. Faults having intermediate fault-surface roughness represented by a JRC value between 5 and 8 could cause the most severe fault slip in terms of seismic moment, while intensely undulating faults release large seismic energy during fault-slip. The results also show that there is a great difference in seismic source parameters between faults with smooth and rough surfaces. Thus, it is imperative to take fault-surface roughness into consideration when modelling of fault-slip in order to adequately estimate the seismic source parameters. It is also found out that the PPV has a strong correlation with the energy released during the fault-slip. Furthermore, the excess shear stress, which is defined by the difference between static and dynamic friction laws, significantly contributes to the energy released. These results imply that the estimation of the excess shear stress by determining the dynamic and static friction laws is vital for the prediction of PPV induced by fault-slip, which in turn is of quite an importance when proposing rock support systems to sustain the influence of seismic waves on mine developments.

CHAPTER 5

Dynamic modelling of fault-slip induced by stress waves due to stope production blasts

5.1 Abstract

Seismic events could take place due to the interaction of stress waves induced by stope production blasts with faults located in close proximity to stopes. The occurrence of such seismic events needs to be controlled in order to ensure the safety of the mine operators and the underground mine workings. This paper presents the results of a dynamic numerical modelling study of fault-slip induced by stress waves resulting from stope production blasts. First, the calibration of a numerical model having a single blast hole is performed using a charge weight scaling law in order to determine blast pressure and damping coefficient of the rockmass. Subsequently, a numerical model of a typical Canadian metal mine encompassing a fault parallel to a tabular ore deposit is constructed, and the simulation of stope extraction sequence is carried out with static analysis until the fault exhibits slip burst conditions. At that point, the dynamic analysis begins by applying the calibrated blast pressure to the stope wall in the form of velocities generated by the blast holes. It is shown from the results obtained from the dynamic analysis that the stress waves reflected on the fault create a drop of normal stresses acting on the fault, which entails a reduction in shear stresses while resulting in fault-slip. The influence of blast sequences on the behaviour of the fault is also examined assuming several types of blast sequences. Comparison of the blast sequence simulation results indicates that carrying out the blasts simultaneously could be beneficial in terms of controlling the magnitude of fault slip as the shear waves induced by the blast pressure tend to cancel each other, whereas conducting blasts separately could induce larger seismic events on the fault.

5.2 Introductoin

Seismic events that take place in underground mines could exert a severe influence on mining activities, depending on the magnitude and energy of the events. The seismic events involve a number of mechanisms by which the seismic events occur, such as propagation of cracks due to stress re-distribution around mine openings and slip along geological discontinuities due to unclamping induced by extraction of stopes (Cai et al., 2001; Castro et al., 2009). Slip along faults is one of the mechanisms for the seismic events to occur and could inflict severe damage to mine openings as not only compressive stresses increase in the vicinity of the fault but also seismic waves arising from the events induce high particle velocities pertaining to damage of rockmasses (Blake & Hedley, 2003; Ortlepp, 2000; B.G. White & Whyatt, 2010). Hence, controlling the occurrence of fault- slip related to seismic events is of high importance in order to ensure stable production and safe operations in underground mines.

Fault-slip is induced by either a decrease in normal stresses acting on the fault or an increase in shear stresses. Although the direct causes for fault-slip are straightforward, a number of complicated mechanisms that induce the stress change along the fault exist, such as creep behaviour of rockmasses and interactions of geological structures with the fault. Interactions of stress waves induced by mining activities, such as stope production blasts and mine development blasts, with nearby faults are one of such mechanisms and could trigger fault slip due to stress changes induced by reflection and refraction of the waves. Many attempts have been made analytically and numerically for examining the interactions of stress waves with geological structures such as faults and rock joints. The characteristic that the rock joints decrease the amplitude of incident waves was studied (Chen & Zhao, 1998; Daehnke, 1997; Li, Ma, & Huang, 2010). According to these studies, the degree to which the stress waves attenuate due to the presence of discontinuities is strongly dependent upon stiffness of the discontinuities, pre-stress and infilling materials. Attenuation

is mainly attributed to the reflection of seismic waves on the surfaces of the discontinuities. Sharafisafa and Mortazavi (2011) investigated the effect of a fault on blast-induced stress waves with a numerical model encompassing a fault and single blast hole by use of discrete element method. They found out that significant attenuation of the stress waves occurs along the fault due to the reflection of the waves and that the reflected stress waves give rise to tensile stress fields in areas surrounding the fault. Li et al. (2010) also reported that when the stress waves pass through rock joints, unclamping occurs due to the combination of transmitted and reflected waves.

Many studies have been conducted in order to examine an effect of mining activities, such as extraction of stopes, on the behaviour of faults or shear zones (Alber et al., 2009; Hofmann & Scheepers, 2011; Potvin et al., 2010; Sneilling et al., 2013). The studies have elucidated a relation between the progress of mining sequence and the occurrence of seismic events in terms of cumulative seismic moment, locations and areas of seismic events. However, the relationship between blast-induced stress waves and the occurrence of seismic events has not yet been fully studied. In the light of the aforementioned studies regarding the interactions of stress waves with the discontinuities, it is postulated that stress waves arising from stope production blasts could give rise to fault-slip due to the reduction in normal stresses acting on the fault when the waves reflect on the fault surface. Estimating the magnitude of the fault-slip and energy released during the fault-slip is indispensable in order to propose proper support system for mine openings located in vicinity of the fault (Hedley, 1992). Hence, it is imperative to examine the seismic response of a fault to stress waves resulting from stope production blasts quantitatively.

In the present study, the interactions of stress waves arising from stope production blasts with a fault in vicinity of the stope are investigated. First, calibration of a numerical model with a single blast hole is performed with respect

to blast pressure and damping coefficient of rockmass, using a charge weight scaling law obtained from a case study. A numerical model of a typical Canadian metal mine encompassing a fault parallel to a tabular ore deposit is then constructed, and the simulation of stope extraction sequence is carried out with static analysis until the fault exhibits slip burst conditions. Subsequently, based on the stress state obtained from the static analysis, dynamic analysis is performed, in which blast vibrations are applied to a stope wall in the form of velocity, which is obtained from the calibrated numerical model. Through the dynamic analysis, the interactions of the stress waves with the fault are examined in terms of increments of stress state and shear displacements on the fault.

5.3 Calibration of blast vibration

Blast vibrations used to examine the interactions of stress waves with a nearby fault are calibrated with a numerical model encompassing a single blast hole, to which blast pressure is applied with dynamic analysis. The calibration is performed by comparing results obtained from the numerical analysis with peak particle velocities calculated from a charge weight scaling law.

5.3.1 Charge weight scaling law

Henning and Mitri (2010) examined production blast-induced vibrations in the hanging wall of an orebody that is mined out with open stope mining method with delayed backfill. The mine for the case study is located in the Abitibi region of the province of Quebec, Canada. The blast vibration data was compiled considering non-distinct and overlapping waveforms, and the compiled data was analyzed statistically using scaled distance relationship (Holmberg & Persson, 1979). Consequently, site-specific constants for the following charge weight scaling law were obtained.

$$ppv = k\frac{W^{\alpha}}{R^{\beta}} \tag{5-1}$$

where PPV, R and W are peak particle velocity, radial distance from the center of a blast hole and explosive charge per delay, and k, α, and β are the site-specific constants dependent upon the characteristics of in-situ rockmass properties. In the case that stress waves travel through rockmasses, β is approximately twice as much as α (Gool, 2007). Hence, $\beta = 2\alpha$ is assumed in the present study. While PPV can be calculated with Equation 5-1, the charge weight scaling law is valid provided that the blast that induces the blast vibrations can be considered a point source (Yang, Rocque, Katsabanis, & Bawden, 1994). Therefore, the present study employs a charge weight scaling law modified by Persson, Holmberg, and Lee (1994), which was used for modelling production blast-induced vibration (Gool, 2007; Sartor, 1999). The charge weight scaling law is given as:

$$ppv = k\left(\frac{L}{R_0}\right)^{\frac{\beta}{2}}\left\{\omega - \arctan\left(\frac{R_0 \tan\omega - H}{R_0}\right)\right\}^{\frac{\beta}{2}} \tag{5-2}$$

where R_0, ω, L, and H are the horizontal distance between the explosive and the geophone, the angle shown in Figure 5-1, linear charge density, and the height of the explosive in a blast hole, respectively. Equation 5-2 is obtained by integrating Equation 5-1 over the length of a blast hole; thus, constants in Equation 5-2 correspond with those in Equation 5-1. According to Henning and Mitri (2010), the maximum charge per delay in Equation 5-1 for a transverse stope, which is 30m height, is 175 kg. Assuming 2.5m of stemming, the linear charge density is calculated to be 6.36 kg/m. The site-specific constants calculated by Henning and Mitri (2010), which are substituted into Equation 5-2, are listed in Table 5-1.

Table 5-1: Site-specific constants in charge-scaling law used for calibration

	k	β	L (kg/m)
Constants	496	1.19	6.36

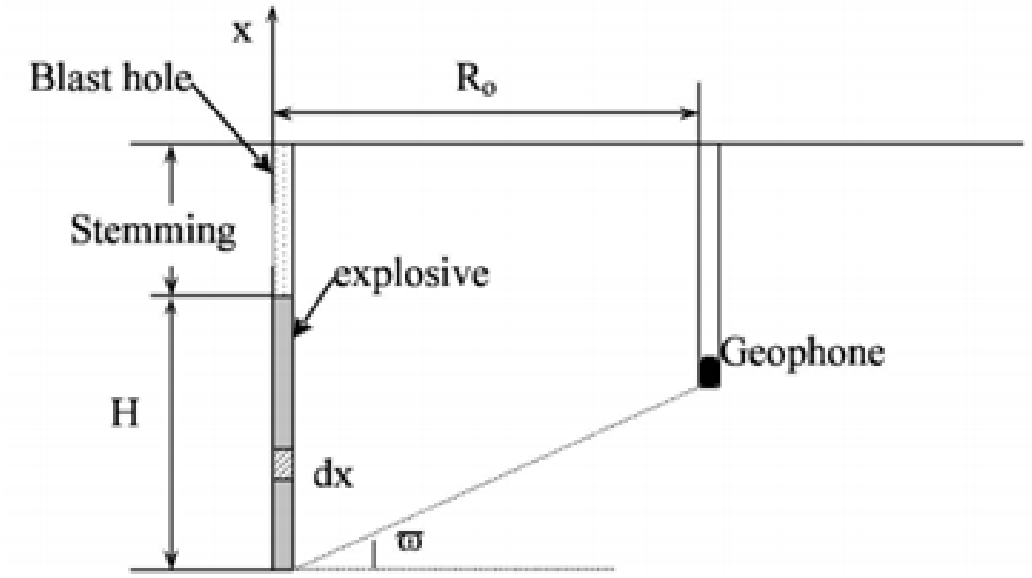

Figure 5-1: Geometry showing the constants used for scale-charging law (Gool, 2007)

5.3.2 Calibration of production blast-induced blast vibration

Estimating appropriate blast pressure and damping coefficient of rockmass is required in order to simulate production blast-induced vibrations that are obtained from Equation 5-2. To perform the calibration, a numerical model is generated with FLAC3D (Itasca, 2009). Note that this numerical model is utilized only for the calibration and is different from that for examining the effect of stope production blasts on a nearby fault. Detonation of the explosives exerts extremely high blast pressure on the boundary of a blast hole, depending on type of explosive and coupling ratio, which results in fracturing the zone around the blast hole (Saharan, 2004). Simulating the rock fracture zones surrounding the blast hole is beyond the scope of this study. Considering the fact that the purpose of the calibration is

to replicate PPV obtained from Equation 5-2, employing the concept of equivalent cavity (Sharpe, 1942) is deemed to be sufficient. The concept is that a cavity of which diameter is presumed to be the same as that of the maximum length of the fracture generated around the blast hole is modelled instead of modelling an actual blast hole in the numerical model. According to Brady and Brown (1993), the radius of the cavity is estimated to be approximately 4 to 6 times the radius of the blast hole. In addition, there are a couple of equations to estimate the radius of the cavity (Kexin, 1995; Mosinets & Garbacheva, 1972). Considering the above-mentioned information, the radius of the equivalent cavity is set at 6 times the radius of a blast hole of the transverse stope for the case study (Henning & Mitri, 2010).

Figure 5-2 illustrates a plan view of a quarter of the numerical model developed for the calibration. It can be seen from the figure that the model plan view is 40m x 40m in and is 33m high. The radius of the equivalent cavity is 0.3 m. A sectional view of the numerical model is illustrated in Figure 5-3. As shown in the figure, the equivalent cavity is 30 m deep, which corresponds with the height of the stope to be modelled, and blast pressure is applied to a wall of the equivalent cavity, assuming 2.5 m stemming in the upper part of the cavity. Gool (2007) used a numerical model encompassing a blast hole that is 3 m deep in order to calibrate the numerical model with a charge weight scaling law. Although Gool (2007) reported that a blast-hole length of 3 m is sufficient to model the blast pressure, it was found from the preliminary analysis that a longer hole is required in order to obtain stable numerical results. Bullets A and B, shown in Figure 5-3 are observation points, where peak particle velocities are observed during the dynamic analysis in order to calibrate the blast pressure and damping coefficient. Locations of the points A and B are 2.0 m and 12.1 m away from the wall of the equivalent cavity, respectively. A positional relationship between the points and equivalent cavity corresponds with that between a stope wall and nearby fault to be modelled in order to investigate stress wave interactions.

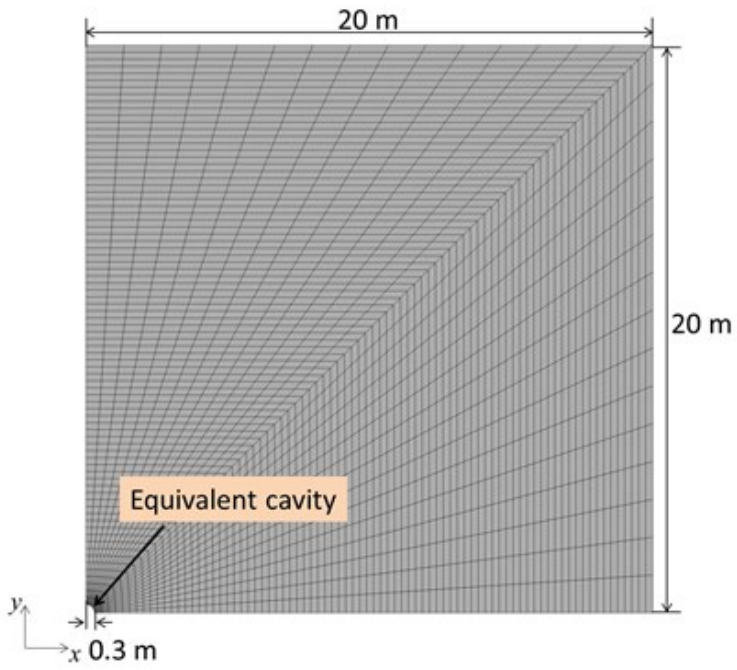

Figure 5-2: A Plan view of a numerical model for calibration

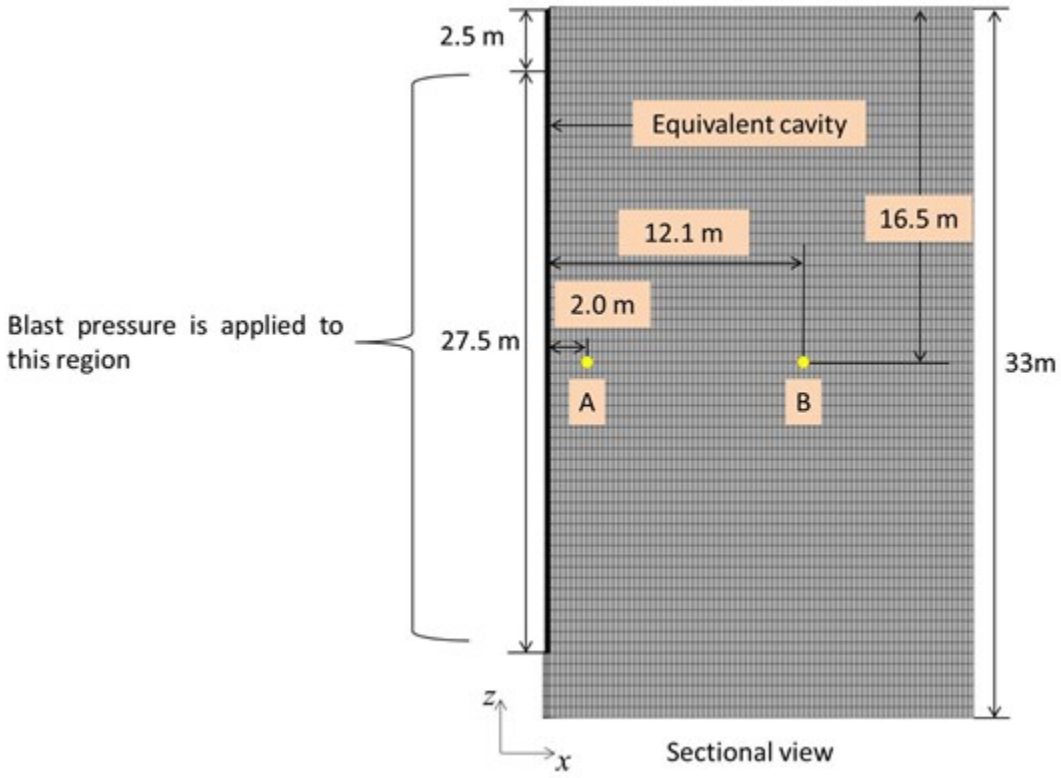

Figure 5-3: A sectional view of a numerical model for calibration

5.3.3 Blast pressure applied to wall of equivalent cavity

Blast pressure that varies with time is applied to the wall of the equivalent cavity, assuming stemming height of 2.5 m, where no pressure is applied. The following equation was used to simulate time varying blast pressure (Gool, 2007; Jiang, Blair, & Baird, 1995) :

$$p(t) = p_0 t^n e^{-\phi t} \tag{3}$$

where p(t) and p_0, are time varying blast pressure and initial detonation pressure, respectively; and n and ϕ are constants. Further, $p_0 = p_p(\phi e/n)^n$, where p_p is the effective peak borehole pressure. The authors used 1 and 2000 for n and ϕ, respectively. Figure 5-4 depicts an example of blast pressure profile derived from Equation 5-3. As can be seen in the figure, blast pressure drastically rises immediately after the blast commences, then it reaches the peak borehole pressure, p_p, when t = 0.5 ms. Afterwards, the blast pressure gradually decreases as time goes by. The blast pressure profile in the figure captures the feature of blast pressure (Saharan, 2004) in that fall time is much longer than rise time.

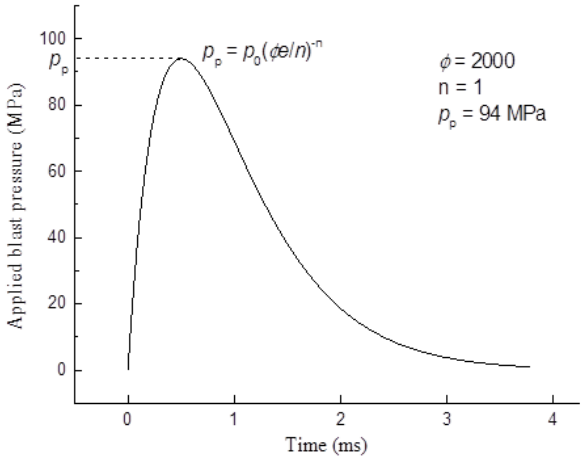

Figure 5-4: Blast pressure profile

5.3.4 Mechanical properties of rockmass and analysis conditions

Henning and Mitri (2010) obtained site-specific constants for the charge weight scaling law based on blast vibration measurements in hanging wall. Therefore, the mechanical properties of the rockmass in hanging wall are used for the numerical model. Table 5-2 lists the elastic modulus, E, cohesion, C, the angle of friction, ϕ, Poisson's ratio, ν, the unit weight of the rockmass, γ, tensile strength, σ_T, dilation angle, ψ.

Table 5-2: Mechanical properties of the rockmass used for model calibration

	E (GPa)	C (MPa)	ϕ (˚)	ν	γ (kN/m3)	σ_T (MPa)	ψ (˚)
HW[1]	31	2.6	38	0.21	25.51	1.1	9.25

[1] Hanging wall

Dynamic analysis is carried out with the mechanical properties of the rockmass. Viscous boundaries (Lysmer & Kuhlemeyer, 1969) are applied to the model in order to prevent stress waves induced by the blast pressure from reflecting on the model boundaries. Mesh sizes of the numerical model are optimized in order to realize practical calculation time and reliable results. According to the manual of FLAC3D code, the coefficient of local damping, which is embodied in FLAC3D code, is given as:

$$\alpha_L = \pi D \tag{5-4}$$

where α_L and D are the local damping coefficient and a fraction of critical damping. Based on the numerical model and input data, calibration is performed in order to obtain the peak borehole pressure, p_p, and the coefficient of local damping so that peak particle velocities computed from the numerical model agree with those calculated from Equation 5-2.

5.3.5 Calibration of numerical model

Procedure of the calibration is as follows. First, dynamic analyses are conducted for different local damping coefficients while keeping the peak borehole pressure, p_b, constant. The peak borehole pressure is 74 MPa. The results obtained from the dynamic analyses are depicted in Figure 5-5, where the left vertical axis shows the ratio of PPV at point A shown in Figure 5-3 to PPV at point B. As can be seen, as a fraction of critical damping increases, the ratio increases. This is due to the fact that the amount of energy absorbed between the points increases with the increasing damping coefficients. The ratio of the decrease in PPV calculated from Eq. 2 using geometries of the numerical model and site-specific constants in Table 1 is 3.954. Thus, by obtaining a polynomial fit denoting a relation between the damping coefficient and the ratio of the decrease in PPV, a calibrated fraction of critical damping can be obtained as shown in Figure 5-5; and the value is 4.758 %. Triangular bullets in Figure 5-5 represent PPV, which is obtained from the dynamic analyses, at point A for each local dumping coefficient. As the calibrated fraction of critical damping is 4.758 %, one can calculate PPV at point A for the calibrated damping coefficient without conducting additional dynamic analysis, by substituting the damping ratio into an equation of a polynomial fit denoting PPV at point A. As a result, 1.524 m/s can be obtained as PPV at point A. As PPV calculated from Eq. 2 for the point is 1.84 m/s, the peak borehole pressure can be calibrated, assuming PPV at point A is linearly proportional to the peak borehole pressure. Consequently, 94 MPa can be obtained as the peak borehole pressure, which induces PPV of 1.84 m/s at point A.

In order to verify the calibrated blast pressure and the local damping coefficient, dynamic analysis is carried out with the calibrated values. The results are depicted in Figure 5-6. As shown in the figure, PPV obtained from the dynamic analysis is almost consonant with that calculated from Eq. 2, though there are slight discrepancies in PPV in areas between 6 m and 10 m away from

the center of the equivalent cavity. The results from the numerical analysis especially agree well with those estimated from the equation at points 2 m and 12 m away from the center of the equivalent cavity. The locations correspond with those for the fault and stope wall to be modelled for the case study. Hence, the results obtained from the calibration are considered sufficient for analysis to investigate the effect of production blast-induced stress waves on the fault.

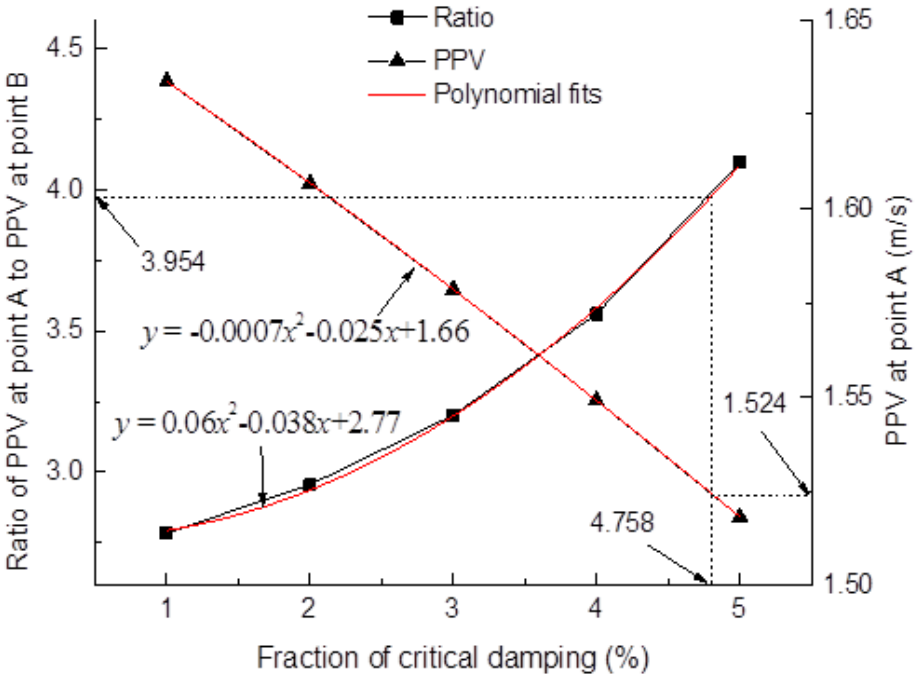

Figure 5-5: Graphs for calibration with respect to blast pressure and local damping coefficient

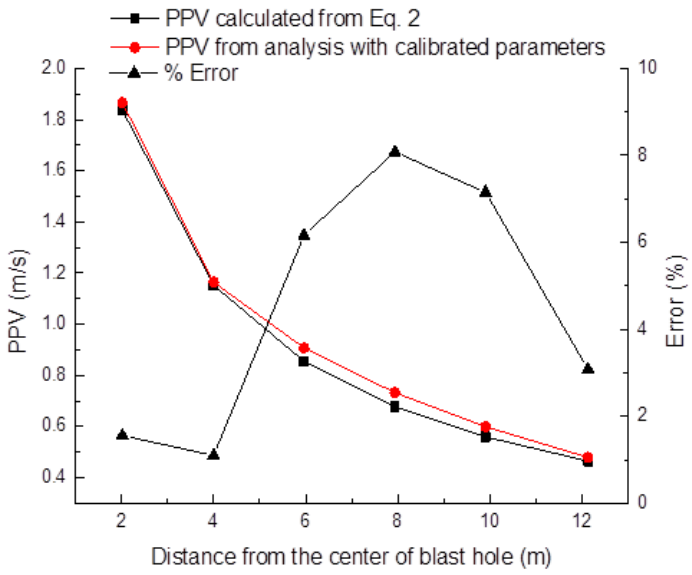

Figure 5-6: Calibrated blast vibrations

5.4 Case study

A case study is conducted on the basis of mechanical properties of rockmasses obtained by Henning (1998) and the calibrated blast pressure and local damping coefficient. For the case study, a numerical model with a fault is generated by means of FLAC3D code. After conducting static analysis while extracting stopes in the model, dynamic analysis is performed, in which blast vibrations are applied to a stope wall in the form of velocities. The velocities to be applied are obtained from dynamic analysis with the model shown in Figures 5-2 and 5-3, using the calibrated values. Based on the results, interactions of stress waves with the fault are examined. In addition, the influence of blast sequence on the behaviour of the fault is also investigated employing a couple of types of blast pattern.

5.4.1 Model description

Gool (2007) investigated an effect of stope production blasts on backfill with numerical models encompassing part of a mine for a case study. While much of the stresses that the backfill picks up in static conditions are due to its own

weight, the stress states on faults are strongly dependent upon many factors, such as in-situ stress state, mining sequence, and geological structures. Hence, it is imperative to replicate mining sequence with a mine-wide model before simulating stope production blasts. The numerical model generated for this case study is illustrated in Figure 5-7. The height, length and width of the model are 300 m, 300 m, and 312 m respectively. The steeply dipping, tabular orebody is 22 m wide and dips at 80˚. The fault colored in blue in the figure runs parallel to the orebody and is modelled with interface elements. The distance between the orebody and the fault is 10 m. The configuration of the model features geological structures frequently encountered in Canadian Shield (Bewick et al., 2009).

Stopes are modelled inside the orebody, and the geometries are illustrated in Figure 5-8. As shown in the figure, the height and strike length of the stope are 30 m and 20 m respectively; and the width of the stope varies with the height. On each level, stopes on hanging wall side and footwall side are separately modelled and extracted.

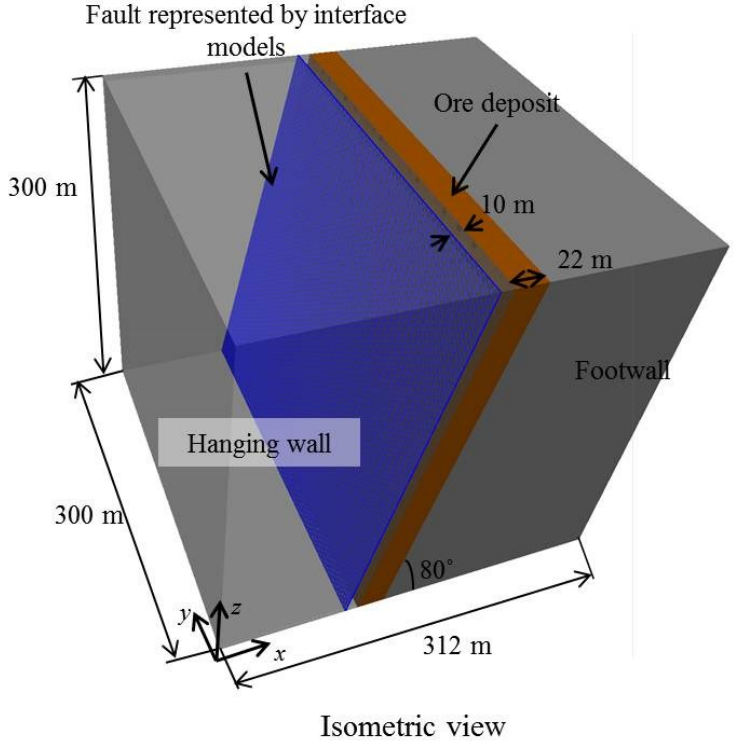

Figure 5-7: Numerical model geometry

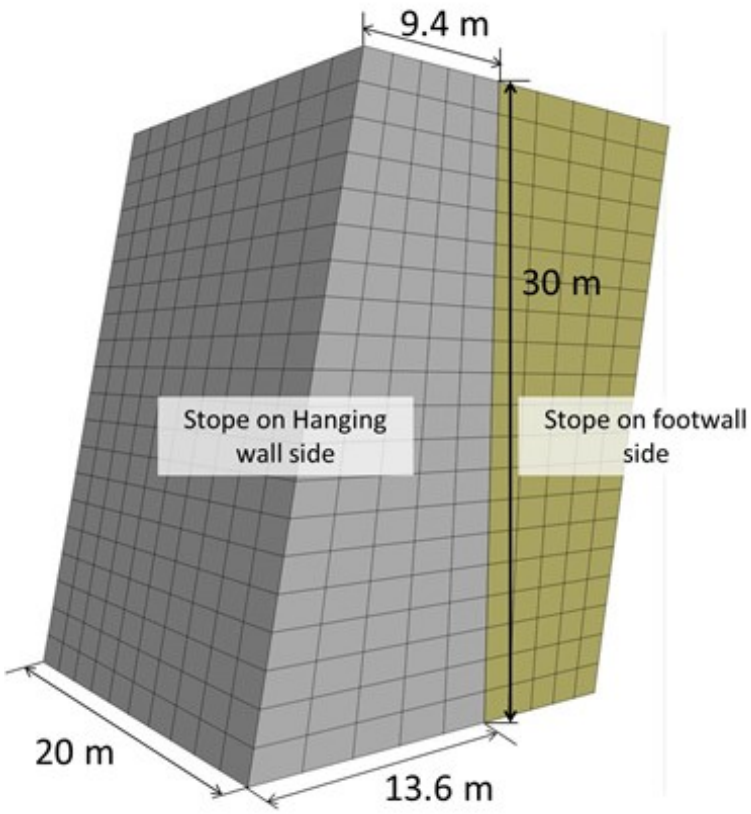

Figure 5-8: Stope geometry modelled in the orebody

5.4.2 Analysis procedure

The orebody shown in Figure 5-7 is mined out with sublevel stoping method employing bottom-up mining, with static analysis. The stopes mined out during the static analysis are illustrated in Figure 5-9. As shown in the figure, all the stopes on 3 levels and half of stopes on 4th level are extracted prior to the dynamic analysis. The numerical model for the case study are discretized densely so that an effect of mesh size on propagation of stress waves induced by production blast vibrations is minimized. As extracting each stope separately for the model is time-consuming, stopes on the same side are extracted together on each level during the static analysis. The stress state of the fault after extracting the stopes shown in Figure 5-9 with the static analysis is shown to be burst-prone conditions, which facilitates examining the effect of the stress waves on the fault, especially in terms of possibility of the waves causing the fault to slip.

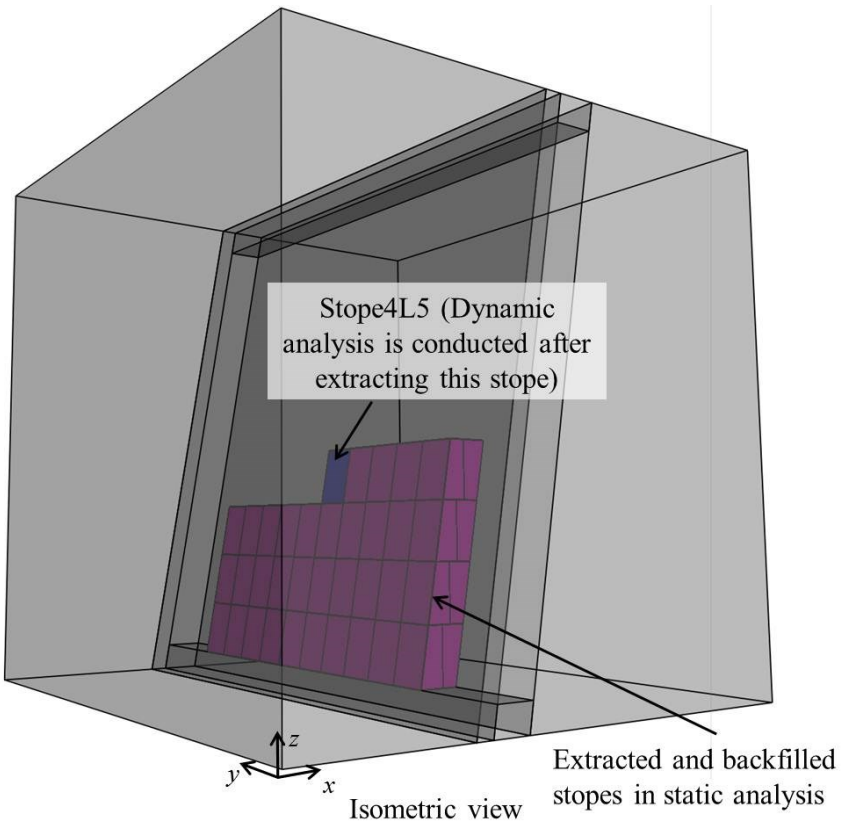

Figure 5-9: Stope extracted and backfilled in static analysis

Based on the stress state after extracting stope4L5 shown in Figure 5-9, the dynamic analysis is carried out while applying blast pressure to grid points on a wall of stope4L5 on hanging wall side in the form of velocity. As shown in Figure 5-8, the stope wall is a rectangular measuring 20 × 30.5 metres, on which 231 grid points exist. The velocities to simulate the blast pressure are applied to the grid points. In the following section, a methodology to obtain the velocities, which vary with positional relationships between the grid points and assumed blast holes, is described in detail.

5.4.3 Blast pressure applied to a stope wall of stope4L5

In the present study, blast sequences are taken into consideration, assuming several blast holes in the vicinity of the stope wall. The velocities applied to the wall of stope4L5 are obtained considering a positional relationship between

locations of the grid points on the stope wall and the blast holes. The velocities applied to a given grid point located h m above the bottom of the stope and d m away from the blast hole are obtained by picking up time-varying velocities of a grid point in the calibrated model, of which location is h m above the bottom of the equivalent cavity and horizontally d m away from the cavity. The velocities picked up from the calibrated model are applied to the grid point on the stope wall after converting coordinate system as the model for the calibration has different coordinate system from the model for the case study. Thus, every grid point has different time-varying velocities, which are deemed to be capable of simulating blast vibrations induced by the assumed blast holes since blast vibration attenuation that could arise between the blast holes and the grid points as well as the positional relationships is taken into consideration.

Figure 5-10 schematically illustrates the magnitude and direction of the velocities applied to the grid points on the stope wall in the case that a blast hole located at the center of the blast holes is assumed to be blasted. For this study, nine blast holes are assumed in the vicinity of the stope wall. They are located 2 m away from the stope wall, and the distance between each blast hole is 2 m. As can be seen in the plan view of stope4L5, the magnitude of the velocities is relatively large in the vicinity of the blast hole, and as the distance between the blast hole and the grid point increases, the magnitude of the velocities decreases. The magnitude of the velocities also varies vertically. As shown in the sectional view of stope4L5, in upper and lower areas, the magnitude of velocities is relatively small; on the other hand, large velocities are applied near the center of the stope.

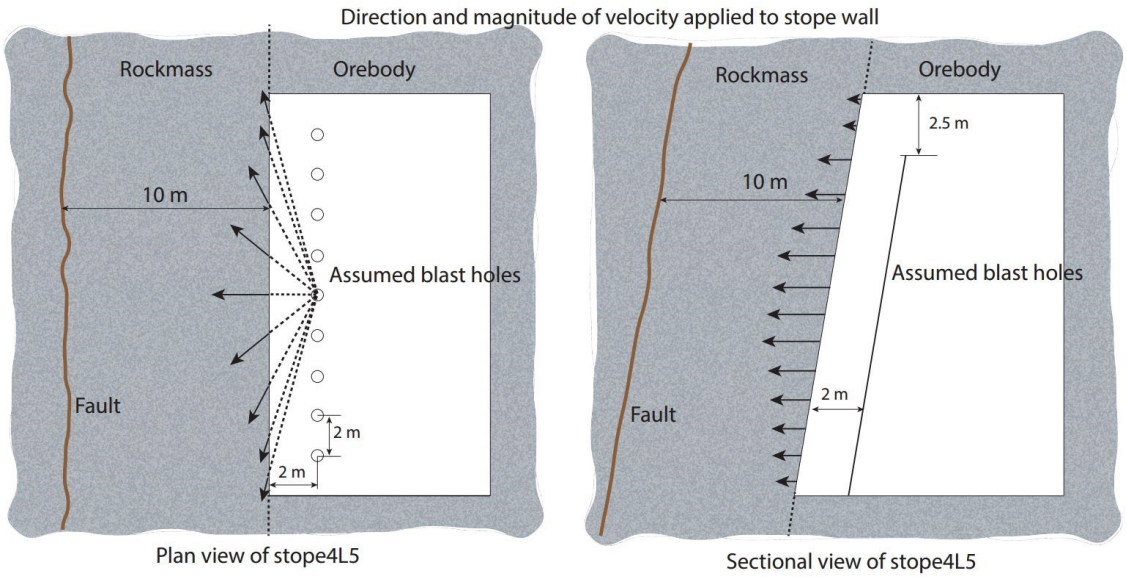

Figure 5-10: Schematic illustration showing the magnitude and direction of velocities applied to grind points on a wall of stope4L5 on hanging wall side

5.4.4 Blast sequence

During the dynamic analysis, the velocities are applied to the grid points while assuming that the blasts are sequentially performed. The simulated blast sequences are illustrated in Figure 5-11. As can be seen in the figure, three types of blast sequences are assumed, namely A, B, and C. For each blast sequence, blasts are performed in the order corresponding to numbers illustrated in the figure. For instance, for the blast sequence A, blasts are separately performed; for the blast sequence C, on the other hand, all the blasts are simultaneously carried out. An interval between blasts of 100 ms is considered for all blast sequences. In the case of the blast sequence A, the ninth blast is performed 800 ms after the first blast.

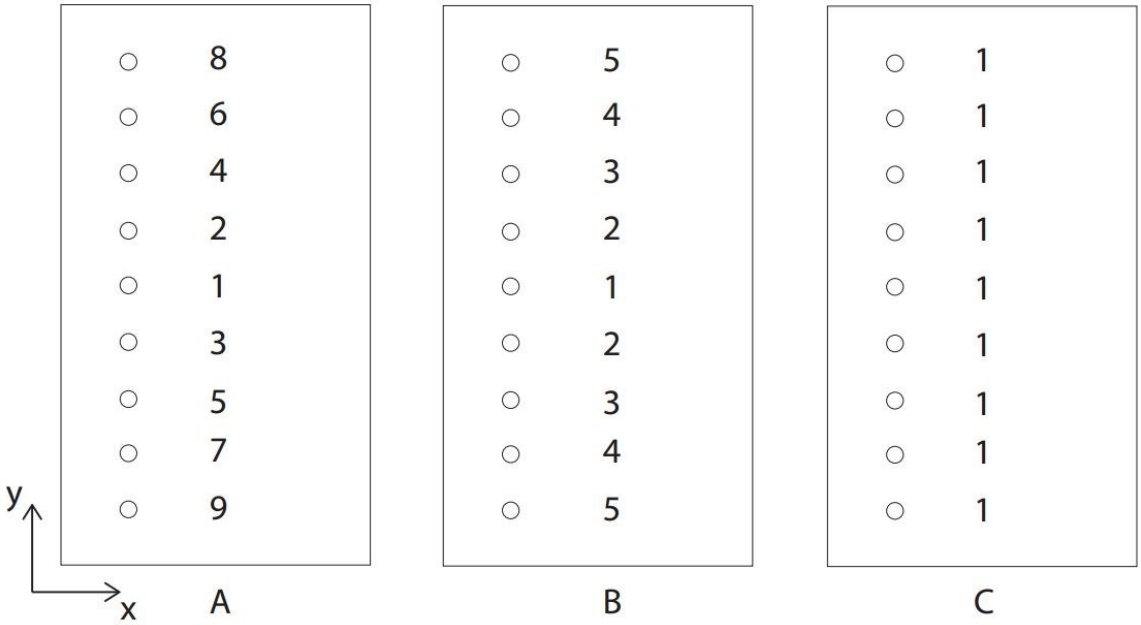

Figure 5-11: Simulated blast sequences shown on a plan view of Stope4L5

Blast vibrations are set to 0 m/s 10 ms after each blast since the velocities due to each blast become small enough to be negligible after the elapsed time; also conducting dynamic analysis with the model for the calibration to obtain the velocities after 10 ms is time-consuming. Figure 5-12 shows an example of velocities applied to the center point of the stope wall during the dynamic analysis in the case of the blast sequence B. Five peaks in the figure correspond with 5 blasts performed during the blast sequence, and as can be seen, the velocities in x-direction are much larger than the others. This is due to the fact that blast pressure is applied in the direction perpendicular to the wall of the equivalent cavity when blast vibrations are calibrated. It can be also seen that the velocities in x-direction decrease immediately after the onset of each blast and become apparently negligible, compared to the peak value. This confirms that the duration time of 10 ms to apply blast vibrations to the grid points for each blast is reasonable.

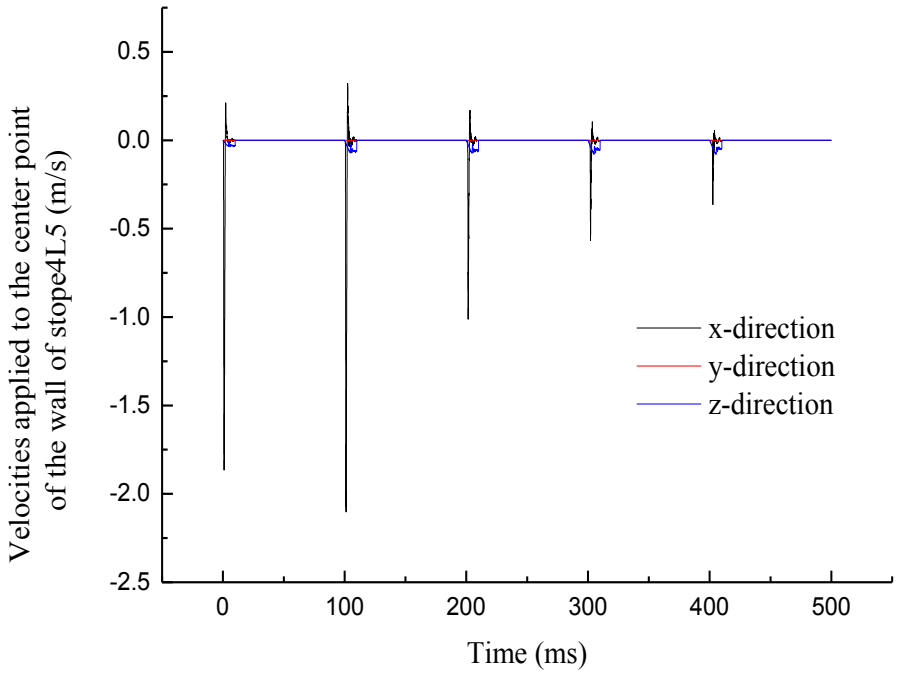

Figure 5-12: Velocities applied to the center point of the wall of stope4L5 during dynamic analysis

5.4.5 Mechanical properties of rockmass, backfill and fault

The mechanical properties of the rockmasses to be modelled are based on the case study (Henning, 1998). Table 5-3 lists the elastic modulus, E, cohesion, C, internal friction angle, ϕ, the unit weight, γ, Poisson's ratio, ν, tensile strength, σ_T, and dilatancy angle, ψ, of the rockmasses and backfill material.

Table 5-3: Rockmass mechanical properties

	E (GPa)	C (MPa)	ϕ (˚)	ν	γ (kN/m^3)	σ_T (MPa)	ψ (˚)
HW[1]	31	2.6	38	0.21	25.5	1.1	9.3
Ore	115	11.5	48	0.1	25.5	5.9	12.0
FW[2]	49	4.3	39	0.15	25.5	1.8	9.5
BF[3]	2.5	0.1	35	0.35	23.0	N/A	0.0

1 Hanging wall

2 Footwall

3 Backfill

Mohr-Coulomb criterion is employed for a friction law to determine stress states on the fault. Regarding the mechanical properties of the fault, Table 5-4 lists the friction angle on fault-surface, ϕ_f, shear stiffness, k_s, and normal stiffness, k_n, of the fault. According to Ivins and Lyzenga (1986), cracks and fractures in fault zones could decrease modulus of elasticity to one-tenth of that of surrounding rockmass. Regarding the friction angle, the basic friction angles of typical rock joints fall between 21° and 38° (Barton & Choubey, 1977). Based on the information, the mechanical properties of the fault shown in the table are determined for this study.

Table 5-4: Mechanical properties of the fault

	ϕ_f (°)	k_n (GPa/m)	k_s (GPa/m)
Fault	30	3.1	1.28

5.4.6 Initial stress state

The vertical in-situ stress, σ^o_v, which is in the z-direction in Figure 5-7, is determined by the overburden pressure as:

$$\sigma^o_v = \gamma H \tag{5-5}$$

where γ and H are the unit weight of the rockmass and the depth below ground surface. According to Arjang (1991), steeply dipping orebodies in the Canadian Shield have the characteristics that the maximum horizontal stress is in the direction perpendicular to orebody and the direction of minimum horizontal stress is parallel to the orebody strike. The characteristics are replicated for the present study. The magnitude of maximum and minimum horizontal stresses is determined by the following equations proposed by Diederichs (1999).

$$k_{\max} = 1 + \frac{25}{\sqrt{H}} \tag{5-6}$$

$$k_{\min} = 1 + \frac{8}{\sqrt{H}} \tag{5-7}$$

$$\sigma^{o}{}_{H\max} = k_{\max}\sigma^{o}{}_{v} \tag{5-8}$$

$$\sigma^{o}{}_{H\min} = k_{\min}\sigma^{o}{}_{v} \tag{5-9}$$

where k is the ratio of horizontal stress to vertical in-situ stress. By employing equations 5-6 to 5-9, the maximum and minimum horizontal stresses, which vary with the depth below ground surface, can be obtained. In this study, the depth at the top boundary of the model is set at 1500 m, and the unit weight of overlying rockmass is assumed to be 25.5 kN/m3. Furthermore, the maximum horizontal in situ stress is oriented perpendicular to the orebody strike. This setting of initial stress states is based on the research by Zhang and Mitri (2008). The calculated initial stress state according to the depth is listed in Table 5-5.

Table 5-5: Initial stress state at a depth of 1500 m

Depth (m)	k_{max}	k_{min}	γ (kN/m^3)	σ^{o}_{v} (MPa)	σ^{o}_{Hmax} (MPa)	σ^{o}_{Hmin} (MPa)
1500	1.65	1.21	25.5	38.25	62.94	46.15

5.5 Results and discussion

Interactions of blast-induced stress waves with the fault are first examined and discussed with regard to the blast sequence B, based on increments of shear displacements and stresses on the fault during the dynamic analysis. After that, an effect of blast sequences on fault slip is investigated on the basis of

seismic source parameters computed for each blast sequence shown in Figure 5-11.

5.5.1 Blast-induced stress wave interactions with the fault

Change in slip tendency as well as that in shear and normal stresses is examined at an observation point shown in Figure 5-13 during the dynamic analysis, in which blasts are carried out according to the blast sequence B. The slip tendency is given as:

$$Slip\ tendency = \frac{\tau}{\tau_p} \tag{5-10}$$

where τ and τp are shear stress on the fault and peak shear strength as determined by Mohr-Coulomb criterion, respectively. The slip tendency and stresses observed at the point are shown with respect to time in Figure 5-14. As the blast sequence B consists of 5 blasts, the total duration is 500 ms as shown in the figure. It can be seen from the figure that a rise in normal stress by approximately 2MPa takes place immediately after the onset of the blast sequence. It is reasonable to consider that the rise in normal stress is a response of the fault to the blast-induced stress waves reaching fault surfaces, as the stress waves is mainly composed of compression waves. The rise in normal stress decreases slip tendency since the peak shear strength is linearly proportional to normal stress. These results indicate that the stress waves arising from blast pressure induce less burst-prone conditions when reaching the fault. After the rise, it is found out that a reduction in normal and shear stresses takes place and that slip tendency returns to 1.0. The implication of the change in the stresses and slip tendency is the occurrence of slip on the fault. Sharafisafa and Mortazavi (2011) showed that stress waves reflected on a fault give rise to tensile stresses around the fault. In light of the study, a reasonable explanation for this case is that the reflected waves reduce the normal stresses to a level at

which stress states on the fault reach equilibrium with respect to the friction law and that the reduction in the normal stresses causes the shear stresses on the fault to drop, obeying the friction law. Slip along the fault is expected to occur due to energy released from the shear stress drop. After the reduction in normal and shear stresses, the stresses are found to recover. However, it should be noted that the stresses never reach the same stress level as before because static stresses on the fault have changed due to the slip induced by the reflected waves. The same change is found to occur as the blast sequence proceeds, which corresponds with 5 blasts carried out during the blast sequence B. As shown in the figure, the normal and shear stresses eventually decrease by 0.75 MPa and 0.3 MPa, respectively, compared to the stress states before the dynamic analysis. This graph clearly shows the interactions of the stress waves with the fault.

Shear displacement increments induced by the reduction in the normal and shear stresses at the observation point are shown in Figure 5-15. As can be seen in the figure, the shear displacements increase at 5 steps during the dynamic event. The steps are evidently attributed to 5 blasts performed during the blast sequence B. The figure also shows an effect of locations of the blast holes on the increment of the shear displacement. As can be seen, the increase in the shear displacement resulting from 1st blast is 0.3 mm, whereas the last blast induces no more than 0.1 mm. This is due to the fact that the last blast is performed in blast holes located away from the observation point. It is found out that the shear displacement eventually increases by approximately 1 mm at the point.

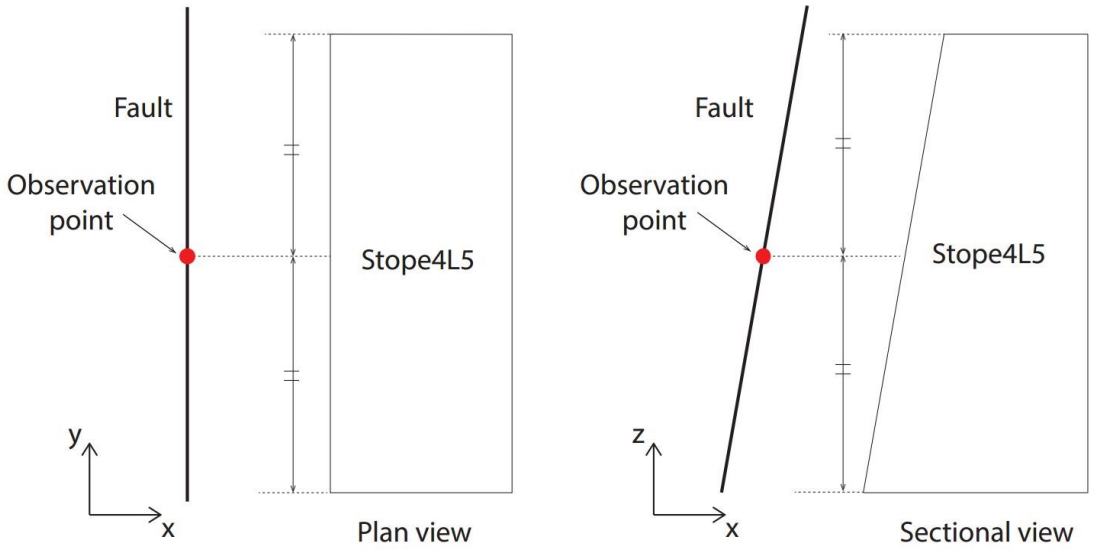

Figure 5-13: Observation point on the fault to investigate change in displacement and stresses

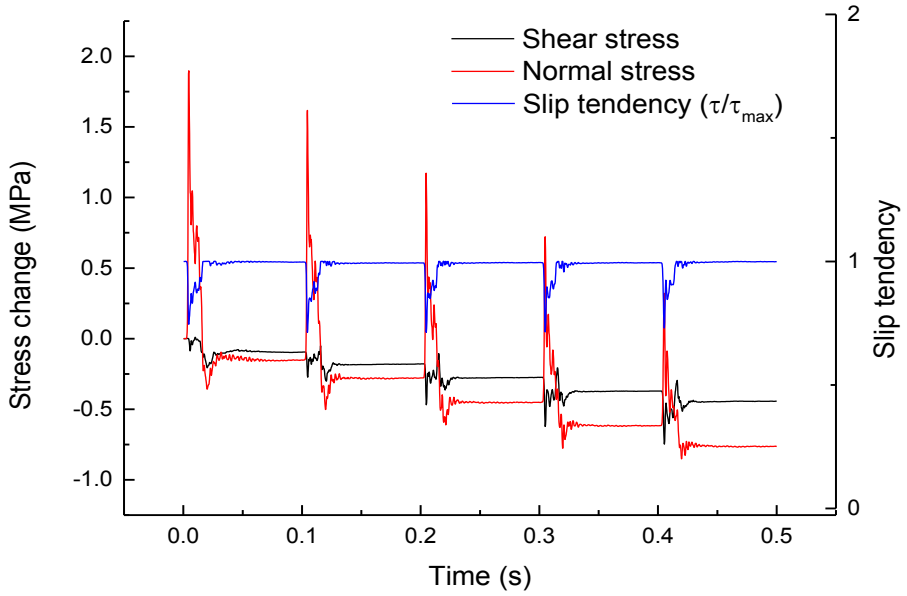

Figure 5-14: Change in shear displacements and stresses on the fault during dynamic analysis for blast sequence B

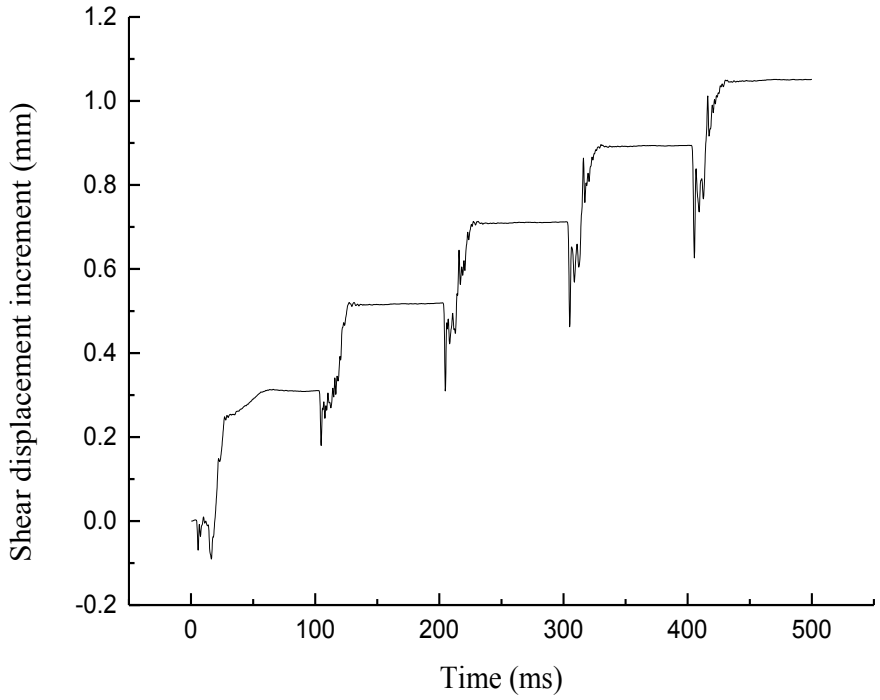

Figure 5-15: Shear displacement increments at the center point of the stope wall during dynamic analysis for stope sequence B

5.5.2 Effect of blast sequences on the behaviour of the fault

The effect of blast sequences on behaviour of the fault is examined with regard to seismic source parameters computed on the basis of results obtained from the dynamic analysis. In the present study, the following seismic parameters are adopted to investigate dynamic sliding behaviour: seismic moment, Mo, moment magnitude, Mw, and energy released during fault slip, E_s. The seismic moment and moment magnitude are commonly used in the study of mining-induced seismicity (Domanski & Gibowicz, 2008; Hedley, 1992; Hofmann & Scheepers, 2011; Sneilling et al., 2013); they are given by

$$M_o = GDA \tag{5-11}$$

$$M_w = \frac{2}{3}\log M_o - 6.0 \tag{5-12}$$

where G, D, and A represent shear modulus, average shear displacement, and area where sliding takes place. The seismic energy E_s represents the sudden energy released along the faulting area "A" subjected to the slip "D" and is thus given by.

$$E_s = 0.5\Delta\sigma DA \tag{5-13}$$

$\Delta\sigma$ in Equation 5-13 represents stress drop defined as the average difference between stress on the fault before a seismic event and stress after the event and is expressed as follows.

$$\Delta\sigma = \frac{1}{A}\int_s [\sigma(t_2) - \sigma(t_1)]dS \tag{5-14}$$

It is noteworthy that the calculated energy does not accurately represent the seismically radiated energy, but the energy can be employed as an index to compare the blast sequences proposed above.

The seismic moment and moment magnitude for the blast sequences, A, B, and C are depicted in Figure 5-16. The effect of blast sequences on the behaviour of the fault is clearly shown in the figure. It is first found out that the blast sequence C, in which every blast hole is blasted simultaneously, induces the most severe seismic event as of 100 ms after the onset of the blast sequences, of which seismic source parameters are 1.4×10^{10} N·m and 0.74 for the seismic moment and moment magnitude, respectively. The moment magnitude would not pose serious threats to nearby mine opening, but it cannot be considered negligible in mine planning. The difference in seismic source parameters between the blast sequences at the time is due to the fact that only the blast hole located at the center of the holes is blasted for the blast sequences B and C. It should be noted that while the seismic moment and moment

magnitude for blast sequence C remain almost the same after 100 ms, those for the blast sequences B and C keep increasing until the last blast is performed. According to the figure, seismic moment increases to 4.9×10^{10} N·m and 3.7×10^{10} N·m for the blast sequences B and C, respectively, which are significantly larger than that for the blast sequence A. The large difference in the eventual seismic source parameters between the sequences are considered to pertain to superposition of the velocities applied to the stope wall. For instance, when 2nd blast is carried out for the blast sequence B, y-component of the velocities applied to grid points located on the perpendicular bisector of a line between the blasted holes are canceled out due to symmetry. The results imply that the y-component, which is cancelled out when blasts are conducted simultaneously, plays an important role in generation of stress waves that cause the fault to slip. From a viewpoint of properties of the stress waves, y-component of the velocities is presumed to induce shear waves along the stope wall, which propagate towards the fault. Thus, it is reasonable to assume that not only longitudinal waves resulting from the velocities applied to the stop wall but also the shear waves are critical in the interactions of the stress waves with the fault and have an influence that cannot be negligible on fault slip occurrence.

Energy released during fault slip, E_s, is shown in Figure 5-17 for the blast sequence A, B, and C. As is the case with the seismic moment and moment magnitude, E_s for the blast sequence A is eventually the largest among the blast sequences, and the value is 1.46 MJ, while E_s for blast sequences B and C is 0.68 MJ and 0.08 MJ, respectively, as of 900 ms after the beginning of the analysis. Although the characteristic is the same between the seismic source parameters, a difference in E_s between the blast sequences is much larger than that in seismic moment and moment magnitude. As can be seen in figure, there is eventually an 18 times difference in E_s between the blast sequence A and C. According to Hedley (1992), energy released during fault slip is an important factor to correlate a magnitude of seismic events with damage induced by the

event. Hence, the results imply that seismic events induced by the blast sequence A could inflict more severe damage to nearby mine openings than that induced by the blast sequence B and C. Presumably, carrying out blasts simultaneously induce high peak particle velocities around the stope, which could result in rock strength deterioration and ore dilution. Therefore, in terms of preventing rockmasses from yielding, performing blasts separately is deemed to be desirable. However, the results indicate that conducting blasts simultaneously could control fault slip by cancelling particle velocities causing shear waves that are considered to affect the evolution of fault slip. Consequently, it would be ideal to propose blast sequence taking into account both of the aspects when faults are found in the vicinity of stopes to be blasted.

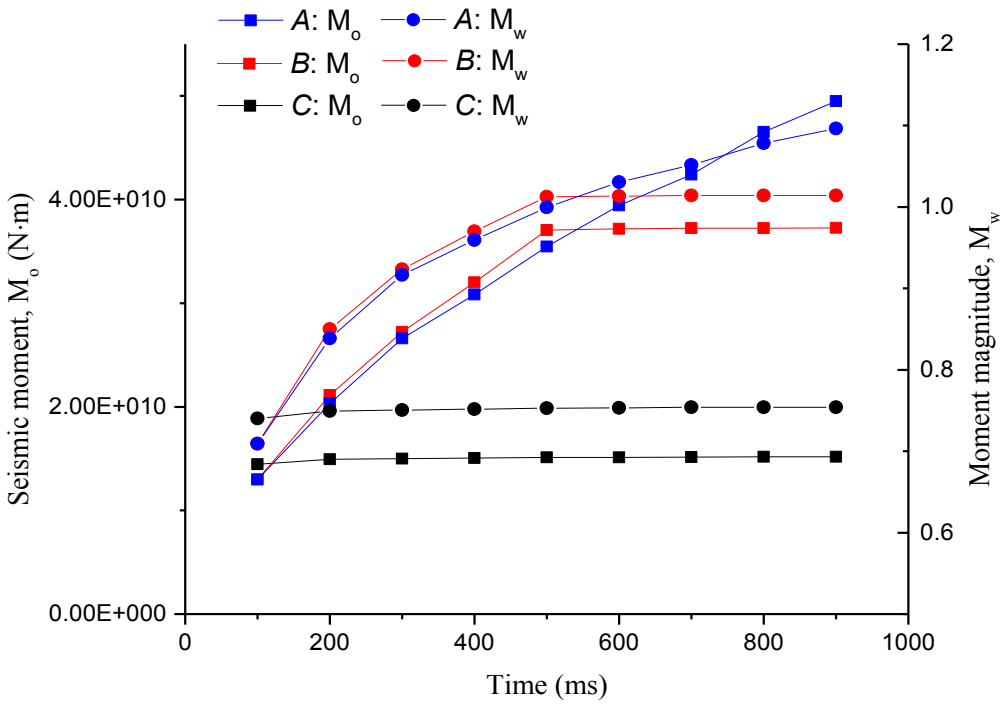

Figure 5-16: Seismic moment and moment magnitude generated by blast sequences, A, B, and C

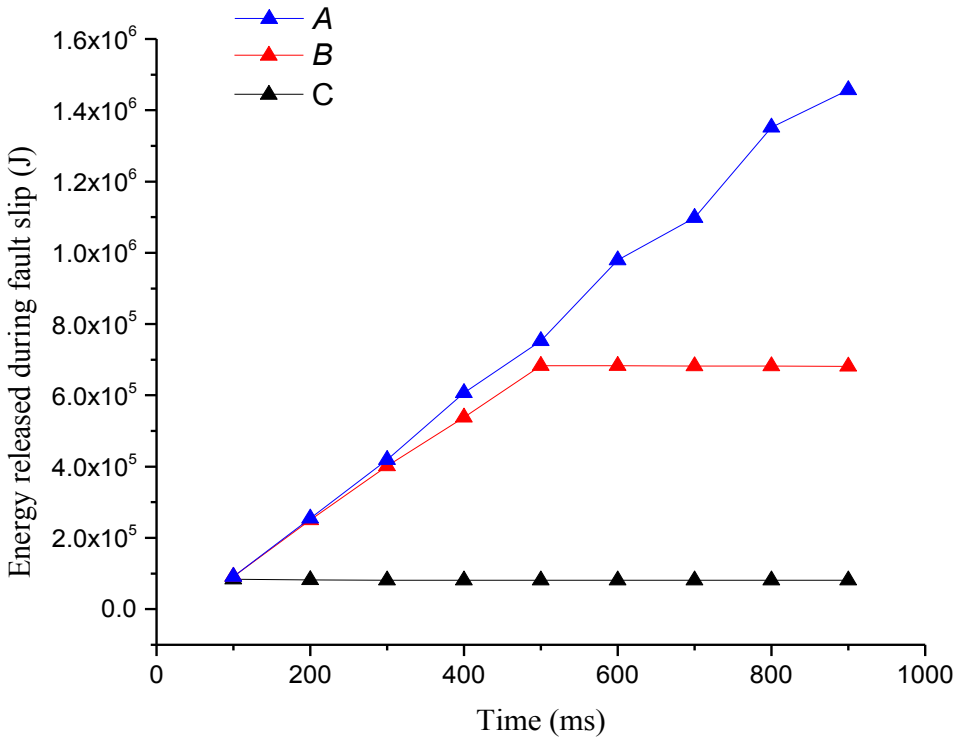

Figure 5-17: Energy released during fault-slip for the blast sequence, A, B, and C

5.6 Conclusions

For the purpose of examining interactions of blast-induced stress waves with a nearby fault, a numerical model of a mine case study is generated, which encompasses a fault running parallel to a steeply dipping, tabular ore body that is mined out with sublevel stoping method with delayed backfill. Based on the numerical model, static analysis is carried out to simulate the extraction of stopes before conducting dynamic analysis. On the basis of the results obtained from the static analysis, dynamic analysis is launched, in which blast pressure calibrated with a charge weight scaling law is applied to the stope wall in the form of velocities while considering alternative blast sequences. The results obtained from the dynamic analysis indicate that a reduction in normal stresses on the fault due to the reflected stress waves on the fault causes the fault to slip while releasing energy that results from a shear-stress drop on the fault. As the blast

sequences proceed, the normal and shear stresses continue to decrease, resulting in fault slip. The effect of blast sequences on the behaviour of the fault is also examined in terms of seismic source parameters. It is found that seismic moment and energy released during fault slip significantly differ depending on the selected blast sequences. The results furthermore show that carrying out blasts simultaneously could help control fault slip as stress waves are cancelled out due to a positional relationship between the blast-hole location and grid points on the stope wall to which velocities are applied. On the other hand, performing blasts separately could result in larger seismic events due to shear waves arising from the blasts. A difference in energy released during fault slip between the different types of blast sequence is found to be especially large compared to that in seismic moment. This implies that performing blasts separately could cause more severe damage on nearby openings as energy radiated during fault slip is strongly correlated with damage induced by the fault slip. Hence, it can be concluded that although conducting blast separately is considered to be desirable in terms of preventing rockmasses from deteriorating due to high particle velocities, simultaneous blasting might be an option when faults are found in close proximity to stopes to be blasted.

CHAPTER 6

Simulating intense shock pulses due to asperities during fault-slip

6.1 Abstract

Seismic waves arising from fault-slip that occurs in underground mines could inflict severe damage to mine openings. Experimental results have revealed that intense shock pulses could generate due to the unloading of fault surface asperities that move apart during the fault-slip. This study focuses on examining the effect of fault surface asperities on the seismic waves arising from fault-slip. By means of a mine-wide model, dynamic analyses are carried out in order to simulate collision and unloading of fault surface asperities. Saeb and Amadei's model and Barton's shear strength model are newly implemented into constitutive models of FLAC3D code for the analyses. Parametrical study is conducted with the dynamic analyses in order to examine the most influential factor on the generation of intense seismic waves. The results reveal that stress release due to the unloading of the asperities has a significant influence on the intensity of seismic waves, while the collision of asperities, stiffness of the fault, and asperity geometry have a much lesser influence. When the stress release is large, the peak particle velocity excited by seismic waves is found to increase threefold, compared to that for fault-slip occurring along a planar surface. It indicates that significant deterioration of rockmasses could be induced due to the high particle velocities. This study has numerically confirmed the hypothesis that intense shock pulses could occur due to the unloading of fault surface asperities.

6.2 Introduction

In underground hard rock mines, the occurrence of rockbursts is not uncommon at great depths, and severe damage to mine openings is occasionally inflicted due to the violent failures of rockmasses (Blake & Hedley, 2003; Kaiser & Cai, 2012; B. G. White & Whyatt, 1999). Rockbursts are generally characterized into 3 types, namely strain burst, pillar burst, and fault-slip burst, according to the volume of rockmasses involved and underlying mechanism by which the rockbursts are induced (Blake & Hedley, 2003). Among the types of rockbursts, fault-slip bursts could cause the most significant damage to large areas that extend over several levels in underground mines given that intense seismic waves arise from the fault-slip. In such a case, seismic waves play a critical role in causing damage to mining openings, while stress changes induced by the fault-slip would be limited to areas in the vicinity of the fault.

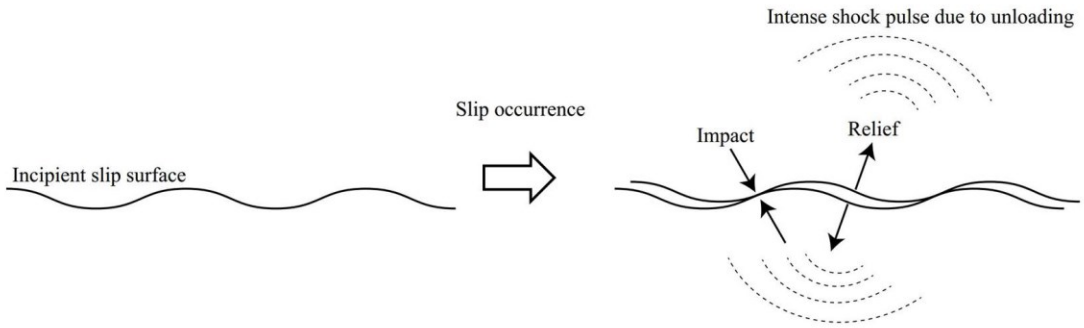

Figure 6-1: Slip along a non-planar surface and generation of intense shock pulse

The propagation of seismic waves excites the particle velocity of rockmass, and there is a strong correlation between the particle velocity and rockmass damage (Brinkmann, 1987; Hedley, 1992) as an increase in stresses induced by the propagation of seismic waves is proportional to the particle velocity (Brady & Brown, 1993). Thus, it is imperative to estimate peak particle velocity excited by the seismic waves in order to optimize secondary support systems for sustaining additional loads and deformations induced by the seismic waves. Although there

are a number of studies that examine the influence of seismic waves on underground openings (Directorate, 1996), these studies are mainly based on numerical models, in which seismic waves are applied to its boundaries in the form of displacement, velocity, or acceleration. In other words, neither the mechanisms by which seismic events take place nor the locations of the seismic events are considered. Through the studies, it is certainly possible to examine the effect of seismic waves on mine openings, such as the extent of yielding zones and stress changes, whereas from a practical engineering view point, it would be difficult to propose optimized secondary support systems to accommodate the energy and deformation induced by the seismic waves since the characteristics of seismic waves expected from seismic events cannot be estimated. Hence, developing a methodology which considers source mechanisms and the locations of seismic events is of paramount importance in order to estimate the intensity of seismic waves accurately.

As described above, an appreciation of the characteristics of seismic waves arising from rockbursts is indispensable, especially when fault-slip is involved that seismically radiates a large amount of energy while inducing shear rupture and slip movements. Gay and Ortlepp (1979) conducted microscopic analysis of infilling materials on fault surfaces arising from significantly violent seismic events that took place in a deep South Africa gold mine. Ortlepp (2000) further investigated the electron micrographs of the micro-cataclastic materials showing remarkably uniformity in size and shapes of rhombic dodecahedron; and the author mentioned that the characteristics are inconceivable as ordinarily crystallographic structures for the material. The author postulated that the particular morphology results from intense shock unloading that takes place when fault-slip takes place along a non-planar, incipient or pre-existing surface as shown in Figure 6-1. In other words, violent tensile failure due to sudden reduction in normal stresses acting on the fault gives rise to the formation of the infilling materials that have the particular structure. It was further discussed that

locally intense shock pulses could generate as a result of the sudden release of the stresses acting on the fault where significant impact asperities occur at intervals. It is then suggested that the generation of the intense shock pulses could be one of plausible explanations for rockburst damage that is locally significant as shown in Figure 6-2.

Figure 6-2: Localized damage to a mine tunnel (Ortlepp, 2000)

Although the plausible mechanism of generation of locally intense seismic waves has been proposed, a specific framework for estimating peak particle velocity expected from the intense seismic waves has not yet been established. Thus, a better understanding of the mechanism is required in order to propose practical support systems for the locally intense shock pulses. It is found from Figure 6-1 that a number of factors, such as the amount of slip displacements and the size of impact asperities could have an influence on the characteristics of the generated seismic waves. A rise in normal stresses due to the impact that occurs when the asperities collide is also assumed to be an influential factor since a normal stress level prior to the unloading would more or less affect the

unloading. This paper focuses on simulating the intense shock pulse, considering these factors that could affect the characteristics of the intense shock pulses, with the purpose of establishing a methodology to estimate the peak particle velocity quantitatively.

6.3 Methodology

In this study, examining the effect of fault surface asperities on the generation of intense shock pulse is attempted. It is admittedly ideal to develop a numerical model encompassing a fault on which asperities as shown in Figure 6-1 are modelled, and to conduct numerical analysis with a numerical simulation technique that can allow for the dynamic motion of the asperities colliding and moving apart. However, shear rupture due to fault-slip in underground mines extends to large areas (Hofmann & Scheepers, 2011; Ortlepp, 2000; Swanson, 1992), and the occurrence of fault-slip is strongly dependent upon mining-induced stress state (Alber et al., 2009; Potvin et al., 2010; Sjoberg et al., 2012) as well as in-situ stress state. Thus, constructing a mine-wide scale model is essential in order to simulate fault-slip induced by mining activities. However, it is difficult to simulate fault surface asperities in the model as a significantly large number of nodal points and zones would be required for the modelling. Considering these facts, for this study, FLAC3D code (Itasca, 2009), which adopts explicit finite difference method, is utilized, and a couple of constitutive laws governing the behaviour of faults are implemented into the code with C++ programming language to simulate the intense shock pulses. Furthermore, new constants are proposed and incorporated into the constitutive models to allow for the simulation of fault-surface asperities that are difficult to actually model. The analysis procedure is first explained in detail. A detailed description of the analysis and the constitutive models is then provided.

6.3.1 Analysis procedure

In the present study, one static analysis and two dynamic analyses are conducted in sequence. Figure 6-3 depicts the overall procedure. As shown in the figure, static analysis is first performed with a numerical model encompassing a steeply dipping, tabular orebody and fault running parallel to the orebody. During the static analysis, stopes in the orebody are extracted following mining sequences as per sublevel stoping method with delayed backfill. The reason why the extraction of stopes and backfilling are carried out prior to simulating fault-slip is to simulate mining-induced stress re-distribution on the fault. As reported in many studies (Hofmann & Scheepers, 2011; McGarr, Spottiswoode, & Gay, 1975; Sneilling et al., 2013; B. G. White & Whyatt, 1999), the occurrence of fault-slip in underground mines is strongly associated with the stress re-arrangement, such as unclamping of fault surfaces (Castro et al., 2009), due to mining activities. Hence, the static analysis is intended to only simulate slip potential induced by the mining activities. Subsequently, dynamic analysis is carried out on the basis of the stress state obtained from the static analysis in order to simulate fault-slip. As shown in the flowchart, fault-slip resulting from asperity shear is simulated. This is due to the fact that faults in underground mines cannot be considered planar (Ortlepp, 2000; Ryder, 1988; Wallace & Morris, 1986), and as shear stress acting on the faults reaches peak shear strength, asperities on the fault are expected to be sheared off (Ryder, 1988). Excess stress determined by a difference between shear strength allowing for the asperities and that for planar surfaces is fault-slip driving force. Although shear rupture within intact rocks is another possible source for fault-slip (Hofmann & Scheepers, 2011), a pre-existing fault is modelled in the present study, so that asperity shear is a more plausible source for the fault-slip. Thus, a shear strength model allowing for undulation and asperities on the fault is required in order to simulate the fault-slip due to asperity shear. Regarding the shear strength model, an explanation is provided later.

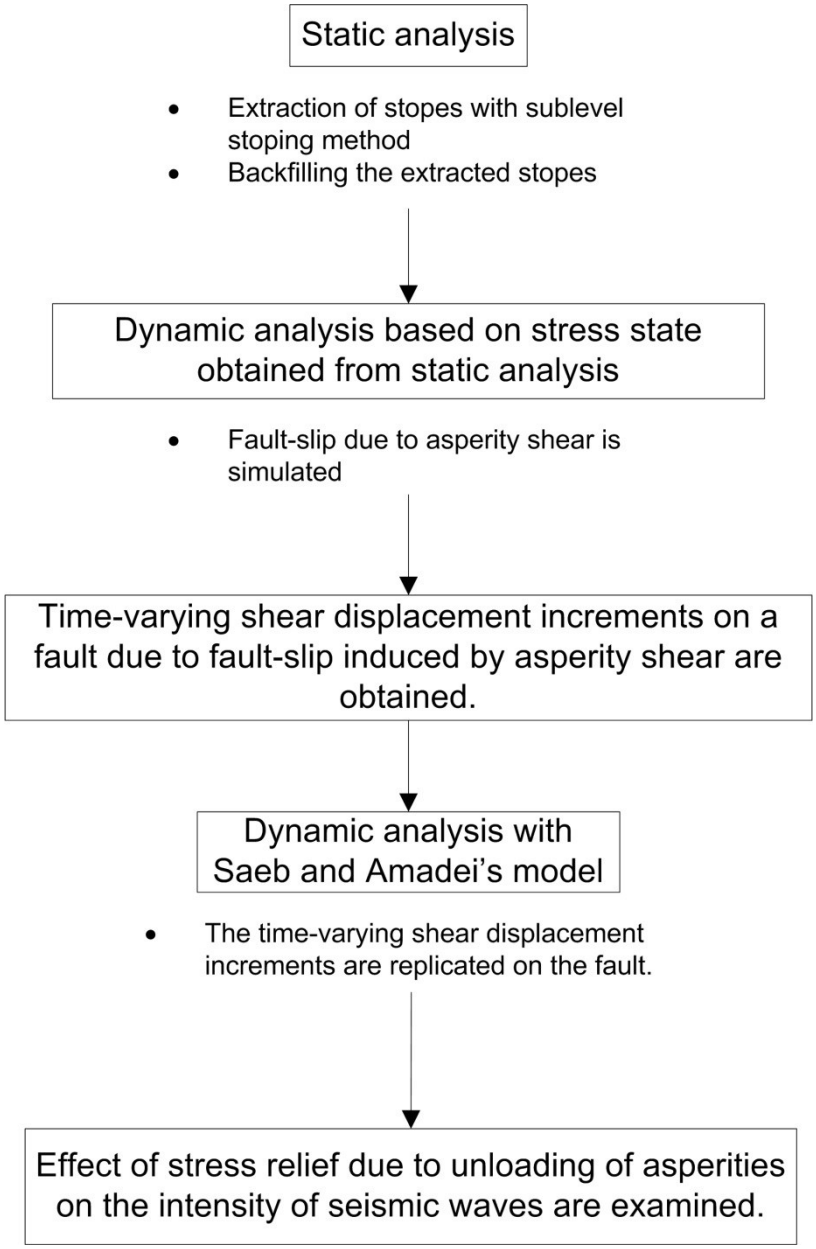

Figure 6-3: Analysis procedure

After the dynamic analysis, shear displacement increments on the fault, which are caused by fault-slip due to asperity shear, are obtained with respect to dynamic time. Based on the time-varying shear displacement increments, it is attempted to examine the effect of asperities on the intensity of seismic waves. The methodology developed for this study is to apply the time-varying shear displacement increments to grip points on the fault with dynamic analysis while considering the phenomena that asperities collide with each other and move

away, which are not taken into consideration during the preceding dynamic analysis. The reason why the dynamic analysis to examine the asperity effect on the intensity of seismic waves is separately performed is to conduct a parametrical study regarding fault-surface properties, such as asperity height and length, using an identical shear displacement increments. Simultaneously considering the two phenomena, namely fault-slip due to asperity shear and interactions of the asperities, make it difficult to understand how stress release that takes place when asperities move apart is related to the generation of locally intense seismic waves. Although the two phenomena admittedly occur at the same time in real situations, the purpose of this study is to examine the effect of asperities on seismic waves. Thus, in the present study, the phenomena are simulated separately, and the asperity effect can be consequently assessed from the dynamic analysis.

6.3.2 Shear strength model and its implementation

As mentioned above, fault-slip due to asperity shear is simulated in the present study. The only shear strength model available for FLAC3D code used to simulate fault-slip is the classical Mohr-Coulomb criterion, which is based on a friction law for planar surfaces. It is impossible to take into account asperity shear with Mohr-Coulomb criterion. Thus, a shear strength model allowing for undulation and asperities of fault surfaces needs to be employed and implemented into constitutive models of FLAC3D that can represent faults and/or fault zones. FLAC3D has two types of constitutive models that are capable of simulating slip behaviour of geological discontinuities, namely an interface model and a ubiquitous joint model. The former is widely utilized to model the geological discontinuities, which are represented as zero-thickness interfaces with the model. However, FLAC3D code does not allow users to modify the model. Thus, instead of the model, the ubiquitous joint model is employed in the present study, into which new constitutive models are incorporated with C++ programming language. It is noteworthy that the interface model and ubiquitous joint model

give almost exactly the same results in terms of shear displacements, normal stress, and shear stress when compared for the same geological discontinuity (Cappa & Rutqvist, 2010). Therefore, the interface models can be replaced with the ubiquitous joint models when modelling fault-slip.

To date, a number of shear strength models for geological discontinuities with non-planar surfaces have been proposed and modified (Asadollahi & Tonon, 2010; Barton, 1973; Indraratna et al., 2005; Ladanyi & Archambault, 1970; Seidel & Haberfield, 2002). Amongst the models, Barton's shear strength model (Barton, 1973), which can allow for joint surface roughness and joint wall compressive strength, is employed and incorporated into the ubiquitous joint models of FLAC3D code. The Barton's model is given as:

$$\tau = \sigma_n \tan\left[JRC \log_{10}\left(\frac{JCS}{\sigma_n} \right) + \phi_b \right] \tag{6-1}$$

where σ_n and ϕ_b are effective normal stress acting on the joint and the basic friction angle of the joint, respectively; *JRC* and *JCS* are the joint roughness coefficient and joint wall compressive strength. *JRC* ranges from 0 to 20 (Barton & Choubey, 1977), where *JRC* of 20 represents the roughest, undulating tension surfaces that would normally be found in a rockmass. *JCS* can be estimated based on the uniaxial compressive strength of the rockmass, considering the degree to which the joint surfaces are weathered.

Sainoki and Mitri (2013) incorporated Barton's model into FLAC3D with the ubiquitous joint model by obtaining derivatives of the failure criterion and potential function for Barton's model. In their work, the fault-slip is driven by the excess shear stress determined by the difference between Barton's shear strength model and the classical Mohr-Coulomb criterion. The present study adopts the same methodology, whereby fault-slip is modelled by changing *JRC*

from a value that represents rough fault surfaces to zero representing planar surfaces. Note that the change in *JRC* is carried out only for areas where shear stress acting on the fault exceeds the maximum shear strength determined by Barton's model. During the dynamic analysis, shear displacement increments are recorded at each time step for all the grip points on the fault. As a result, time-varying shear displacement increments are obtained. The obtained shear displacement increments are then replicated on the fault in the form of time-varying velocity to examine the effect of asperities on the generation of intense seismic waves. Note that replicating the obtained shear displacement increments for all the grid points on the fault is significantly time-consuming; hence the replication is conducted only for grid points of which the maximum particle velocity is greater than 0.5 m/s. The criterion has been determined on the basis of a relation between the maximum particle velocity and relative shear displacements of grid points on the fault. The relative shear displacements of grid points with low particle velocities are quite small, so that such grid points do not exert a large influence on the generation of intense shock pulses. For the second dynamic analysis, a constitutive model that can simulate the shear behaviour of a dilatant rock joint is newly incorporated. Barton's shear strength model that is used to obtain time-varying shear displacement increments due to asperity shear is no longer employed during the second dynamic analysis. In the following section, the constitutive model employed for the second dynamic analysis and new constants proposed to simulate the unloading of asperities are introduced.

6.3.3 Method to simulate shear behaviour of a dilatant rock joint

After obtaining time-varying shear displacement increments along the entire fault, the shear displacement increments are duplicated on the fault with dynamic analysis using a different constitutive model from the preceding dynamic analysis. With the newly incorporated constitutive model, the behaviour that asperities collide and move away while releasing accumulated stresses is simulated to examine the effect of fault surface asperities on seismic waves. In order to model

the behaviour, a constitutive model allowing for shear behaviour of dilatant rock joints (Saeb & Amadei, 1992) has been newly implemented into the ubiquitous joint model of FLAC3D code. It is to be noted that the ubiquitous joint model to which Saeb and Amadei's model (Saeb & Amadei, 1992) is applied does not consider slip behavior of the fault since slip behaviour is given in the form of time-varying shear displacement increments to the grid points on the fault. The formulations proposed by the authors are given as:

$$k_{nn} = \frac{\partial \sigma_n}{\partial v} = \frac{1}{\frac{-uk_2}{\sigma_T}\left(1-\frac{\sigma_n}{\sigma_T}\right)^{k_2-1}\tan i_0 + \frac{V_m^2 k_{ni}}{\left(k_{ni}V_m - \sigma_n\right)^2}} \tag{6-2}$$

$$k_{nt} = \frac{\partial \sigma_n}{\partial u} = \frac{-\left(1-\frac{\sigma_n}{\sigma_T}\right)^{k_2}\tan i_0}{\frac{-uk_2}{\sigma_T}\left(1-\frac{\sigma_n}{\sigma_T}\right)^{k_2-1}\tan i_0 + \frac{V_m^2 k_{ni}}{\left(k_{ni}V_m - \sigma_n\right)^2}} \tag{6-3}$$

$$d\sigma_n = \frac{Kk_{nt}}{K - k_{nn}} du \tag{6-4}$$

where σ_T, V_m, i_0, and K are uniaxial compressive strength of joint wall, the maximum joint closure, the initial inclination angle of asperity, and the stiffness of host rock, respectively; k_2 is a constant and has a suggested value of 4 (Saeb & Amadei, 1992); k_{nn} and k_{nt} are two normal stiffness coefficients; u and du denote shear displacement and a shear displacement increment during a time interval, which is given from the preceding dynamic analysis. The equations above directly relate shear displacement increments to an increase in normal stress due to dilatancy resulting from the collision of asperities. Importantly, the increase in normal stress is related to the stiffness of a joint itself and surrounding rockmass. For instance, if $K = 0$, there is no increase in normal stress due to the dilatant behaviour, which corresponds with a case of shear movements occurring along a

geological discontinuity in a rock slope on the ground. In that case, the slope surface is considered free boundary. On the contrary, in a case of underground mines, it is conceivable that the stiffness has more or less an influence on the rise in normal stress.

To conduct analysis considering the collision and unloading with the ubiquitous joint models, there are a couple of points to consider: (a) the ratio of area with asperities responsible for the collision to the entire fault area; (b) the behaviour of the asperities moving away. First, asperities which are responsible for the rise in normal stress would not be situated over the entire fault since a portion of the asperities is sheared off during the fault-slip; hence the ratio needs to be taken into consideration in the numerical simulation. Secondly, it is impossible to simulate the behaviour of the asperities moving away after the collision since modelling each asperity on the fault is significantly difficult on a mine-wide scale, considering the capability of personal computers available. Modelling each asperity on the fault would require a considerable number of grid points and zones in the numerical model. Thus, in the present study, stress release rate is newly proposed and incorporated in the numerical code. The amount of normal stress that decreases due to the unloading at each time step during the dynamic analysis is computed on the basis of the stress release rate. It should be noted that the stress release rate is applied only to normal stress. This is because Ortlepp (2000) indicated that tensile failure due to a sudden reduction in “normal stress” is a source for locally intense seismic waves. Furthermore, in order to conduct the parametrical study to examine the effect of fault surface asperities on seismic waves, it is indispensable to use the same shear displacement increments on the fault, which is affected by shear stress release. For these two reasons, the release in shear stress is not considered for the second dynamic analysis to simulate intense shock pulses. The aforementioned constants are implemented into codes of FLAC3D as follows:

$$d\sigma_n = r_c \frac{Kk_{nt}}{K - k_{nn}} du \qquad \because 2(n-1)L \le u \le (2n-1)L \quad (n = 1,2,3\cdots) \tag{6-5}$$

$$d\sigma_n = -r_m \sigma_n \qquad \because (2n-1)L \le u \le 2nL \quad (n = 1,2,3\cdots) \tag{6-6}$$

$$L = \frac{H_a}{\tan\phi_a} \tag{6-7}$$

where r_c represents the ratio of asperity area responsible for the increase in normal stress to the entire fault, and r_m is the release rate in normal stress while asperities move apart, respectively. L, H_a, and ϕ_a denote asperity length, asperity height, and the inclination angle of asperities as shown in Figure 6-4, respectively. The rise in normal stress during the collision of asperities is computed from Equation 6-5, and the reduction in normal stress during the unloading behaviour is calculated from Equation 6-6. As shear displacement increments of the entire fault with respect to each time interval are obtained from preceding dynamic analysis, the increase and decrease in normal stress on the fault can be computed according to the shear displacement increments. As can be seen from Equations 6-5 and 6-6, it is assumed during the dynamic analysis that the collision of the asperities takes place prior to the unloading behaviour. In other words, Equation 6-5 is first applied during the analysis. Equation 6-6 is then applied after the total shear displacement increments reach L, which is equal to half of the asperity length as shown in Figure 6-4.

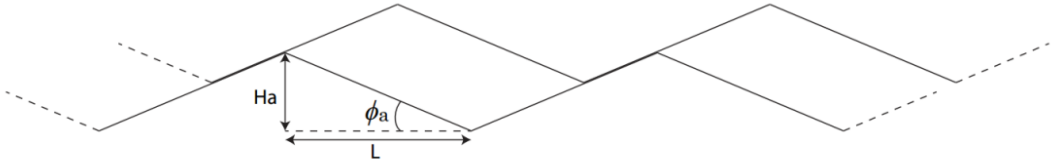

Figure 6-4: Schematic illustration showing asperity geometry

6.4 Numerical model description

Throughout the static and dynamic analyses, the same numerical model generated with FLAC3D code is used. The model encompassing the fault and orebody on a mine-wide scale is depicted in Figure 6-5. It is seen from the figure that the orebody is 22 m wide and steeply dips at 80°. The fault runs parallel to the orebody and is represented by the ubiquitous joint models. The distance between the fault and orebody is 30 m for this study. The length, height and width of the model have been determined after conducting preliminary analysis to examine a boundary effect on the behaviour of the fault. The intervals of each grid point are also considered, and the model has been discretized densely enough to simulate stress changes resulting from mining sequences on the fault. Although the discretization is dense enough to obtain stable results in terms of stress and displacement increments on the fault, it is too large to simulate fault surface asperities. Therefore, the method discussed in the precious section has been developed and applied to the analysis. Finally, the total numbers of grid points and zones in the model are 210798 and 195840, respectively.

The stopes extracted and backfilled during the static analysis are shown in Figure 6-6. The extraction of the stopes proceeds according to the numbers illustrated in the figure, which correspond with the mining sequences of bottom-up sublevel stoping method. On each sublevel, stopes are extracted from hanging wall to footwall side. The height and strike lengths of the stopes are 30 m and 200 m, respectively. The stope strike length is admittedly longer compared to those generally planned in underground mines (Zhang & Mitri, 2008). However, modelling each stope and conducting numerical analyses to extract the stopes are significantly time-consuming. Furthermore, the purpose of the static analysis is to simulate high slip potential resulting from long-range mining sequences for the entire fault. The effect of extraction of each stope on the fault is not focused on. Therefore, the aforementioned stope geometries are modelled for the present study. As shown in the figure, the mining sequences proceed until extraction of Stope7H with the static analysis. The dynamic analysis to simulate fault-slip due

to asperity shear is performed on the basis of the stress state after extracting the Stope 7H.

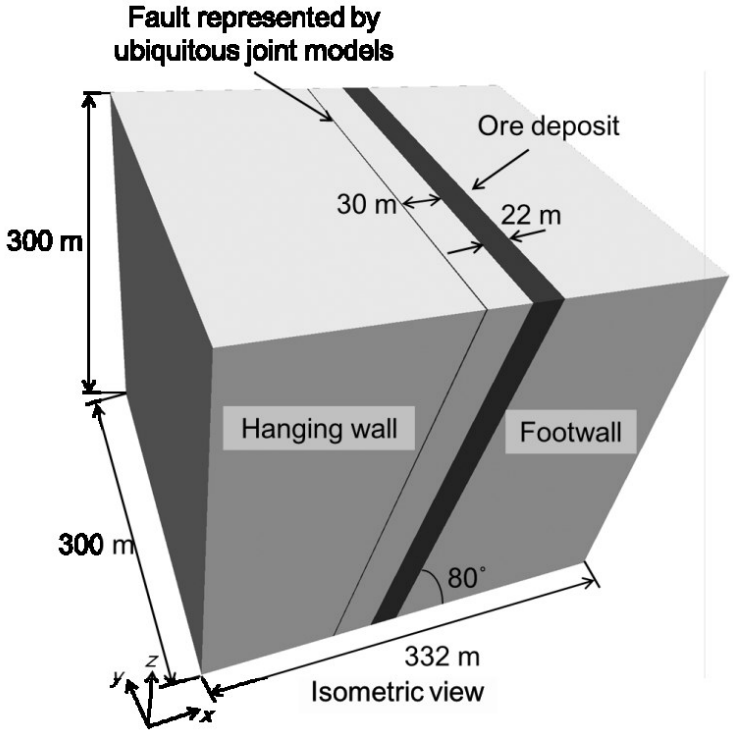

Figure 6-5: Numerical model used for static and dynamic analyses

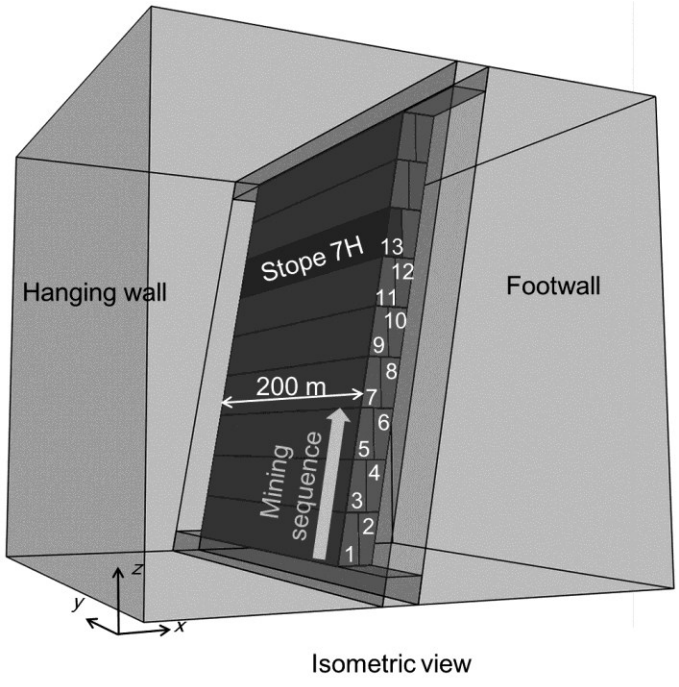

Figure 6-6: Mining sequence proposed

6.5 Rockmass mechanical properties and analysis conditions

The rockmass mechanical properties applied to the numerical model are based on a case study (Henning, 1998). Table 6-1 lists the elastic modulus, E, cohesion, C, internal friction angle, ϕ, the unit weight, γ, Poisson's ratio, ν, tensile strength, σ_T, and dilatancy angle, ψ, of the rockmasses and backfill material.

Table 6-1: Rockmass mechanical properties

	E (GPa)	C (MPa)	ϕ (˚)	ν	γ (kN/m^3)	σ_T (MPa)	ψ (˚)
HW[1]	31	2.6	38	0.21	25.5	1.1	9.3
Ore	115	11.5	48	0.1	25.5	5.9	12.0
FW[2]	49	4.3	39	0.15	25.5	1.8	9.5
BW[3]	2.5	0.1	35	0.35	23.0	N/A	0.0

[1] Hanging wall

[2] Footwall

[3] Backfill

Regarding the mechanical properties of the fault, the values shown in Table 6-2 are applied. As explained in the previous section, fault-slip due to asperity shear is modelled during the dynamic analysis; hence joint roughness coefficient is changed from 20, which represents a joint with significantly rough surfaces, to 0 for a planar surface when the shear stress reaches the maximum shear strength. The basic friction angles of typical rock joints fall between 21˚ and 38˚ (Barton & Choubey, 1977). Considering the data, the friction angle of the fault is set at 30˚ for the static analysis. The dynamic coefficient of friction is generally difficult to obtain and continuously alters during the slip (Ruina, 1983). In addition, simulating the mechanism accurately is quite challenging. Hence, in the present study, the dynamic coefficient of friction is obtained by changing the friction angle

to 25˚ for the area where a slip takes place during the dynamic analysis. As the ubiquitous joint models are used to model the fault, modulus of elasticity also needs to be considered. The modulus of elasticity is set at one-tenth of that for rockmass in hanging wall since cracks and fractures that exist in the fault zones are assumed to decrease modulus of elasticity (Brady & Brown, 1993; Bernard Budiansky & O'Connell, 1975).

Table 6-2: Mechanical properties of the fault

	E (GPa)	JRC	JCS (MPa)	ϕ (˚)	C (MPa)	ν	γ (kN/m^3)	σ_T (MPa)	ψ (˚)
Static Analysis	3.1	20	120	30	0	0.21	25.5	0	0
After slip occurs in dynamic analysis	3.1	0	120	25	0	0.21	25.5	0	0

A parametrical study is carried out with respect to the constants in Equations 6-2 to 6-7 which determine the characteristics of the collision and unloading. Table 6-3 shows each model for the parametric study. As shown in the table, 19 models are generated, and r_c, r_m, H_a, ϕ_a, K, and k_{ni} vary between the models. It is noteworthy that the parametrical study is conducted for the same time-varying shear displacement increments obtained from the preceding dynamic analysis, thus making it possible to examine the effect of the properties on the intensity of seismic waves more accurately.

Table 6-3: Models for a parametrical study

Model	r_c	r_m	H_a (mm)	ϕ_a (°)	K (GPa/m)	k_{ni} (GPa/m)
1	0.1	0.01	10	40	2	1
2	0.01					
3	0.001					
4	0.01	0.1	10	40	2	1
5		0.001				
6	0.01	0.01	20	40	2	1
7			5			
8			1			
9	0.01	0.01	10	50	2	1
10				30		
11	0.01	0.01	10	40	20	1
12					10	
13					0.1	
14					0.05	
15	0.01	0.01	10	40	1	40
16						20
17						0.2
18						0.01
19	0	0	0	0	N/A	N/A

The vertical in-situ stress, σ^o_v, which is in the z-direction in Figure 6-5, is calculated by the overburden pressure as follows:

$$\sigma^o{}_v = \gamma H \tag{6-8}$$

where γ and H are the unit weight of the rockmass and the depth below ground surface. According toArjang (1991), steeply dipping orebodies in the Canadian Shield have the characteristics that the maximum horizontal stress is in the direction perpendicular to orebody and the direction of minimum horizontal stress is parallel to the orebody strike. This is adopted in the present study. The magnitude of maximum and minimum horizontal stresses is determined by the following equations proposed by Diederichs (1999).

$$k_{\max} = 1 + \frac{25}{\sqrt{H}} \tag{6-9}$$

$$k_{\min} = 1 + \frac{8}{\sqrt{H}} \tag{6-10}$$

$$\sigma^o{}_{H\max} = k_{\max}\sigma^o{}_v \tag{6-11}$$

$$\sigma^o{}_{H\min} = k_{\min}\sigma^o{}_v \tag{6-12}$$

where k and σ^0_H are ratio of horizontal stress to vertical in-situ stress, and horizontal in-situ stress, respectively. In this study, the depth at the top boundary of the model is set at 3100 m below the ground surface. The value seems too large when compared to mining depths of typical Canadian mines. However, Camadian mines such as Kidd Creek in Timmins, Ontario and Laronde mine in Cadillac, Quebec have mining depths in excess of 3 km. More importantly, according to Ortlepp (2000), shear displacements during fault-slip could be up to 10 cm. The objective to carry out the first dynamic analysis is to obtain reasonable time-varying shear displacement increments during fault-slip that

could be a source for the intense shock pulses. As a result of a number of preliminary analyses, it is found that the depth assumed in this study is required in order to obtain shear displacements that are comparable to those reported by Ortlepp (2000) under these conditions.

During the static analysis, model boundaries are fixed in the direction perpendicular to the boundaries. The boundary conditions are changed to viscous when dynamic analysis is carried out in order to prevent seismic waves arising from fault-slip from reflecting on the model boundaries. The timestep used for the dynamic analysis is automatically calculated based on the volume of each zone of the model, P-wave velocity obtained from rockmass mechanical properties and the face area of each zone (Itasca, 2009). Regarding the attenuation of elastic waves, local damping embodied in FLAC3D is taken. According to the manual of FLAC3D, coefficient of local damping is given as:

$$\alpha_L = \pi D \tag{6-13}$$

where α_L and D are the local damping coefficient and a fraction of critical damping. It operates by adding or subtracting mass from a grid point at certain times during a cycle of oscillation. Although local damping cannot capture the energy loss properly when wave forms are complicated, it enables frequency-independent damping. According to ABAQUS (2003), a fraction of critical damping for rock falls between 2 and 5 %. Thus, 5 % of critical damping is adopted for this study; and this damping system is deemed sufficient at this stage, considering the focus of the study.

6.6 Results and discussion

The results obtained from the second dynamic analysis, in which the collision and unloading of fault surface asperities are simulated with Equations 6-2 to 6-7, are discussed in this section. First, the propagation of seismic waves obtained

from Model 19 assuming a completely planar surface is depicted in Figure 6-7 in order to give a general idea of how seismic waves propagate from the hypocenter. Particle velocities excited by the seismic waves arising from the fault-slip are shown on sectional views of the model along y = 130 m. As shown in the figure, fault-slip takes place in the vicinity of the stope extracted immediately before the dynamic analysis. The maximum particle velocity is 0.99 m 2ms after the onset of the analysis. After 25 ms, the seismic waves propagate around the hypocenter extensively, and the maximum particle velocity decreases to 0.60 m/s. Finally, the propagation of seismic waves increases particle velocity across the whole model, and the maximum velocity drops to 0.08 m/s. This figure indicates that the particle velocity of the rockmass takes the maximum value immediately after the onset of fault-slip; and it follows that the particle velocity rapidly decreases as seismic waves propagate through the rockmass.

Figure 6-8 depicts the propagation of seismic waves for Model 2, which considers the collision and unloading of fault surface asperities. As shown in the figure, the maximum particle velocity for Model 2 is the same as that for Model 1 at the beginning of the dynamic analysis. However, it is seen from the figure that a difference in the maximum particle velocity between the models becomes evident as time goes by. 25 ms after the onset of the analysis, the maximum particle velocity increases rapidly to 2.90 m/s, and comparable high particle velocity continues at least until 50 ms. These particle velocities are significantly greater than those for Model 19, in which a planar surface is assumed. It is considered that the results reflect sudden stress relief due to the unloading of fault surface asperities. In other words, for Model 2, shear displacement increments around areas where the intense shock pulses generate become large enough that Equation 6-6 is applied instead of Equation 6-5. Although the maximum particle velocity eventually decreases to 0.47 m/s after 100 ms, the value is still greater than that for Model 19. These long-lasting high particle velocities could cause more deterioration of rockmass in the environs of the fault.

Peak particle velocities found from figures are 2.90 m/s and 0.99 m/s for Model 2 and 19 during the seismic events, respectively. Hence, the results suggest that a sudden stress drop due to the unloading of fault surface asperities could cause extremely high particle velocities that induce severe damage to the rockmass. The simulated extremely high particle velocity coincides with that observed in deep gold mines (e.g. peak particle velocity of 3 m/s at Tau Tona gold mine and PPV of 2.3 m/s at Mponeng gold mine reported by Milev et al. (2002a))

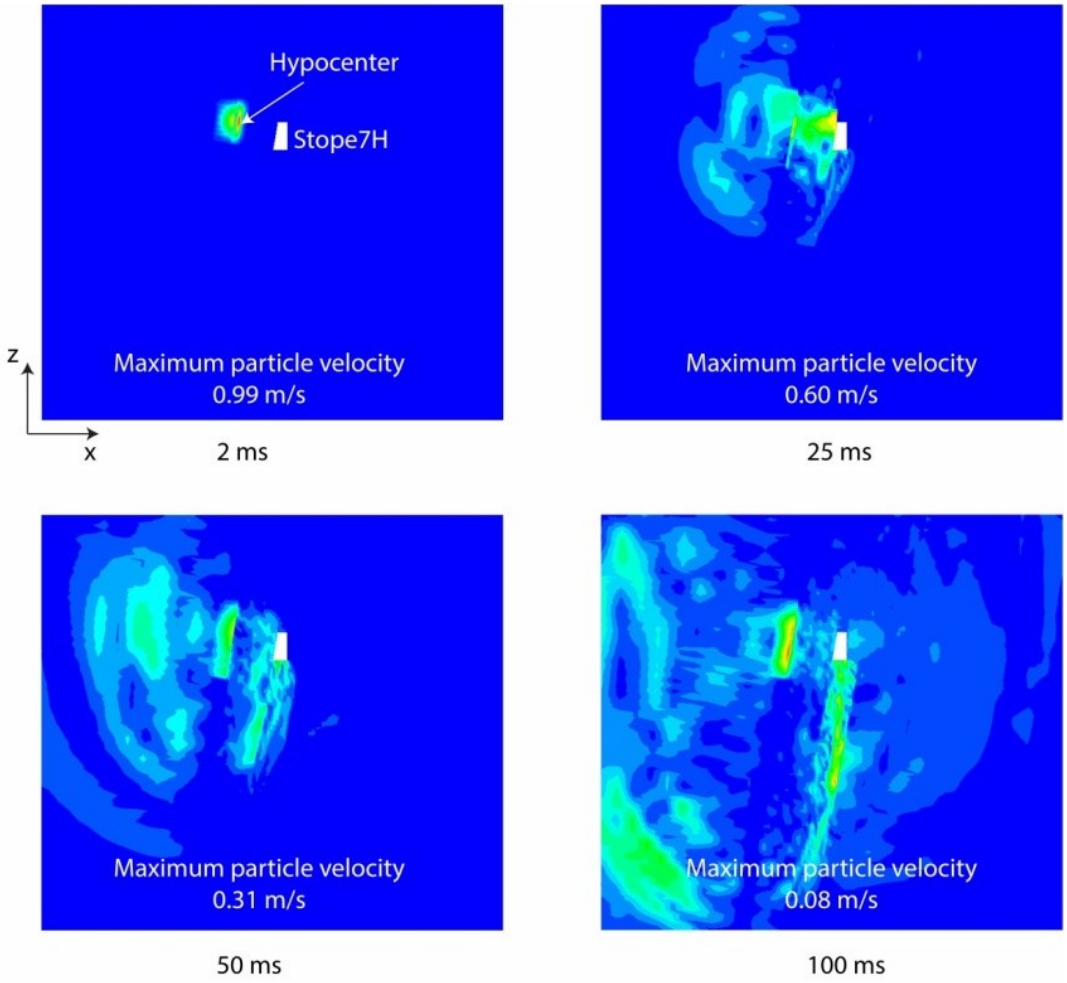

Figure 6-7: Particle velocities excited by propagation of seismic waves arising from fault-slip on sectional views along y = 130 m for Model 19

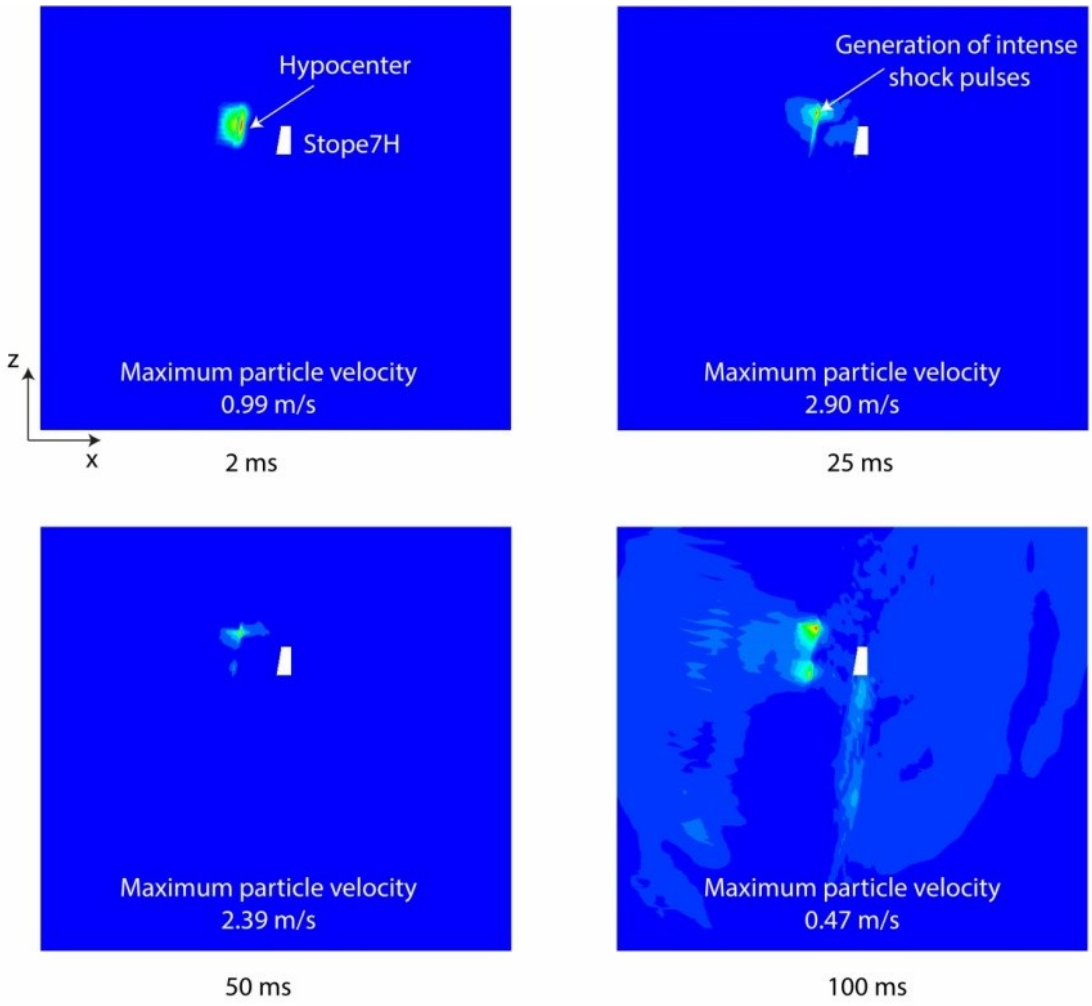

Figure 6-8: Particle velocities excited by propagation of seismic waves arising from fault-slip on sectional views along y = 130 m for Model 2

Results of the parametrical study conducted for the parameters in Table 6-3 are shown in Figure 6-9. In the figure, the maximum particle velocities at certain times for each model are compared with those for Model 2. Figure 6-9a shows the results obtained from models with different r_c in Equation 6-5, which denotes a ratio of asperity area responsible for the collision to the entire fault area. As can be seen from the figure, the maximum particle velocities for each model almost coincide. Although a slight difference in the maximum particle velocity amongst the models is observed, it can be negligible, considering absolute values of the particle velocities. Thus, these results indicate that the collisions of fault surface asperities during the fault-slip do not significantly affect the intensity of seismic

waves in terms of particle velocity, at least under the conditions shown in Table 6-3. The increase in normal stress due to the collision is also a function of the stiffness of surrounding rockmasses, K, and the stiffness of the fault, k_{ni}, as can be seen from Equations 6-2 to 6-4. For the parametrical study, K ranges from 0.05 GPa/m to 20 GPa/m, and k_{ni} varies between 0.1 GPa/m and 40 GPa/m. It is found from Figure 6-9e and 9f that the parameters also do not exert a large influence on the intensity of seismic waves.

In contrast to these results, there are evident differences in the maximum particle velocities between models shown in Figures 6-9b, 6-9c, and 6-9d. Figure 6-9b shows results obtained from models with different r_m in Equation 6-6, which denotes a stress release rate during the unloading of fault surface asperities. For the parametrical study, rm ranges from 0.001 to 0.1. As shown in Figure 6-9b, the maximum particle velocity is 3.9 m/s 50 ms after the onset of dynamic analysis when r_m = 0.1 (Model 4). The particle velocity is almost 13 times higher than that of Model.19 at that time. Even in the case that r_m = 0.01, the particle velocity is still significantly higher than that obtained from Model 19. On the other hand, when r_m decreases to 0.001, the maximum particle velocities are approximately same as those for Model 19 shown in Figure 6-7. These results imply that the stress release rate, r_m, has a significant influence on the intensity of seismic waves, especially when the rate is large. These results further indicate the importance of carrying out numerical simulation that relates the stress release rate, r_m, to actual stress release that would take place along fault surface asperities, using a numerical model in which asperities are modelled on an actual size. When the relation is established, it is possible to estimate the high particle velocity excited by intense shock pulses accurately. Figure 6-9c shows the effect of asperity height, which varies between 1 mm and 20 mm for the parametrical study, on the intensity of seismic waves. It is found from the figure that the maximum particle velocities do not differ between the models until 2 ms. This is because the influence of collisions on the seismic waves is negligible as indicated in Figures 6-9a, 6-9e, and 6-9f. After 5 ms, the difference in the

maximum particle velocity between the models becomes clear. It is found from Figure 6-9c that particle velocity takes the peak value 10 ms after the onset of the analysis when H_a = 1 mm and 5 mm. On the other hand, when H_a = 10 mm, particle velocity reaches the peak value 25 ms after the onset of the analysis. In addition, when H_a = 20 mm, a significant increase in particle velocity is not observed during the dynamic analysis. It is considered that these characteristics reflect asperity length, L, since the unloading of fault surface asperities is simulated after shear displacement increments reach the asperity length (see Equation 6-6), which is dependent upon asperity height and asperity inclination angle. Therefore, a similar tendency can be found in Figure 6-9d, in which models with different asperity inclination angles are compared. As can be seen in the figure, in the case that asperity inclination angles are large, particle velocity takes the maximum value earlier, compared with the model with a low asperity inclination angle. More importantly, although the height and inclination angle of asperity contribute to the characteristics of seismic waves, peak particle velocity observed during the seismic events is not significantly affected by the parameters. For example, for Model 2, peak particle velocity is 2.90 m/s as shown in Figure 6-8; and for Model 8, peak particle velocity is 2.98 m/s. The difference in the particle velocity is 0.08 m/s, which is quite small when compared with the influence exerted by stress release rates as shown in Figure 6-9b.

Finally, peak particle velocity normalized on the basis of that for Model 19 is shown in Figure 6-10. The peak particle velocity represents the maximum particle velocity at the observation time shown in Figure 6-9 during seismic events. As discussed above, it can be seen from the figure that the influence of fault geometry, such as the height and inclination angle of asperity, on the intensity of seismic waves is not significant. For instance, although peak particle velocity for Model 8 is almost twice as large as that for Model 19, the difference is mainly due to stress release rates because there is not a large difference in peak particle velocity between Models 7 and 8 as shown in Figure 6-9c. Likewise, r_c

and the stiffness of surrounding rockmass and the fault do not have a large influence on peak particle velocity (see Models 1 to 3 and 11 to 18). Evidently, the most influential factor to peak particle velocity excited by seismic waves is a stress release rate, r_m. According to the figure, peak particle velocity for Model.4, in which r_m is set at 0.1, is approximately 3 times larger than that for a planar surface. The high peak particle velocity is considerable and large enough to cause significant damage to rockmasses (Saharan, 2004), thereby suggesting that conducting further analysis to relate a stress release rate with an actual stress release rate is of paramount importance. Although the results obtained from this study show that asperity surface geometry does not significantly affect the characteristics of seismic waves in terms of peak particle velocity, the stress release rate is presumed to be inherently related to fault surface geometry. Due to the limitations of numerical simulation approach attempted for this study, the relation cannot be obtained from the conducted analyses. Hence, further analysis is required for a better understanding of the relation. When the relation is developed, the simulation technique proposed in the present paper can be an efficient method to estimate extremely high peak particle velocity that could be induced by seismic waves arising from fault-slip that occurs along a fault with significant asperities.

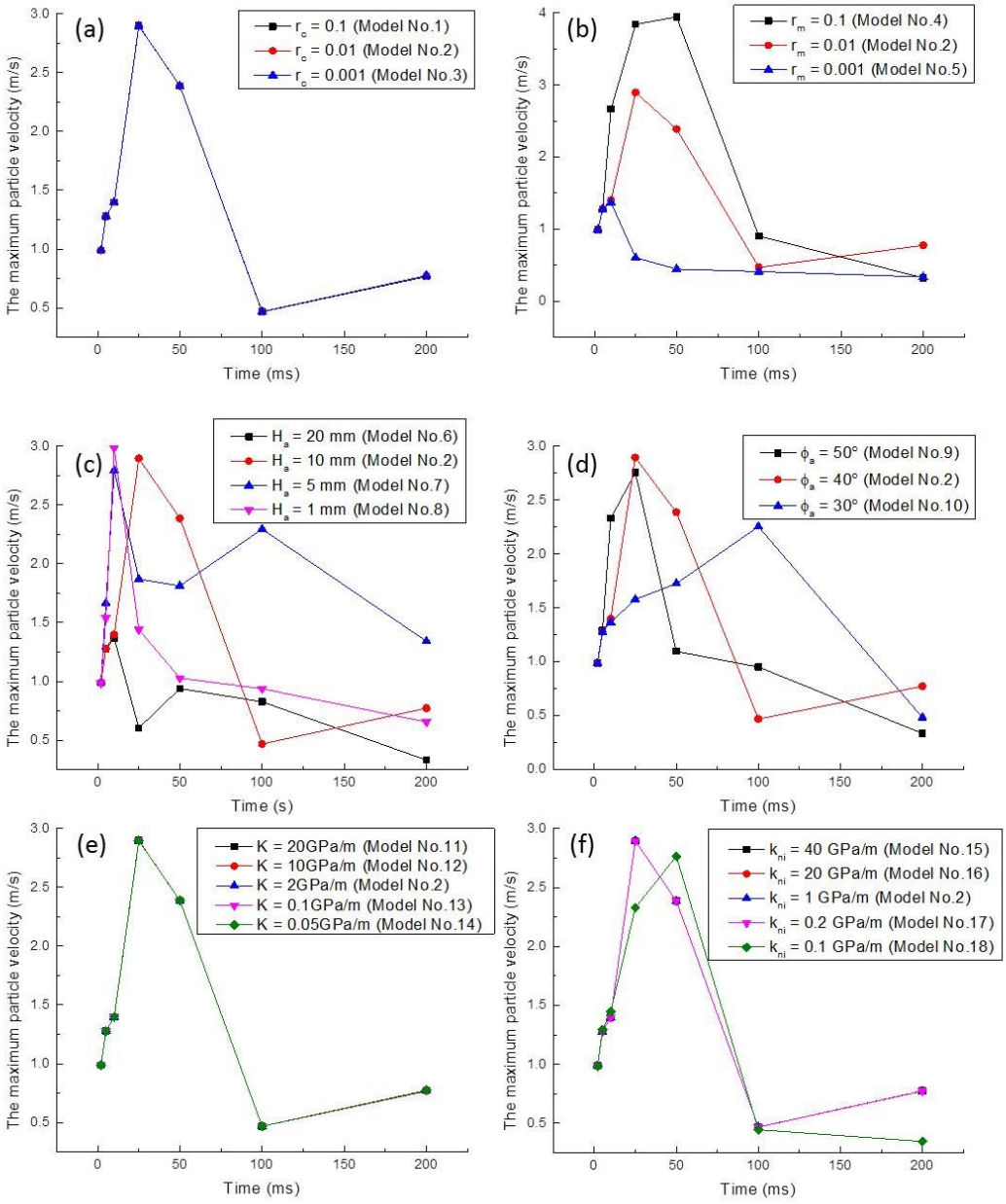

Figure 6-9: Effect of fault-surface properties and boundary conditions on the intensity of seismic waves: a) effect of asperity area ratio, b) effect of stress release rate, c) effect of asperity height, d) effect of asperity inclination angle, e) effect of the stiffness of rockmass, and f) effect of the initial shear stiffness of asperities

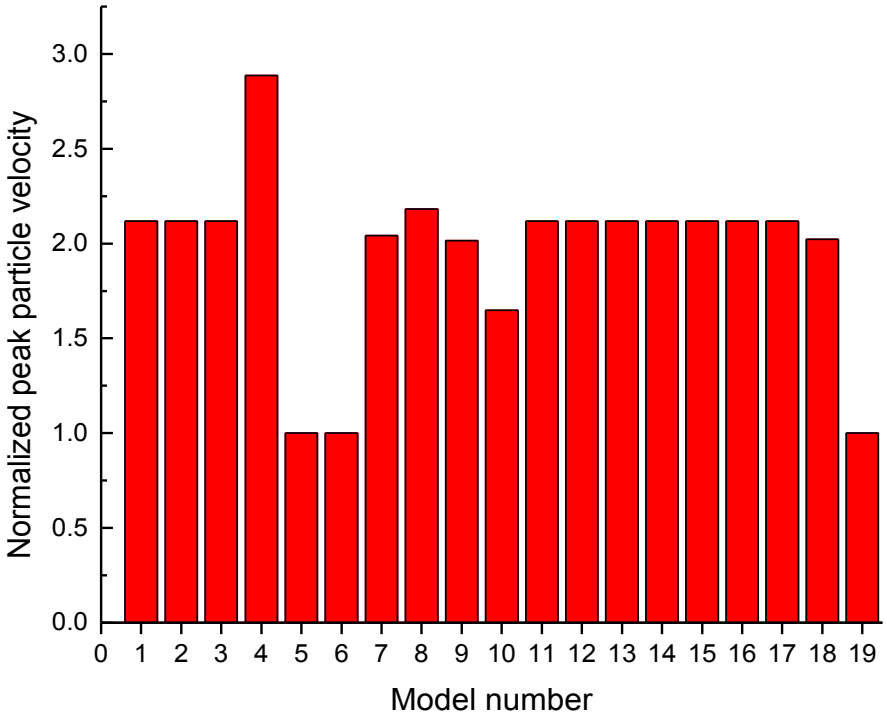

Figure 6-10: Peak particle velocity normalized on the basis of Model 19

6.7 Conclusions

The effect of fault surface asperities on the intensity of seismic waves arising from fault-slip is examined with a mine-wide model encompassing a fault in the vicinity of a multi-level mining zone of a steeply dipping tabular orebody. In order to simulate fault-slip, Barton's model is newly incorporated into FLAC3D with C++ programming language. In addition, Saeb and Amadei's model is implemented to simulate the collision of fault surface asperities during the fault-slip. A sudden stress drop due to unloading of the asperities during fault-slip is simulated by implementing a stress release rate into the constitutive model. After initiating stress re-distribution due to a sequence of stope extractions with static analysis, dynamic analysis takes over out with the newly developed constitutive models.

The results obtained from the analysis show that the effect of collision of fault surface asperities on the intensity of seismic waves is negligible. On the other hand, the unloading of fault surface asperities has a significant influence on the characteristics of seismic waves when the stress release rate is large. The results also show that high particle velocity could continue for a long period of time due to the unloading, which could cause the deterioration of the rockmass. More importantly, when the stress release rate is high, the peak particle velocity could be three times higher than that obtained from a model with planar surface. In addition, the velocity is found to be high enough to cause severe damage to rockmasses. It can be concluded that the stress release rate is the most influential factor that affects the intensity of seismic waves. However, due to the limitation of numerical simulation approach employed in the present study, the relation between the stress release rate and the geometry of the asperities of the undulating fault surfaces is still unclear. Hence, conducting further study is recommended in order to establish that relation. When such relation is derived, the simulation technique proposed in the present study can be quite an efficient method to estimate peak particle velocity excited by intense shock pulses arising from the unloading of fault surface asperities.

CHAPTER 7

Back analysis of fault-slip in burst prone environment

7.1 Abstract

In deep underground mines, stress re-distribution induced by mining activities could cause fault-slip. Seismic waves arising from fault-slip occasionally induce rock ejection when hitting the surfaces of mine openings, and as a result, severe damage could be inflicted. In general, it is difficult to estimate fault-slip-induced ground motion in the vicinity of mine openings because of the complexity of the dynamic response of faults and the presence of geological structures. In this paper, a case study is conducted for Garson Mine, Sudbury, Canada, which is known for its seismic activities. Using a microseismic database collected from the mine, a back analysis of fault-slip is carried out with mine-wide numerical model. The back analysis is conducted to estimate the physical and mechanical properties of causative fracture or shear zones. One large seismic event is selected for the back analysis after performing microseismic analysis to detect a fault-slip related seismic event. In the back analysis, the shear zone properties are calibrated with respect to moment magnitude of the seismic event and peak particle velocity (PPV) recorded by strong ground motions sensor. The calibrated properties are then validated through comparison with peak ground acceleration recorded by accelerometers. Lastly, ground motion in active mining areas is estimated by conducting dynamic analysis with the calibrated values. The present study indicates that it would be possible to predict the magnitude of seismic events that might occur in the near future by applying the calibrated properties to the numerical model. Although the case study is conducted for Garson Mine, the same methodology can be applied to other mines suffering from fault-slip related seismic events.

7.2 Introduction

Fault-slip that occurs in underground mines occasionally entails intense seismic waves, which could inflict severe damage when hitting the surfaces of nearby mine openings (Ortlepp, 2000). The damage to rockmasses can be predicted on the basis of peak particle velocity (PPV) excited by the seismic waves (Saharan, 2004), seismic moment and seismically radiated energy of the seismic events (Hedley, 1992). To date, a number of studies have been conducted numerically and analytically to estimate these values. McGarr (2002) proposed a formulation to predict near-field PPV provided that seismic efficiency of mining-induced tremors is less than 6 % (McGarr, 1999). Back analysis to simulate seismic source parameters has been also carried out by many researchers. Hofmann and Scheepers (2011) simulated the fault-slip area by calibrating the cohesive strength of a causative fault with seismic moment. Potvin et al. (2010) and Sjoberg et al. (2012) conducted back analysis with seismic moment, considering an increase in shear displacements on causative geological structures for each mining stage.

Although the seismic moment of fault-slip related seismic events and near-field particle velocity excited by seismic waves might be approximated with the aforementioned methods, it is not still straightforward to estimate PPV in the vicinity of mine openings for the following reasons. First, the formulation proposed by McGarr (2002) is applicable only in the vicinity of source regions; hence ground motion in active mining areas cannot be estimated in the case that seismic events occur remotely from the mining areas due to regional unclamping (Castro et al., 2009). Second, the back analyses have been carried out under static conditions by means of the classical Mohr-Coulomb criterion, which indicates that the results obtained from the back analyses are not validated with respect to the dynamic behaviour of rockmass, such as PPV. Furthermore, as reported by Ryder (1988), the cause for fault-slip in underground mines is a sudden stress drop induced by asperity shear on fault surfaces. The classical

Mohr-Coulomb criterion cannot take fault surface asperities into account. As the seismic source parameters of fault-slip is strongly dependent on the fault surface properties (Sainoki & Mitri, 2013), it is postulated that the intensity of seismic waves is also affected by the fault surface properties. Static analyses adopted in the previous studies cannot simulate either propagation of the seismic waves or ground motion excited by the seismic waves.

For these reasons, there is still a strong need to develop a methodology to simulate fault-slip that occurs in underground mines with dynamic analysis, so that the magnitude of particle velocity excited by seismic waves within active mining areas can be estimated. Based on the estimated particle velocity, selection of appropriate support system to control ground motion due to the seismic waves can be achieved. This is of paramount importance for stable production and safety for mine workers.

In the present study, back analysis of a fault-slip related seismic event that occurred in Garson Mine, Sudbury, Canada is attempted in a dynamic condition, considering asperity shear as the cause for the seismic event. The back analysis is carried out with respect to the physical and mechanical properties of causative fracture/shear zones within which the seismic event took place. Moment magnitude (i.e. seismic moment) estimated from recorded wave forms in the mine and far-field PPV recorded by a strong ground motion sensor are used for the calibration of the properties. The calibrated values are then validated with ground acceleration recorded by accelerometers.

7.3 Garson Mine

Garson Mine is located in Sudbury, Ontario, Canada, where copper-nickel orebodies have been mined out since 1898. As of now, the upper orebodies above 4700 level (1432 m below the surface) have been fully exploited. Mining is then being conducted from 5100 level to 4700 level in accordance with mining

sequences as per bottom-up sublevel stoping method, which is a general mining method for a steeply dipping, tabular ore deposits (Zhang & Mitri, 2008). Figure 7-1 shows general geology of Garson Mine at 5100 level. As shown in the figure, there are two orebodies called #1-Shear and #4-Shear, in which stopes are being extracted. #1-Shear extends from surface to 5600 level and dips generally at 75˚ to south with an average width of 9 m. #4-shear orebody extends from 2800 level to at least 6000 level and dips sub-parallel to the #1-Shear orebody at 60˚ to south. As another important feature of Garson Mine geology, there are shear/fracture zones identified in the vicinity of the orebodies, which are shown in the figure and referred to as 2500-Shear. The width of 2500-Shear ranges approximately from 15 m to 150 m, and the shear/fracture zones strike north-west and dip approximately 85˚ to east.

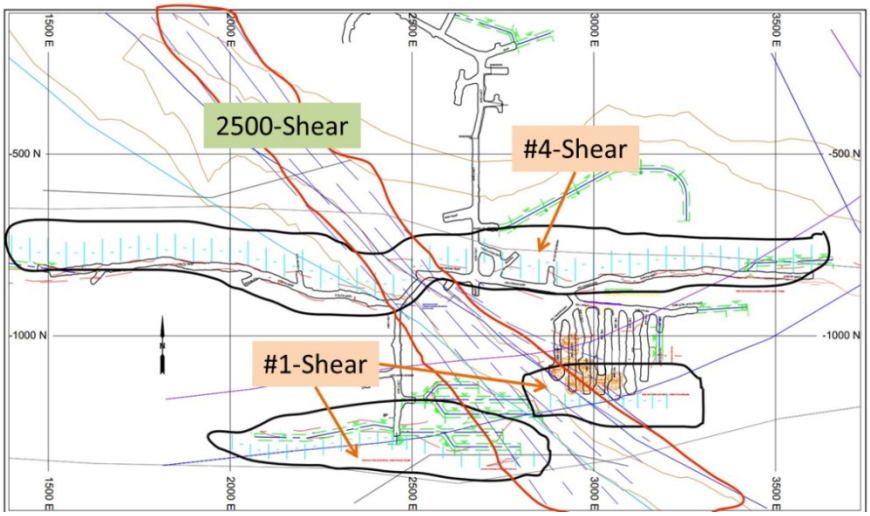

Figure 7-1: Plan view at 5100 level showing orebodies and shear zones

Rocks in Garson Mine are generally classified into five types, namely Norite (NR), Greenstone (GS), Olivine Diabase (OLDI), Massive Sulphide (MASU), and Metasediment (MTSD). Norite and Metasediment are generally located in footwall and hanging wall, respectively. Greenstone appears to be a subdivision of the more massive rock within the metasediments of the hanging wall, and the orebodies consist of Massive Sulphide. The Olivine Diabase, which is depicted as lines colored in brown in Figure 7-1, is a bifurcated dyke and can be divided

into two units, namely north limb and south limb. The south limb runs sub-parallel to 2500-Shear at 5100 level and crosses the orebodies. The detailed rockmass properties are shown in a later section.

7.4 Microseismic analysis of Garson Mine

Microseismic activities in Garson Mine have been recorded for more than 5 years with microseismic monitoring system that consists of 29 uniaxial accelerometers, 5 triaxial accelerometers and one strong ground motion sensor (4.5Hz geophone). The accelerometers, which are installed near active mining areas, are capable of measuring acceleration up to 1.3 m/s2. The strong ground motion (SGM) sensor is, on the other hand, installed near the ground surface and capable of capturing large seismic events with low frequencies, of which moment magnitude ranges from 0 to 3. By utilizing these types of instruments, both of small and large seismic events can be detected, and seismic source parameters for each seismic event are calculated on the basis of wave forms recorded by the microseismic monitoring system. The calculations are conducted with ESG microseismic software (ESG, 2011).

There are a number of sources for seismic events in underground mines, such as production blasts and rockbursts. Although seismic events resulting from the blasts can be distinguished from the other seismic events with ESG software, it is still necessary to specify fault-slip related seismic events from amongst seismic events including both of strain and fault-slip burst. This is because the back analysis conducted in the present study aims at simulating a fault-slip related seismic event and estimating the properties of shear/fracture zones where the seismic event took place. To do so, the present study adopts magnitude time history (MTH) analysis and time between events (TBE)-rate chart proposed by Hudyma and Beneteau (2012). The detailed descriptions of the methods are provided in the author's publications. With the methods, the sources of seismic events can be identified for each cluster of seismic events that occur

in the same area. Hence, as the first step to apply the methods, seismically active zones in Garson Mine are divided into 6 regions as shown in Figure 7-2a.

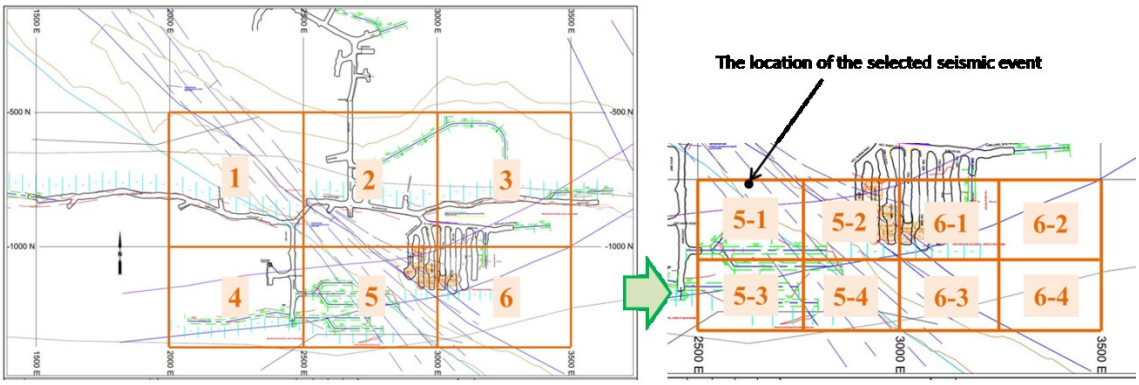

Figure 7-2: Divided regions for MTH analysis and TBE-rate chart: (a) Initially divided regions; (b) Additionally divided regions for more detailed analysis

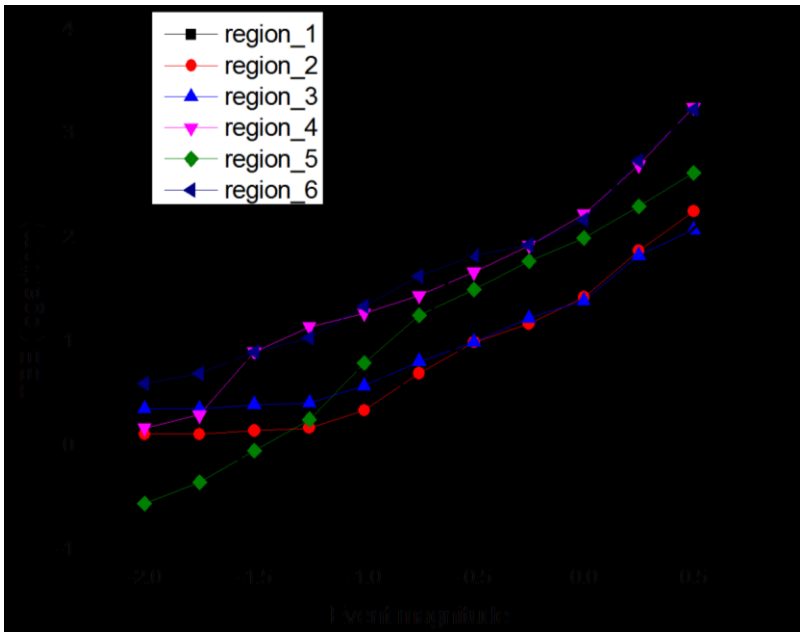

Figure 7-3: TBE-rate chart

TBE-rate chart is then created for the 6 regions, which is shown in Figure 7-3. According to Hudyma and Beneteau (2012), low TBE-rate indicates seismic events induced by stress re-adjustments that occur immediately after mine developments and mining activities. On the other hand, high TBE-rate can be

considered seismic events resulting from rockmass shearing and fracturing. It is found from the figure that clusters of seismic events that occurred in regions 5 and 6 show comparatively high TBE-rates for the whole range of event magnitude. Thus, the regions are further divided into small zones to carry out more detailed analysis as shown in Figure 7-2b. MTH analysis and TBE-rate chart are applied to the additionally divided zones. As a result, it is found out that seismic events that occurred in regions 5-1, 5-2, and 6-1 seem to be caused by rockmass fracturing and shearing. Considering the fact that these regions include 2500-Shear, the results of the analyses appear to be quite reasonable. Based on that, a large seismic event that occurred in region 5-1 on March 27th in 2012 has been chosen for the back analysis. Table1 shows the location and source parameters of the seismic event, which have been estimated on the basis of recorded wave forms by means of ESG software.

Table 7-1: Seismic source parameter of the seismic event selected for back analysis

	North	East	Depth (m)	Seismic moment (N·m)	Moment magnitude	Source radius (m)
Source information	-1001	2602	1520	1.6×10^{11}	1.47	46.7

7.5 Numerical model

Mine-wide Garson Model generated by Shnorhokian et al. (2013) with FLAC3D to conduct stress analysis is utilized for the present study. As explained in the precious section, back analysis is carried out for the seismic event that occurred within 2500-Shear. Hence, there is a need to model 2500-Shear as causative shear/fracture zones, which are not considered in the previous study. To do so, constitutive models that were used to conduct the stress analysis

(Shnorhokian et al., 2013) have been changed in order to model 2500-Shear. In this section, first, the geometry of mine-wide Garson Model is shown. Afterwards, the detailed descriptions of the constitutive models that are newly applied to mine-wide Garson model are provided.

7.5.1 Model descriptions

Figure 7-4 shows the geometry of mine-wide Garson model and its geology. As shown, a very large model has been created in order to generate pre-mining stress state and to prevent model boundaries from affecting analysis results. The width, height, and length of the model are 1220 m, 610 m, and 1220 m, respectively. Within the model, 2500-Shear has been newly modelled; and the shear zones are 60 m wide, strike north-west and dip at 85° to east. The source region of the seismic event are modelled inside of 2500-shear as shown in Figure 7-5. It is presumed that the selected seismic event took place by failure along pre-existing weak planes within the shear/fracture zones. Thus, the dip and dip angle of the source region (failure plane) are assumed to be the same as those for 2500-Shear. The dimensions of the source region are determined from the source radius shown in Table 7-1.

As can be seen in Figure 7-4, orebodies are located around the center of the model. Stopes are modelled within the orebodies and extracted in accordance with mining sequences of Garson Mine. Careful consideration has been given in generating meshes around the active mining areas, where zones have been densely discretized, while in the vicinity of the model boundaries the number of grid point is reduced in order to decrease calculation time. The total number of zones and grid points in the model is 1146310 and 1186080, respectively.

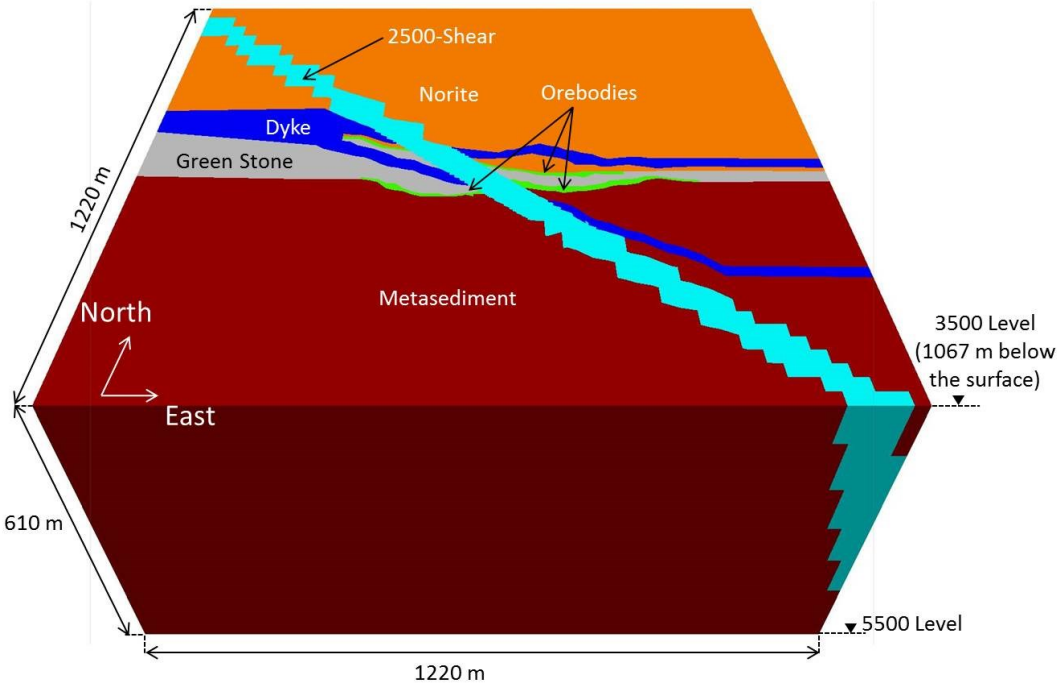

Figure 7-4: Model geometry and geology in Garson Mine

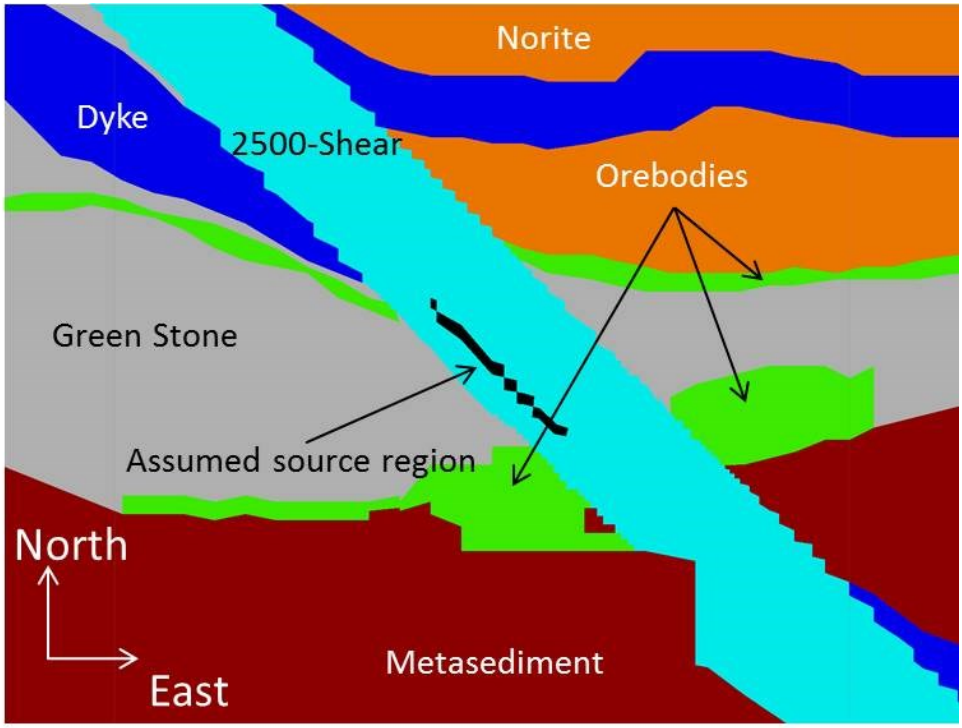

Figure 7-5: Plan view of 5000 level showing source regions

7.5.2 Constitutive models applied to zones within 2500-Shear

Pre-mining stress state in the mine-wide Garson Model has been simulated with boundary traction method (Shnorhokian, Mitri, Thibodeau, & Moreau-Verlaan, 2012; Shnorhokian et al., 2013). For the analysis, isotropic elastic models were applied to the entire zones of mine-wide Garson Model. The boundary traction method makes it possible to simulate high stress state resulting from a difference in the stiffness of rocks. In Garson Mine, it has been shown that dyke shown in Figure 7-4 plays an important role in causing seismic events (Bewick et al., 2009) as it has high stiffness, compared to those of the surrounding rockmasses. Although the high stress state within dyke has been successfully simulated with the boundary traction method, it has been additionally found out in the present study that slip potential defined by the difference between the maximum shear strength and shear stress takes negative values with respect to the strike and dip of 2500-Shear in the source region of the seismic event selected for the back analysis. It indicates that any fault-slip related seismic events never happen in the region. Hence, in the present study, further analyses have been conducted in order to simulate high slip potential within the source region; and it is found out that a difference in shear stiffness generates high slip potential within the source region. According to Bandis et al. (1983) and Brady and Brown (1993), shear stiffness of rockmasses including joints are strongly dependent on joint spacing and joint surface roughness. Therefore, it is presumed that shear stiffness of shear/fracture zones increases with the increasing joint roughness and joint spacing. Hence, it is postulated that high slip potential had been generated within the source region prior to the occurrence of the seismic event due to the difference in shear stiffness resulting from either joints with significantly rough surfaces or wide joint spacing, compared to those of the surrounding regions.

In order to simulate the difference in shear stiffness, a transversely anisotropic model, which was initially developed by Bruggeman (1937) and used

to simulate fault zones (Ivins & Lyzenga, 1986), is applied to the entire zones within 2500-Shear, excluding the source region of the seismic event. For the source region, it is necessary to apply a constitutive model that is capable of simulating fault behaviour during fault-slip. According to Ryder (1988), fault-slip in underground mines is driven by a sudden stress drop due to breakage of asperities on fault surfaces, although stress re-distribution resulting from mining activities is the trigger for the fault-slip. To date, a number of shear strength models that allow for the physical properties of fault surfaces, such as roughness and asperity height, have been developed (Barton et al., 1985; Barton & Choubey, 1977; Ladanyi & Archambault, 1970). Sainoki and Mitri (2013) incorporated Barton's shear strength model into a ubiquitous joint model of FLAC3D with C++ programming language and simulated fault-slip induced by stope extraction, considering asperity shear. In the present study, the same constitutive model is applied to zones within the source region in order to simulate fault-slip due to asperity shear.

Barton's shear strength model used for the ubiquitous joint model is expressed as:

$$\tau_{\max} = \sigma_n \left(JRC \log\left(\frac{JCS}{\sigma_n} \right) + \phi_b \right) \tag{7-1}$$

where τ_{max} and σn represent the maximum shear strength and normal stress acting on a joint, respectively; and *JRC*, *JCS* and ϕ_b represent joint surface roughness, joint wall compressive strength and basic friction angle, respectively. As can be seen from Equation 7-1, the shear strength model can take joint surface roughness into consideration. It is also found from the equation that the maximum shear strength derived from Barton's model is always greater than that obtained from Mohr-Coulomb failure criterion when cohesive strength = 0. During dynamic analysis to simulate fault-slip, when shear stress on failure planes

exceeds the maximum shear strength determined by Equation 7-1, *JRC* in the equation is changed to 0 since asperities on the failure planes are assumed to be sheared off due to slip. The residual stress arising from the change in *JRC* is the fault-slip driving force during the dynamic analysis. Regarding the ubiquitous joint model, its weak plane along which slip occurs is assumed to have the same dip and dip angle as those of 2500-Shear.

7.5.3 Rockmass properties

The same rockmass mechanical properties as those used by Shnorhokian et al. (2013) are applied to the rockmasses excluding the zones of 2500-Shear and the source region. The rockmass properties are shown in Table 7-2.

Table 7-2: Mechanical properties of rockmasses in Garson Mine

	NR	OLDI	GS	MTSD	MASU
Modulus of elasticity (GPa)	56	86	65	45	44
Poisson's ratio	0.25	0.26	0.23	0.24	0.30

As mentioned above, a transversely isotropic model is applied to zones within 2500-Shear, excluding the source region of the seismic event, in order to simulate high slip potential conditions resulting from the difference in shear stiffness of rockmasses. By means of the constitutive model, shear moduli of rockmasses with respect to a plane with the same dip and dip angle as those for 2500-Shear are changed to small values compared to those of the surrounding rockmasses. Preliminary analysis was carried out to determine the shear moduli of rockmasses within 2500-Shear. During the analysis, pre-mining stress states were first simulated with the boundary traction method. Stopes in the orebodies were then extracted in accordance with mining sequences provided by the mine until the same period in which the seismic event occurred. The purpose of the

preliminary analysis is to examine slip potential; hence slip behaviour was not simulated within the source region. A number of models with different shear moduli were generated, and the analysis procedure was carried out for each model. It was found out from the analyses that slip potential of rockmasses within the source region became positive when shear moduli of rockmasses within 2500-Shear except the source region was one-tenth of rockmasses where it occurs. As reported by Morrow, Shi, and Byerlee (1982) and B. Budiansky and O'Connell (1976), cracks and fractures could decrease shear moduli of rockmasses up to one-fifteenth. In addition, Bandis et al. (1983) proposed an equation that relates joint surface roughness with the shear stiffness of the joint, and shear moduli of rockmass are directly affected by the shear stiffness of joints included in the rockmass. With the equations, it is readily found that the shear moduli of rockmasses could drastically change, depending on joint properties. Hence, the result obtained from the preliminary analysis is not an unreasonable value. Table 7-3 shows the shear moduli of rockmasses within 2500-Shear excluding the source region.

Table 7-3: Mechanical properties of rockmasses within 2500-Shear excluding source regions of the seismic event

	NR	OLDI	GS	MTSD	MASU
Shear modulus with respect to a plane with dip and dip angle of 85˚ and 45˚ (GPa)	2.3	3.4	2.6	1.8	1.7
Shear modulus for other direction (GPa)	23	34	26	18	17

For the source region, the ubiquitous joint model with Barton's model is applied. Hence, it is necessary to find basic friction angles of rockmasses with the region. In the present study, basic friction angles shown in Table 7-4 are estimated on the basis of publications (Alejano, Gonzalez, & Muralha, 2012;

Barton, 1973).

Table 7-4: Basic friction angles of rockmasses within source regions of the seismic event

	OLDI	GS
Basic friction angle (˚)	36	32

With back analysis carried out in the present study, determining the physical and mechanical properties of the causative shear/fracture zones, namely fault surface roughness and dynamic friction angle, is attempted. After determining the shear moduli of rockmasses within 2500-Shear except the source region, additional preliminary analysis was conducted while simulating fault-slip with the ubiquitous joint model. It was then found out that unrealistically small dynamic friction angle is required in order to simulate fault-slip of which magnitude coincides with that estimated from recorded wave forms. Dynamic friction angle is strongly dependent on slip rates during fault-slip. According to Yuana and Prakash (2008), the coefficient of kinetic friction of rock-analog materials ranges from 0.2 to 0.3 when slip rate is between 2 and 5 m/s. The experimentally obtained coefficient of kinetic friction is approximately equivalent to friction angles between 12˚ and 17˚. According to Dieterich and Kilgore (1996), when slip rates are less than 1 mm/s, the coefficient of friction of granite drops to 0.65, which is approximately equivalent to a friction angle of 33˚. In light of the knowledge, scaling factor is applied to the basic friction angles in Table 7-3 so that the dynamic friction angle calibrated with the back analysis falls into reasonable values. As a result of the preliminary analysis to determine the scaling factor, it was found out that reasonable dynamic friction angle is obtained when scaling factor is 0.8. Thus, the basic friction angles multiplied by 0.8 are applied to zones with the ubiquitous joint model.

7.5.4 Analysis condition of static and dynamic analyses

During static analysis to simulate pre-mining stress and stope extraction, model boundaries are fixed in the direction perpendicular to the boundary. For dynamic analysis to simulate fault-slip in the source region, the boundary conditions are changed to viscous in order to prevent the model boundaries from reflecting seismic waves arising from the fault-slip. The timestep used for the dynamic analysis is automatically calculated based on the volume of each zone of the model, P-wave velocity obtained from rockmass mechanical properties and the face area of each zone (Itasca, 2009). Regarding the attenuation of seismic waves, local damping embodied in FLAC3D is taken. According to the manual of FLAC3D, coefficient of local damping is given as:

$$\alpha_L = \pi D \tag{7-2}$$

where α_L and D are the local damping coefficient and a fraction of critical damping. It operates by adding or subtracting mass from a grid point at certain times during a cycle of oscillation. Although local damping cannot capture the energy loss properly when wave forms are complicated, it enables frequency-independent damping. According to ABAQUS (2003), a fraction of critical damping for rock falls into 2 to 5 %. Thus, 2 % of critical damping is tentatively adopted as an initial value. An appropriate damping coefficient is estimated later through the back analysis by comparing PPV computed from the dynamic analysis with a recorded value.

7.6 Back analysis

Figure 7-6 shows procedure of the back analysis. As shown in the figure, joint roughness coefficient (JRC) in Equation 7-1 and the dynamic friction angle of rockmasses within the source region are first assumed. Afterwards, static analysis is carried out, in which stopes are extracted in the orebodies in

accordance with mining sequences in the mine after simulating pre-mining stresses with boundary traction method. The mining sequences proceed until the same period, in which the seismic event took place. Based on stress state obtained from the static analysis, dynamic analysis is performed while simulating fault-slip in the source region by changing *JRC* to 0 for the zones where shear stress exceeds the maximum shear strength. On the basis of relative shear displacement increments and velocities of grid points obtained from the dynamic analysis, moment magnitude and peak particle velocity (PPV) are computed and compared with those estimated from recorded wave forms. If the values do not coincide, analysis is conducted again from the static analysis, assuming different rockmass properties. The back analysis is carried out until the most appropriate properties are estimated. Afterwards, validation of the calibrated values is conducted using ground peak acceleration observed by accelerometers.

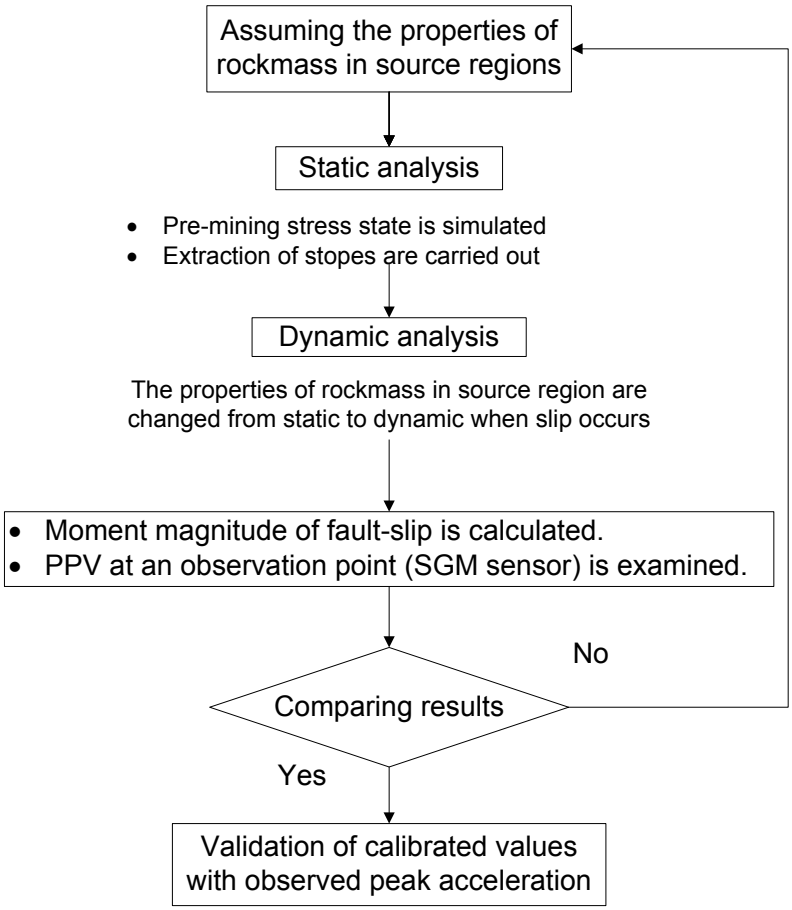

Figure 7-6: Procedure of back analysis

7.6.1 Calibration with moment magnitude

In the present study, the source region is modelled by means of the ubiquitous joint model. When the assumed failure plane is completely parallel to faces of cube-shaped zones, seismic moment of fault-slip induced during the dynamic analysis can be computed as follows.

$$u = \gamma a \tag{7-2}$$

$$D = \frac{\sum\left(u \times a^2\right)}{\sum a^2} = \frac{\sum\left(\gamma a \times a^2\right)}{\sum a^2} \tag{7-3}$$

$$M_s = DAG = \frac{\sum\left(\gamma a \times a^2\right)}{\sum a^2} \times \sum a^2 \times G = \sum\left(\gamma V\right)G \tag{7-4}$$

where u, γ, and a in Equation 7-2 represent a relative shear displacement increment, shear strain increment on the failure plane and length of the cube-shaped zone. A, D, V, and G represent slip area, average shear displacement, volume of the zone, and shear modulus, respectively. Although the assumed failure plane that has the same dip and dip angle as those of 2500-Shear is not parallel to any faces of zones in the source region, Equation 7-4 is employed to approximate the seismic moment as it is not possible to compute accurate seismic moment for the numerical model.

Table 7-5 shows the calibrated properties and moment magnitude computed from numerical models using the calibrated values. As shown in the table, dynamic friction angles have been determined for *JRC* of 0, 5, and 10 so that computed moment magnitude coincides with that estimated from recorded wave forms. It should be noted that it is impossible to determine only one combination of *JRC* and the dynamic friction angle on the basis of moment magnitude because moment magnitude obtained from numerical analysis can be adjusted

by changing the combinations as shown in the table. Hence, further calibration is carried out using PPV obtained from strong ground motion (SGM) sensor.

Table 7-5: Calibrated *JRC* and dynamic friction angle

Model No.	*JRC*	Dynamic friction angle (˚)	Moment magnitude
1	0	23	1.51
2	5	22	1.42
3	10	19	1.50

7.6.2 Calibration with peak particle velocity

In order to determine the most appropriate combination of *JRC* and dynamic friction angle, PPV has been examined. As the SGM sensor that records ground velocity is installed close to the ground surface which is outside of the generated numerical model, PPVs on a line between the locations of the SGM sensor and hypocenter of the seismic event are investigated for each numerical model using the calibrated properties shown in Table 7-4. Figure 7-7 shows PPVs on the line when *JRC* = 0 and dynamic friction angle = 23˚. As shown in the figure, PPV is investigated at six observation point on the line. In order to extrapolate PPV at the location of SGM sensor, many fitted curves are tentatively generated employing various kinds of functions, such as polynomial and exponential ones. As a result, power functions are found to be the most suitable to simulating seismic wave attenuation within the numerical model. Squared coefficient of correlation of the fitted curve shown in the figure is approximately 0.999. Based on the fitted curve, PPV at the location of SGM sensor can be extrapolated.

Likewise, PPV at the location of SGM sensor is calculated for *JRC* = 5 and 10. Additionally, for each model, dynamic analysis is performed changing damping coefficient as damping exerts a large influence on propagation of seismic waves.

Figure 7-8 summarizes the results. It is found from the figure that PPV is less than an observed value for the whole range of damping coefficient when *JRC* = 0. The result indicates that the combination of *JRC* = 0 and a dynamic friction angle = 23˚ is not appropriate, although moment magnitude obtained from the model is in a good agreement with that estimated from recorded wave forms. In the same way, although a model with *JRC* = 10 and 0% damping provides exactly the same PPV as the recorded value, 0% damping is unrealistic. Thus, the combination also appears not to be appropriate. Lastly, for a model with *JRC* = 5 and 0% damping, PPV extrapolated from results is greater than the observed value; and when damping is changed to 2 %, extrapolated PPV is less than the observed value. It indicates that PPV estimated from numerical analysis certainly coincides with the observed value when an appropriate damping is selected between 0 % and 2 % when *JRC* = 5 and a dynamic friction angle = 22˚.

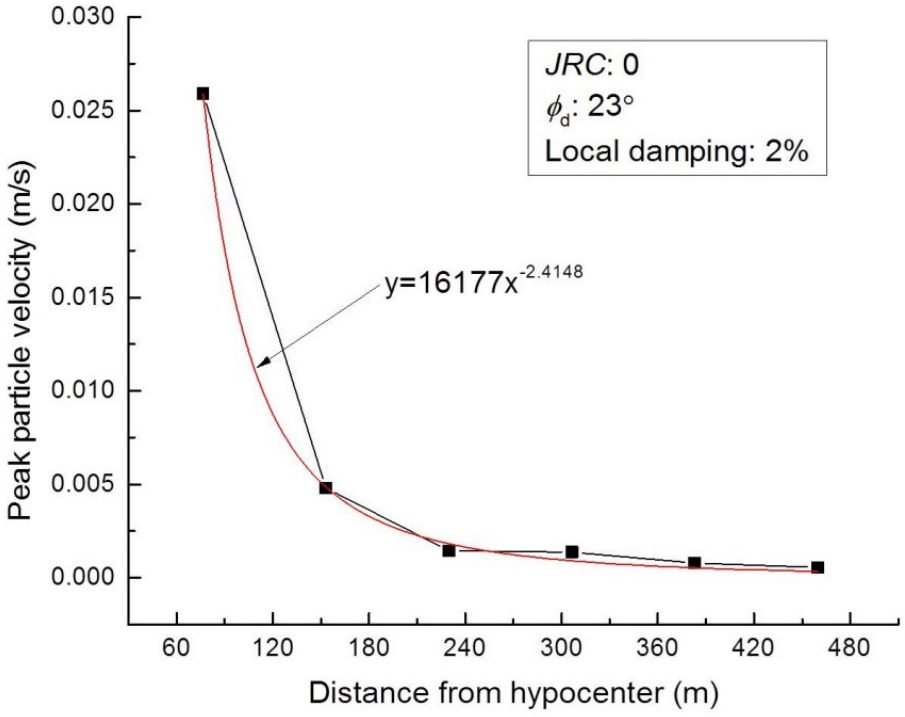

Figure 7-7: PPV on a line between SGM sensor and hypocenter of the seismic event

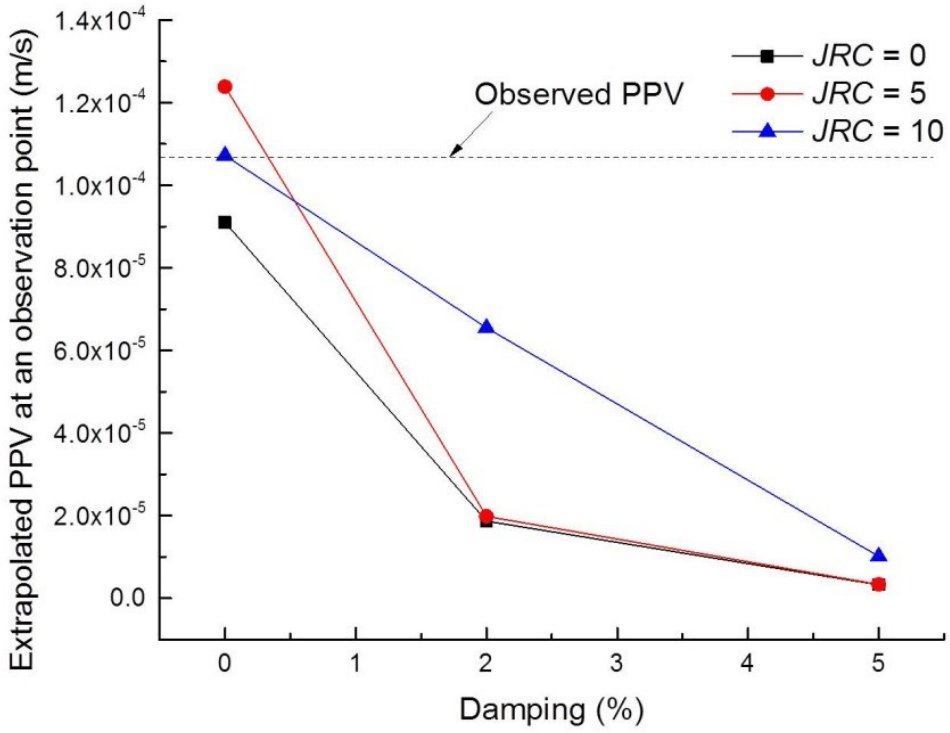

Figure 7-8: Extrapolated PPV at the location of SGM sensor

7.6.3 Validation of calibrated numerical model

JRC and a dynamic friction angle have been calibrated to 5 and 23˚, respectively, by means of the aforementioned methods. The next step is validating the calibrated properties. As mentioned in the previous section, ground acceleration is recorded in Garson Mine with 34 accelerometers installed in the environs of active mining areas, which are included inside of the mine-wide Garson Model. The peak ground acceleration recorded by the accelerometers is utilized for the validation by comparing that with results obtained from dynamic analysis using the calibrated properties. The maximum allowable acceleration for the installed accelerometers is 1.3 m/s2; hence unrealistically low peak acceleration was observed in the vicinity of the source region when the seismic event took place. Considering the fact, peak acceleration in the z-direction (depth direction) obtained from 6 uniaxial accelerometers located between 300 m and

780 m from the source region is used for the validation.

Figure 7-9 shows peak acceleration obtained from the dynamic analysis using the calibrated properties. The peak acceleration is determined on the basis of results until 300 ms after the onset of the dynamic analysis. Considering the distances between the accelerometers and source region, the observation time is deemed sufficient. Broken lines in Figure 7-9 show peak acceleration in z-direction, which is the same direction as that for the uniaxial accelerometers. As shown in the figures, dynamic analysis is performed for 0 % and 2 % damping. This is because appropriate damping appears to fall between 0 % and 2% as shown in Figure 7-8. Thus the upper and lower boundaries of the peak acceleration can be estimated by conducting dynamic analysis for the two damping conditions. It is found from Figure 7-9 that the observed peak acceleration falls exactly between the upper and lower peak acceleration obtained from the dynamic analysis except one location 500 m away from the source region, while peak acceleration in the z-direction obtained from the dynamic analysis is smaller than the observed values for the whole locations. As a reason why the peak acceleration in the z-direction obtained from the dynamic analysis is smaller than the observed values, it is postulated that initial motion of the simulated fault-slip differs from that of the actual seismic event, that is to say, fault-slip extended in directions different from the assumed failure plane during the seismic event in reality. Although the simulated peak ground acceleration in the z-direction is smaller compared to the observed values, these results indicate that a reasonable estimation of peak ground acceleration in the vicinity of active mining areas could be performed on the basis of the calibrated values since the simulated peak acceleration still falls into reasonable values. This validation then suggests that the calibrated properties and assumptions made for conducting the back analysis are reasonably acceptable.

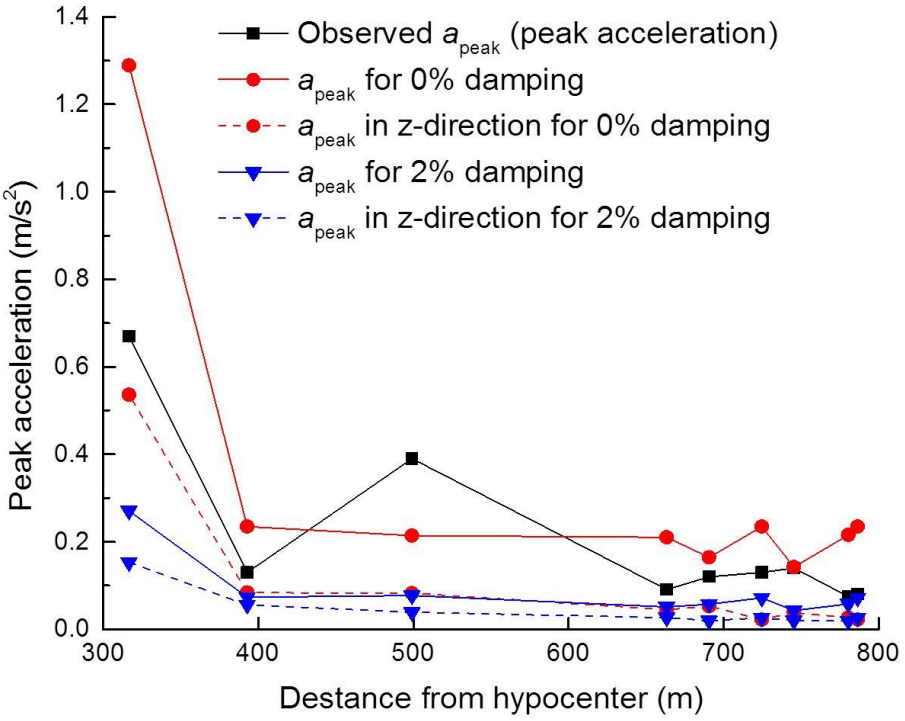

Figure 7-9: Comparison of peak ground acceleration

7.7 Simulating peak particle velocity in active mining areas

Lastly, propagation of seismic waves arising from the simulated seismic event is shown with respect to ground velocity. Although McGarr (2002) proposed the equation to estimate near-field peak particle velocity, the equation is valid only in the vicinity of source regions of seismic events provided that rupture velocity is known. In the present study, fault properties are calibrated in terms of moment magnitude and peak particle velocity, and the calibrated values are then validated with peak ground acceleration. Thus, quite reasonable ground motion could be estimated by performing dynamic analysis with the calibrated values. Figure 7-10 depicts ground motion induced by propagation of seismic waves arising from the seismic event simulated with the calibrated values. The illustrated area is from 2500E to 3500E and from -500N to -1500N, which correspond with the scale shown in Figure 7-1. An active mining area, where

stopes are extracted and mine openings are located, is also shown in the Figure 7-10. The simulated ground motion is considered the upper boundary as 0 % damping is taken for the analysis. As shown in the figure, seismic waves propagate through rockmasses from the source region to the active mining area as time passes. Based on this figure, the intensity of ground motion that could occur in the vicinity of the active mining area can be estimated; and on the basis of the information, proposing appropriate ground support system could be achieved. For this case, particle velocities of rockmasses within the active mining area reach approximately 0.6 m/s.

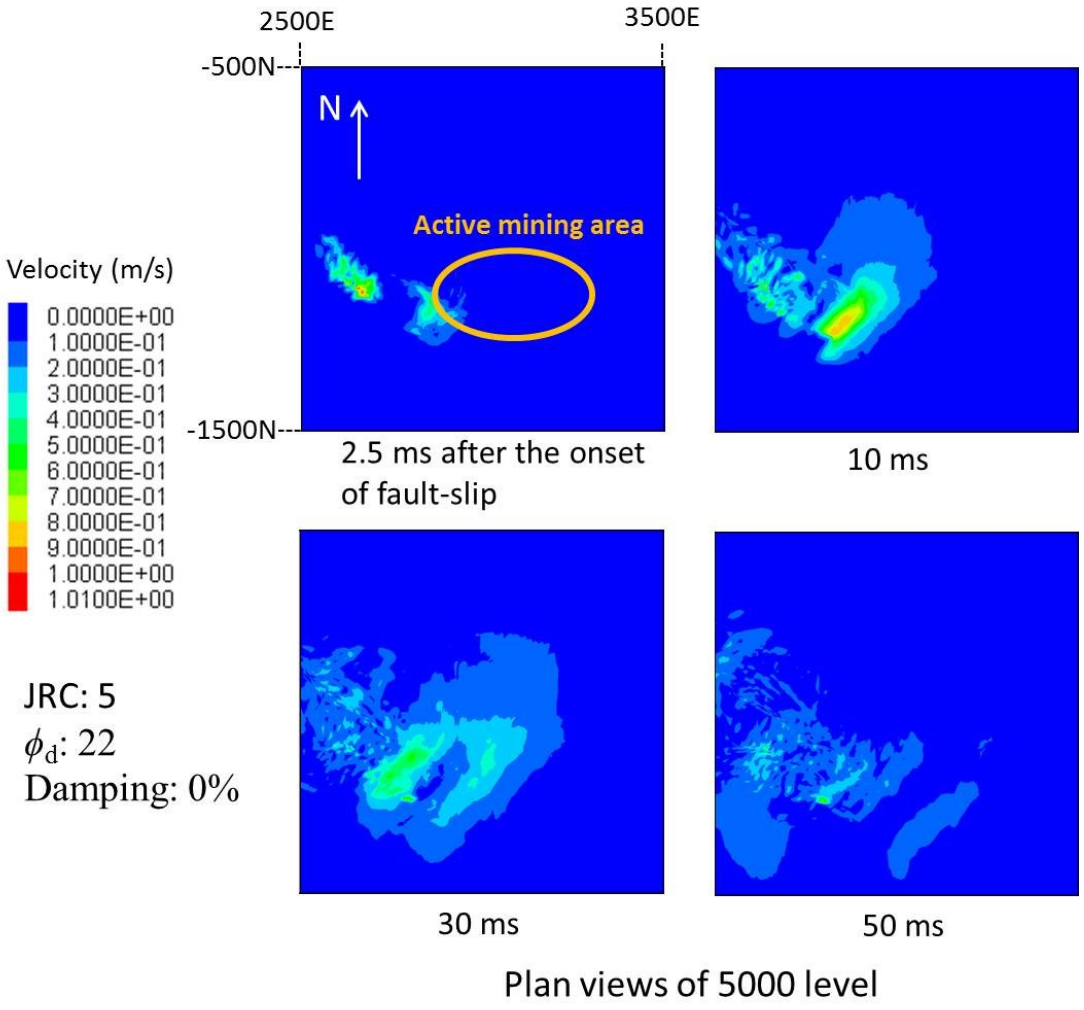

Figure 7-10: Ground motion induced by a seismic event simulated with calibrated values

7.8 Conclusions

In the present study, back analysis of a fault-slip related seismic event that took place within shear or fracture zones in Garson Mine is carried out. The shear zones excluding the source region of the seismic event are treated as transversely isotropic in order to simulate the difference in shear stiffness between the shear zones and source region. A ubiquitous joint model with Barton's shear strength model is applied to zones within the source region in order to simulate fault-slip. Back analysis is conducted by comparing moment magnitude of the seismic event and peak particle velocity recorded by strong ground motion sensor with results obtained from the dynamic analysis. As a result, surface roughness and a dynamic friction angle of failure plane are calibrated with the back analysis. In addition, the calibrated properties are validated with peak ground acceleration recorded by six uniaxial accelerometers. These results indicate that the simulation technique developed and employed for the back analysis could be useful in order to determine the physical and mechanical properties of causative shear/fracture zones in underground mines, which are generally difficult to obtain. By conducting the back analysis for other seismic events within the shear/fracture zones, the physical and mechanical properties of rockmasses within the zones could be statistically estimated. Thus, it would be possible to predict seismic events that could occur in response to planned mining activities. Although the present study is conducted for Garson Mine, the developed methodology can be applicable to other mines suffering from seismic events that occur especially in shear/fracture zones.

CHAPTER 8

Effect of slip-weakening distance on seismic source parameters of mining-induced fault-slip

8.1 Abstract

Fault-slip caused by mining activities in underground mines could cause severe damage to nearby mine openings due to seismic waves arising from the fault-slip. A better understanding of seismic source parameters, such as seismically radiated energy and the maximum slip rate, is of pivotal importance in estimating the damage induced by the fault-slip. It is widely recognized that dynamic behaviour of fault-slip is largely affected by slip-weakening behaviour. In the present study, the effect of the slip-weakening behaviour on the seismic source parameters of fault-slip is investigated using a mine-wide numerical model encompassing a fault running parallel to an orebody. A linear slip-weakening law is employed in a parametrical study with respect to characteristic slip-weakening distance, d_0, assuming two types of fault-slip: (a) zonal fault-slip taking place across the fault; (b) local fault-slip taking place within limited areas of the fault, i.e., it is assumed that fault-slip is arrested by surrounding rockmasses. Results obtained from the dynamic analysis indicate that seismically radiated energy and slip rates are significantly affected by d_0 for both types of fault-slip. On the other hand, the seismic moment is susceptible to d_0 only for zonal fault-slip, given that d_0 is smaller than the maximum shear displacement increment during the fault-slip. These results imply that considering slip-weakening distance is critical in estimating seismically radiated energy and slip rates, whereas slip-weakening behaviour might not have a large influence on seismic moment of local fault-slip.

8.2 Introduction

Stress redistribution induced by mining activities in underground mines could cause fault-slip inducing severe seismic waves, which occasionally inflict significant damage to mine openings (Blake & Hedley, 2003) . At present, a number of methods can be used to estimate the damage induced by seismic events in underground mines. For instance, a damage threshold to rockmasses has been proposed by Brinkmann (1987) on the basis of peak particle velocities induced by blasts. A relationship between magnitude of seismic events in underground mines and damage to rockmasses has also been proposed by Hedley (1992). Although the damage to rockmasses induced by seismic events can be estimated by means of these methods, it is indispensable that information on seismic source parameters, such as moment magnitude, seismically radiated energy, and peak particle velocity (PPV) be known prior to the use of the methods.

Numerical analysis is widely recognized as a tool to estimate seismic source parameters as well as mechanical properties of causative faults. Hofmann and Scheepers (2011) simulated fault-slip area by conducting back analysis while calibrating the cohesion and friction angle of a causative fault. Back analysis of fault-slip with moment magnitude has been carried out (Potvin et al., 2010; Sjoberg et al., 2012). In addition, determining the friction angle of a causative fault was attempted by Alber (2013). Although the aforementioned studies have been carried out for fault-slip that occurs in underground mines, the analyses were basically performed in static conditions, which cannot take into account the dynamic behaviour of fault-slip. As damage to rockmasses induced by seismic waves pertains to peak particle velocity of the rockmass, the dynamic behaviour of fault-slip, such as slip rates and seismically radiated energy, must be considered so as to estimate the damage properly.

The dynamic behaviour of fault-slip to be simulated is an intricate

phenomenon, which is dependent upon a number of factors, such as in-situ stress, materials existing on fault surfaces, geometries of fault surface asperities, and a slip rate. Significant attempts have been made in order to obtain dynamic friction laws capable of simulating a relationship among shear stress acting on a fault, shear displacement increments and slip rates during fault-slip (Dieterich, 1978; Dieterich & Kilgore, 1996; Ohnaka, 2003; Perrin et al., 1995; Ruina, 1983). The proposed dynamic friction laws can be generally classified into two types: slip-weakening friction laws and rate- and state-dependent friction laws. The former, which was initially proposed by Ida (1972), relates shear stress acting on a fault with shear displacement increments; characteristic slip-weakening distance, d_0, controls the change in shear stress (Bizzarri, 2011, 2012). The latter, which was initially established by Ruina (1983), relates the change in shear stress with a slip rate and state, which is a function of the slip rate. By means of the two types of dynamic friction laws, the simulation of fault-slip associated with earthquakes has been attempted by many researchers in the field of geophysics (Bizzarri, 2012; Oglesby & Mai, 2012; Tinti et al., 2004) for a better understanding of the dynamic behaviour of fault-slip, such as a relationship between slip rates and rupture velocities. While a number of studies have been carried out with respect to the dynamic behaviour of fault-slip in the field of geophysics, the friction laws have been barely applied to simulation of fault-slip taking place in underground mines; the classical Mohr-Coulomb criterion has been basically employed with static analyses for the aforementioned fault-slip studies in underground mines. Hence, the dynamic behaviour of fault-slip in underground mines is still unclear in mining contexts.

For this study, a linear slip-weakening law is adopted to simulate the dynamic behaviour of fault-slip that occurs in underground mines. Other dynamic friction laws such as non-linear slip-weakening laws (Chambon et al., 2006b) and rate- and state-dependent friction laws, require several constants, which are difficult to obtain without conducting experiments using rock samples. In addition, Ohnaka

(2003) indicates that a slip-dependent constitutive law is a unifying law that can simulate a broad range of shear failure from laboratory-scale frictional slip to field-scale rupture as an earthquake source. Considering these facts, employing the slip-weakening friction law and investigating the effect of characteristic slip-weakening distance on seismic source parameters of fault-slip are of paramount importance to gain fundamental knowledge about the dynamic behaviour of fault-slip taking place in underground mines, which leads to stable production and safe operation through proposing an appropriate support system for such seismic events.

8.3 Implementation of a linear slip-weakening law into FLAC3D

A linear slip-weakening friction law, which is widely used to analyze earthquake source dynamics (Bizzarri, 2011; Oglesby & Mai, 2012), is employed. Shear stress acting on a fault during fault-slip is linearly expressed as follows:

$$\tau = \left[\mu_u - \left(\mu_u - \mu_f\right)\frac{u}{d_0} \right]\sigma_n \quad u < d_0$$
$$\tau = \mu_f \sigma_n \quad u \geq d_0 \qquad (8\text{-}1)$$

where τ and σ_n is the maximum shear strength and normal stresses acting on the fault, respectively; μ_u and μ_f are the coefficients of static and kinetic friction, respectively; u and d_0 are dynamic relative shear displacement and characteristic slip-weakening distance, respectively. As can be seen from Equation 8-1, the shear stress acting on the fault decreases with the increasing relative shear displacement, which can be physically interpreted as shear of fault surface asperities, thermal weakening and thermal pressurization of pore fluid within the fault (Bizzarri & Cocco, 2006c; Ohnaka, 2003; Yuana & Prakash, 2008). When the relative shear displacement exceeds the characteristic slip-weakening distance, the maximum shear strength is a function of only the normal stress.

In order to apply Equation 8-1, we need to determine the coefficients of static and dynamic friction. For this study, Barton's shear strength model (Barton & Choubey, 1977) is employed for the static friction law, which can take fault surface roughness into consideration. The friction model is given as follows:

$$\tau = \sigma_n \tan\left[JRC \log_{10}\left[\frac{JCS}{\sigma_n} \right] + \phi_b \right] \tag{8-2}$$

where ϕ_b is a basic friction angle; *JRC* and *JCS* are joint roughness coefficient and joint wall compressive strength, respectively. According to Barton and Choubey (1977), a joint roughness coefficient varies from 0 to 20. Significant rough joint surfaces generated with tensile failure correspond with *JRC* of 20. When *JRC* is equal to 0, Equation 8-2 is equivalent to the classical Mohr-Coulomb failure criterion. By means of Barton's shear strength model, the maximum shear strength that increases with the degree of interlocking of joint surface asperities can be simulated. For the coefficient of dynamic friction, the classical Mohr-Coulomb failure criterion is adopted because the fault surface asperities are presumably sheared off due to collision of the asperities during fault-slip (Ryder, 1988). The dynamic friction law is given as follows:

$$\tau = \sigma_n \tan\phi_d \tag{8-3}$$

where ϕ_d is a dynamic friction angle. The coefficients of Equations 8-2 and 8-3 are substituted into μ_u and μ_f in Equation 8-1 as coefficients of static and kinetic friction. Sainoki and Mitri (2013); (Sainoki & Mitri, 2014b) simulated fault-slip induced by asperity shear with Barton's shear strength model and the classical Mohr-Coulomb failure criterion as static and dynamic friction laws, respectively, assuming perfect elasto-plastic behaviour to calculate residual stress. Likewise, for the present study, the calculation of the residual stress arising from the

change from static to kinetic friction during an increase in relative shear displacements is performed with the same method by obtaining derivatives of a failure criterion derived from Equation 8-1 with respect to the normal and shear stresses.

In order to analyze the dynamic behaviour of fault-slip with the slip-weakening friction law, FLAC3D code (Itasca, 2009) is used, which allows the user to implement new constitutive models with C++ programming code (Cai et al., 2001). The aforementioned equations are implemented into FLAC3D code as a ubiquitous joint model because FLAC3D code does not allow the user to modify zero-thickness interface elements, which are commonly utilized to simulate geological discontinuities. A study to compare the behaviour of a fault represented by ubiquitous joint models with the behaviour of a fault represented by zero-thickness interface elements was carried out by Cappa and Rutqvist (2010); the study clearly shows that normal and shear stresses and shear displacements along the faults do not differ between ubiquitous joint models and zero-thickness interface elements. Hence, it is presumed that the ubiquitous joint model can be used to simulate fault-slip.

8.4 Numerical model description

It is important to simulate mining sequences and corresponding stress re-distribution prior to simulating fault-slip since its behaviour is strongly dependent upon ambient stresses. Thus, a mine wide model encompassing a fault running parallel to a steeply dipping, tabular orebody (Sainoki & Mitri, 2014a) is generated by means of FLAC3D code. In the orebody, stopes are extracted and backfilled in accordance with mining sequences as per sublevel stoping method. Figure 8-1 illustrates the numerical model. The length, width, and height of the model were determined on the basis of preliminary analyses so as to minimize the influence of model boundaries on the stress distribution on the fault. As

shown in the figure, the fault is located in hanging wall, 30 m away from the orebody, which dips at 80˚.

Figure 8-2 illustrates stopes within the orebody and mining sequences as per sublevel stoping method. As shown in the figure, two stopes are extracted from hanging wall to footwall on each level; and after extracting each stope backfill is applied. In the present study, stope strike length was set at 200 m, which is admittedly long, compared to those planned in real underground mines (Zhang & Mitri, 2008). However, investigating the effect of the extraction of each stope on the fault is not the scope of this study. The purpose of simulating the mining sequences is to simulate the regional unclamping (Castro et al., 2009) induced by the extraction of a large volume of the orebody, so that the shear stress acting on the fault reaches the maximum shear strength determined by the static friction law. For these reasons, the aforementioned stope geometry is adopted. It can be seen from the figure that the extraction of stopes is carried out until Stope7H, which represents a stope on the hanging wall side on 7th level.

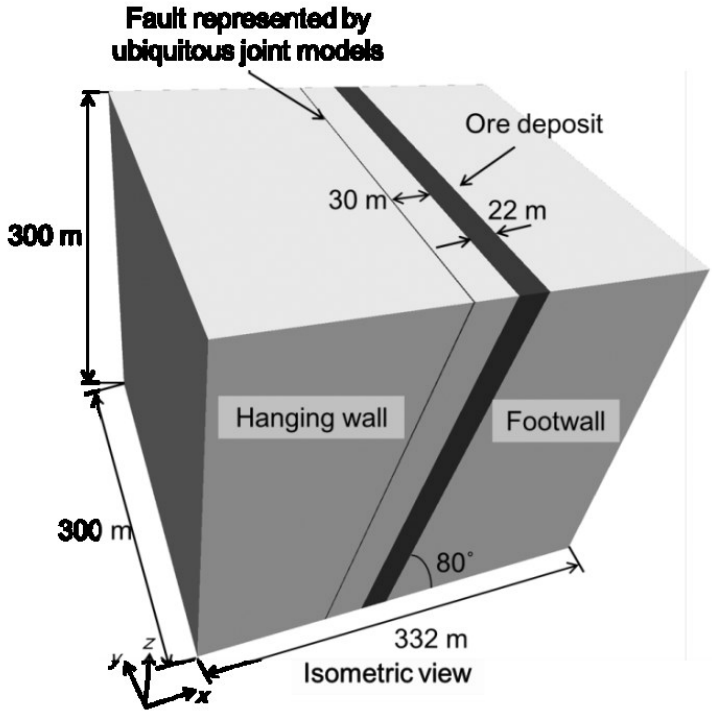

Figure 8-1: Numerical model used for static and dynamic analyses

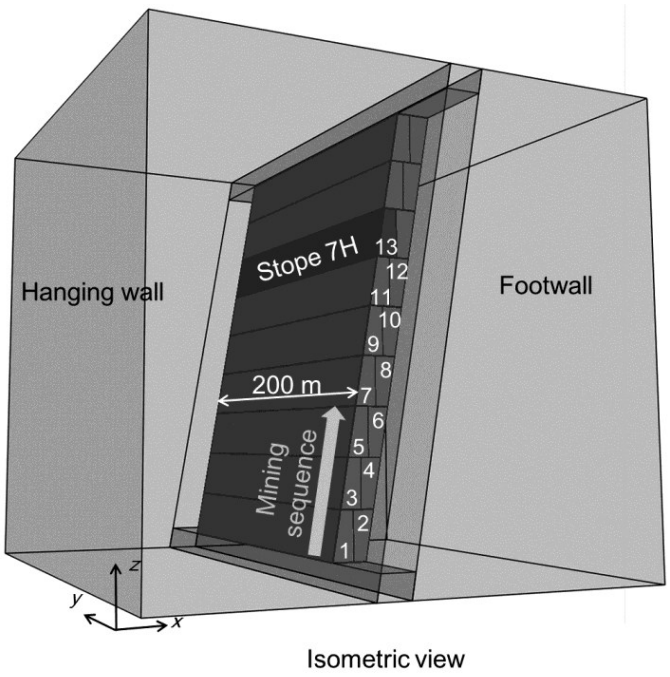

Figure 8-2: Mining sequence modelled

8.5 Analysis procedure

Figure 8-3 shows the analysis procedure. As mentioned in the preceding section, the extraction and backfilling of the stopes is first carried out with static analysis. At this stage, the analysis is performed in a static condition because the analysis is aimed at simulating stress changes due to mining activities; investigating stress waves that could be induced by the stope extraction is not intended. It is to be noted that Barton's shear strength model is applied to the fault without considering the slip-weakening behaviour until this stage. Based on a stress state after extracting Stope7H, dynamic analysis is performed. At the beginning of the dynamic analysis, normal and shear stresses acting on the fault are examined to check if the shear stress satisfies the failure criterion derived from Barton's shear strength model. After checking the stresses, *JRC* in Equation 8-2 is slightly decreased for zones where the failure criterion is satisfied, in order to trigger fault-slip. The reduction in *JRC* is physically interpreted as breakage of fault surface asperities. Residual stress resulting from the slight decrease in *JRC* triggers fault-slip. Afterwards, the linear slip-weakening law defined by Equation

8-1 is applied to the zones, so that fault-slip is driven by residual stress resulting from the slip-weakening behaviour. The specific values with respect to the friction laws are shown in the following section.

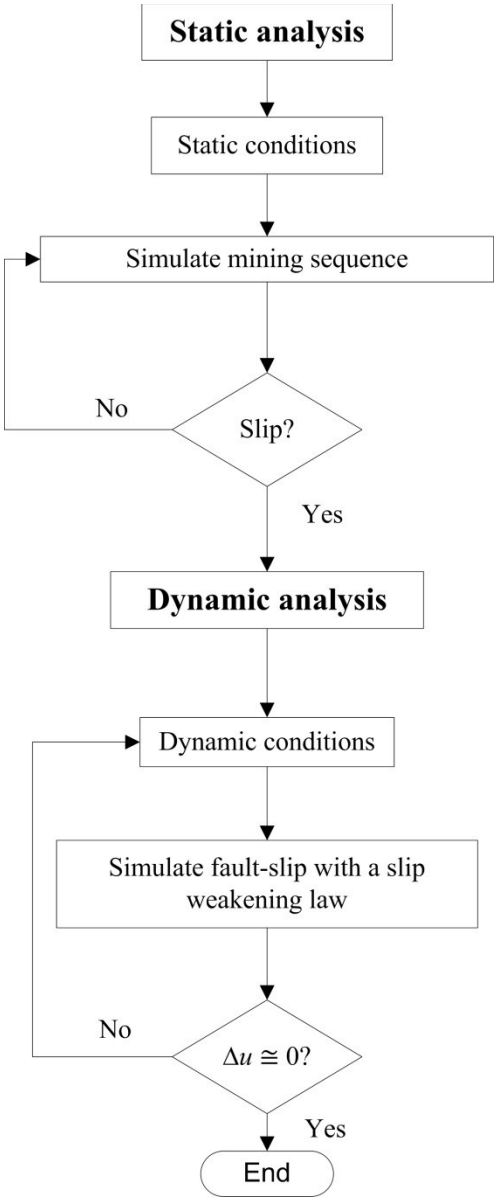

Figure 8-3: Flowchart of analysis procedure

8.6 Analysis condition

In this section, analysis conditions, such as boundary conditions, a damping coefficient, and an initial stress state, are described. In addition, in the present

study the effect of characteristic slip-weakening distance on seismic source parameters is investigated for two types of fault-slip, namely fault-slip that extends over a large area and fault-slip that occurs within limited areas. Analysis conditions for the two types of fault-slip are explained below.

8.6.1 Boundary conditions, time step and damping coefficient

During the static analysis, the model boundaries shown in Figure 8-1 are fixed in the direction perpendicular to the plane of the boundary. When dynamic analysis is performed, the boundary condition is changed to viscous so as to prevent seismic waves arising from fault-slip from reflecting the model boundaries.

A timestep used for the dynamic analysis is automatically calculated based on the volume of each zone of the model, P-wave velocity obtained from rockmass mechanical properties and the face area of each zone (Itasca, 2009). Regarding the attenuation of the seismic waves arising from the fault-slip, local damping embodied in FLAC3D is taken. According to the manual of FLAC3D, a coefficient of local damping is given as:

$$\alpha_L = \pi D \tag{8-4}$$

where α_L and D are the local damping coefficient and a fraction of critical damping. It operates by adding or subtracting mass from a grid point at certain times during a cycle of oscillation. Although local damping cannot capture the energy loss properly when wave forms are complicated, it enables frequency-independent damping. According to ABAQUS (2003), a fraction of critical damping for rock falls between 2 and 5 %. Thus, 2 % of critical damping is adopted for this study; and this damping system is deemed sufficient at this stage because seismic source parameters discussed in the latter section are not dependent upon the propagation of seismic waves. Whereas the seismic wave

attenuation is strongly susceptible to the damping of rockmasses, slip behaviour itself is not.

8.6.2 Type of fault-slip simulated

In underground mines, fault-slip related seismic events take place in a wide range of magnitudes. When fault-slip involves rupture over a large area, it entails an event of high magnitude (Ortlepp, 1992). For the purpose of this study, this type of fault-slip will be termed zonal. On the other hand, the extent of fault-slip is limited when it takes place within geologically disturbed areas such as shear or fracture zones, where stresses are locally concentrated (McGarr et al., 1975). For the purpose of this study, this type of fault-slip will be defined as local. For a zonal fault-slip, the dynamic analysis is performed without particular conditions as shown in Figure 8-4(a), whereas for a local fault-slip, a limited area is defined as shown in Figure 8-4(b). It should be noted that the same stress state obtained from the static analysis is used as an initial stress state of the dynamic analyses for both types of fault-slip.

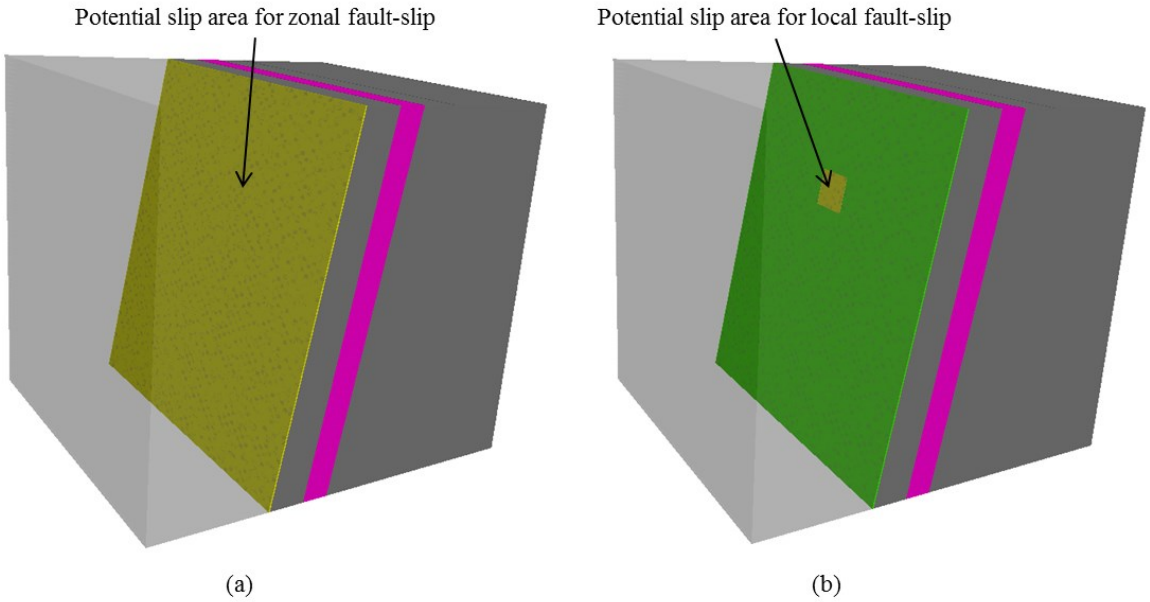

Figure 8-4: Fault-slip potential area: (A) Fault-slip is simulated across the fault;

(B) Fault-slip is simulated only within the indicated area

8.6.3 Initial stress state

Before carrying out the static analysis, pre-mining stresses are applied to the mine-wide model. The vertical in-situ stress, σ^o_v, which is in the z-direction in Figure 8- 5, is calculated by the overburden pressure as follows:

$$\sigma^o_v = \gamma H \tag{8-5}$$

where γ and H are the unit weight of the rockmass and the depth below ground surface, respectively. In the present study, it is assumed that the maximum horizontal stress is in the direction perpendicular to the orebody and the direction of minimum horizontal stress is parallel to the orebody strike. The magnitude of maximum and minimum horizontal stresses is calculated by the following equations proposed by Diederichs (1999).

$$k_{\max} = 1 + \frac{25}{\sqrt{H}} \tag{8-6}$$

$$k_{\min} = 1 + \frac{8}{\sqrt{H}} \tag{8-7}$$

$$\sigma^o_{H\max} = k_{\max}\sigma^o_v \tag{8-8}$$

$$\sigma^o_{H\min} = k_{\min}\sigma^o_v \tag{8-9}$$

where k is the horizontal to vertical in-situ stress ratio, and σ^0_H is the horizontal in-situ stress. In this study, the depth at the top boundary of the model is set at 1500 m below ground surface.

8.6.4 Mechanical properties of rockmass and fault

The mechanical properties of the rockmasses in the hanging wall, orebody,

and footwall shown in Figure 8-1 are based on a previous case study (Henning, 1998). Table 1 lists the elastic modulus, E, cohesion, C, internal friction angle, ϕ, the unit weight, γ, Poisson's ratio, ν, tensile strength, σ_T, and dilatancy angle, ψ, of the rockmasses and backfill material.

Table 8-1: Rockmass mechanical properties

	E (GPa)	C (MPa)	ϕ (˚)	ν	γ (kN/m3)	σ_T (MPa)	ψ (˚)
HW1	31	2.6	38	0.21	25.5	1.1	9.3
Ore	115	11.5	48	0.1	25.5	5.9	12.0
FW2	49	4.3	39	0.15	25.5	1.8	9.5
BW3	2.5	0.1	35	0.35	23.0	N/A	0.0

1 Hanging wall

2 Footwall

3 Backfill

The mechanical and physical properties of the fault for the static analysis are listed in Table 2. As mentioned by Ivins and Lyzenga (1986), fractures and cracks within fault zones could decrease shear moduli of rockmasses up to one-fifteenth. Hence, in the present study, the modulus of elasticity for the fault is assumed to be 3.1 GPa, which is one-tenth of the rockmass in hanging wall. As for the friction angle, the basic friction angles of typical rock joints fall between 21˚ and 38˚ according to Barton and Choubey (1977). Therefore, a friction angle of 30˚ is taken. A joint roughness coefficient of 10 is assumed, which is an intermediate value between 0 and 20. It is noteworthy that Barton's shear strength model is valid when the normal stress acting on a joint is less than joint wall compressive strength (*JCS*). Based on the pre-mining stress state before carrying out the static analysis, *JCS* shown in table 2 was determined so that the value is greater than the maximum normal stress acting on the fault.

Table 8-2: Mechanical properties of a fault represented by ubiquitous joint models

	E (GPa)	JRC	JCS (MPa)	ϕ_b (°)	v	γ (kN/m3)	σ_T (MPa)	ψ (°)
Static analysis	3.1	10	120	30	0.21	25.5	0	0

At the beginning of the dynamic analysis, *JRC* is reduced from 10 to 8 so as to trigger fault-slip only where the shear stress acting on the fault reaches the maximum shear strength determined by Barton's shear strength model. After fault-slip is triggered by the change in *JRC*, it is driven by the residual stress resulting from slip-weakening behaviour determined by Equation 8-1. The purpose of this study is to investigate the effect of slip-weakening behaviour on sesimic source parameters of fault-slip. Hence, a parametrical study is conducted with respect to characteristic slip-weakening distance, d_0 in Equation 8-1. To date, the linear slip-weakening law has been estimated by experiments and applied to a number of analyses for simulating dynamic behaviour of faults by many researchers. The value of d_0 significantly varies between the studies. For instance, Oglesby and Mai (2012) assumed d_0 of 0.4 m to simulate fault-slip as a source of an earthquake; Bizzarri (2012) took d_0 of 0.05 m to investigate a correlation between the maximum slip rate and rupture velocity. According to experimental results (Okubo & Dieterich, 1984), d_0 falls between 2 μm and 40 μm. Yuana and Prakash (2008) examined slip-weakening behaviour using a modified torsional Kolsky bar; and it was found out that a decrease in frictional resistance requires a few mm of slip. It is clear from these studies that the characteristic slip-weakening distance is strongly scale-dependent and difficult to determine without conducting shear tests using rock samples obtained from the field. In addition, it was found out from preliminary analysis that the maximum shear displacement that could occur on the modelled fault is approximately 3 cm. The simulated shear displacement falls within a reasonable range, considering the

fact that shear displacements up to 100 mm were observed as a result of violent rockbursts that took place in a deep gold mine in South Africa (Ortlepp, 2000). Based on the result and previous studies, values for d_0 of 1, 3, 5, 7, and 9 mm were adopted for the current parametric study.

Regarding the dynamic friction angle in Equation 8-3, 15° is taken, which corresponds to a coefficient of kinetic friction of 0.27. As indicated by Yuana and Prakash (2008), a coefficient of kinetic friction strongly depends on slip rates during fault-slip. Whereas coefficients of kinetic friction fall between 0.70 and 0.76 when slip rates are less than 1 mm/s (Dieterich, 1978, 1979a), it could decrease to 0.2 when a slip rate exceeds 5m/s (Yuana & Prakash, 2008). More importantly, as reported by Milev et al. (2002b), peak particle velocities observed during seismic events in underground mines occasionally exceed 2.0 m/s, and as reviewed by McGarr (1991), near-fault peak ground motion can be estimated as half of the maximum slip rate. Thus, it is found that the maximum slip rate of fault-slip that occurs in underground mines could exceed 4.0 m/s. In addition, the preliminary analysis results show that the fault-slip rate exceeds 3.0 m/s. From these facts, the aforementioned dynamic friction angle is taken for the present study. Although the coefficient of kinetic friction is dependent on slip rate, it was kept constant in the present study in order to investigate the effect of characteristic slip-weakening distances on seismic source parameters.

8.7 Results and discussion

The results obtained from the parametric study are shown and discussed with respect to seismic source parameters, namely seismic moment, slip rate, seismically radiated energy, and the maximum shear displacement increment on the fault. For the current study, the near-field energy is calculated as seismically radiated energy on the basis of a formula proposed by McGarr and Fletcher (2001). The equation is expressed as follows.

$$E_{nf} = \frac{A}{2}\rho\beta\int \dot{D}(t)^2\,dt \tag{8-10}$$

where E_{nf} is the near-field energy radiated from fault-slip; A is fault-slip area; ρ and β are the density of rockmasses and S-wave velocity, respectively; $\dot{D}(t)$ is a time-dependent slip rate. In reality, a fraction of near-field energy propagates into far-field as seismically radiated energy. Almost all of the near-field energy is dissipated resulting in permanent deformation in the vicinity of the fault. The other seismic source parameters, namely seismic moment and moment magnitude, are calculated as follows:

$$M_o = GDA \tag{8-11}$$

$$M_w = \frac{2}{3}\log M_o - 6.0 \tag{8-12}$$

where M_o and M_w are seismic moment and moment magnitude; G is shear modulus of a rockmass. The results obtained from the dynamic analyses are compared in terms of the aforementioned seismic source parameters as well as the maximum slip rate, D_{max}, and shear displacement increment, D_{max}, on the fault. The seismic source parameters when d_0 = 1 mm are shown in Table 3 as base cases for the two types of fault-slip illustrated in Figure 8-4.

Table 8-3: Seismic source parameters obtained from dynamic analysis when d_0 = 1mm

	E_{nf} (MJ)	M_o (N·m)	M_w	$\dot{D}_{max}$ (m/s)	D_{max} (m)
Fault-slip that occurs across the fault	227	4.39×10^{11}	1.7	3.3	0.032
Fault-slip that occurs within limited area	10	1.4×10^{10}	0.7	3.3	0.017

As can be seen in the table, there are large differences in seismic source parameter magnitudes between zonal and local fault-slips, excluding the maximum slip rate of 3.3 m/s. The discrepancies are attributed to the difference in fault-slip potential area shown in Figure 8-4. As expected, zonal fault-slip has larger seismic response. The implication of the same maximum slip rate is that it is strongly dependent upon the maximum stress drop induced by the slip-weakening behaviour. As can be seen from the results in Table 3, the maximum shear displacement increment D_{max} during the dynamic analysis exceeds d_0 (of 1mm) for both types of fault-slip. Thus, the maximum stress drop taking place on the fault is theoretically the same. These results indicate that even a fault-slip of small magnitude could lead to strong ground motion with high peak particle velocity given that characteristic slip weakening distance d_0 is small enough compared to shear displacements induced by the fault-slip.

Next, the effect of characteristic slip-weakening distance, d_0, on the seismic source parameters is shown in Figure 8-5 by normalizing the parameters with respect to their values when d_0 = 1 mm. Figure 8-5 shows the normalized seismic source parameters for the zonal fault-slip. It is found from the figure that d_0 affects all of the seismic source parameters. In particular, it appears that d_0 exerts a significant influence on the near-field energy and seismic moment. To be more precise, the near-field energy is decreased to one-tenth with the increase of d_0, which indicates that slip rates significantly reduce across fault-slip area since near-field energy is a function of a slip rate. Regarding the seismic moment, it is reduced to approximately one-fifth. It is remarkable that a small change in d_0 results in significant differences in the seismic source parameters. Figure 8-6 (a) and (b) depict the shear displacement increments induced by the fault-slip when d_0 = 1 mm and 9 mm, respectively. As shown in the figures, when d_0 = 1 mm, the zonal fault-slip extends to a large area from 7th level where Stope7H is extracted before the dynamic analysis. On the other hand, the zonal fault-slip area is significantly limited when d_0 = 9 mm. These results indicate that estimating the

seismic source parameters of zonal fault-slip is difficult, even though the occurrence of the fault-slip might be predicted with fault stability analysis. Further consideration to characteristic slip-weakening distance must be given so as to estimate the magnitude of fault-slip properly. Although the most conservative result can be obtained assuming that d_0 is equal to 0, the effect of characteristic slip-weakening distance, d_0, on the seismic source parameters needs to be taken into consideration for proposing an appropriate rock support system.

Figure 8-7 shows the normalized seismic source parameters for local fault-slip as defined in Figure 8-4 (b). Interestingly, there are clear differences in the effect of d_0 on the seismic source parameters between the two types of fault-slip. While d_0 has an influence on all of the seismic parameters to a certain extent for a zonal fault-slip as shown in Figure 8-5, it seems that d_0 exerts an influence on only the near-field energy and slip rates for the fault-slip occurring in localized area. It is found from Figure 8-7 that the near-field energy and the maximum slip rate are significantly decreased to approximately one-fifth with the increase of d_0. On the other hand, the maximum shear displacement increments on the fault during the fault slip remain almost the same in spite of the increase in d_0; although seismic moment is slightly reduced to approximately four-fifth, the effect of the increase in d_0 on seismic moment is quite small compared to that for zonal fault-slip. The result that the small effect of d_0 on seismic moment in Figure 8-7 indicates that the dynamic shear displacements induced during a local fault-slip are larger than d_0, i.e., the friction law has completely switched from Barton's shear strength model to the dynamic friction law determined by Equation 8-3 as the shear displacements increase. Thus, a stress drop resulting from slip-weakening behaviour is the same in spite of d_0. Figure 8-8 (a) and (b) depict shear displacement increments induced by the fault-slip when d_0 = 1 mm and 9 mm, respectively. It can be seen from the figures that the shear displacement increments reach the characteristic slip-weakening distance within the limited fault-slip area in spite of the slip-weakening distance, thus resulting in the same

level of stress drop within the area. These results imply that seismic moment can be reasonably estimated to some extent for fault-slip that occurs within small regions due to local high slip potential provided that d_0 is smaller than shear displacement increments induced during the fault-slip. On the other hand, as mentioned above, slip rate and near-field energy are significantly affected by d_0, which corresponds with the results shown in Figure 8-5. This is ascribed to a rate of the stress change resulting from the slip-weakening behaviour. As can be seen from Equation 8-1, stresses on the fault could drastically change when d_0 is small, whereas the change becomes moderate with the increasing d_0. Evidently, a sudden reduction in stresses during a short period of time causes high slip rates, which lead to intense ground motion in the environs of the fault. This implies difficulty in predicting peak particle velocity excited by seismic waves arising from fault-slip. For instance, the maximum slip rate is 3.3 m/s when d_0 = 1 mm for the local fault-slip occurring as shown in Table 3. Near-fault peak particle velocity calculated from the maximum slip rate is 1.65 m/s because near field particle velocity is simply equal to a half of the maximum slip rate (McGarr, 1991). According to a damage threshold with respect peak particle velocity, the particle velocity is high enough to inflict damage to an intact hard rock (Brinkmann, 1987). The maximum slip rate decreases to 0.8 m/s when d_0 = 9 mm, which results in near-fault peak particle velocity of 0.4 m/s. According to the threshold, the peak particle velocity could cause detachment of rocks in unlined tunnels. It is clear that an appropriate support system is completely different between the two cases, although seismic moment and moment magnitude do not largely differ between the two seismic events. It is thus concluded that while seismic moment might be accurately estimated without considering d_0 in the case of local fault-slip when d_0 is small compared to shear displacement increments, there is still a need to consider d_0 so as to estimate the maximum slip rate properly, which pertain to peak particle velocities in the vicinity of the fault.

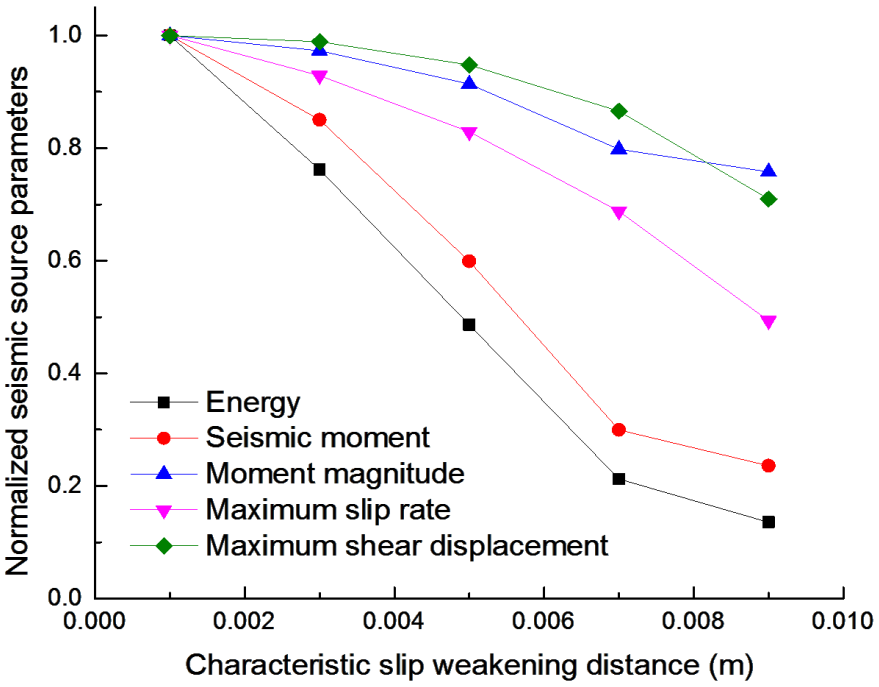

Figure 8-5: Normalized seismic source parameters for fault-slip that occurs across the fault

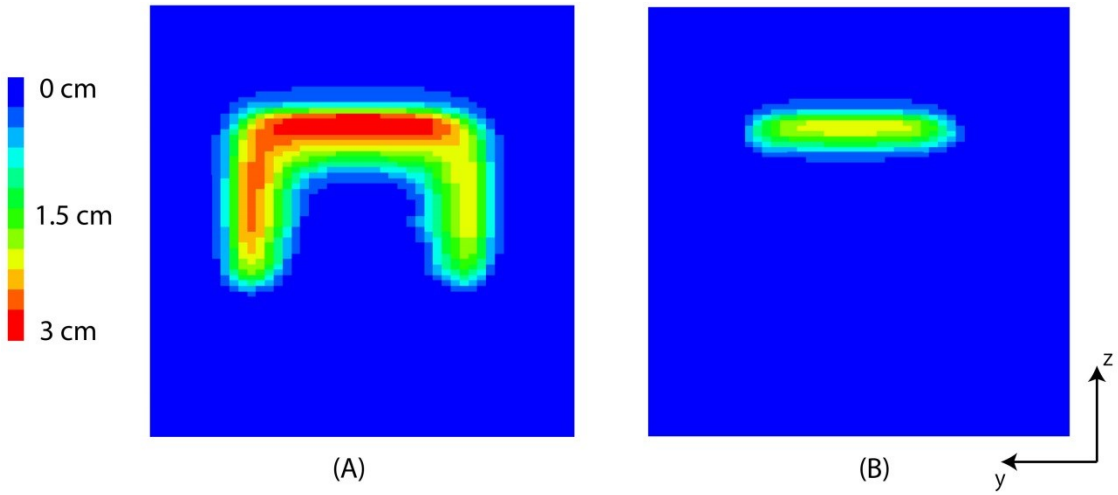

Figure 8-6: Shear displacement increments induced by fault-slip taking place across the fault (A) d_0 = 1 mm; (B) d_0 = 9 mm

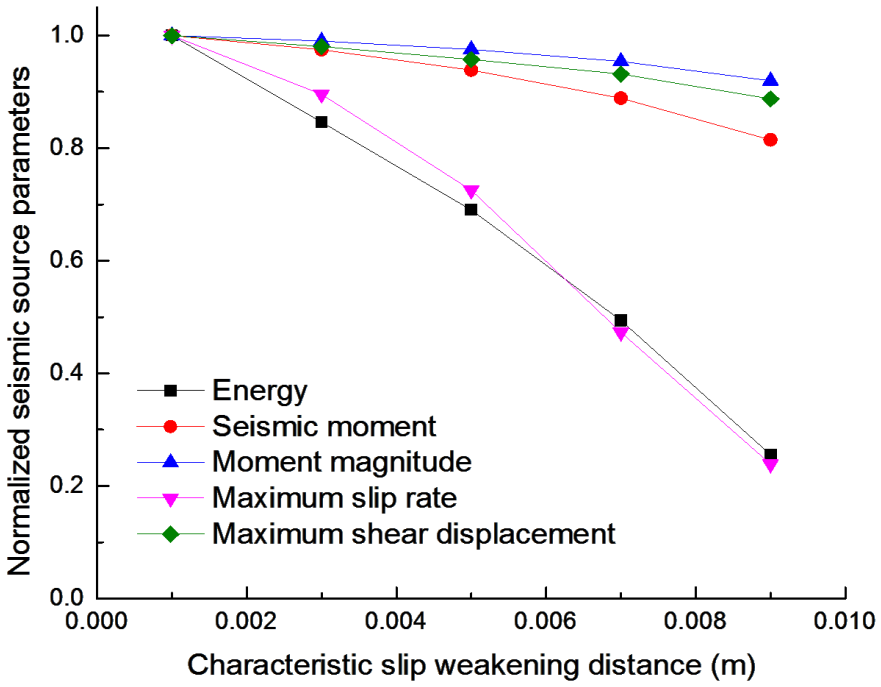

Figure 8-7: Normalized seismic source parameters for fault-slip that occurs within the limited area

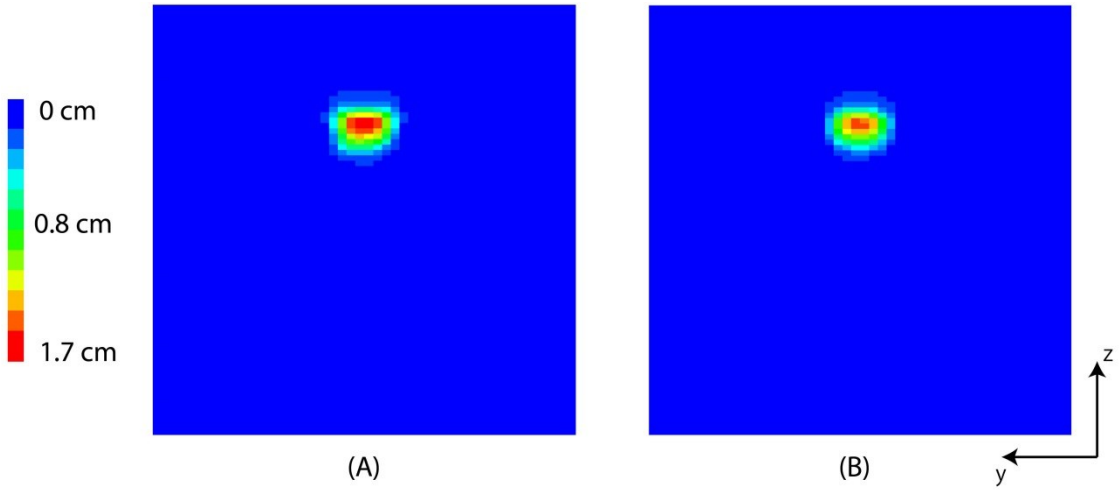

Figure 8-8: Shear displacement increments induced by fault-slip taking place within the limited area: (A) d_0 = 1 mm; (B) d_0 = 9 mm

8.8 Conclusions

The effect of characteristic slip-weakening distance, d_0, on seismic source parameters of fault-slip is investigated with a linear slip-weakening friction law. A parametrical study is carried out with respect to d_0 with a mine-wide model encompassing a hanging wall fault and orebody. Calculations of the seismic source parameters are based on the results obtained from dynamic analysis. Two types of fault-slip are considered when the dynamic analysis is conducted: (a) zonal fault-slip taking place across the fault; (b) local fault-slip taking place within limited areas of the fault. It is shown that seismically radiated energy and slip rates significantly decrease due to a slight increase in d_0 for both types of fault-slip, while the seismic moment is affected by the increase in d_0 only for zonal fault-slip. In case of local fault-slip, the seismic moment remains almost unaffected with respect to d_0. These results indicate that it is difficult to estimate the seismic source parameters of zonal fault-slip without a proper estimation of d_0, while the seismic moment of local fault-slip arrested within limited areas could be precisely estimated to some extent given that the coefficients of static and dynamic friction are already known. It is also concluded that considering the characteristic slip-weakening distance is of pivotal importance in estimating the intensity of ground motion induced by fault-slip, which is indispensable for proposing an appropriate support system for seismic events taking place in underground mines.

CHAPTER 9

Conclusions and suggestions for future work

In this thesis, the dynamic behaviour of fault-slip has been investigated, considering various factors that might affect fault behaviour. In this chapter, the conclusions obtained from each study are summarized. Afterwards, in light of knowledge gained through those studies, suggestions for future work are proposed.

9.1 Conclusions obtained from numerical analyses using conceptual models

First, a model parametric study has been carried out with respect to factors that could exert an influence on the behaviour of a fault. The study has then revealed that mining depth, friction angles, and fault locations (hanging wall or foot wall) exert a large influence on the maximum relative shear displacement along the fault, while the dilation angle and stiffness of the fault do no. Likewise, seismic source parameters of the fault-slip are also affected by the influential factors. The maximum slip rates appear to increase with the maximum slip, although their locations do not coincide – this being the case due to stope extraction. It is also found out that extremely high rupture velocity could be induced by stope extraction, which implies that a severe seismic event could be caused. The study also implies that the use of the classical Mohr-Coulomb criterion as a friction law for mining-induced fault-slip could underestimate the magnitude of the fault-slip because the friction law considers neither fault surface asperities nor its slip weakening behaviour.

Second, Barton's shear strength model has been implemented into FLAC3D code with C++ programming language in order to simulate fault-slip due to asperity shear and investigate the effect of fault surface roughness on the severity of fault-slip. The study has shown that faults with intermediate fault

surface roughness could cause the most severe fault-slip in terms of seismic moment, while intensely undulating faults could release large seismic energy during fault-slip. The results thus indicate that taking fault surface roughness into consideration is imperative in order to estimate the magnitude of fault-slip in underground mines properly. The study also shows that near-fault peak particle velocity (PPV) excited by seismic waves has a strong correlation with seismically radiated energy, which implies that large excess shear stress resulting from asperity shear plays an important role in the generation of the intense seismic waves inducing high PPV. Thus, proper estimations of dynamic and static friction laws are of pivotal importance for the prediction of PPV.

Third, the interactions of stress waves arising from stope production blasts with a nearby fault have been examined, considering a couple of blast sequences. It has been found out that performing blasts simultaneously could help control fault-slip as stress waves are cancelled out due to a positional relationship between blast-hole locations and grid points on a stope wall, while performing blasts separately could cause larger seismic events due to shear waves arising from the blasts. The results also show that the difference between the blast sequences is remarkable, especially in terms of seismically radiated energy, compared to the moment magnitude of the induced fault-slip, which indicates that carrying out blasts separately could cause severe damage as energy radiated during fault-slip is strongly correlated with the damage of rockmass. Thus, it can be concluded that although conducting blasts separately is considered desirable in terms of preventing rockmass from deteriorating, simultaneous blasting might be one option when faults are found in the vicinity of stopes.

Fourth, the effect of fault surface asperities on the intensity of seismic waves arising from fault-slip has been investigated with Saeb and Amadei's constitutive model, which is implemented into FALC3D code, considering the collision and

unloading of the asperity during the fault-slip. Results obtained from the analysis have demonstrated that the collision of asperities does not strongly affect the property of seismic waves, while a significant increase in PPV could be induced due to the unloading of asperities. It has been shown that when the stress release is large, PPV could be 3 times as high as that obtained from a model, in which a planar fault is modelled. More importantly, it is found out that the PPV induced by the large stress release is high enough to cause severe damage to rockmass. These results have shown that the stress release due to the unloading of asperities moving apart is the most influential factor that affects the intensity of seismic waves amongst factors investigated. However, further study is strongly recommended in order to determine a relation between a stress release rate during the unloading and the geometry of asperities.

Lastly, the effect of slip-weakening distance, d_0, on seismic source parameters of fault-slip has been examined with a linear slip-weakening law. Two types of fault-slip have been considered: fault-slip extending across the fault and fault-slip taking place within limited regions. It has been demonstrated that seismically radiated energy and slip rates significantly decrease with increasing d_0 for both types of fault-slip, while seismic moment is susceptible to d_0 only for fault-slip taking place across the fault. These results indicate that it is difficult to estimate the seismic source parameters of fault-slip extending across a fault without a proper estimation of d_0, while the seismic moment of fault-slip arrested within limited areas could be properly estimated provided that the coefficients of kinetic and static friction are already known.

9.2 Conclusions drawn from a case study

Back analysis of fault-slip that occurred within shear and fracture zones in Garson Mine, Sudbury, Ontario, Canada has been carried out in order to calibrate the physical and mechanical properties of faults within the shear and fracture zones. By means of seismic source parameters, PPV, and peak

acceleration obtained from installed microseismic monitoring systems, fault surface roughness and a dynamic friction angle have been calibrated and validated with a mine-wide Garson Model while considering the heterogeneity of mechanical properties of the shear and fracture zones. Through the back analysis, a methodology to estimate the physical and mechanical properties of a fault while considering dynamic behaviour of the fault and rockmass has been developed. Although the study is carried out for Garson Mine, the developed methodology can be applicable to other mines suffering from seismic events that occur within shear and fracture zones or on pre-existing faults.

9.3 Suggestions for future work

In this thesis, fault-slip analyses considering fault properties and various phenomena that are encountered in underground mines have been presented. However, there are still many study problems to be addressed for the better understanding of the behaviour of faults in underground mines. The following problems should be further discussed.

- A relationship between the geometry of fault surface asperities and stress release that occurs when the asperities move apart should be studied, so that the stress release rate modelled in the present study can be related to the actual geometry of asperities.

- A case study of blast-induced fault-slip should be carried out. In this thesis, it is demonstrated that stope production blasts could induce seismic events on nearby faults. In order to verify the results, carrying out the case study is recommended.

- In the present study, a couple of constitutive models governing fault behaviour have been considered. However, there are a number of static and dynamic shear strength models that can take into account various

phenomena taking place during fault-slip. Thus, it should be carried out to simulate fault-slip with those friction laws in order to investigate how those friction laws affect the behaviour of faults.

- Through the case study, the methodology to calibrate the physical and mechanical properties of faults has been proposed. Based on the methodology, empirical relationships to help estimate fault-slip potential and its seismic source parameters should be developed. When it is established, it would be very helpful for proposing support systems in burst-prone environments where faults are found.

Statements of contributions

In this study, dynamic modelling of mining-induced fault-slip is attempted for the first time, considering a wide range of factors that have been previously rarely taken into account. The effects of fault constitutive model, surface asperities, stope production blasts, and slip-weakening behaviour due to abrasion of the asperities on mining-induced fault-slip behaviour have been adequately analyzed and described through a characteristic case study of a steeply dipping, deeply seated ore deposit in a sublevel mining system.

Novel methodologies to take into account the aforementioned factors in dynamic modelling of fault-slip have been developed. In addition, a new methodology to determine the physical and mechanical properties of faults has been proposed using seismic source parameters, peak particle velocity, and peak acceleration recorded by seismic monitoring systems installed in an underground mine.

CHAPTER 10

References

ABAQUS. (2003). ABAQUS online documentation: Ver 6.4-1.: Dassault Systemes, France.

Aki, K., & Richards, R.G. (1980). *Quantitative Seismology: Theory and Method*. San Francisco: Freeman.

Alber, M. (2013). *Strength of faults - A concern for mining engineers?* Paper presented at the Eurock, Poland.

Alber, M., Fritschen, R., Bischoff, M., & Meier, T. (2009). Rock mechanical i nvestigations of seismic events in a deep longwall coal mine. *International Journal of Rock Mechanics and Mining Science, 46*, 408-420.

Alejano, L. R., Gonzalez, J., & Muralha, J. (2012). Comparison of different techniques of tilt testing and basis friction angle variability assessment. *Rock mechanics and rock eng, 45*, 1023-1035.

Andrews, D. J. (2010). Ground motion hazard from supershear rupture. *Tectonophysics, 493*, 216-221.

Arjang, B. (1991). Pre-mining stresses at some hard rock mines in the Canadian Shield. *CIM Bull, 84*(946), 80-86.

Asadollahi, Pooyan, & Tonon, Fulvio. (2010). Constitutive model for rock fractures: Revisiting Barton's empirical model. *Engineering Geology, 113*, 11-32.

Bandis, S., Lumsden, A.C., & Barton, N. (1981). Experimental studies of scale effects on the shear behaviour of rock joints. *Int. J. Rock Mech Min Sci & Geomech 18*, 1-21.

Bandis, S., Lumsden, A.C., & Barton, N.R. (1983). Fundamentals of rock joint deformation. *International JOurnal of Rock Mechanics and Mining Science & Geomechanics, 20*(6), 249-268.

Barton, N. (1973). Review of a new shear-strength criterion for rock joints *Engineering Geology, 7*, 287-332.

Barton, N. (1982). *Modelling rock joint behavior from in situ block test: implications for nuclear waste repository design*, Columbus, OH.

Barton, N., Bandis, S, & Bakhtar, K. (1985). Strength, Deformation and Conductivity Coupling of Rock Joints. *international Journal of Rock Mechanics and Mining Science & Geomechanics, 22*(3), 121-140.

Barton, N., & Bandis, S. (1982). *Effects of block size on the shear behaviour of jointed rock.* Paper presented at the 23rd U.S. Symposium on Rock Mechanics, Berkeley, California.

Barton, N., & Choubey, V. (1977). The shear strength of rock joints in theory and practice. *Rock Mechanics, 10*, 1-54.

Beeler, N. M., Tullis, T. E., & Weeks, J. D. (1994). The roles of time and displacement in the evolution effect in rock friction. *Geophysical research letters, 21*(18), 1987-1990.

Ben-Zion, Y., & Sammis, C. G. (2003). Characterization of Fault Zones. *Pure and applied geophysics, 160*, 677-715.

Bewick, R.P., Valley, B., runnals, S., Whitney, J., & Krynicki, Y. (2009). *Global approach to managing deep mining hazard.* Paper presented at the the 3rd CANUS Rock Mechanics Symposium, Toronto.

Bischoff, M., Cete, A., Fritschen, R., & Meier, T. (2010). Coal Mining Induced Seismicity in the Ruhr Area, Germany. *Pure and applied geophysics, 167*, 63-75.

Bizzarri, A. (2009). Can flash hearing of asperity contacts prevent melting? *Geophysical research letters, 36*(L11304). doi: 10.1029/2009GL037335

Bizzarri, A. (2011). On the deterministic description of earthquakes. *Reviews of geophysics, 49*(RG3002).

Bizzarri, A. (2012). Rupture speed and slip velocity: What can we learn from simulated earthquake? *Earth and Planetary Science Letters, 317*, 196-203.

Bizzarri, A., & Belardinelli, M. E. (2008). Modelling instantaneous dynamic triggering in a 3-D fault system: application to the 2000 June South

Iceland seismic sequence. *Geophysical Journal International, 173*, 906-921. doi: 10.1111/j.1365-246X.200803765.x

Bizzarri, A., & Cocco, M. (2003). Slip-weakening behavior during the propagation of dynamic ruptures obeying rate- and state-dependent friction laws. *Journal of Geophysical Research, 108*(B8). doi: 10.1029/2002JB002198

Bizzarri, A., & Cocco, M. (2006a). Correction to "A thermal pressurization model for the spointaneous dynamic rupture propagation on a three-dimentional fault: 1. Methodological approach". *Journal of Geophysical Research, 111*(B11).

Bizzarri, A., & Cocco, M. (2006b). A thermal pressurization model for the spontaneous dynamic rupture propagation on a three-dimensional fault: 1. Traction evolution and dynamic parameters. *Journal of Geophysical Research, 111*(B5).

Bizzarri, A., & Cocco, M. (2006c). A thermal pressurization model for the spontaneous dynamic rupture propagation on a three-dimensional fault: 1. Methodological approach. *journal of Geophysical Research, 111*(B5).

Bizzarri, A., Cocco, M., Andrews, D. J., & Boschi, E. (2001). Solving the dynamic rupture problem with different numerical approaches and constitutive laws. *Geophysical Journal International, 144*, 656-678.

Bizzarri, A., & Spudich, P. (2008). Effects of supershear rupture speed on the high-frequency content of S waves investigated using spontaneous dynamic rupture models and isochrones theory. *Journal of Geophysical Research, 113*(B5).

Blake, Wilson, & Hedley, David G.F. (2003). *Rockbursts case studies from North America Hard-Rock Mines.* . Littleton, Colorado, USA: Society for Mining, Metallurgy, and Exploration.

Boatwright, J. (1996). Frictional constraints on crustal faulting. *Journal of Geophysical Research, 101*(B6), 13895-13909.

Brace, W.F., & Byerlee, J.D. (1966). Stick-slip as a mechanism for earthquakes. *Science, 153*(3739), 990-992.

Bradbury, K. K., Barton, D. C., Solum, J. G., Draper, S. D., & Evans, J. P. (2007). Mineralogic and textural analyses of drill cuttings from the San Andreas Fault Observatory at Depth (SAFOD) boreholes: Initial interpretations of fault zone composition and constraints on geologica models *Geosphere, 3*(5), 299-318.

Brady, B.H.G., & Brown, E.T. (1993). *Rock mechanics : For underground mining*. London: Chapman & Hall.

Brinkmann, J. R. (1987). *Separating shock wave and gas expansion breakage mechanism*. Paper presented at the 2nd International Symposium rock fragmentation by blasting.

Bruggeman, D.A.G. (1937). Berechnung verschiedener physikalischer Konstanten von heterogenen Substanzen. *Ann. Phys., 24*, 636-679.

Budiansky, B., & O'Connell, R. J. (1976). Elastic moduli of a cracked solid. *Int. J. Solids Struct, 12*, 81-97.

Budiansky, Bernard, & O'Connell, Richard J. (1975). Elastic moduli of a cracked solid. *International Journal Solids Structures, 12*, 81-97.

Byerlee, J. D. (1968). Stick slip, stable sliding, and earthquakes-effect of rock type, pressure, stain rate, and stiffness. *Journal of geophysical research, 73*(18), 6031-6037.

Cai, M., Kaiser, P.K., & Martin, C.D. (2001). Quantification of rock mass damage in underground excavations from microseismic event monitoring. *International Journal of Rock Mechanics and Mining Science, 38*, 1135-1145.

Cappa, Frederic, & Rutqvist, Jonny. (2010). Modeling of coupled deformation and permeability evolution during fault reactivation induced by deep underground injection of CO2. *International Journal of Greenhouse Gas Control, 5*, 336-346.

Carter, T.G., & Bewick, R. P. (2012). *Structural geology guidelines for aiding characterization of deep mining fault behaviour* (2nd ed.). Sudbury, Ontario, Canada: CEMI.

Castro, L.A.M., Carter, T.G., & Lightfoot, N. (2009). *Investigating factors influencing fault-slip in seismically active structures.* Paper presented at the 3rd CANUS Rock Mechanics Symposium, Toronto.

Cello, G., Gambini, R., Mazzoli, S., Read, A., Tondi, E., & Zucconi, V. (2000). Fault zone characteristics and scaling properties of the Vald'Agri Fault System (Southern Apennines, Italy). *Journal of Geodynamics, 29*, 293-307.

Cello, G., Tondi, E., Micarelli, L., & Invernizzi, C. (2001). Fault zone fabrics and geofluid properties as indicators of rock deformation modes. *Journal of Geodynamics, 32*, 543-565.

Chambon, G., Schmittbuhl, J., & Corfdir, A. (2006a). Frictional response of a thick gouge sample: 1. Mechanical measurements and microstructures. *Journal of Geophysical Research, 111*(B09308), 1-17.

Chambon, G., Schmittbuhl, J., & Corfdir, A. (2006b). Frictional response of a thick gouge sample: 2 Friction law and implications for faults. *Journal of Geophysical Research, 111*(B09308).

Chen, S.G., & Zhao, J. (1998). A study of UDEC modelling for Blast wave propagation in jointed rock masses. *International Journal of Rock Mechanics and Mining Science, 35*(1), 93-99.

Chester, F. M. (1994). Effects of temperature on friction: Constitutive equations and experiments with quartz gouge. *Journal of Geophysical Research, 99*(B4), 7247-7261.

Chester, F. M., & Chester, J. S. (1998). Ultracataclasite structure and friction processed of the Punchbowl fault, San Andreas system, California. *Tectonophysics, 295*, 199-221.

Chester, F. M., & Logan, J. M. (1986). Implications for mechanical properties of brittle faults from observations of the Punchbowl Fault Zone. *Pure and applied geophysics, 124*, 79-106.

Childs, C., Manzocchi, T., Walsh, J. J., Bonson, C. G., Nicol, A., & Schopfer, M. P. J. (2009). A geometric model of fault zone and fault rock thickness variations. *Journal of Structural Geology, 31*, 117-127.

Clough, G. W., & Duncan, J. M. (1969). Finite Element Analyses of Port Allen and Old River Locks *Contract report - U.S. Army Engineer Waterways Experiment Station*.

Cocco, M., Bizzarri, A., & Tinti, E. (2004). Physical interpretation of the breakdown process using a rate- and state-dependent friction law. *Tectonophysics, 378*, 241-262.

Company, Atlas Powder. (1987). *Explosives and Rock Blasting*.

Cowie, P. A., & Scholz, C. H. (1992). Physical explanation for the displacement-length relationship of faults using a post-yield fracture mechanics model. *Journal of Structural Geology, 14*(10), 1133-1148.

Daehnke, A. (1997). *Stress Wave and Fracture Propagation in Rock*.

Dawers, N. H., & Anders, M. H. (1995). Displacement-length scaling and fault linkage. *Journal of Structural Geology, 5*, 607-614.

Diederichs, M.S. (1999). *Instability of hard rockmass: the role of tensile damage and relaxation* (PhD), University of Waterloo, Waterloo, Canada.

Dieterich, J. H. (1972). Time-Dependent Friction in Rocks. *Journal of Geophysical Research, 77*(20), 3690-3697.

Dieterich, J. H. (1978). Time-dependent friction and the mechanics of strike-slip. *Pure and applied geophysics, 116*, 790-806.

Dieterich, J. H. (1979a). Modeling of Rock Friction1. Experimental Results and Constitutive Equations. *Journal of Geophysical Research, 84*(B5), 2161-2168.

Dieterich, J. H. (1979b). Modeling of Rock Friction2. Simulation of Preseismic Slip. *Journal of Geophysical Research, 84*(B5), 2169-2175.

Dieterich, J. H., & Kilgore, B. (1996). *Implications of fault constitutive properties for earthquake prediction.* Paper presented at the National academy of science, U.S.A.

Directorate, CAMIRO. Mining Division.; Mining Research. (1996). *Canadian rockburst research program, 1990-1995 : a comprehensive summary of*

five years of collaborative research on rockbursting in hardrock mines: Sudbury, Ontario: CAMIRO Mining Division.

Domanski, Boguslaw, & Gibowicz, Slawomir Jerzy. (2008). Comparison of source parameters estimated in the frequency and time domains for seismic events at the Rudna copper mine, Poland. *Acta Geophysica, 56*(2), 324-343.

Dow, J. O., Jones, M. S., & Harwood, S. A. (1990). A generalized Finite Difference Method for Solid Mechanics. *Numerical Methods For Partical Differential Equations, 2*, 137-152.

Dunham, E. M., & Bhat, H. S. (2008). Attenuation of radiated ground motion and stresses from three-dimensional supershear rupture. *Journal of Geophysical Research, 113*(B8).

ESG. (2011). WaveVis. Kingston, ON, Canada: ESG solutions.

Fairhurst, C. (1964). On the validity of Brazilian test for brittle materials. *International Journal of Rock Mechanics and Mining Science, 1*, 535-546.

Feit, G.N., Malinnikova, O. N., & Zykov, V. S. (2002). Prediction of rockburst and sudden outburst hazard on the basis of estimate of rock-mass energy. *Journal of Mining Science, 38*(1), 61-63.

Francis, T. W., Thomson, K. C., & Kuenzler, H. (1972). Stick-slip propagation velocity and seismic source mechanisms. *Bulletin of the Seismological society of America, 62*(6), 1621-1628.

Frehner, M., Schmalholz, S. M., Saenger, E. H., & Steeb, H. (2008). Comparison of finite difference and finite element methods for simulating two-dimensional scattering of elastic waves. *Physics of the Earth and Planetary Interiors, 171*, 112-121.

Gay, N. C., & Ortlepp, W. D. (1979). Anatomy of a mining-induced fault zone. *Geological Society of America Bulletin, 90*, 47-58.

Gibowicz, S. J., & Kijko, A. (1994). *An introduction to mining seismology*. the University of California: Academic Press.

Gool, Bronwyn van. (2007). *Effects of blasting on the stability of paste fill stopes at Cannington Mine.* (PhD), James Cook University.

Hai-min, W., Yi-ming, S., & jun-gao, Z. (2011). Implementation and verification of interface constitutive model in FLAC3D. *Water Science and Engineeing, 4*(3), 305-316.

Hanks, T.C., & Kanamori, H. (1979). A moment magnitude scale. *Journal of Geophysical Research, 84*, 2348-2350.

Hasegawa, H. S. (1983). Lg spectra of local earthquakes recorded by the eastern Canada telemetered network and spectral scaling. *Bulletin of the Seismological society of America, 73*(4), 1041-1061.

Hedley, D.G.F. (1992). *Rockburst handbook for ontario hard rock mines*: Minister of supply and services Canada

Helmstetter, A., & Shaw, B. E. (2009). After slip and aftershock in the rate- and state-friction law. *Journal of Geophysical Research, 114*(B01308). doi: 10.1029/2007JB005077

Henning, J. (1998). *Ground control strategies at the bousquet 2 mine.* (Master), McGill University, Montreal, QC, Canada.

Henning, J., & Mitri, Hani S. (2010). Production blast-induced vibrations in longhole open stoping - a case study. *International Journal of Geotechnical Earthquake Engineering, 1*(2), 1-11.

Hobbs, S. W., Griggs, A. B., & Hobbs, R. E. (1965). Geology of the Coeur d'Alene district, Shoshone County, Idaho (Vol. 478, pp. 1-145). Washington: UNITED STATES GOVERNMENT PRINTING OFFICE, WASHINGTON.

Hofmann, G.F., & Scheepers, L.J. (2011). Simulating fault slip areas of mining induced seismic tremors using static boundary element numerical modelling. *Mining Technology, 120*(1), 53-64.

Holmberg, R., & Persson, P.A. (1979). *Design of tunnel perimeter blast hole patterns to prevent rock damage*. Paper presented at the Tunnelling '79 London.

Holub, K. (1996). Space-time Variations of the Frequency-energy Relation for Mining-induced Seismicity in the Ostrava-Karvina Mining District. *PAGEOPH, 146*(2), 265-280.

Homand, F., Belem, T., & Souley, M. (2001). Friction and degradation of rock joint surfaces under shear loads. *International Journal for Numerical and Analytical Method in Geomechanics, 25*, 973-999.

Hudyma, M., & Beneteau, D. L. (2012). *Time - A Key Seismic Source Parameter.* Paper presented at the 21st Canadian Rock Mechanics Symposium ROCKENG12 - ROCK ENGINEERING FOR NATURAL RESOURCES.

Ida, Y. (1972). Cohesive force across the tip of a longitudinal-shear crack and Griffith's specific surface energy. *Journal of Geophysical Research, 77*(20), 3769-3778.

Ide, S., & Takeo, M. (1972). Determination of constitutive relations of fault slip based on seismic wave analylsis. *Journal of Geophysical Research, 102*(B12), 27379-27391.

Indraratna, B., Haque, A., & Aziz, N. (1999). Shear behaviour of idealized infilled joints under constant normal stiffness. *geotechnique, 49*(3), 331-355.

Indraratna, B., Jayanathan, M., & Brown, T. (2008). Shear strength model for overconsolidated clay-infilled idealized rock joints. *Geotechnique, 58*(1), 55-65.

Indraratna, B., Welideniya, S., & Brown, T. (2005). New Shear Strength Criterion for Infilled Rock Joints. *Geotechnique, Institution of Civil Engineerings, 55*(3), 215-226.

Itasca. (2009). FLAC3D - fast Lagrangian analysis of continua (Version 4.0). U.S.A.: Itasca Consulting Group Inc. .

Ivins, E. R., & Lyzenga, G. A. (1986). Stress patterns in an interplane shear zone: an effective anisotropic model and implications for the transverse ranges, California. *Philosophical Transactions of the Royal Society A, 318*, 285-347.

Jiang, J.J., Blair, D.P., & Baird, G.R. (1995). Dynamic respoinse of an elastic and viscoelastic full-space to a spherical source. *International Journal for Numerical and Analytical Method in Geomechanics, 19*, 181-193.

Kaiser, P. K., & Cai, M. (2012). Design of rock support system under rockburst conditions. *Journal of Rock Mechanics and Geotechnical Engineering 4*(3), 215-227.

Kanamori, H. (2001). Energy budget of earthquakes and seismic efficiency *Earthquake thermodynamics and phase transformations in the earth's interior* (pp. 293-305): Academic Press.

Kexin. (1995). Maintenance of roadways in soft rock by roadway-rib destress blasting. *China Coal Society, 20*(3), 311-316.

Kim, Y., Peacock, D. C. P., & Sanderson, D. J. (2004). Fault damage zones. *Journal of Structural Geology, 37*, 423-436.

Kostrov, B. (1974). Seismic moment and energy of earthquake and seismic flow of rock. *Izv. Acad. Sci., USSR, Phys. Solid Earth (Engl. Transl.), 1*, 23-40.

Kulatilake, P.H.S., Shou, G., Huang, T.H., & Morgan, P.M. (1995). New peak shear strengh criteria for anisotropic rock joints. *International Journal of Rock Mechanics and Mining Science & Geomechanics, 32*(7), 673-697.

Kulhawy, R. H. (1975). Stress deformation properties of rock and rock discontinuities. *Engineering Geology, 9*, 327-350.

Ladanyi, B., & Archambault, G. (1970). *Simulation of shear behaviour of a jointed rock mass.* Paper presented at the Eleventh Symposium on Rock Mechanics The University of California, Berkeley, California.

Lee, S., Hong, E., Bae, S., & Lee, I. (2006). Modelling of rock joint shear strengh using surface roughness parameter, Rs. *Tunnelling and Underground Space Technology, 21*, 239.

Li, Jianchun, Ma, Guowei, & Huang, Xin. (2010). Anlysis of wave propagation thourgh a filled rock joint. *Rock Mechnics and Rock Engineeing, 43*, 789-798.

Lockner, D. A., Byerlee, J. D., Kuksenko, V., Ponomarev, A., & Sidrin, A. (1991). Quasi-static fault growth and shear fracture energy in granite. *Nature, 350*(6313), 39-42.

Luo, X., Creighton, A., & Gough, J. (2010). Passive seismic monitoring of mine-scale geothermal activity: A trial at Lihir Open Pit Mine. *Pure and applied geophysics, 167*, 119-129.

Lutzenkirchen, V., & Loew, S. (2011). Late Alpine brittle faulting in the Rotondo granite (Switzerland): deformation mechanisms and fault evolution. *Swiss Journal of Geosciences, 104*, 31-54.

Lysmer, J., & Kuhlemeyer, R.L. (1969). Finite dynamic model for infinite media. *Journal of Engineering Mechanics, 95*(EM4), 859-877.

McGarr, A. (1991). Observations constraining near-source ground motion estimated from lacally recorded seismograms. *Journal of Geophysical Research, 96*(B10), 495-508.

McGarr, A. (1999). On relating apparent stress to the stress causing earthquake fault slip. *Journal of Geophysical Research, 104*(B2), 3003-3010.

McGarr, A. (2002). Control of strong ground motion of minig-induced earthquakes by the strength of the seismogenic rock mass. *The Journal of The South African Institute of Mining and Metallurgy*, 225-229.

McGarr, A., & Fletcher, J. B. (2001). A method for mapping apparent stress and energy radiation applied to the 1994 Northridge earthquake fault zone - revisited. *Geophysical research letters, 28*(18), 3529-3532.

McGarr, A., Pollard, D. D., & Gay, N. C. (1979). *Observations and analysis of structures in exhumed mine-induced faults.* Paper presented at the 8th - Analysis of Actual Fault-zones in Bedrock.

McGarr, A., Spottiswoode, M., Gay, N. C., & Ortlepp, W. D. (1979). Observation relevant to seismic driving stress, stress drop, and efficiency. *Journal of Geophysical Research, 84*(B5), 2252-2261.

McGarr, A., Spottiswoode, S. M., & Gay, N. C. (1975). Relationship of mine tremors to induced stresses and to rock properties in the focal region. *Bulletin of the Seismological Society of America, 65*(4), 981-993.

Mikula, P. A. (2002). *the Australian perspective: seismic risk management at Mt Charlotte Gold Mine. Mine seismicity and rockburst management in UG mines.* Paper presented at the ACG International Seminar on Deep and High Stress Mining.

Milev, A. M., Spottiswoode, S. M., Noble, B. R., Linzer, L. M., Zyl, M. Van, Daehnke, A., & Acheampong, E. (2002a). The meaningful use of peak particle velocities at excavation surfaces for the opetimisation of the rockburst criteria for tunnels and stopes: Safety in Mines Research Advisory Committee

Milev, A. M., Spottiswoode, S. M., Noble, B. R., Linzer, L. M., Zyl, M. van, Daehnke, A., & Acheampong, E. (2002b). The meaningful use of peak particle velocities at excavation surfaces for the optimisation of the rockburst criteria for tunnels and stopes: CSIR: Division of Mining Technology.

Morrow, C. A., Shi, L. Q., & Byerlee, J.D. (1982). Strain hardening and strength of clay-rich fault gouges. *Journal of Geophysical Research, 87*, 6771-6780.

Mosinets, V.N., & Garbacheva, N.P. (1972). A seismological method of determining the parameters of the zones of deformaiton of rock by blasting. *Soviet Mining Science, 8*(6), 640-647.

Newland, P. L., & Allely, B. H. (1957). Volume changes in drained triaxial tests on granular materials. *Geotechnique, 7*, 17-34.

Nielsen, S., & Carlson, J. M. (2000). Rutpure pulse characterization: self-healing, self-similar, expanding solutions in a continuum model of fault dynamics. *Bulletin of the Seismological society of America, 90*, 1480-1497.

Noda, H., & Shimamoto, T. (2009). Constitutive properties of clayey fault gouge from the Hanaoka fault zone, southwest Japan. *Journal of Geophysical Research, 114*(B04409), 29. doi: 10.1029/2008JB005683

Nuttli, O. W. (1973). Seismic wave attenuation and magnitude relations for eastern North America. *Journal of Geophysical Research, 78*, 876-885.

Oglesby, D. D. (2008). Dynamic models of earthquakes on the North Anatolian fault zone under the Sea of Marmara: Effect of hypocenter location. *Geophysical research letters, 35*(18).

Oglesby, D. D., & Mai, P. M. (2012). Fault geometry, rupture dynamics and ground motion from potential earthquakes on the North Anatolian Fault under the Sea of Marmara *Geophysical Journal International, 188*, 1071-1087.

Ohnaka, M. (2003). A constitutive scaling law and a unified comprehension for frictional slip failure, shear fracture of intact rock, and earthquake rupture. *Journal of Geophysical Research, 108*(B2), ESE 6-1.

Ohnaka, M., Kuwahara, Y., & Yamamoto, K. (1987). Constitutive relations between dynamic physical parameters near a tip of the propagationg slip zone during stick-slip shear failure. *Tectonophysics, 144*, 109-125.

Ohnaka, M., & Yamashita, T. (1989). A cohesive zone model for dynamic shear faulting based on experimentally inferred constitutive relation and strong source parameters. *Journal of Geophysical Research, 94*(4), 4089-4104.

Okubo, P. G., & Dieterich, J. H. (1984). Effects of physical fault properties on frictional instabilities produced on simulated faults. *Journal of Geophysical Research, 89*(B7), 5817-5827.

Ortlepp, W.D. (1992). Note on Fault-slip motion inferred from a study of micro-cataclastic particles form an underground shear rupture. *PAGEOPH, 139*(3/4), 677-694.

Ortlepp, W.D. (1997). Rock fracture and rockbursts: an illustrative study. *The South African Institute of Mining and Metallurgy*, 255.

Ortlepp, W.D. (2000). Observation of mining-induced faults in an intact rock mass at depth. *International Journal of Rock Mechanics and Mining Science, 37*, 423-426.

Papaliangas, T., Lumsden, A.C., & Manolopoulou, S. (1993). The effect of frictional fill thickness on the shear strength of rock discontinuity. *Int. J. Rock Mech Min Sci & Geomech, 30*(2), 81-91.

Patton, F. D. (1966). *Multiple modes of shear failure in rocks.* Paper presented at the 1st Congre. Int. Soc. Rock. Mech. , Lisbon.

Perrin, G., Rice, J. R., & Zheng, G. (1995). Self-healing pulse on a frictional surface. *J. Mech. Phys. Solids, 43*(9), 1461-1495.

Persson, P.A., Holmberg, R., & Lee, J. (1994). *Rock blasting and explosives engineering*. Boca Raton, Florida: CRC Press, Inc.

Potvin, Y., Jarufe, J., & Wesseloo, J. (2010). Interpretation of seismic data and numerical modelling of fault reactivation at El Teniente, Reservas Norte sector. *2010, 119*(3), 175-181.

Reches, Z., & Lockner, D. A. (1994). Nucleation and growth of faults in brittle rocks. *Journal of Geophysical Research, 99*(B9), 159-173.

Rice, J. R., & Ben-Zion, Y. (1996). *Slip complexity in earthquake fault models.* Paper presented at the Earthquake Prediction: The Scientific Challenge, Irvine, CA.

Ruina, A. (1983). Slip instability and state variable friction laws. *Journal of Geophysical Research, 88*(12), 10359-10370.

Ryder, J. A. (1988). Excess shear stress in the assessment of geologically hazardous situations. *Journal of South African Institute of Mining and Metallurgy, 88*(1), 27-39.

Saeb, S. (1989). *Effect of boundary conditions on the behavior of a dilatant rock joint.* (Ph.D.), University of Colorado at Boulder.

Saeb, S. (1990). *A variance on the Ladanyi and Archambault's shear strength criterion*. Paper presented at the Int. Conf. on Rock Joints, Loen, Norway.

Saeb, S., & Amadei, B. (1992). Modelling rock joints under shear and normal loading. *International Journal of Rock Mechanics and Mining Science, 29*(3), 267-278.

Sagy, A., Brodsky, E. E., & Axen, G. J. (2007). Evolution of fault-surface roughness with slip. *The Geology Society of America, 35*(3), 284-286.

Saharan, Mani Ram. (2004). *Dynamic modelling of rock fracturing by destress blasting.* (PhD), McGill University, Montreal, QC, Canada.

Sainoki, A., Fukuda, D., Kaneko, K., & Kodama, J. (2009). *Elasto-plastic pnalysis of rock slope with geological discontinuity.* Paper presented at the Annual Conference and General Assembly of Korean Society for Rock Mechanics, Suwon, Korea.

Sainoki, A., Fukuda, D., Kodama, J., & Kaneko, K. (2010). *Evaluation of frictional sliding along geological discontinuity in rock slope.* Paper presented at the 6th Asian Rock Mechanics Symposium - Advances in Rock Engineering, the 2010 ISRM-Sponsored International Symposium, New Delhi, India.

Sainoki, A., & Mitri, H. S. (2012). *Dynamic Numerical Modelling of Seismic Response due to Fault-slip*. Paper presented at the Tonnels and Underground Spaces: Sustainability and Innovation, Montreal, Canada.

Sainoki, A., & Mitri, H. S. (2013). *Comparative study of shear strength models for fault-slip analysis.* Paper presented at the Sinorock Shanghai.

Sainoki, A., & Mitri, H.S. (2014a). Dynamic behaviour of minig-induced fault slip. *International Journal of Rock Mechanics and Mining Science, 66c*, 19-29.

Sainoki, A., & Mitri, H.S. (2014b). Dynamic modelling of fault slip with Barton's shear strength model. *International Journal of Rock Mechanics and Mining Science*. doi: 10.1016/j.ijrmms.2013.12.023

Salamon, M. D. G. (1970). Statiliby, instatility and design of pillar workings. *International Journal of Rock Mechanics and Mining Science, 7*, 613-631.

Sartor, T. (1999). *Modelling vibration induced damage from blasting at the Cannington Mine.* (Undergraduate), The University of Queensland, Brisbane, Australia

Schlische, R. W., Young, S. S., Ackermann, R. V., & Gupta, A. (1996). Geometry and scaling relations of a population of very small rift-related normal faults. *Geology, 24*(8), 683-686.

Seidel, J.P., & Haberfield, C.M. (1995). The application of energy principles to the determination of the sliding resistance of rock joints. *Rock Mech. Rock Eng. , 28*(4), 211-226.

Seidel, J.P., & Haberfield, C.M. (2002). A theoretical model for rock joints subjected to constant normal stiffness direct shear. *International Journal of Rock Mechanics and Mining Science, 39*, 539-553.

Shan, C., Javandel, I., & Witherspoon, P. A. (1995). Characterization of leaky faults: Study of water flow in aquifer-fault-aquifer systems. *Water Resources Research, 31*(12), 2897-2904.

Sharafisafa, M., & Mortazavi, A. (2011). *Numerical analysis of the effect of a fault on blast-induced wave propagation*. Paper presented at the 45th U.S. Rock Mechanics / Geomechanics Symposium, San Francisco, California.

Sharpe, J.A. (1942). The production of elastic waves by explosion pressure. *Geophysics, 7*(2), 144-154.

Shearer, P.M. (1999). *Introduction of seismology*. Cambridge: THE PRESS SYNDICATE OF THE UNIVERSITY OF CAMBRIDGE.

Shen, B., Stephansson, O., einstein, H. H., & Ghahreman, B. (1995). Coalescence of fractures under shear stresses in experiments. *Journal of Geophysical Research, 100*(B4), 5975-5990.

Shiption, Z. K., Evans, J. P., Abercrombie, R. E., & Brodsky, E. E. (2006). The Missing Sinks: Slip Localization in Faults, Damge Zones, and the Seismic Energy Budget. *Geophysical Monograph Series*.

Shnorhokian, S., Mitri, H. S., Thibodeau, D., & Moreau-Verlaan, L. (2012). *Analysis of the influence of the mining sequence on a remnant pillar with FLAC3D.* Paper presented at the 21st Canadian Rock Mechanics Symposium, RockEng 12, Edmonton, AB, Canada.

Shnorhokian, S., Mitri, H. S., Thibodeau, D., & Moreau-Verlaan, L. (2013). *Optimizing stope sequence in a diminishing ore pillar: a case study.* Paper presented at the World Minig Congress, Montreal

Sileny, J., & Milev, A. (2008). Source mechanism of mining induced seismic events - Resolution of double couple and non double couple models. *Tectonophysics, 456*, 3-15.

Simon, R. (1999). *Analysis of fault-slip mechanisms in hard rock mining.* (Ph.D.), McGill University, Montreal, Canada.

Sjoberg, J., Perman, F., Quinteiro, C., Malmgren, L., Dahner-Lindkvist, C., & Boskovic, M. (2012). Numerical analysis of alternative mining sequences to minimize potential for fault slip rockbursting. *Mining Technology, 121*(4), 226-235.

Sneilling, Paige E., Godin, Laurent, & McKinnon, Stephen D. (2013). The role of geologic structure and stress in triggering remote seismicity in Creighton Mine, Sudbury, Canada. *International Journal of Rock Mechanics and Mining Science, 58*, 166-179.

Sobolev, G. A. (1986). The study of barrier fracture in relation to earthquake and rockburst prediction. *Pure and applied geophysics, 124*, 811-824.

Swanson, P. L. (1992). Mining-induced seismicity in faulted geologic structures: an analysis of seismicity-induced slip potential. *Pure and applied geophysics, 139*, 657-676.

Tajdus, A., Flisiak, J., & Cala, M. (1997). *Estimation of rockburst hazard basing on 3D stress field analysis.* Paper presented at the The 4th international symposium on rockbursts and seismicity in mines, Krakow, Poland.

Tinti, E., Bizzarri, A., Piatanesi, A., & Cocco, M. (2004). Estimates of slip weakening distance for different dynamic rupture models. *Geophysical research letters, 31*(L02611).

Toledo, P.E.C., & Freitas, M.H. (1993). Laboratory testing and parameters controlling the shear strength of filled rock joints. *Geotechnique, 43*(1), 1-19.

Trifu, C. I., & Urbancic, T. I. (1996). Fracture coalescence as a mechanism for earthquake: obsrevations based on mining induced microseismicity. *Tectonophysics, 261*, 193-207.

Urbancic, T. I., & Trifu, C.-I. (1998). Shear zone stress release heterogeneity associated with two mining-induced events of M 1.7 and 2.2. *Tectonophysics, 289*, 75-89.

Urbancic, T. I., & Trifu, C. (2000). Recent advances in seismic monitoring technology at Canadian mines. *Journal of Applied Geophysics, 25*, 225-237.

Wallace, R. E., & Morris, T. (1986). Characteristics of faults and shear zones in deep mines. *Pure and applied geophysics, 124*, 107-125.

Wang, J. (2009). A numerical study of comparison of two one-state-variable, rate- and state-dependent friction evolutions. *Earthquake Science, 22*, 197-204. doi: 10.1007/s11589-009-0197-9

Wang, J. A., & Park, H. D. (2001). Comprehensive prediction of rockburst based on analysis of strain energy in rocks. *Tunnelling and Underground Space Technology, 16*, 29-57.

White, B. G., & Whyatt, J. K. (1999). *Role of fault slip on mechanisms of rock burst damage, Lucky Friday Mine, Idaho, USA*. Paper presented at the 2nd Southern African Rock Engineering Symposium. Implementing Rock Engineering Knowledge, Johannesburg, S. Africa.

White, B.G., & Whyatt, J.K. (2010). Role of fault slip on mechanisms of rock burst damage, Lucky Friday Mine, Idaho. U.S.A.: The National Institute for Occupational Safety and Health.

Wibberley, C. A. J., & Shimamoto, T. (2003). Internal structure and permeability of major strike-sip fault zones: the Median Tectonic Line in Mie Prefecture, Southwest Japan.

Wilson, J. E., Chester, J. S., & Chester, F. M. (2003). Microfracture analysis of fault growth and wear processes, Punchbowl Fault, San Andreas system, California. *Journal of Structural Geology, 25*, 1855-1873.

Yang, R.L., Rocque, P., Katsabanis, P., & Bawden, W.F. (1994). Measurement and analysis of near-field blast vibration and damage. *Geotechnical and Geological Engineering, 12*, 169-182.

Yuana, F., & Prakash, V. (2008). Use of a modified torsional Kolsky bar to study frictional slip resistance in rock-analog materials at coseismic slip rates. *International Journal of Solids and Structures, 45*, 4247-4263.

Zhang, Y., & Mitri, H. (2008). Elastoplastic stability analysis of mine haulage drift in the vicinity of mined stopes. *International Journal of Rock Mechanics and Mining Science, 45*, 574-593.

Zhi-hua, L., Lin-ming, D., Cai-ping, L., Zong-long, M., & An-ye, C. (2008). Study on fault induced rock bursts. *Journal of china university of Mining & Technology, 18*, 321-326.